UNIVERSITY OF STRATHCLYDE
Department of Physics

High performance III-nitride light-emitting diodes for visible light communications and micro-displays

by

Shuailong Zhang

A thesis presented in fulfilment of the
requirements for the degree of
Doctor of Philosophy

January 2015

Declaration of Authorship

This thesis is the result of the author's original research. It has been composed by the author and has not been previously submitted for examination which has led to the award of a degree.

Signed: _____

Date: _____

Frontispiece

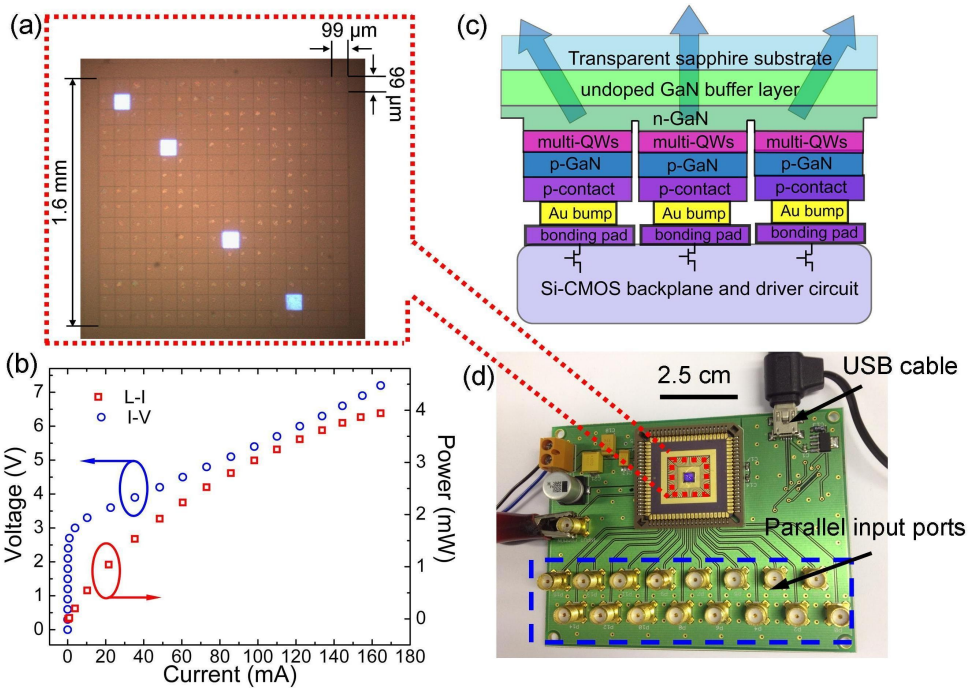

Micro-LED pixels driven by CMOS electronics
(Cover of *Journal of Lightwave Technology*, 31, 1211(2013)).

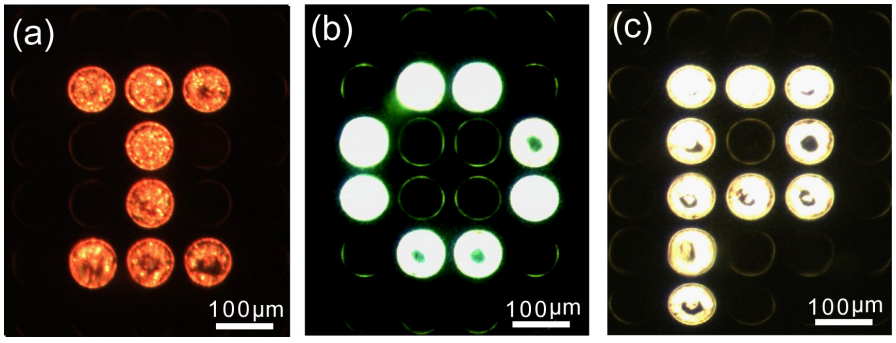

Controllable colour-tunable emission pattern 'IOP' (abbreviation for the Institute of Photonics) generated by a CMOS-controlled micro-LED array.

Dedicated to my parents, Dr Li Zhang & Dr Zheng Zhang

Acknowledgements

This PhD work was completed in Prof. Martin Dawson's group in the Institute of Photonics, University of Strathclyde. Upon the completion of my thesis, I would like to express my heartfelt thanks to the people who helped me throughout my PhD studies.

First of all, I would like to thank my supervisor, Dr Erdan Gu, for giving me this opportunity to study at Institute of Photonics, University of Strathclyde. He inspired me, encouraged me and guided me using his patience, knowledge and wisdom throughout my PhD studies. I also gratefully acknowledge Prof. Martin D. Dawson for his guidance and encouragement. I am deeply impressed by his patience, passion and insights in guiding me to do research throughout the course of my studies. A big thanks goes to Dr Jonathan J. D. McKendry, with whom I spent most of my time. He taught me and guided me in many aspects from literature reading, experiment design to paper writing. Many thanks to my past and present colleagues at the Institute of Photonics, including Dr Ian M. Watson, Dr Yujie Chen, Dr Yanfeng Zhang, Dr Johannes Herrnsdorf and Dr Zheng Gong. In addition, I'd like to thank everyone in the Institute of Photonics for making it such a nice place to work and a place which can be called home. Thanks for making colourful memories that I will cherish forever.

I have been lucky to be involved in several research projects and work with researchers from other institutes and universities. In particular, I would like express my gratitude to Mr Scott Watson and Dr Anthony E. Kelly from Glasgow University for helping me to do measurements on visible light communications, Mr Wafi Zuhdi and Dr Robert Henderson from University of Edinburgh for designing CMOS control chips, Dr Wei Yang, Dr Zhizhong Chen, Prof. Xiaodong Hu, and Prof. Guoyi Zhang from Peking University for doing capacitance measurements and providing novel LED materials. I benefitted a lot from these successful collaborations, which not only improved my experimental skills but also broadened my academic horizons. In addition, I would like to acknowledge the financial support from the Joint Laboratory of Advanced Optoelectronic Materials and Devices, Wuhan University of Technology, and Institute of Photonics, University of Strathclyde. Special thanks should go to my dear friends Jue Wang, Zhiyao Zhao, Chao Wang, Xueya Li, Hainan Xie and David Walls. Thanks for supporting me and looking after me like my brothers and sisters throughout my years of life in Glasgow.

Finally, I would like to thank my parents from the bottom of my heart for their understanding, support and love. If I am gifted with anything, it is surely from my parents who raised me up. I spent very little time with them during my PhD studies but I know that our hearts are always together.

Abstract

III-nitride micro-pixellated light-emitting diodes (micro-LEDs) are a novel format of light source capable of generating micro-scale, spatially and temporally-controllable light patterns. These devices consist of arrays of LED pixels with diameters in the range of 1 μm to 100 μm and emit light across the ultraviolet-blue-green-red part of the spectrum. In addition, compared with conventional broad-area LED devices, micro-LEDs show improved device performance in many aspects, such as high output power densities and the capability to withstand high injection current densities. For these reasons, micro-LEDs allow the study of interesting LED properties in regimes not accessible to conventional broad-area LEDs and also a wide range of novel LED applications.

The research work presented in this thesis focuses on the novel applications of micro-LEDs in visible light communications (VLC) and micro-displays. Due to a reduced current crowding effect and superior thermal management capabilities, micro-LEDs can be driven at very high current densities, resulting in high modulation bandwidths of the devices. For this reason, optical data transmission was demonstrated from individual micro-LED pixels at bit rates of up to 1 Gbit/s using a high-speed probe under a binary amplitude modulation scheme. To make a more practical VLC system, micro-LED devices were integrated with specifically-designed complementary metal-oxide-semiconductor (CMOS) electronics, which allow individual micro-LED pixels to be conveniently controlled via a simple computer interface. Such CMOS-controlled micro-LED devices have been demonstrated for data transmission at bit rates of up to 512 Mbit/s by modulating a single CMOS/micro-LED pixel and 1.5 Gbit/s by modulating four CMOS/micro-LED pixels simultaneously. Apart from the application in VLC, CMOS-controlled micro-LED devices can also be used to implement micro-display systems. A colour-tunable micro-display system capable of delivering high-resolution micro-scale dynamic images and tuning its colour from red to green has been demonstrated based on new LED epitaxial LED structures, micro-LED fabrication, and the CMOS technology.

Other work reported in this thesis includes using micro-LEDs for data transmission in plastic optical fibre and investigating the modulation characteristics of colour-converters such as colloidal quantum dots and light-emitting polymer. A detailed study on size-dependent capacitance in III-nitride micro-LEDs, especially the negative capacitance (NC) effect, has also been reported in this thesis. This capacitance research sheds light on the mechanisms underlying the NC effect and is potentially useful for improving the LED performance for VLC and other applications.

Contents

List of Figures

List of Tables

Abbreviations

AC	Alternating current
AM	Amplitude modulation
APD	Avalanche photodiode
BER	Bit-error ratio
BERT	Bit-error ratio test system
BOE	Buffered oxide etch
CIDs	Consecutive identical digits
CMOS	Complementary metal-oxide-semiconductor
CQD	Colloidal quantum dot
CRI	Colour rendering index
CW	Continuous wave
DC	Direct current
DH	Double heterostructure
DMD	Digital micro-mirror display
EBL	Electron-blocking layer
EDX	Energy-dispersive X-ray
EL	Electroluminescence
EQE	External quantum efficiency
FM	Frequency modulation
FPGA	Field-programmable gate array
GUI	Graphical user interface
ICP	Inductively coupled plasma
IOP	Institute of Photonics
IQE	Internal quantum efficiency
IR	Infrared

LCOS	Liquid crystal on silicon
LD	Laser diode
LED	Light-emitting diode
LEE	Light extraction efficiency
LEP	Light-emitting polymer
MIMO	Multiple-input multiple-output
MOCVD	Metal organic chemical vapour deposition
MOSFET	Metal-Oxide-Semiconductor Field Effect Transistor
MQW	Multi-quantum-well
NC	Negative capacitance
NMOS	N-type MOSFET
NRZ	Non-return-to-zero
OFDM	Orthogonal frequency division multiplexing
OLED	Organic light-emitting diode
OOK	On-off-keying
PAM	Pulse amplitude modulation
PCB	Printed circuit board
PECVD	Plasma-enhanced chemical vapour deposition
PhC	Photonic crystal
PIC	Programmable interface controller
PL	Photoluminescence
PM	Phase modulation
PMOS	P-type MOSFET
POF	Plastic optical fibre
PRBS	Psuedo-random bit sequence
QCSE	Quantum-confined Stark Effect
QW	Quantum well
RCLED	Resonant-cavity LED
RIE	Reactive ion etching
SDM	Space-division multiplexing
SEM	Scanning electron microscope
SMA	SubMiniature Version A
SRH	Shockley-Read-Hall

SSL	Solid-state lighting
TEM	Transmission electron microscope
USB	Universal serial bus
UV	Ultraviolet
VCO	Voltage-controlled oscillator
VCSELs	Vertical Cavity Surface Emitting Lasers
VLC	Visible light communications

Materials

AlGaN	Aluminium Gallium Nitride
AlN	Aluminium Nitride
BBEH-PPV	Poly[2,5-bis(2',5'-bis(2"-ethylhexyloxy)phenyl)-p-phenylenevinylene]
CHDV	1,4-cyclohexyldimethanol divinyl ether
GaAs	Gallium Arsenide
GaAsP	Gallium Arsenide Phosphide
GaN	Gallium Nitride
HF	Hydrofluoric
InAlN	Indium Aluminium Nitride
InGaN	Indium Gallium Nitride
InN	Indium Nitride
PMMA	Polymethylmethacrylate
SiC	Silicon Carbide
THF	Tetrahydrofuran

Chapter 1

Introduction

This thesis focuses on the development of novel III-nitride micro-pixellated light-emitting diodes (micro-LEDs) and their applications for optical communications and micro-displays. As such, this chapter functions as a general introduction to light-emitting diodes (LEDs), with a particular focus on LEDs fabricated from III-nitride materials. The basic concept of using LEDs for optical communications in the visible spectrum, i.e. the concept of visible light communications (VLC), is also introduced. In section 1.1, the historical development of LEDs and their general applications are presented. In section 1.2, the basic operating principles of LEDs are described, along with a detailed introduction of the carrier recombination processes in the LED structures. In section 1.3, the properties of III-nitride materials and the background of III-nitride LEDs are introduced. The challenges and future prospects of III-nitride LEDs are also presented in the same section. In section 1.4, the background of a newly emerging LED-based technology, VLC, is introduced. Finally, an outline of this thesis is given in section 1.5.

1.1 Development and applications of light-emitting diodes

During the last 100 years, significant progress has been achieved in the field of light-emitting diodes (LEDs), making them reliable, bright and efficient light sources for a variety of applications, including familiar every day uses ranging from car headlights to flat panel television (Figure 1.1). Therefore, it is hard to link the modern LED technology with the first LED, which was accidentally produced by British inventor Henry Joseph

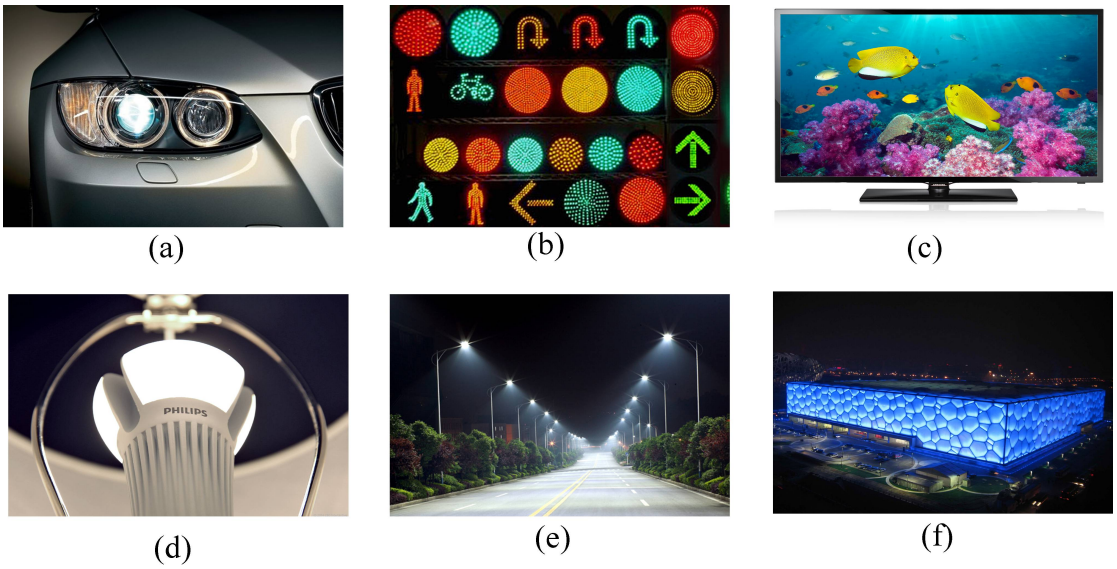

FIGURE 1.1: Typical applications of LEDs: (a) car headlights in BMW 5 series; (b) LED-based traffic light; (c) Samsung F5000 LED back-lit television; (d) Philips 100-watt replacement white-light LED lamp; (e) LED street lighting in Manchester, United Kingdom; (f) LED decorative light used in Beijing National Aquatics Centre, China.

Round in 1907 [1]. There, dim yellowish light was observed by using metal electrodes to touch a crystal-metal-point-contact structure fabricated from Silicon Carbide (SiC). At that time, the material properties were poorly controlled, and the mechanism of light emission was not well understood. In 1928, Lossev reported detailed investigations of the interesting luminescence phenomenon observed in SiC crystals [2]. Although the physical origin of the luminescence was still not fully understood, it was proven that the light was not generated by the visible electromagnetic radiation caused by heat glow (incandescence), but rather in response to the passage of current. The phenomenon where light emission is observed from a material with current passing through was thus termed 'electroluminescence'.

Prior to the 1950s, SiC and II-VI semiconductors had become well known materials for LED research [3]. However, they were later replaced by the III-V compound semiconductors postulated and demonstrated in the early 1950s [4, 5]. The novel man-made III-V semiconductors were proved to be optically very active and thus attracted a lot of research interest. It is generally accepted that the research on III-V semiconductors accelerated the development of LEDs with different emission wavelengths and laid the foundation for modern LED technology. The first infrared (IR) (870nm-980nm) LED based on Gallium Arsenide (GaAs) was developed in 1962 [6, 7]. In the same year, the first commercial red-emitting LED based on Gallium Arsenide Phosphide (GaAsP) was

put into market by the General Electric Corporation [8]. In 1968, Monsanto Corporation started mass production of GaAsP LEDs, indicating the start of the era of solid-state lamps [9, 10]. In the early 1970s, by doping GaAsP with optically active impurities such as nitrogen (N), green-emitting LEDs were achieved, making the emission spectra of LED extend from red to green [11].

Although relatively efficient red-to-green LEDs have been available since the late 1960s, it was not until early 1990s that LEDs capable of covering the blue to ultraviolet (UV) part of the spectrum were developed based on III-nitride materials [12–15]. III-nitride materials were considered as possible candidates for blue and ultraviolet (UV) LEDs as early as the 1960s, and the first single-crystal film of Gallium Nitride (GaN) was produced by Maruska in 1969 [16]. However, due to the low crystal quality and the inability to produce p-type GaN, most of the research aiming at developing III-nitride materials for visible LEDs was terminated in the 1970s. Instead, a lot of effort had been put into work to develop blue-emitting LEDs based on SiC, which can be grown with better crystal quality compared with III-nitride materials. However, SiC LEDs proved be an inefficient (0.03%) approach owing to the material's indirect bandgap nature. The breakthroughs on III-nitride materials began from 1986, when the crystal quality of GaN films was significantly improved by the incorporation of low-temperature Aluminium Nitride (AlN) buffer layer before the deposition of main GaN film [17]. By growing on an AlN buffer layer, the defect-density in the main GaN overlayer can be significantly reduced, which has become a standard process to grow high-quality III-nitride materials. In addition, it was found that the Mg acceptors can be activated by electron-beam irradiation and high temperature post-growth annealing [18, 19]. Thus, the difficulties in achieving p-type GaN had been overcome. These breakthroughs opened the door to the development of efficient visible III-nitride LEDs. In 2014, the Nobel Prize in Physics was awarded jointly to Isamu Akasaki, Hiroshi Amano and Shuji Nakamura for the invention of efficient blue III-nitride LEDs.

After decades of steady effort, it is now possible to fabricate LEDs with light emission ranging across the entire visible spectrum based on nitride, arsenide, and phosphide III-V materials. IR and UV light can also be generated by LEDs. Apart from the success in expanding the emission spectra of LEDs, further improvements were made to reduce the fabrication cost and increase the output power of LEDs by using multi-quantum-well (MQW) active regions, optimised substrate technology, chip-shaping, etc.

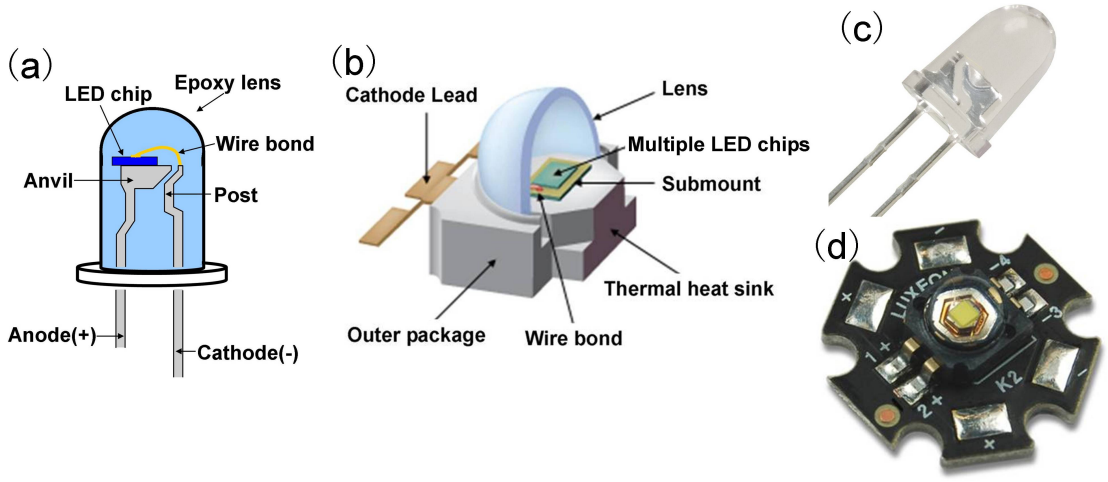

FIGURE 1.2: Schematic packages of (a) a single-chip LED and (b) a high-power multiple-chip LED; images of (c) a single-chip LED and (d) a high-power multiple-chip LED (Luxeon K2 LED packaged on printed circuit board).

[20–22]. A typical LED package, which is familiar to most people, is a semiconductor chip encapsulated by a polymer dome, as shown in Figure 1.2 (a). Such a package usually consists of a single 300×300 μm^2 LED chip bonded on a metal frame via thin gold wires. The metal frame has two leads, one for the positive anode contact and another for the negative cathode contact. The epoxy resin is deposited on the chip in liquid phase and shaped into a dome shape after a thermal curing process to provide mechanical protection for the LED chip and direct the output light beam. The refractive index of the epoxy (∼1.5) also aids light to escape from the chip. For high-power applications, multiple LED chips are normally packaged together, as shown in Figure 1.2 (b). The basic structure of a high-power packaged LED is similar to that shown in Figure 1.2 (a), but requires an additional heat sink to prevent the LEDs being damaged by overheating during operation. Images of a single-chip LED and a high-power multiple-chip LED are shown in Figure 1.2 (c) and (d), respectively. At present, a single-chip LED is available from as low as a few cents per device, with a typical high power LED costing in the region of $5.

As the cost of LED products reduces and high power LEDs across wide visible spectrum become available, new LED applications emerge constantly, as shown in Figure 1.1. Of these applications, the most important one is for 'solid-state lighting' (SSL), creating white light for general illumination [22]. There are several important parameters which indicate the performance of white-light sources for illumination. Luminous efficacy of optical radiation, measured in the units of lumens (lm) per watt (W) of optical power, is

defined as the conversion efficiency of optical power to luminous flux, while the luminous flux, measured in the unit of lm, represents the power perceived by the human eye. Luminous efficiency of a light source, measured in the units of lm per W of electrical input power, is defined as the luminous flux of the light source divided by the electrical input power. In the lighting community, luminous efficiency is often referred to as source luminous efficacy. The colour rendering index (CRI) is a quantitative measure of the ability of a light source to reveal the colours of various objects faithfully in comparison to an ideal light source. In contrast to conventional light sources, LEDs have the capability of converting electricity to visible light with incomparably high luminous efficiency [22–24], with the additional advantage that they have operating lifetimes that exceed 100,000 hours, compared to 1000 hours typical for an incandescent bulb. Therefore, efficient white-light LED lamps can be used to replace traditional lamps, such as incandescent and fluorescent light sources, bringing huge interest in reducing energy consumption and carbon emission. Figure 1.3 shows a comparison of the luminous efficiency of conventional white-light sources with that expected from white LED technology (blue-emitting LED with yellow phosphor). Luminous efficiency of 160-213 lm/W should be attainable for white LEDs in the near future [23]. It is estimated that the energy consumption could be reduced by around 1000 TWh per year, the equivalent of about 230 typical 500 MW coal plants, reducing greenhouse gas emission by about 200 million tonnes, if all conventional white-light sources in the world were replaced by the energy-efficient LED light sources [22]. Figure 1.4 shows the three most popular approaches to achieve white LED light sources, which are a blue LED with yellow phosphors; a UV LED with blue and yellow phosphors; and a device that combines blue, green and red LEDs together. Naturally, each scheme has advantages and disadvantages. The advantage of using a blue LED with yellow phosphor for white lighting is high theoretical luminous efficacy, along with low fabrication cost. However, this scheme has a low CRI, which is not ideal for indoor uses. UV LEDs with phosphor mixtures provide a better CRI but at the expense of low luminous efficiency. The third approach, a combination of three LEDs with different wavelengths, offers dynamic control of the white light and may lead to a higher luminous efficiency than UV-phosphor LEDs, but will be surely the most expensive approach compared with the others.

Despite these limitations and challenges, cost-effective high-performance white LEDs are expected to be available in the next couple of years once mass-produced commercial

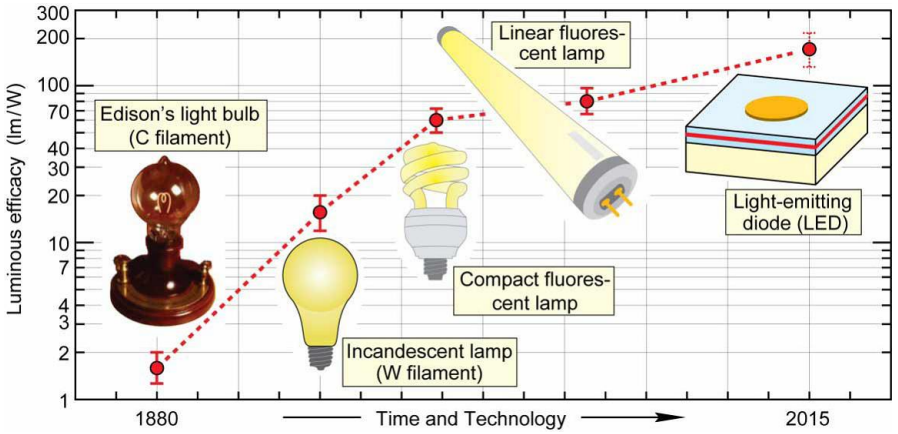

FIGURE 1.3: Comparison of the luminous efficiency (source luminous efficacy) of conventional light sources with LED-based light sources, from [23].

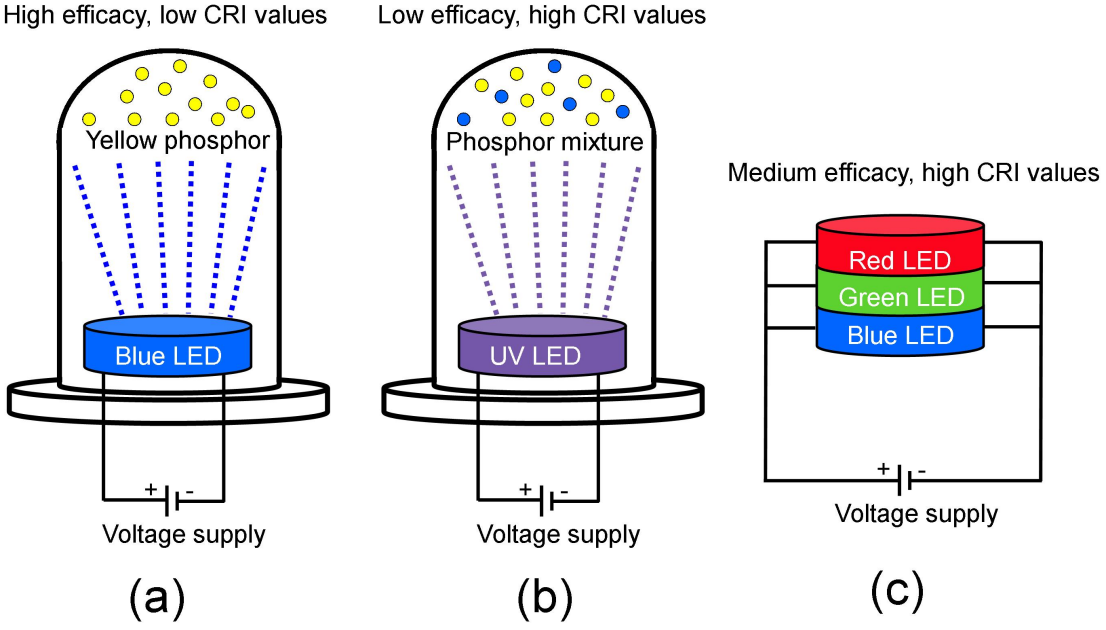

FIGURE 1.4: Three approaches to generate white light based on LEDs: (a) a blue LED with yellow phosphor; (b) an UV LED with blue and yellow phosphor mixture; (c) blue, green and red LEDs combined together.

LEDs have comparable performance metrics to the best LEDs in research labs today. In addition, when averaged over the lifetime of different white-light sources, LED lighting has already become a cheaper solution compared with incandescent bulbs and compact fluorescent lamps and will soon become more so [22]. Therefore, it is anticipated that LEDs will be the ultimate choice for the lighting industry and lead us to a more energy-efficient and brighter future.

1.2 Operating principles of light-emitting diodes

The materials that LEDs are fabricated from, and which enable them to emit light, are semiconductors. Intrinsic semiconductors are pure semiconductors without any impurity atoms and lattice defects. In an intrinsic semiconductor, when an electron breaks free from the electrostatic confinement of its parent atom, it becomes a delocalised electron in the semiconductor and leaves a vacancy in its original place, known as a 'hole'. This hole can be filled by another delocalised electron and the hole itself can be regarded as a positively charged carrier capable of moving freely in the semiconductor. Hence, there are two types of free carriers in a semiconductor, namely electrons and holes. Based on solid-state energy band theory, the periodic atomic arrangement and manifold energy levels of atoms in a semiconductor crystalline material lead to the energy band structure of a semiconductor which consists of a valence band and a conduction band separated by a bandgap. The bandgap represents the energy gap between the valence band and conduction band, and no carrier states can exist in the bandgap. In terms of the energy band theory, free electrons are located at the bottom of conduction band while free holes are located at the top of valence band. The free electrons in the conduction band may fall into the valence band and recombine with the free holes. In this process, the excess energy can be released by the generation of photons and the excess energy is determined by the energy difference between the conduction band and valence band of a semiconductor, i.e. the value of the bandgap. Therefore, the energy and wavelength of the photons emitted by the semiconductor are determined by the value of the bandgap. This relation can be expressed as follows:

$$E_g = E_c - E_v \tag{1.1}$$

$$\lambda = \frac{h \cdot c}{E_g} \tag{1.2}$$

where E_g is the value of bandgap, E_c is the minimum-energy state of the conduction band, E_v is the maximum-energy state of valence band, h is Planck constant and c is the speed of light in vacuum. Therefore, it is possible to generate light in semiconductor materials by injecting electrons into the conduction band of the semiconductor materials

and providing low-energy sites ('holes') in the valence band into which they can recombine, thereby creating light of a wavelength corresponding to the energy gap between the conduction band and the valence band. However, when the electrons recombine with holes, the excess energy can also be released in the form of heat or increased lattice-atom vibrations. Releasing the energy in the form of photons or heat correspond to two important carrier recombination mechanisms in semiconductors, i.e. radiative recombination and non-radiative recombination. For obvious reasons, radiative recombination is the preferred recombination process for LEDs. Details of the two carrier recombination mechanisms will be discussed in the sub-section 1.2.3.

In general, semiconductors can be separated into two categories, namely direct and indirect bandgap semiconductors [25]. Figure 1.5 shows the schematic simplified band structure of direct and indirect bandgap semiconductors and the related electron-hole recombination processes. The energy state in the conduction band and the energy state in the valence band are each characterised by a certain crystal momentum. The crystal momentum represents the allowed momentum of electrons within the crystal and is directly proportional to the electron wavenumber k [25]. Interactions among electrons and holes are required to satisfy the conservation of energy and crystal momentum. For direct bandgap semiconductors, as shown in Figure 1.5 (a), the minimum-energy state in the conduction band and the maximal-energy state in the valence band coincide in k-space. Thus, band-to-band electron transitions can occur directly without the violation of the conservation of crystal momentum. In contrast, in an indirect bandgap semiconductor (Figure 1.5 (b)), the minimum-energy state in the conduction band and the maximal-energy state in the valence band do not coincide in k-space. Therefore, band-to-band electron transitions must occur with the assistance of lattice vibrations (phonons) to conserve momentum. In other words, for radiative recombination to occur in an indirect bandgap semiconductor, the electron transition must also involve the absorption or emission of a phonon, where the phonon momentum equals the difference between the electron and hole momentum. Consequently, the involvement of the phonon makes this indirect transition much less likely to occur compared with direct transition, which is why radiative recombination is far slower in indirect bandgap materials than in direct bandgap ones. Therefore, efficient LEDs are always made of direct bandgap materials such as GaN and GaAs, not indirect bandgap ones such as the previously mentioned SiC.

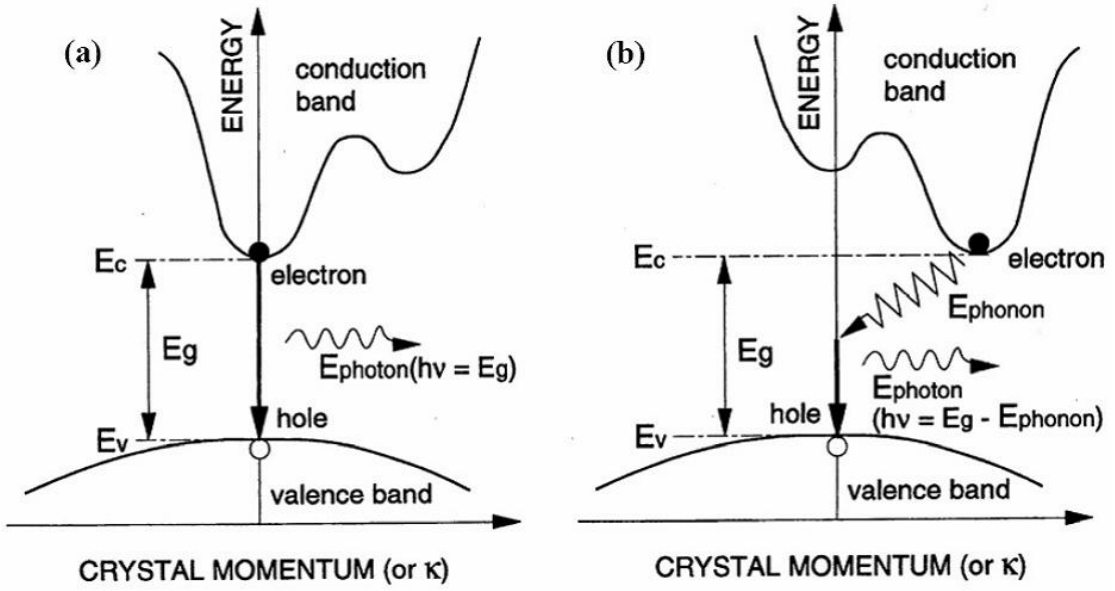

FIGURE 1.5: Schematic band structures of (a) direct and (b) indirect bandgap semiconductors and related electron-hole recombination processes, from [25].

The generation of photons requires free electrons from the conduction band to recombine with the free holes in the valence band. Therefore, it is desirable to fabricate LEDs from materials with a lot of free electrons in the conduction band or holes in the valence band. For intrinsic semiconductor materials, the generation of a negatively-charged electron is always accompanied with the generation of a positive-charged hole. So there are equal numbers of free electrons and holes in intrinsic semiconductors and they are neutrally charged. Semiconductors can also be intentionally doped with dopants (impurities) to make them p-type or n-type. In general, dopants can be classified as donors or acceptors. When a donor atom substitutes an original atom in an intrinsic semiconductor, a free electron is produced in the conduction band without creating a free hole in the valence band. In contrast, an acceptor atom can produce a free hole in the valence band without creating a free electron in the conduction band. Therefore, semiconductors doped with donors are negatively charged and called n-type semiconductors, in which the electrons are the majority carriers; semiconductors doped with acceptors are positively charged and called p-type semiconductors, in which the holes are the majority carriers.

1.2.1 P-n junction (see also chapter 6)

The basic structure of an LED is the p-n junction, which is formed at the boundary or interface between p-type and n-type semiconductors, as shown in Figure 1.6. The

p-n junction is typically created by epitaxial growth technology (i.e. growing a layer of crystal doped with one type of dopant on top of a layer of crystal doped with another type of dopant), rather than being two separate p-type and n-type semiconductors integrated together. A p-n junction consisting of single crystalline material is known as p-n homojunction and the bandgap is the same across the whole homojunction. In contrast, a p-n junction consisting of different crystalline materials is known as p-n heterojunction and the bandgap is different across the heterojunction. In this sub-section, the general introduction of p-n junction will be based on a p-n homojunction.

For an unbiased p-n junction, the density of holes in p-type semiconductors is much higher than that in n-type semiconductors, resulting in a large density gradient of holes at the boundary region between p-type and n-type semiconductors. Therefore, influenced by the density gradient, holes tend to diffuse from hole-rich p-type region towards the electron-rich n-type region and recombine with the electrons there. Similarly, electrons from the electron-rich n-type region tend to diffuse towards the hole-rich p-type region and recombine with the holes there. As a result, the carriers, i.e. electrons and holes, are depleted at the boundary region between p-type and n-type semiconductors due to the diffusion-induced carrier recombination. This region is known as the depletion region of the p-n junction, where free carriers are absent and only ionised dopant atoms are left. As shown in Figure 1.6 (a), positively charged donor atoms are left in the n-type region and negatively charged acceptor atoms are left in the p-type region, creating a built-in electric field which resists the further diffusion of electrons and holes. The voltage of this built-in electric field is known as diffusion voltage (V_D), which is given by [26]:

$$V_D = \frac{kT}{e} \cdot ln\frac{N_A N_D}{n_i^2} \tag{1.3}$$

where k is the Boltzmann constant, T is the temperature, e is the elementary charge, N_A and N_D are the acceptor and donor concentrations, respectively, and n_i is the intrinsic carrier density of the semiconductor. The diffusion voltage represents the barrier that free carriers must overcome in order to reach the region with opposite conductive type. Finally, balanced by the diffusion voltage, carriers in the p-n junction reach thermal equilibrium under zero-bias conditions. As shown in Figure 1.6 (a), the valence and conduction bands through the p-n junction bend to accommodate the Fermi level (E_F) through the p-type and n-type regions. In the p-type region the Fermi level is near the

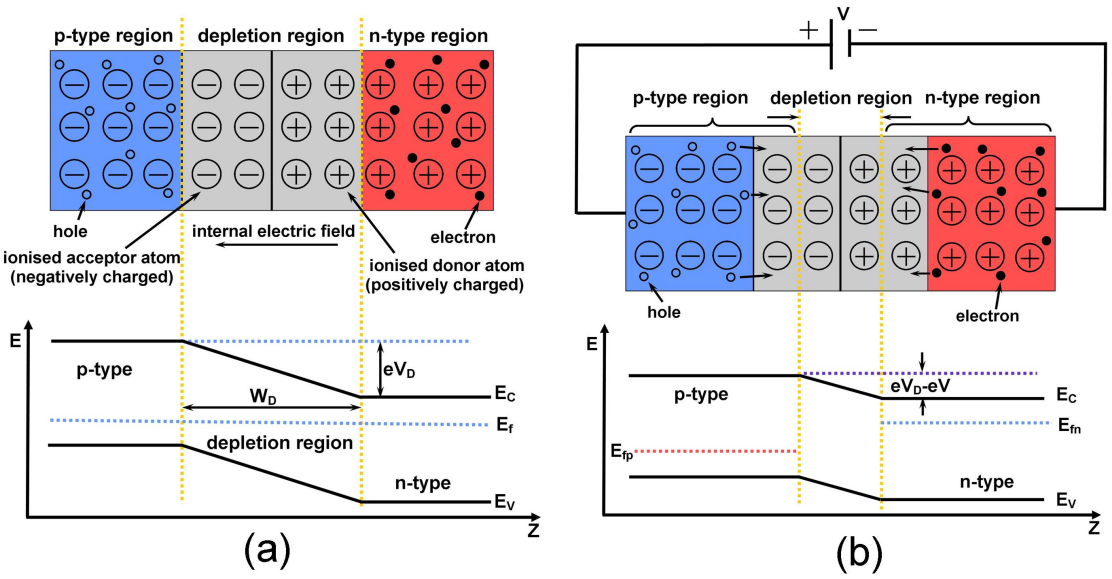

FIGURE 1.6: Schematic of a p-n junction and corresponding energy band diagram under (a) zero bias and (b) forward bias. Here, Z is the spatial dimension perpendicular to the p-n junction.

top of valence band and in the n-type is near the bottom of conduction band, and must remain constant across the junction under zero bias (thermal equilibrium).

When a bias voltage is applied to the p-n junction, the voltage is going to drop across the depletion region as it is highly resistive due to the absence of free carriers. An external bias therefore decreases or increases the built-in electric field in the depletion region for forward or reverse bias, respectively. Under reverse-bias conditions, the built-in electric field in the depletion region is intensified and the width of depletion region (W_D) increases accordingly, which further resists the diffusion of free carriers. Therefore, it is generally considered that no current flows through the p-n junction under reverse-bias conditions. In contrast, under forward-bias conditions, the built-in electric field in the depletion region is weakened and the width of depletion region decreases, as shown in Figure 1.6 (b). Therefore, electrons and holes start to diffuse into the regions of opposite conductive type and current flow increases. Under forward-bias conditions, the carriers no longer maintain equilibrium and the Fermi energy separates to stay consistent with those in the n-type and p-type regions. With the increase of forward bias, more carriers will diffuse into the regions of opposite type where they will recombine and generate photons, thereby resulting in the light emission. Thus, in order to achieve light emission from LEDs, a forward bias needs to be applied.

The current-voltage (I-V) characteristic of a p-n junction is very important to evaluate

its performance as it reflects the flow of carriers in response to a bias voltage. The equation describing the I-V characteristic of an ideal p-n junction was first developed by Shockley and is known as the Shockley equation, which is given as follows:

$$I = I_s \cdot [exp(eV/kT) - 1)] \tag{1.4}$$

$$I_s = eA\left(\sqrt{\frac{D_p}{\tau_p}} \cdot \frac{n_i^2}{N_D} + \sqrt{\frac{D_n}{\tau_n}} \cdot \frac{n_i^2}{N_A}\right) \tag{1.5}$$

where A is the cross-sectional area of the p-n junction, $D_{n,p}$ and $\tau_{n,p}$ are the electron and hole diffusion constants and the electron and hole minority-carrier lifetimes, respectively. Under typical forward-bias conditions, the diode voltage $V \gg kT/e$, and thus $[exp(eV/kT) - 1] \approx exp(eV/kT))$. Using Equation 1.3, the Shockley equation can be rewritten for forward-bias conditions:

$$I_s = eA\left(\sqrt{\frac{D_p}{\tau_p}} \cdot N_A + \sqrt{\frac{D_n}{\tau_n}} \cdot N_D\right) \cdot exp[e(V - V_D)/kT] \tag{1.6}$$

where V is the forward bias voltage and V_D is the diffusion voltage. The exponential part of Equation 1.6 illustrates that the current strongly increases as the applied bias voltage approaches and exceeds the diffusion voltage V_D. The voltage at which the current starts to strongly increase is called threshold voltage, V_{th}. For an ideal p-n junction with highly doped p-type region and n-type region, the Fermi level is uniform across the p-n junction under thermal equilibrium and close to both the top of the valence band of the p-type region and the bottom of the conduction band of the n-type region [26]. Thus, the threshold voltage can be approximated by the bandgap energy divided by the elementary charge

$$V_{th} \approx V_D = E_g/e \tag{1.7}$$

The threshold voltage of III-nitride p-n junctions is around 2.5 to 3.5 V, higher than LEDs fabricated from other semiconductor materials, such as GaAs and GaAsP. This is mainly due to the wide bandgap nature of III-nitride materials. Figure 1.7 shows the I-V curve of a III-nitride p-n juction device fabricated by our group.

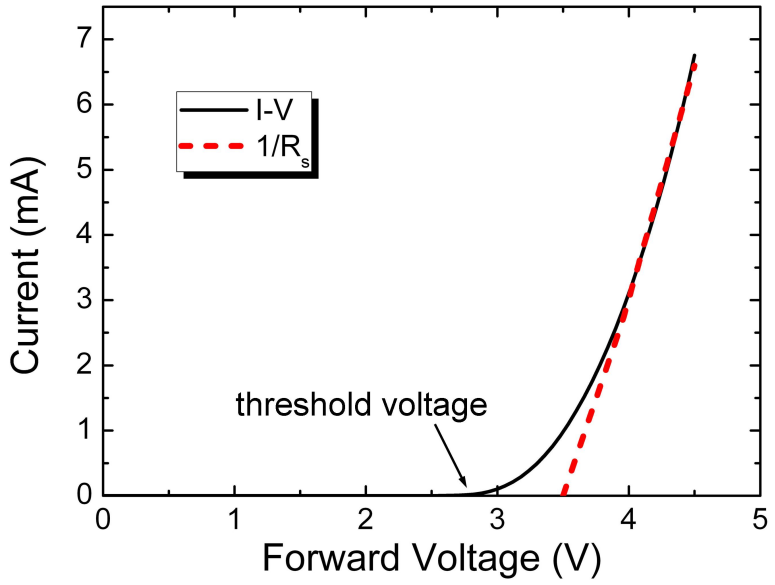

FIGURE 1.7: Typical I-V curve of an LED, from real data taken on one of our III-nitride devices (InGaN LED).

The Shockley equation presents the theoretical I-V characteristic of an ideal p-n junction. To describe the experimentally measured characteristic, the following equation is used:

$$I = I_s \cdot exp[eV/(n_{ideal}kT)] \tag{1.8}$$

where n_{ideal} is the ideality factor of the p-n junction. For a perfect p-n junction, the ideality factor is one, i.e. $n_{ideal} = 1.0$. For real p-n junctions, the ideality factors have values of typically $n_{ideal} = 1.1 - 1.5$. However, values as high as $n_{ideal} = 2.0$ have been found in III-V arsenide and phosphide p-n junctions, and values as high as $n_{ideal} = 7.0$ have been found in III-nitride p-n junctions. A detailed investigation of the ideality factor can be found in [27]. In addition, a real LED device has parasitic series resistance, R_s, and a voltage drop occurs at the series resistance. For III-nitride LEDs, the series resistance is mainly caused by electrical contact resistance and bulk resistance occurring in p-type materials with low hole mobility and concentration. Therefore, the I-V characteristic of a forward biased p-n junction, as given by Equation 1.8, needs to be modified as follows:

$$I = I_s \cdot exp[e(V - IR_s)/(n_{ideal}kT)] \tag{1.9}$$

For sufficiently large voltages, the I-V characteristic of a p-n junction becomes linear and the series resistance is given by the tangent to the I-V curve, as shown in Equation 1.10 and Figure 1.7:

$$R_s = dV/dI \tag{1.10}$$

(R_s is calculated to be 151 Ω in the curve of Figure 1.7.) Apart from contact resistance and material properties, series resistance is also influenced by the device format. Details of the influence of LED device size on series resistance will be presented in chapter 2.

1.2.2 P-n heterojunctions and quantum well structures

For many applications, it is desirable to have an LED device capable of generating light efficiently. Therefore, it is important to increase the radiative recombination rate in LED devices. The radiative recombination rate is given by the bimolecular recombination equation [26]:

$$R_{radiative} = Bnp \tag{1.11}$$

where B is the bimolecular recombination coefficient, and n and p are the concentrations of electrons and holes, respectively. It is clear that a high concentration of carriers increases the radiative recombination rate and makes the LEDs more efficiently in generating light. Figure 1.8 (a) shows the carrier distribution in a p-n homojunction under forward bias. The mean distance a minority carrier diffuses before recombination is known as the diffusion length, which is denoted as L_n and L_p for electrons and holes, respectively. Typically, the diffusion length is of the order of several micrometres in a p-n homojunction, which indicates that the minority carriers are distributed over a long distance and the concentration of minority carriers is low [26]. Therefore, a homojunction design is not beneficial for efficient carrier recombination and a structure that confines the movement of carriers and increases the carrier concentration is required for efficient LED design.

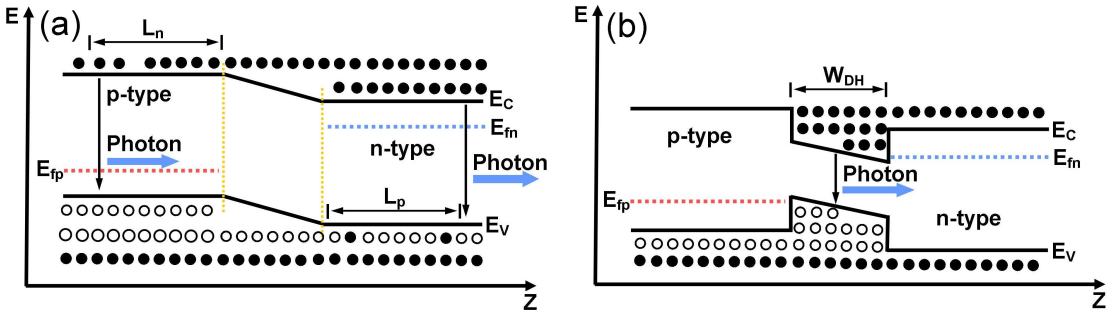

FIGURE 1.8: Distribution of carriers in (a) a p-n homojunction and (b) a p-n heterojunction (a double heterostructure) under forward bias. In homojunctions, carriers diffuse, on average, over diffusion lengths L_n and L_p before recombining. In heterojunctions, carriers are confined by the potential barriers.

In order to achieve high radiative recombination rate, currently all high-performance LEDs employ heterojunctions, which have clear advantages over homojunctions. Heterojuction devices are formed by two types of semiconductors with different bandgap energy. The small-bandgap semiconductor is used as the active region for carriers to recombine and the large-bandgap one is used as the barrier region to confine the movement of carriers. If there are two barriers in a heterojunction, then the structure is called a double heterostructure. Figure 1.8 (b) shows the carrier distribution in a double heterostructure under forward bias. As shown, the potential barriers help confine the carriers injected into the active region of the double heterostructure. This leads to the result that the thickness of the region in which carriers recombine is given by the thickness of active region, W_{DH}, which can be much smaller than the typical diffusion length. Typical diffusion length ranges from 1 μm to 20 μm while W_{DH} normally ranges from 0.01 μm to 1.0 μm. Thus, carriers in the active region of a double heterostructure have a much higher concentration than carriers in a homojunction. Consequently, the radiative recombination rate in a double heterostructure is significantly increased compared with that in a homojunction.

When the active region of a double heterostructure is made thin enough so that it is comparable to de Broglie wavelength of the carriers confined in the active region, the quantum size effect occurs. The de Broglie wavelength is given as follows:

$$\lambda = \frac{h}{p} = \frac{h}{\sqrt{2m^* kT}} \tag{1.12}$$

where h is the Planck constant, m^* is the carrier effective mass, k is the Boltzmann

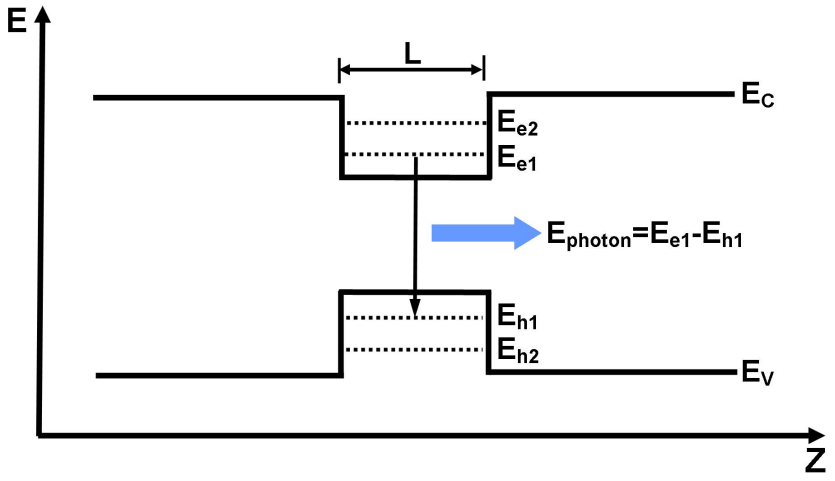

FIGURE 1.9: Band diagram of a QW with quantised energy levels.

constant, and T is the temperature. For III-nitride LEDs, the quantum size effect occurs when the thickness of active region is approximately 10 nm. In this case, the active region of the double heterostructure becomes a quantum well (QW). In the QW, the permitted energy levels of the carriers no longer form an energy band with continuous energy distribution but rather form quantised energy levels with discrete energy values. The values of discrete quantised energy levels can be calculated by solving the Schrödinger equation of the carriers in a one-dimensional potential well. In the case of a one-dimensional infinite-potential well, the discrete quantised energy levels of a carrier are given as follows:

$$E_n = \frac{h^2(n+1)^2}{8m^*L^2}; n = 0, 1, 2, 3, ... \tag{1.13}$$

where h is the Planck constant, n is an integer, m^* is the carrier effective mass, and L is the width of QW. Figure 1.9 shows the band diagram of a QW structure with discrete quantised energy levels. E_{e1} and E_{h1} are the ground energy levels of electrons and hole, respectively (lowest-state energy, $n = 0$). When an LED is in operation, the carriers confined in a QW are restricted to the quantised energy levels with most electrons in the E_{e1} level and most holes in the E_{h1} level. Therefore, the energy of photons emitted by the LED is mainly determined by the energy difference between the E_{e1} level and E_{h1} level. In addition, according to Equation 1.13, the values of the quantised energy levels can be changed intentionally by changing the value of L. For this reason, altering the value of L can be used to control the wavelength of the emitted photons.

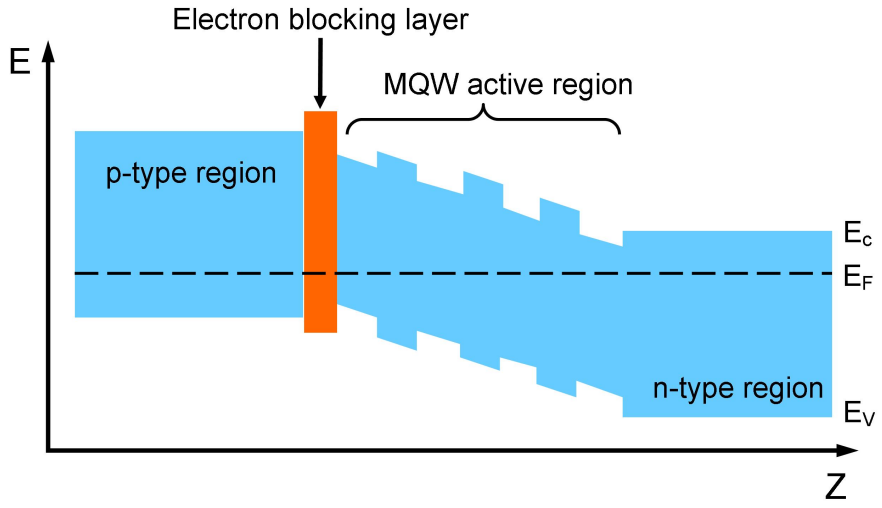

FIGURE 1.10: Illustration of the band diagram of an LED with MQW active region.

Furthermore, since L is very small, the radiative recombination rate is further increased in QW structures compared with that in typical double heterostructures. For these reasons, a QW structure is widely used in high-performance LEDs. As shown in Figure 1.10, the active region of high-performance LEDs normally consists of several closely-spaced QWs, which are referred to as an multi-quantum-well (MQW) structure. Most of the carriers recombine in the MQW and subsequently generate photons according to the energy band structure of an MQW. An electron-blocking layer (EBL) is located at the interface between p-type region and MQW active region. The EBL has higher bandgap energy compared with other adjacent regions and it functions as a potential barrier to prevent energetic electrons overflowing and escaping the MQW, thus increasing the carrier density and radiative recombination rate in the MQW active region.

1.2.3 Radiative recombination and non-raditive recombination

In LEDs, electrons and holes are expected to recombine radiatively, converting the electron energy to photons. However, the non-radiative recombination process cannot be totally eliminated in LEDs. During non-radiative recombination, the electron energy is converted to phonons, i.e. the vibrational energy of lattice atoms. Thus, the electron energy is released in the form of heat. It is obvious that non-radiative recombination is unwanted in LED devices.

Figure 1.11 shows a schematic band diagram illustrating the radiative recombination process and two basic non-radiative recombination processes caused by different physical

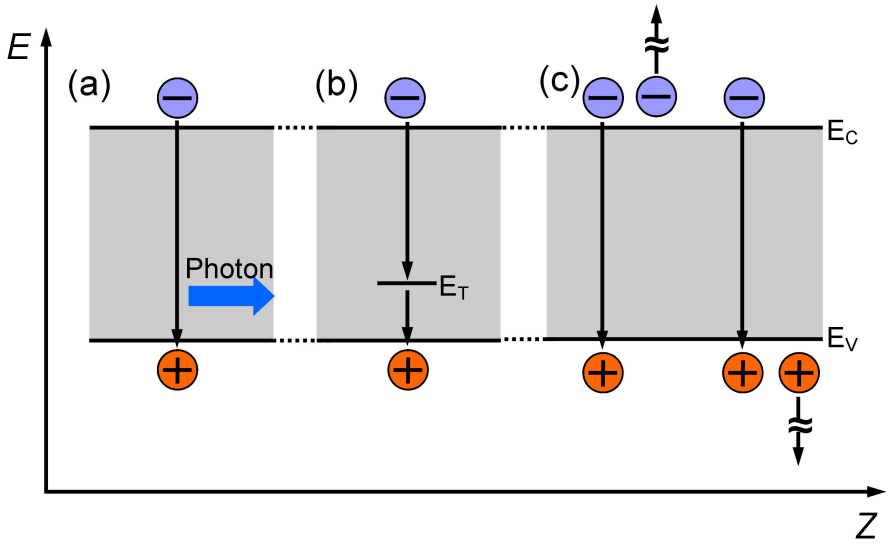

FIGURE 1.11: Band diagram illustrating electron and hole recombination processes: (a) radiative recombination; (b) non-radiative recombination via SRH recombination; (c) non-radiative recombination via Auger recombination. Electrons and holes are shown in blue and orange, respectively.

mechanisms. For radiative recombination (Figure 1.11 (a)), the recombination rate is proportional to the product of electron and hole densities (Equation 1.11). For non-radiative recombination (Figure 1.11 (b) and (c)), there are two basic recombination processes, namely Shockley-Read-Hall (SRH) recombination and Auger recombination. Figure 1.11 (b) shows the process of SRH recombination, which is caused by defects in the crystal structure. These defects include unwanted foreign atoms, native defects and dislocations. For real semiconductors, these defects cannot be totally eliminated. Such defects can form one or several energy levels within the bandgap of semiconductors, represented by the trap level E_T shown in Figure 1.11 (b). These energy levels are efficient non-radiative recombination centres, especially when the energy levels are close to the middle of the bandgap. The SRH recombination rate is closely related to the capture rate of minority carriers by the defects and the concentration of minority carriers. For n-type semiconductors, the SRH recombination rate is given as follows [26]:

$$R_{SRH} = A_n \cdot p \tag{1.14}$$

where A_n is the SRH recombination coefficient for holes and p is the hole density in n-type semiconductors. For p-type semiconductors, SRH recombination rate can be written as:

$$R_{SRH} = A_p \cdot n \tag{1.15}$$

where A_p is the SRH recombination coefficient for electrons and n is the electron density in p-type semiconductors. For LEDs with an MQW active region, most of the non-equilibrium carriers recombine in the MQW. Under direct current (DC) conditions, the hole density and electron density are approximately the same in an MQW, i.e. $p \approx n$. Thus, the SRH recombination rate can be expressed as:

$$R_{SRH} = A_p \cdot n + A_n \cdot p = (A_p + A_n) \cdot n = A \cdot n \tag{1.16}$$

where A is the SRH recombination coefficient and has a unit of s^{-1}.

Figure 1.11 (c) shows the process of Auger recombination, which is another important non-radiative recombination process. In this process, the energy generated via electron-hole recombination is released by the excitation of a free electron high into the conduction band or by the excitation of a hole deep into the valence band. The excited carriers will gradually lose energy by multi-phonon emission and finally reach the band edge. The rate equations of Auger recombination are given by [26]:

$$R_{Auger} = C_p \cdot n \cdot p^2 \tag{1.17}$$

and:

$$R_{Auger} = C_n \cdot n^2 \cdot p \tag{1.18}$$

where C_p and C_n are the Auger coefficients, n is the electron density and p is the hole density. Since two carriers of the same type (either two holes or two electrons) are required for the recombination, the Auger recombination process described in Equation 1.17 is more likely to happen in p-type semiconductors while the Auger recombination process described in Equation 1.18 is more likely to happen in n-type semiconductors.

For LEDs driven under DC conditions, the hole density and electron density are approximately the same in an MQW active region. Thus, the Auger rate equations reduces to:

$$R_{Auger} = (C_p + C_n) \cdot n^3 = C \cdot n^3 \tag{1.19}$$

where C is the Auger coefficient and has a unit of cm^6/s. Due to the cubic carrier concentration dependence, Auger recombination becomes a dominant carrier recombination process at high injection currents.

The internal quantum efficiency (IQE, or η_{int}) of an LED is defined as the ratio between the number of electrons injected into the LED and the number of photons generated by the LED. IQE is an important parameter that evaluates the performance of LEDs. For an ideal LED, each charge quantum-particle (electron) produces a light quantum-particle (photon). However, IQE cannot reach 100% for practical LEDs due to the non-radiative recombination processes mentioned above. The IQE of an LED can be expressed as:

$$\eta_{int} = \frac{P_{int}/(h\upsilon)}{I/e} \tag{1.20}$$

where P_{int} is the optical power emitted from the active region, I is the injection current, and e is the elementary charge. For an LED device with most of the carriers recombining in the MQW active region, I can be expressed as [28]:

$$I = eV_{MQW}(An + Bn^2 + Cn^3) \tag{1.21}$$

where V_{MQW} is the volume of MQW active region. The radiative recombination rate in an MQW active region is given by Equation 1.11. Thus, Equation 1.20 can be modified into:

$$\eta_{int} = \frac{V_{MQW}Bn^2}{eV_{MQW}(An + Bn^2 + Cn^3)/e} = \frac{Bn^2}{An + Bn^2 + Cn^3} \tag{1.22}$$

The radiative recombination lifetime (τ_r) and non-radiative recombination lifetime (τ_{nr}) are defined as:

$$\tau_r = \frac{1}{R_{radiative}} = \frac{1}{Bn^2} \tag{1.23}$$

and:

$$\tau_{nr} = \frac{1}{R_{SRH} + R_{Auguer}} = \frac{1}{An + Cn^3} \tag{1.24}$$

Thus, IQE can also be denoted as:

$$\eta_{int} = \frac{\tau_r^{-1}}{\tau_r^{-1} + \tau_{nr}^{-1}} \tag{1.25}$$

Another important parameter which evaluates the performance of LEDs is the external quantum efficiency (EQE, or η_{ext}), which refers to the ratio of the number of photons emitted by an LED into free space to the number of carriers injected into the LED. In other words, EQE gives the ratio of the number of useful photons to the number of injected charge carriers. The EQE of an LED can be expressed as:

$$\eta_{ext} = \eta_{int} \cdot \eta_{extraction} \tag{1.26}$$

where $\eta_{extraction}$ is the light extraction efficiency (LEE). LEE is defined as the ratio of number of photons emitted into free space to the number of photons generated from the active region, i.e. the escape probability of photons generated in active region. In order to enhance the light output of an LED device, it is important to increase its EQE by improving its IQE and LEE. For improving IQE, wafer materials with better crystal quality and less crystal defects should be used to fabricate the LED. In this case, the SRH non-radiative recombination can be reduced. In addition, LED structures that allow efficient radiative recombination, such as the MQW and EBL, should be employed to increase the radiative recombination rate. For improving LEE, several techniques have been developed to overcome the low escape angle and avoid the wave-guiding effect, including surface roughing, photonic crystal structures, patterned sapphire substrate, etc. [29–31]. The basic idea of these techniques is to increase the number of scattering events and randomise the path of the light rays so that the total reflection effect can be minimised and photons may easily escape the LED structure into free space.

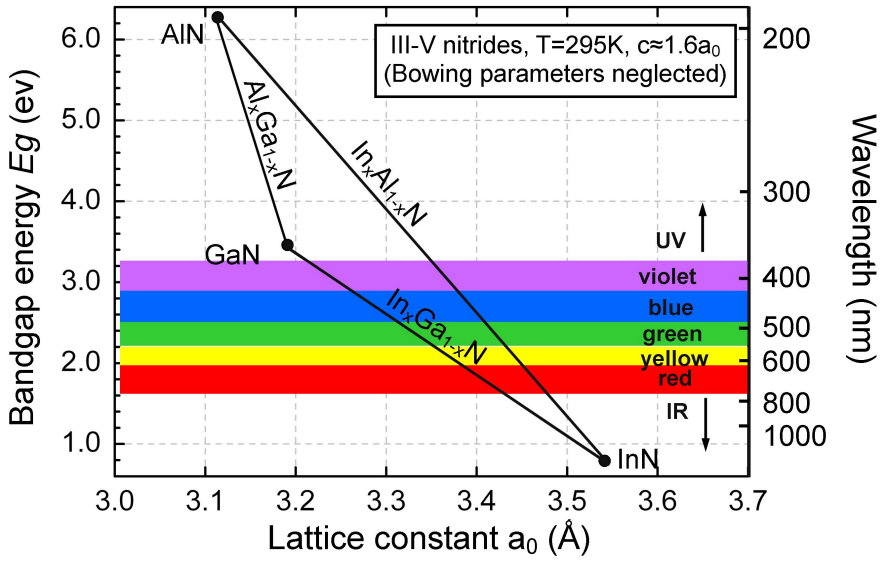

FIGURE 1.12: Bandgap energy and wavelength versus lattic constant for III-nitride materials at room temperature. Data is extracted from [26, 32].

1.3 III-nitride materials and III-nitride LEDs

1.3.1 III-nitride materials

As introduced in section 1.1, III-nitride materials are important semiconductor materials which allow LEDs to efficiently generate light across a wide visible spectrum. For this reason, III-nitride based LEDs have created many new applications and are revolutionising the whole lighting industry. In this thesis, the micro-LED devices are all fabricated from LED wafers based on III-nitride materials. Therefore, it is necessary to introduce the III-nitride materials and their properties in advance, which will be helpful for the further discussion on micro-LEDs and their related applications.

III-nitride materials have three basic binary alloys, Aluminium Nitride (AlN), Gallium Nitride (GaN) and Indium Nitride (InN), and three basic ternary alloys, Indium Gallium Nitride (InGaN), Indium Aluminium Nitride (InAlN) and Aluminium Gallium Nitride (AlGaN). Figure 1.12 shows the bandgap energy versus lattice constant for III-nitride materials. The bandgaps for these materials range from 0.77 eV for InN to 3.42 eV for GaN and 6.28 eV for AlN. By adjusting the relative compositions of individual materials in a ternary alloy, the bandgap energy of the alloy can be 'tuned' in a wide range, which in turn allows the emission wavelength of LEDs made from these III-nitride alloys to span from deep-UV to near-IR. In addition, $In_xGa_{1-x}N$ ternary alloys have direct bandgaps

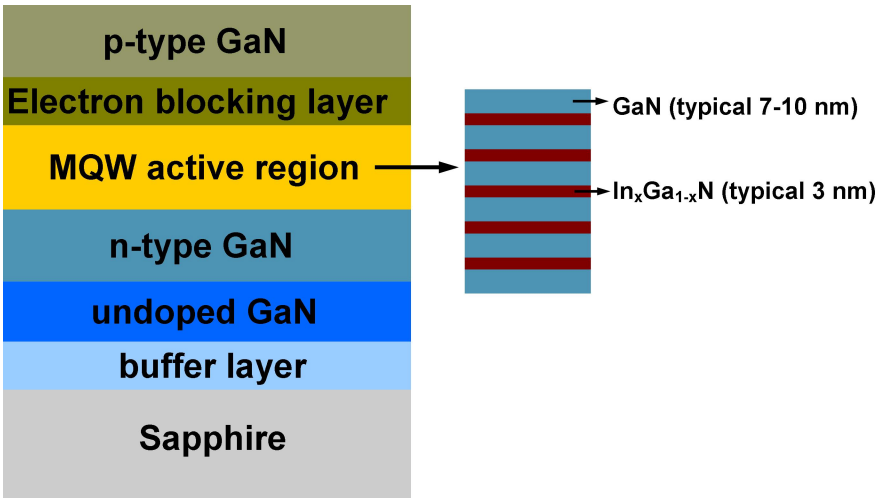

FIGURE 1.13: Schematic epitaxial structure of a typical GaN/$In_xGa_{1-x}N$-based LED wafer grown on a *c*-plane (0001) sapphire substrate. The MQW active region is expanded and shown on the right.

covering the whole visible spectrum, which makes them ideal materials for visible-light LEDs. Here, the subscript notation 'x' represents the relative compositions of InN and GaN in the $In_xGa_{1-x}N$ alloy system, for example $In_{0.3}Ga_{0.7}N$ represents an alloy consisting of 30% InN and 70% GaN. Nowadays, most of the active regions of efficient violet-blue-green emitting LEDs are based on $In_xGa_{1-x}N$ ternary alloys. However, it is difficult to achieve efficient red-emitting LEDs based on high-indium-content $In_xGa_{1-x}N$ ternary alloys. The possible reasons for this difficulty will be discussed later.

The micro-LEDs reported in this thesis are mainly fabricated from LED wafers with standard epitaxial structures. One such epitaxial structure is schematically shown in Figure 1.13. For such structures, the emission wavelength of an LED device is mainly determined by the GaN/$In_xGa_{1-x}N$ MQW active region. By changing the composition of InN and GaN in the $In_xGa_{1-x}N$ alloy, the bandgap of $In_xGa_{1-x}N$ alloy can be tuned, which allows the LED to emit light at a desirable wavelength. Most of III-nitride LED wafers are grown by metal organic chemical vapour deposition (MOCVD) via epitaxial growth technology. In this case, the metal-organic vapours chemically react with each other and deposit materials on the surface of a substrate to form desired crystal structures. The most commonly used substrate for growing III-nitride LED epitaxial layers is sapphire (Al_2O_3). Normally, LED epitaxial layers are grown on a *c*-plane (0001) sapphire substrate [33, 34]. However, the large lattice mismatch between the sapphire and GaN can result in many dislocations in the LED epitaxial layers and reduce the radiative efficiency of the LEDs. To solve this problem, an AlN or GaN buffer layer is first deposited

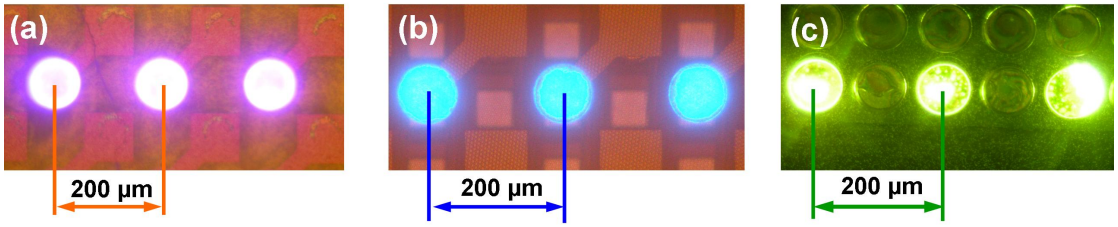

FIGURE 1.14: Microscope image of micro-LED devices with peak emission wavelengths at (a) 405 (b) 450 and (c) 520 nm.

on the sapphire substrate before growing the main epitaxial layers [26]. This buffer layer can relax the strain caused by the lattice mismatch and improve the crystal quality of main LED epitaxial layers. Therefore, by incorporation a buffer layer, the dislocation-density in III-nitride LED epitaxial layers can be significantly reduced. After growing the buffer layer, an un-doped GaN layer is grown, which also functions as a buffer layer for improving the crystal quality of the layers above. On top of the un-doped GaN layer, a Si-doped n-type GaN layer is grown, followed by a GaN/$In_xGa_{1-x}N$ MQW active region, an EBL and a Mg-doped p-type GaN layer. In the GaN/$In_xGa_{1-x}N$-based LED wafer, the EBL is typically made of Mg-doped AlGaN, which has a higher bandgap than GaN and functions as a potential barrier to prevent the overflow and escape of electrons from the MQW. Once the electrons and holes are injected from n-type GaN and p-type GaN into the MQW, they will recombine radiatively and generate photons. Due to the uniformity of each QW layer in the MQW active region, devices made from standard LED wafer materials usually emit light at a single colour. Figure 1.14 shows the microscope images of micro-LED devices made from standard GaN-based LED materials grown on *c*-plane sapphire substrates, with peak emission wavelengths ranging from 405 to 520 nm.

Apart from standard GaN-based LED materials grown on *c*-plane sapphire substrates, III-nitride wafer materials with specifically-designed MQW structures or grown on silicon substrates can also be used to fabricate micro-LED devices to meet different applications [35–38]. Figure 1.15 (a) shows an image of two micro-LED pixels from the same micro-LED array device, fabricated from the same LED wafer material, emitting at green and red under different driving conditions. Details about the corresponding micro-LED devices and their multi-colour performance will be presented in chapter 4, section 4.3. Figure 1.15 (b) shows an image of an LED device made from GaN-based material grown on silicon substrate (GaN-on-silicon). GaN-on-silicon material is cost effective compared

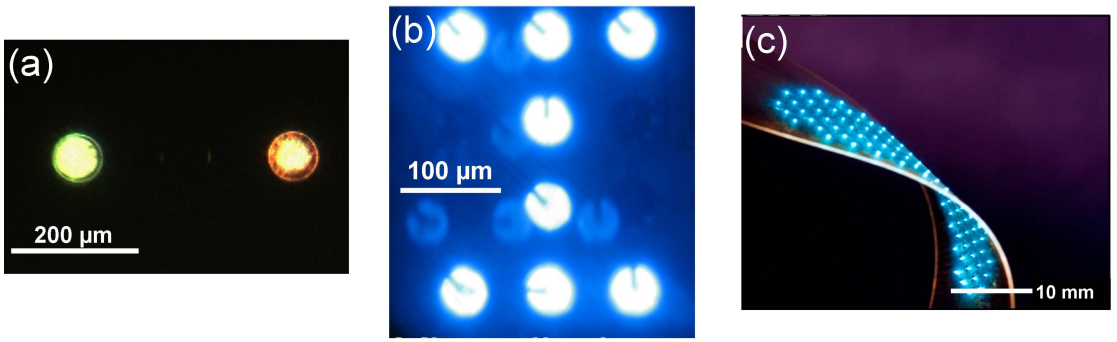

FIGURE 1.15: (a) Microscope image of green and red emission from two micro-LED pixels from the same micro-LED array device. The red pixel is in DC operation at 2 mA and the green pixel is in operation under 0.5% duty cycle at 80 mA; (b) light emission pattern 'I' from a 10×10 micro-LED array made from GaN-on-silicon material [38]; (c) a flexible micro-LED device made from GaN-on-silicon material, from [42].

with the GaN-on-sapphire material [34]. Additionally, such material (GaN-on-silicon) enables flexible LED devices to be fabricated once its silicon substrate is removed and the remaining LED structure is transferred to a flexible substrate, as shown in Figure 1.15 (c). Flexible optoelectronic devices have attracted a lot of research interest due to their wide applications in flexible displays, bio-sensing and other bio-photonics related areas [39–42].

The III-nitride LED materials used in this work all have hexagonal wurtizite crystal structures [32, 43]. Due to the non-centrosymmetric nature of the wurtizite structure, III-nitride materials grown on *c*-plane (0001) sapphire substrates have polarisation charges located at each of the two surfaces of a layer. As a result of these charges, an internal electric field occurs in III-nitride materials, which significantly influences the properties of III-nitride materials and III-nitride-based LEDs [26]. There are two types of polarisation effects in III-nitride materials, namely spontaneous polarisation effect and piezoelectric polarisation effect. The spontaneous polarisation effect is caused by the asymmetry of the atomic bonding as the shift of charge from one atom to another in the basis atoms can produce a negatively charged cation and a positively charged anion. In cubic GaN structures, the cation and anion sublattices are arranged in a way that there is no net polarisation in the material. While in wurtizite GaN structures, the arrangement of cation and anion sublattices can produce a net polarisation in the material [44]. Thus, the direction of the induced internal electrical field is determined by the crystal structure and growth orientation of III-nitride materials. The piezoelectric

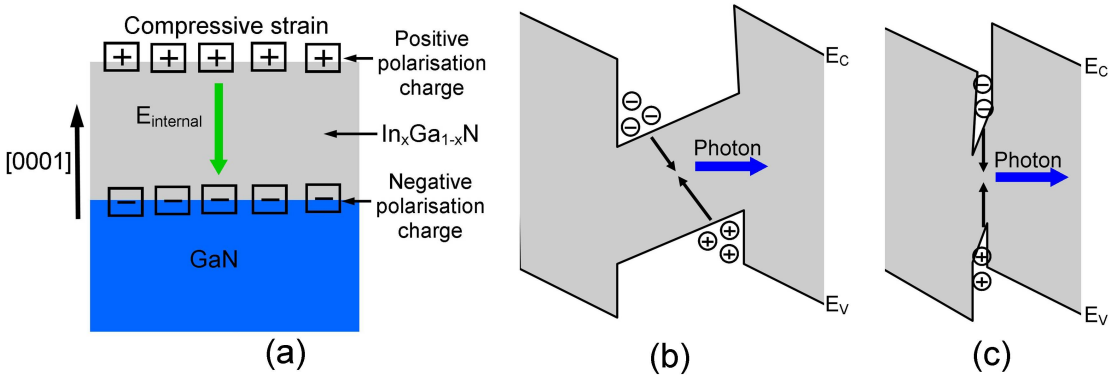

FIGURE 1.16: (a) Surface charges and direction of electric field for strain-induced piezoelectric polarisation in GaN/$In_xGa_{1-x}N$ QW structure; schematic band diagram of (b) thick and (c) thin GaN/$In_xGa_{1-x}N$ QW structure under piezoelectric polarisation effect (substrate on right-hand side).

polarisation effect is caused by the strain in the epitaxial layer, which can be compressive or tensile. Compressive strain in III-nitride materials occurs when a material with larger lattice constant is grown on top of a material with smaller lattice constant. In contrast, tensile strain occurs under the opposite condition. Strain can cause a relative shift between cation and anion sublattices, creating net polarisation in the material. For III-nitride LEDs, the spontaneous polarisation effect is relatively weak but the strain-induced piezoelectric polarisation effect needs to be considered [45–47]. As shown in Figure 1.13, the MQW region of III-nitride LEDs normally consists of several pairs of the GaN/$In_xGa_{1-x}N$ combination. Since the $In_xGa_{1-x}N$ ternary alloy can have a large lattice mismatch to GaN (Figure 1.12), the strong strain-induced piezoelectric polarisation effect can result in a large internal electric field in the MQW region. Figure 1.16 (a) shows the distribution of polarisation charges and the direction of the internal electric field in a GaN/$In_xGa_{1-x}N$ QW structure. A consequence of the internal electric field for the QW structure is shown in Figure 1.16 (b). The internal electric field not only tilts the energy band of QW but also leads to an increased separation of electrons and holes in the QW. In this case, the carrier radiative recombination process is reduced and the redshift of emission wavelength is observed. To minimise the electron-hole separation effect, the thickness of QW layers is normally reduced to 2-3 nm, as shown in Figure 1.16 (c).

The effect of an internal electric field on a QW is known as the quantum-confined Stark Effect (QCSE) [48–50]. As the indium content in the $In_xGa_{1-x}N$ ternary alloy

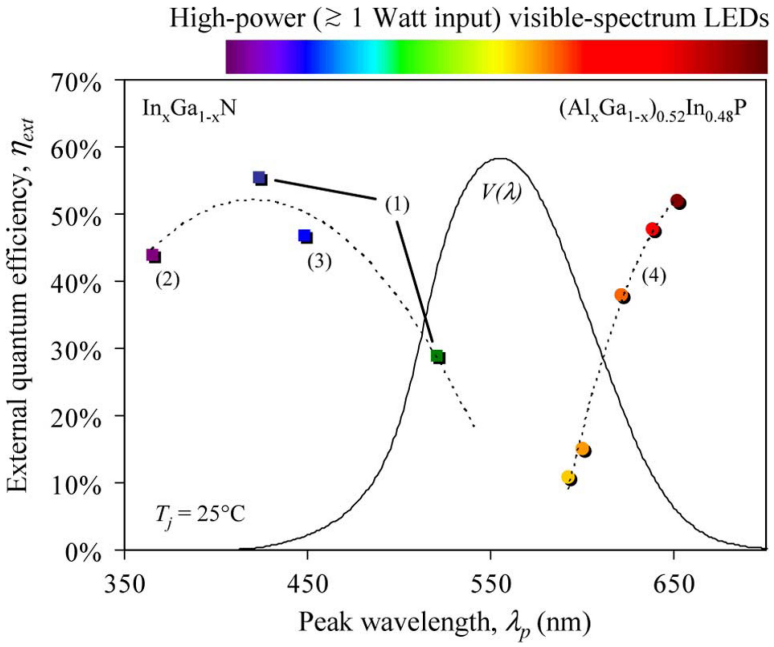

FIGURE 1.17: Summary of EQE versus wavelength for III-nitride LEDs and III-phosphide LEDs, from [24].

increases, the lattice mismatch between $In_xGa_{1-x}N$ and GaN also increases, which results in a stronger QCSE in $In_xGa_{1-x}N$ QWs that emit longer-wavelength light [51]. In addition, miscibility issues make it difficult to form high quality InGaN films when high InN incorporation is attempted. The optimised growth temperature of InGaN alloy is higher than that of InN [52]. Under high growth temperature, the excessive InN compositions can lead to alloy non-homogeneity due to heat-induced clustering effect and may cause the breakdown of the crystallographic structure. Therefore, efficient yellow-to-red III-nitride LEDs are difficult to achieve and the highest achievable In composition in InGaN-based LEDs so far is 0.7 [53]. Additionally, it is still quite challenging to grow efficient green-emitting III-nitride LED materials which have the same high efficiencies as blue-emitting ones [24, 34]. This is known as the 'green gap' in the LED industry, as high-efficiency blue-emitting III-nitride LEDs and red-emitting III-phosphide LEDs are readily available. Figure 1.17 shows the EQE versus wavelength for III-nitride LEDs and III-phosphide LEDs, along with the human eye response $V(\lambda)$ [24]. As shown, the EQE is relatively poor in the green spectral region. The 'green gap' limits many applications of green LEDs, especially their applications for solid-state lighting [22]. One of the possible reasons for the relatively low efficiency of green III-nitride LEDs is the influence of the QCSE. Furthermore, when III-nitride LEDs are under electrical operation, the internal electrical field caused by the polarisation charges can be screened by

the injected carriers, which results in the band flattening of the QW and a blueshift of the emission wavelength [51]. As most of the applications require a constant emission wavelength, the blueshift is generally undesirable. For these reasons, many methods have been proposed to suppress the strain-induced polarisation effect in III-nitride LEDs. For example, micro/nano-scale LED structures have been used to reduce the polarisation effect [54, 55]. Since the edge of LED pillar can relax the strain, the relatively large ratio of the length of LED edge to LED top surface area makes the micro/nano-scale LED format less affected by the polarisation effect and spectral blueshift. More importantly, the growth of non-polar III-nitride materials has been proposed, which can completely remove the polarisation effect in III-nitride merials [56, 57]. In this thesis, the work related to the polarisation effect is the colour-tunable micro-display based on high-indium-content III-nitride micro-LEDs. Details of this work will be presented in chapter 4, section 4.3.

1.3.2 III-nitride LED devices

Figure 1.18 shows two configurations of III-nitride LED devices. Since sapphire is an electrically insulating material, n-type Ohmic contact needs to be made on the n-type GaN. In addition, sapphire has stable chemical and physical properties, which make it difficult to be etched away. Therefore, to form an Ohmic contact on n-type GaN, part of the LED wafer needs to be etched away from the p-type GaN side to expose the n-type GaN material. In this case, both p-type and n-type Ohmic contacts are made on the same side of an LED device. Details of the etching process of III-nitride materials along with other device fabrication processes will be presented in chapter 2, section 2.1. Figure 1.18 (a) shows the top-emission configuration of a typical III-nitride LED device. This is a straightforward LED configuration in which light is extracted from the top p-type GaN side of the device. In order to achieve uniform current injection and a low contact resistance, a p-type Ohmic contact is deposited on the surface of p-type GaN as a current spreading layer. In addition, a thick metal pad for wire bonding is required for top-emission LEDs. However, the current spreading layer and metal pad absorb and block the light emitted from the top surface of LEDs, thus reducing the light output power. To overcome this problem, LEDs with flip-chip configurations have been developed, as shown in Figure 1.18 (b). In this configuration, the n-type and p-type Ohmic contacts are made on the same side of the device, similar to the

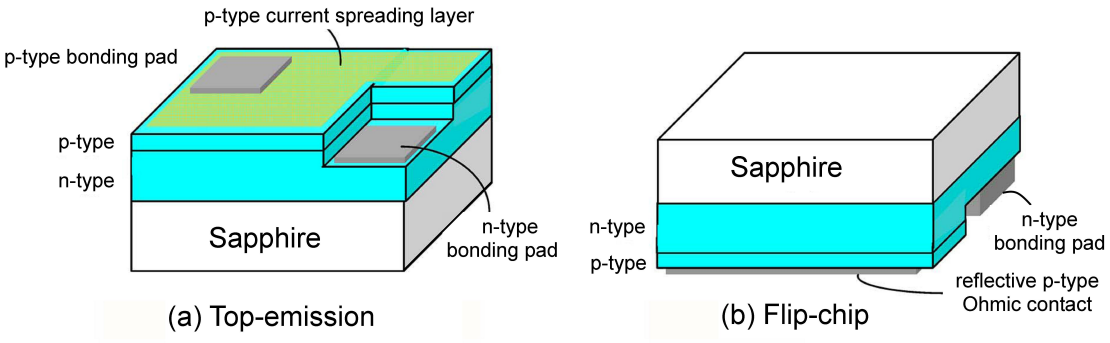

FIGURE 1.18: Two common configurations of III-nitride LED devices: (a) top-emission and (b) flip-chip, from [24]. The micro-LED devices presented in this thesis are all based on these two configurations.

top-emission ones. However, the flip-chip device is operated inverted, with the light extracted from the surface of sapphire substrate. The surface of sapphire substrate is often made rough, which in turn increases the light extraction efficiency of the device. In addition, the current spreading layer and p-metal pad can be made thick. Since a thick current spreading layer reduces the contact resistance and a thick p-metal pad functions as a reflective mirror, the optical output power from the flip-chip LED device is increased. Furthermore, by carefully selecting metal materials with high reflectivity to form current spreading layer and p-metal pad, the optical output of LEDs with flip-chip configurations can be further improved. The III-nitride micro-LEDs presented in this thesis are based on either top-emission or flip-chip configurations. Unless otherwise emphasised, the micro-LEDs used in the experiments refer to flip-chip configurations.

The main differences between micro-LEDs and conventional broad-area LEDs are the device format and LED emitter size. In this thesis, most of the micro-LED devices are developed into an array format, which consists of an array of separate micro-LED emitter pixels with dimensions of 100 μm or less. This contrasts with the large die used in a conventional broad-area LED, which normally have a single emission area ranging from 300×300 μm^2 to 1 mm^2. In other words, a few hundred micro-LED emitter pixels can be fabricated in the same area as a single broad-area LED. Micro-LEDs have many interesting properties compared with their broad-area counterparts. In addition, the array format of micro-LED devices allows them to generate micro-scale spatio-temporal light patterns for many applications. Details of the properties and applications of micro-LED devices will be presented in chapter 2 to chapter 6.

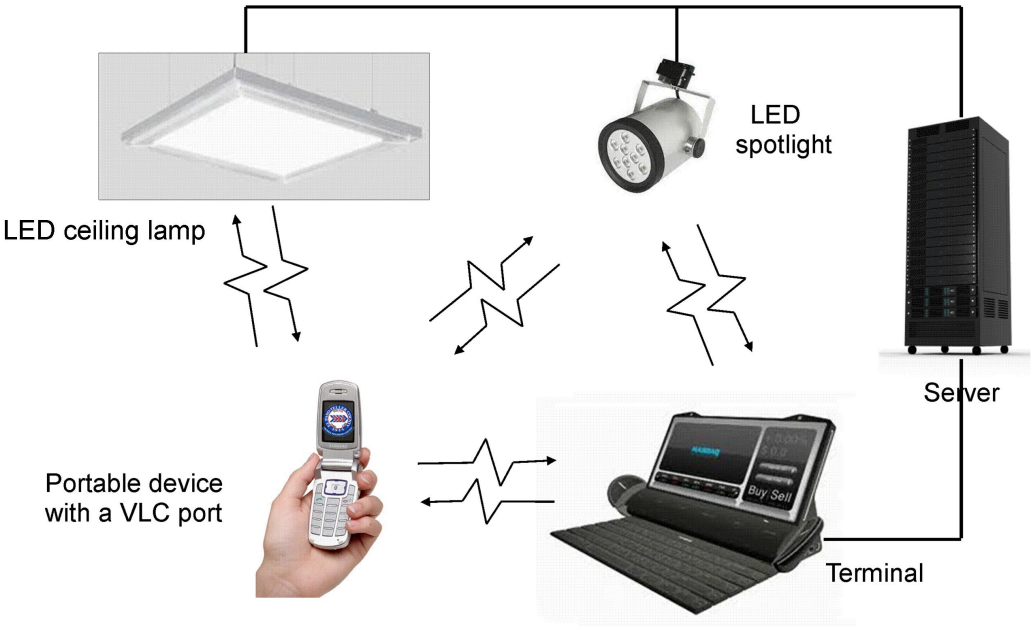

FIGURE 1.19: Illustration of an envisaged indoor VLC network.

1.4 LED-based visible light communications

Visible light communications (VLC) is a data communication technology using visible light (375-780 nm). This technology uses visible sources to transmit optical signals and photo-receivers to receive the transmitted signals, thus establishing high-speed optical communication links between the transmitters and receivers. VLC works by changing the intensity of an optical signal, in which a higher signal intensity normally represents data '1' while a lower signal intensity normally represents data '0'. By changing the intensity of optical signal according to the data input, information can be encoded in the optical signal and subsequently transmitted by the optical transmitter. The history of first VLC system dates back to the 1880s, when Alexander Graham Bell invented the photophone, which transmitted speech on modulated sunlight over several hundred metres [58]. This invention even pre-dates the transmission of speech by radio. However, the development of VLC was very slow due to a lack of suitable optical transmitters: for conventional optical sources, such as fluorescent lamp, a data transmission rate above 15 kb/s is difficult to achieve. The situation changed when the breakthroughs in III-nitride semiconductor materials were achieved in the early 1990s. Since III-nitride LEDs also allow their intensities to be modulated fast enough for data transmission, VLC based on these LEDs, in both free-space and fibre-coupled systems, has become a rapidly growing research area attracting considerable interest [59, 60]. Compared with III-arsenide and

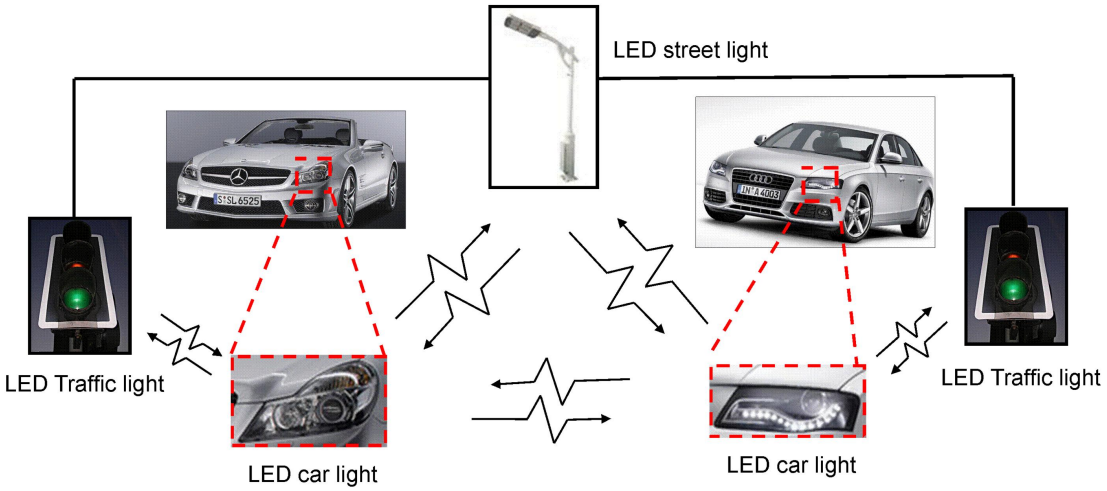

FIGURE 1.20: Illustration of an envisaged street VLC network.

III-phosphide LEDs which were used for VLC as early as 1960s, III-nitride LEDs are capable of generating light across UV-blue-green part of the spectrum, making VLC applicable in a much wider visible spectrum than before. In addition, as the cost of III-nitride LEDs keeps on falling and their efficiencies increasing, there is a potential that they will become the dominant standard for future illumination. Therefore, it is possible to add an extra function on the LED-based illumination light source by utilising modulated LED light for both general illumination and data communications. The approach of using an LED-based light source for such dual applications is also known as Li-Fi, or "light fidelity" technology, which can be used to form a high-speed, bidirectional and easily-accessed VLC network [61]. Figure 1.19 shows the illustration of an envisaged indoor VLC network (Li-Fi system). Apart from indoor VLC network, a street VLC network is also applicable based on LED-based Li-Fi hotspots, as shown in Figure 1.20.

VLC technology is an important complement to conventional radio frequency (RF) communication systems and it is anticipated that this technology will play an important role in future generations of wireless communication networks [60, 61]. VLC technology has the advantage of being able to be used in electromagnetic-sensitive areas such as in aircraft cabins, hospitals, oil refineries and nuclear power plants and without causing electromagnetic interference. In addition, due to the increasing demand of data (Figure 1.21), RF communications has the potential of running out of available radio wave spectrum. RF communications is very close to full spectrum capacity at present, which is known as the 'spectrum crisis' [61]. In contrast, the visible light spectrum is 10,000

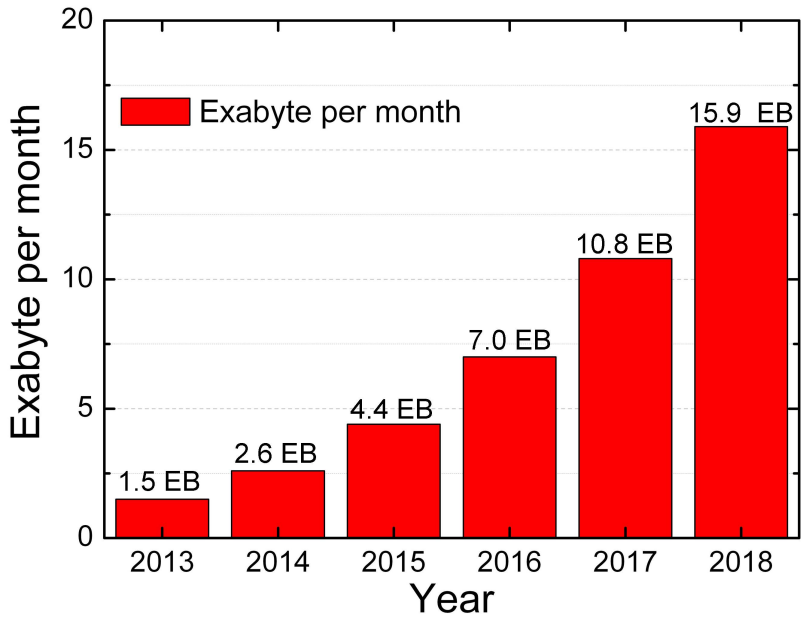

FIGURE 1.21: Global mobile data traffic update and forecast, 2013-2018, from [62].

times larger than the entire radio frequency spectrum. Thus, VLC technology has almost no limitations on spectrum capacity. Besides, VLC technology can be used in places where RF communications is not applicable, such as under water, where water strongly absorbs the radio waves. A data transmission rate of 3.4 Gbit/s based on a commercially available RGB white LED has already been achieved, which is faster than other wireless communication technologies [63]. Moreover, this data rate has a great potential to be improved by using high-speed LED devices and employing advanced encoding and modulation technologies [64, 65]. Although VLC technology is mainly used for short-distance wireless communications, the transmission of modulated LED light from space to ground has also been achieved [66], proving the feasibility of data transmission in long distance using VLC technology.

For fibre-based optical communication systems, IR-emitting GaAs-based LEDs suitable for coupling to silica fibre for data transmission were demonstrated in 1970s [67]. Since then, IR-emitting LEDs have been used for data transmission in silica fibre from low to medium bit rates (up to $\approx$ 1Gbit/s) over a few kilometres [26]. Compared with silica fibre, plastic optical fibre (POF) is cheaper, more robust, and easier to couple light into due to its larger core diameter (typical core diameter 980 microns). Although POF has a high attenuation and the transmission distance is limited to around 100 metres, it can be used for many short-distance networks, as shown in Figure 1.22 (a). Normally, red-emitting GaInP LEDs are used as the light source for data transmission in POF

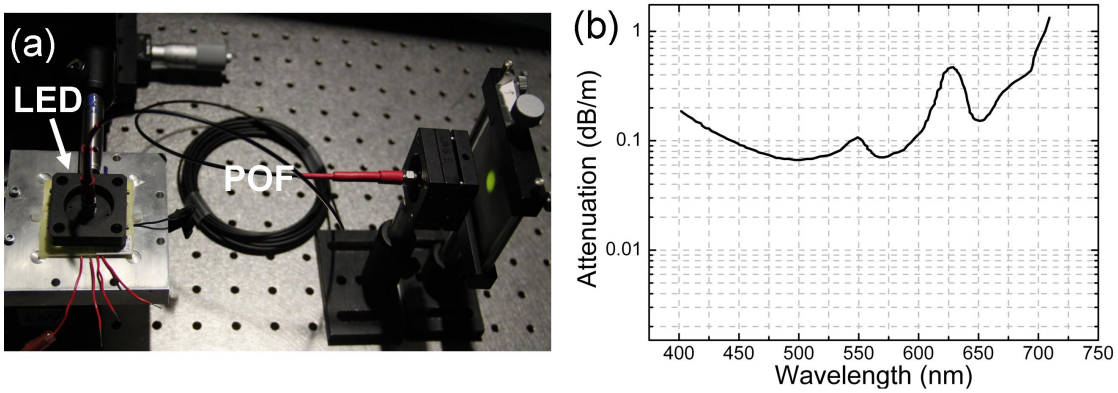

FIGURE 1.22: (a) Transmission of LED light through POF, for applications including vehicles, buildings, and planes; (b) attenuation of a standard PMMA step-index POF (after data sheet of Toray Industries Ltd., 2002).

[26]. Nowadays, POF has been integrated into over 90 models of car sold worldwide and also used for data links in home networks [68, 69]. Most POF links are coupled with either red-emitting Vertical Cavity Surface Emitting Lasers (VCSELs) or red-emitting resonant-cavity LEDs (RCLEDs) for data transmission. This is due to the relative low loss and dispersion in the red region of the spectrum in POF, as shown in Figure 1.22 (b) [26]. In addition, VCSELs and RCLEDs have high directional light output, thus making it easier to couple light into POF. Apart from using red-emitting GaInP LED materials, more recently, there is a growing interest to use III-nitride LEDs for POF-based communications. As shown in Figure 1.22 (b), the optical attenuation minimum in POF is at around 510 nm in the green region, which makes the green-emitting III-nitride LEDs suitable for data communications in POF. In addition, the transmission window in the red region is fairly narrow (630nm-670nm), meaning that red-emitting devices to be used for POF communications require a narrow and well-selected emission linewidth to match the transmission window [26]. In contrast, the transmission window in the green region is wider. Recently, a green GaN-based LED with a modulation bandwidth of up to 400 MHz was reported. By using this green LED, a data transmission rate of 1.07 Gbit/s over 50 metres of POF was achieved [70].

The modulation schemes used in VLC are similar to those used in conventional RF communications. A basic signal can be denoted as:

$$y(t) = A \cdot sin(\omega t + \phi) \tag{1.27}$$

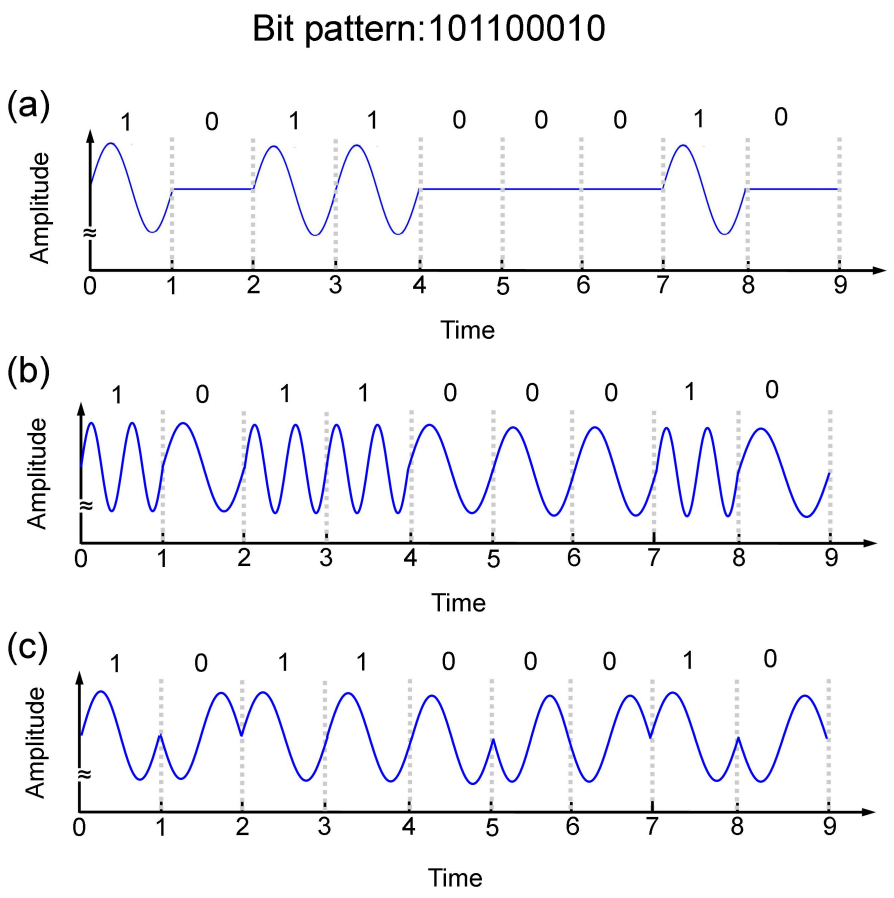

FIGURE 1.23: Illustration of data transmission via (a) AM, (b) FM and (c) PM, respectively.

where A is the signal amplitude, ω is the frequency, ϕ is the phase shift. Depending on which property of the signal is modulated, the modulation schemes can be separated into three basic schemes: amplitude modulation (AM), frequency modulation (FM) and phase modulation (PM). Figure 1.23 (a), (b) and (c) illustrates the transmission of a bit pattern via AM, FM and PM, respectively. By identifying the variation of amplitude, frequency, and phase of the transmitted signal in each modulation scheme, the data can be decoded accordingly. For AM scheme, 'eye diagram' is normally used to evaluate the general performance of the communication system [26]. Details of the eye diagram will be introduced in chapter 3, section 3.3, along with the experimental results. Apart from the basic modulation schemes, much effort has been made to develop high-order modulation schemes for VLC. Such advanced modulation schemes can significantly increase the data transmission rate [60, 71–74]. For example, Orthogonal Frequency Division Multiplexing (OFDM) has been proved to be one such effective modulation scheme [73, 74]. In this thesis, the data transmission results are all achieved based on the basic AM scheme as

the work is mainly focus on the demonstration of novel LED devices and their VLC applications instead of advanced modulation schemes. However, a joint project "Ultra-parallel visible light communications" aiming to integrate high-bandwidth LED arrays with advanced modulation schemes for high-speed parallel VLC is currently under way [75]. Under this project, 3 Gbit/s data transmission has been achieved using a single micro-LED pixel by OFDM modulation and more progress is expected in the near future [65].

This thesis focuses on the development of novel III-nitride micro-LEDs and their applications. As for VLC, micro-LEDs are potentially interesting data transmitters. Compared with conventional broad-area LEDs, micro-LEDs have been demonstrated to have higher modulation bandwidths. In addition, the array nature of micro-LED devices allows for individually modulated pixels in the array to be used for parallel multiple-channel data transmission, which can increase the data transmission capacity significantly. Apart from data transmission in the free space, micro-LEDs can also be used for POF-based communications. Investigation of the modulation characteristics of micro-LEDs along with their data-transmission performance will be presented in detail in the following chapters.

1.5 Outline of the thesis

In this chapter, a general introduction of LED devices, especially III-nitride LED devices, has been given. In addition, a newly emerging LED-based technology, VLC, was also introduced. From chapter 2 to chapter 6, the experimental results and related analysis will be presented in detail. In chapter 2, the fabrication process of micro-LED devices will be first presented. Then, the electrical, optical and modulation properties of the micro-LED devices will be investigated. In chapter 3, complementary Metal-Oxide Semiconductor (CMOS)-controlled micro-LED arrays will be introduced. The performance of CMOS-controlled micro-LED arrays and their applications for VLC will be mainly presented in this chapter. Chapter 4 will demonstrate the use of various micro-LED devices for micro-display applications. A colour-tunable CMOS-controlled micro-display system capable of delivering dynamic images will be presented in this chapter. In chapter 5, micro-LED devices will be used for POF-based data transmission. In addition, the modulation characteristics of different colour-converters will also be investigated in

this chapter. In chapter 6, the capacitance effect of micro-LEDs, especially the negative capacitance (NC) effect, will be systematically studied. Particularly, size-dependent capacitance of micro-LEDs and related analysis will be presented to provide insight into the underlying physics of the NC effect observed in micro-LED devices. Finally, conclusions of the work in this thesis, along with some future perspectives, will be given in chapter 7.

Chapter 2

Fabrication and characterisation of micro-pixellated light-emitting diodes

In this chapter, we will introduce the fabrication of micro-pixellated light-emitting diodes (micro-LEDs) and investigate their modulation characteristics. This chapter contains four individual but closely related sections. Firstly, the main techniques used for micro-LED fabrication are presented in section 2.1. Secondly, a summary of micro-LED devices with different designs and configurations is presented in section 2.2. The electrical and optical properties of the micro-LED devices are also investigated in the same section. Thirdly, the modulation characteristics of micro-LEDs are investigated in section 2.3. Their superior modulation performance and related issues are also discussed and analysed in detail. Finally, a summary of this chapter is presented in section 2.4.

2.1 Micro-LED device fabrication

The performance of micro-LEDs for various applications is highly dependent on the LED material quality and how these micro-LED devices are fabricated. Micro-LED devices fabricated from the same LED wafer material under the same design but with different fabrication processes and conditions can result in very different electrical and optical

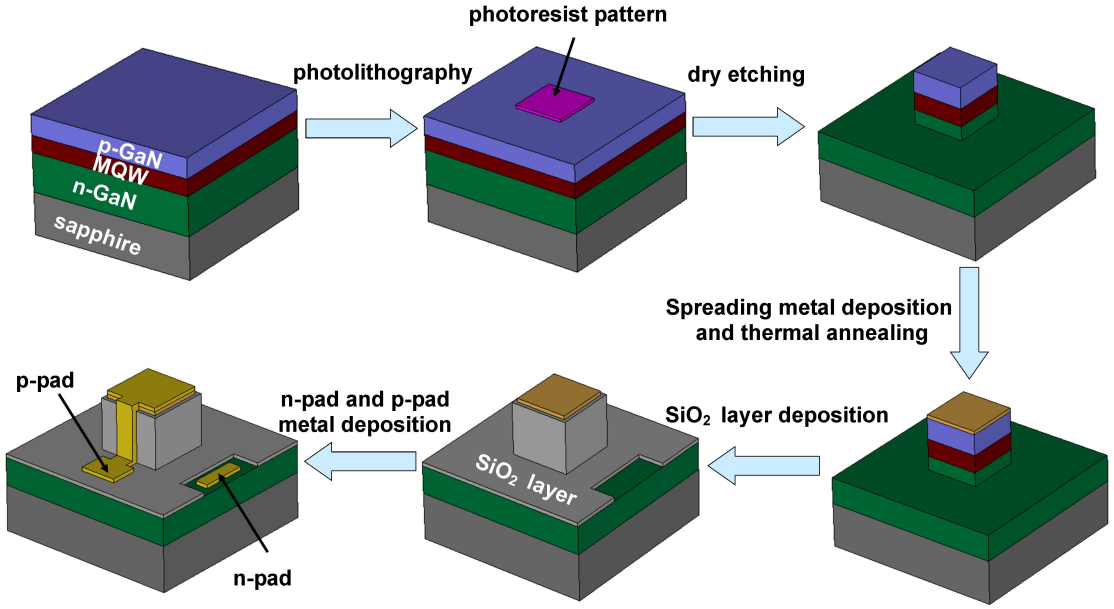

FIGURE 2.1: Schematic process flow for fabricating III-nitride micro-LEDs.

characteristics. In this section, we will introduce the main steps and related techniques used for micro-LED fabrication.

Most micro-LED devices used in this research are made from commercially available high-power III-nitride wafer materials grown on *c*-plane sapphire substrates [76, 77]. A detailed introduction to III-nitride wafer materials can be found in chapter 1, section 1.3. The typical fabrication process of III-nitride-based micro-LED device is schematically shown in Figure 2.1. The main steps include pattern definition via photolithography, pattern transfer via plasma dry etching and formation of individual p-type and n-type metal contacts via metal deposition. However, due to the challenges invovled in the formation of micro-LED structures, additional steps and techniques are required for device fabrication or to improve the device performance. In the following sub-sections, I will overview the main techniques used for micro-LED fabrication and discuss the relevant challenges. Methods to meet these challenges and to improve the device performance are also presented.

2.1.1 Photolithography

Pattern definition is the crucial first step to transfer a designed pattern from a template or mask to a target sample or substrate. In micro-fabrication, a common and widely-used technique for pattern definition is photolithography, which has been developed with

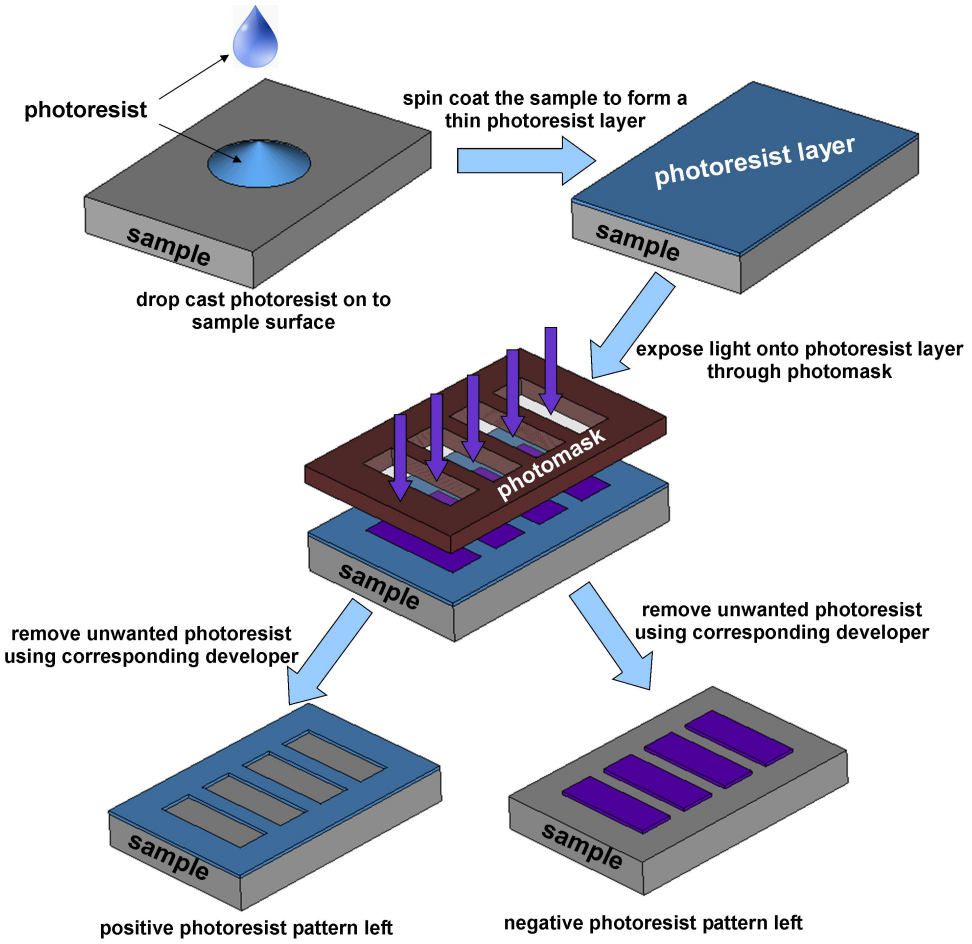

FIGURE 2.2: Schematic process of photolithography to form positive and negative photoresist patterns.

the booming of the modern semiconductor industry and has achieved great success in mass production of large scale integrated circuits. Photolithography technology uses light along with a photomask to generate patterns on to a special photo-sensitive layer, known as a photoresist layer.

Figure 2.2 shows the basic process of photolithography. The first step is to spin coat a layer of photoresist onto the surface of the sample. Usually, liquid photoresist is drop cast onto the sample surface and then the sample is spun up to a certain speed to generate a spin-coated thin-film photoresist layer with even thickness on top of the sample. This photoresist layer is exposed with light through the photomask, which contains specifically-designed patterns consisting of clear and opaque regions. The properties of the photoresist under the clear regions are changed due to a photochemical reaction between the photoresist and exposure light while the properties of the unexposed photoresist remain the same. After this light-exposure process, the sample is dipped into

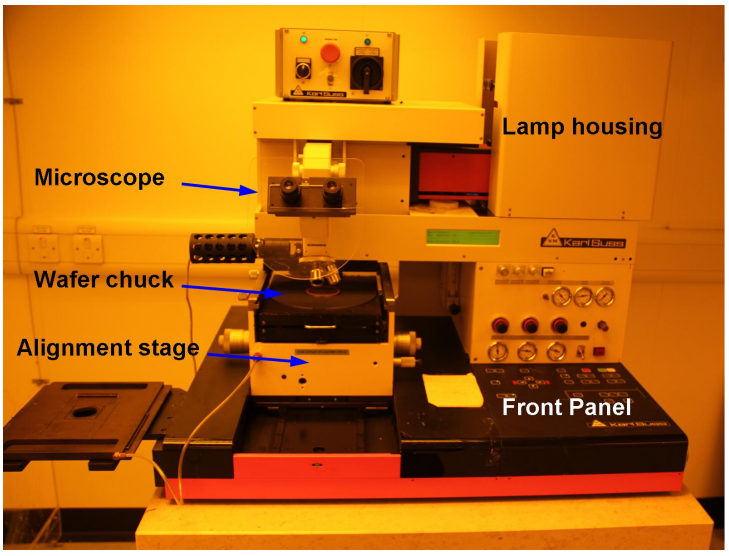

FIGURE 2.3: Image of the Karl Suss MA6 Mask Aligner used for mask alignment and light exposure in the photolithography process.

a suitable developer to remove unwanted photoresist and keep the desired photoresist pattern on the sample. As shown in Figure 2.2, if a positive photoresist layer is used to define the pattern, the final photoresist pattern left on the sample should be identical to the photomask pattern as the exposed photoresist is removed by the developer. Alternatively, if a negative photoresist is used to define the pattern, the final photoresist pattern left on the sample should be complementary to the photomask pattern as the unexposed photoresist is removed by the developer. Although the wavelength of the exposure light used for pattern definition varies depending on the chemical properties of the photoresist material, ultraviolet (UV) light is most widely used. In this work, a Karl Suss MA6 Mask Aligner is used for pattern definition, as shown in Figure 2.3.

Apart from conventional photolithography, maskless pattern definition technologies have also been developed, such as laser/micro-LED writing, inkjet printing and dip-pen writing. As the traditional photolithography requires a photomask with high-resolution pattern features, which is not only expensive but also inflexible in changing patterns, maskless pattern writing has its own advantages and attractive points. Full details about various maskless pattern writing methods and how they are implemented to define photoresist patterns can be found elsewhere [78–80].

2.1.2 Wet etching

Wet etching refers to a process that dissolves unwanted material and removes it subsequently from a substrate using chemical solution. The chemical reaction between the material and chemical solution occurs universally or selectively depending on their chemical characteristics, which can be utilised to remove the unwanted material thoroughly from a substrate or to define a desired pattern on the substrate. For micro-LED device fabrication, hydrofluoric (HF) acid solution is often used to wet etch SiO_2 layers. In our laboratory, the SiO_2 layer is deposited by plasma-enhanced chemical vapour deposition (PECVD) and used as a standard isolation layer for different structures of micro-LEDs. However, pure HF solution reacts intensely with the SiO_2 and has a very high etching rate. Therefore, buffered oxide etch (BOE) is normally used instead of pure HF solution to achieve a more controllable and smooth SiO_2 etching process. The BOE solution used for etching SiO_2 layers is a mixture containing a 6:1 volume ratio of 40% NH_4F in water to 49% HF in water. Using it gives an etching rate of about 100 nm per minute for the SiO_2 layer deposited by PECVD.

2.1.3 Dry etching

Dry etching refers to a process that uses gaseous etchants to remove part of the material from the exposed surface of the sample. There are mainly two mechanisms in dry etching, namely, physical ion bombardment and pure chemical etching. Physical ion bombardment is a dry etching method that uses high-energy ions to remove the material from the sample surface directly and the etching rate is highly dependent on the flux and energy of the applied ions. Pure chemical etching is another dry etching method that uses gaseous etchants to form easily-removed volatile byproducts on the sample surface through chemical reaction. The etching rate of pure chemical etching is highly correlated with the particular chemical reaction that occurs on the exposed sample surface between the gaseous etchants and the etched material. Figure 2.4 (a) shows the schematic process of dry etching.

In our work, plasma dry etching was used to etch SiO_2 and GaN-based materials in the fabrication of III-nitride micro-LED devices. Since wet etching normally produces an isotropic etching profile with low etching resolution, plasma dry etching is more desirable

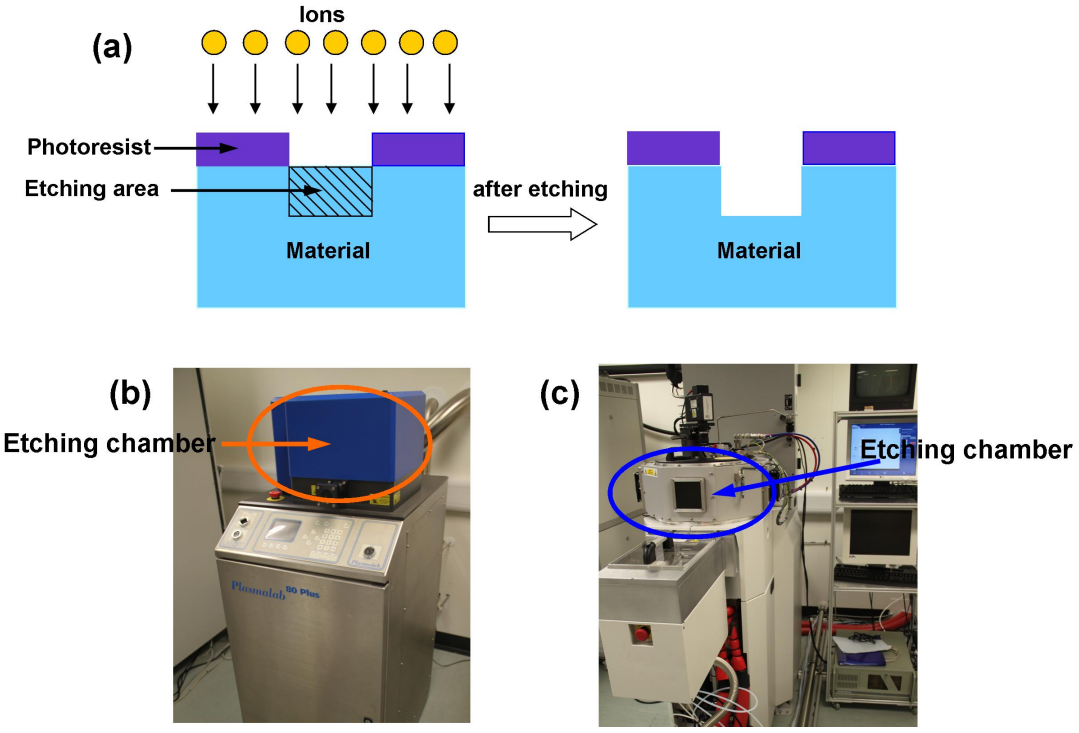

FIGURE 2.4: (a) Schematic diagram of the dry etching process, (b) image of the RIE system and (c) image of the ICP system.

in terms of forming structures with small features that require high etching accuracy and selectivity. A plasma, which is an ionised gas produced by applying a voltage to neutral gas under specific conditions, generates an equal number of free positive and negative ions with high chemical activity. These ions can react with the etched material at the sample surface, hence achieving the purpose of chemical etching in the due course. In addition, the plasma etching includes physical ion bombardment at the sample surface, which may change the chemical properties of the material and accelerate the overall etching process accordingly. In the micro-LED device fabrication, we use two plasma etching tools, namely a reactive ion etching (RIE) system and an inductively coupled plasma (ICP) system. The RIE system is mainly used for etching SiO_2 isolation layer. The ICP system is a modified RIE system with an inductively coupled plasma source which incorporates a radial inductive coil design. Compared with the plasma source in the RIE system, the radial inductive coil can generate high-density plasma, which increases the etching rate significantly. In the micro-LED device fabrication, Ar and Cl_2 plasma are used as the dry etching sources. More details about the two plasma etching systems used for micro-LED device fabrication can be found in the relevant literature [81]. Images of the RIE and ICP systems are shown in Figure 2.4 (b) and (c),

respectively.

2.1.4 Formation of metal contacts

To achieve a fully functional micro-LED device, formation of metal contacts through metal deposition is an important step in the device fabrication process. There are two different metal deposition methods to deposit different metals on p-type and n-type GaN to form contacts, namely electron-beam evaporation and magnetron sputtering.

For p-type GaN, a thin Ni/Au (10 nm/20 nm) bi-layer is normally deposited and used as a current spreading layer and contact metal. Due to the high resistivity of p-type GaN materials, a current spreading layer is required to ensure the uniformity of current injection in p-type GaN [26]. In addition, Pd-based current spreading layers for p-type GaN have also been developed to enhance the performance of micro-LED devices [82]. All of the current-spreading p-contact metals are deposited in a vacuum chamber of an electron-beam evaporator with a pressure of below 7.5×10^{-5} Torr. When the tungsten filament in the vacuum chamber is heated by passing a high current through it, electrons are emitted from the filament and directed to the target metal material under the control of a strong magnetic field. The high kinetic energy of electrons is then transferred into thermal energy at the target metal material surface and the target metal is melted and turned into vapour in this energy transfer process. Once the metal vapour reaches the sample, it coats the sample and adheres to the sample surface. After the sample that was coated with metal vapour is cooled down, the metal contact on p-type GaN is formed. However, in order to activate the p-contact, a thermal annealing process is required, which is important to achieve a low specific contact resistivity for micro-LED devices. Our commonly used annealing process for the Ni/Au contact is to put the device at an optimised temperature of 500 °C in an air ambient for five minutes.

For n-type GaN, a thick Ti/Au (50 nm/200 nm) bi-layer is often deposited and used as the n-type metal contact. In our laboratory, all the n-contact metals are deposited in a vacuum chamber of a magnetron sputter system with a processing pressure lower than 1×10^{-6} Torr. The vacuum chamber is normally filled up with inert Ar gas and under a strong applied electric field, the positively charged Ar ions are accelerated to bombard the target metal surface. Under the bombardment of energetic Ar ions, atoms from the target metal material are sputtered to the sample surface and adhere to it to

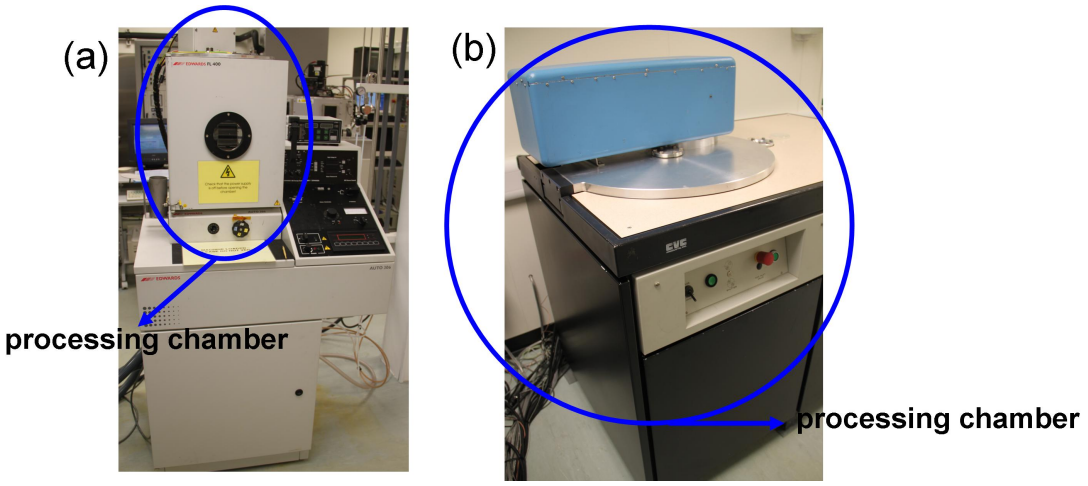

FIGURE 2.5: (a) Image of the electron-beam evaporator; (b) image of the magnetron sputter system.

form a thin n-contact metal film. Apart from forming an n-type metal contact, this method is used to form metal tracks in the micro-LED devices as well. For micro-LED devices in flip-chip formats, metal sputtering can also be used to form additional metal reflectors to enhance the power output of the flip-chip devices. Images of the electron-beam evaporator and magnetron sputter used for metal deposition are shown in Figure 2.5 (a) and (b), respectively.

2.2 Electrical and optical performance of micro-LED devices

Due to wide applications and superior performance in many aspects, micro-LED devices have attracted a lot of interest since being invented. In this section, micro-LEDs with different formats are first introduced. The electrical and optical performance of these micro-LED devices is also given and summarised in this section. It is worth noting that the micro-LED devices reported in this thesis were fabricated by my colleagues in the Institute of Photonics (Dr David Massoubre and Dr Zheng Gong) and my work mainly concentrated on the characterisation and applications of the fabricated devices. However, the characterisation of device performance is important to optimise the device fabrication process and the design parameters of micro-LED devices are normally determined by the requirement of different applications. Therefore, the fabrication, characterisation and applications of micro-LEDs are closely related to each other.

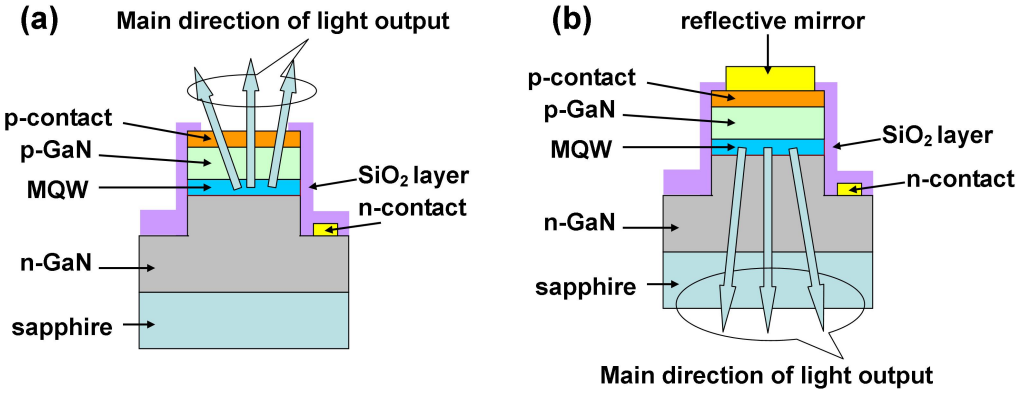

FIGURE 2.6: Schematic structure of a micro-LED pixel with (a) a top-emission configuration, and (b) a flip-chip configuration.

2.2.1 Configurations of micro-LEDs

The conventional 'broad-area' format of LED has achieved great success in solid-state lighting due to its high efficiency and reliability [23, 24]. Such 'broad-area' LED devices are normally fabricated on a large die with a single emission area ranging in area from 300×300 μm^2 to 1 mm^2, which contrasts with the micro-LED devices that normally have a emitter size of 100 μm and below [83, 84]. Standard micro-LED fabrication processes include photolithography, pattern transfer and metal deposition, which have been detailed in section 2.1. In terms of the direction of light extraction, micro-LED devices can be classified into two different kinds, i.e. top-emission device and flip-chip device. Micro-LED devices with a top-emission configuration normally have a thin p-contact metal with low absorption and reflection, which allows the light to be easily extracted from the top side of the micro-LED pillar. However, micro-LED device with a flip-chip configuration is operated inverted, with the light extracted from the backside of the device. On top of its p-contact metal, an additional reflective mirror is usually deposited to enhance the light output from the device. Besides, the sapphire substrate of the flip-chip device is normally polished to increase the surface roughness, allowing more light to be extracted from the device. The schematic structures of top-emission and flip-chip micro-LED devices are shown in Figure 2.6 (a) and (b), respectively. For the applications of VLC and micro-displays, a device with a flip-chip design is preferred as it provides higher output power compared with devices with top-emission configurations [77].

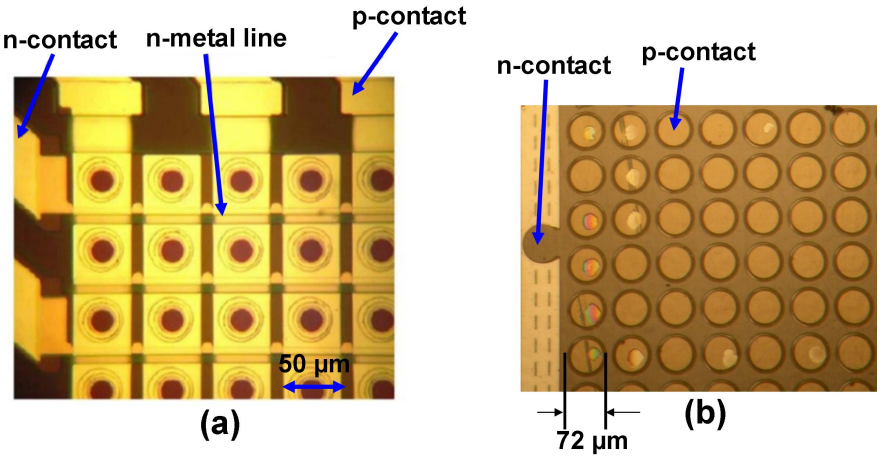

FIGURE 2.7: Microscope image of a section of (a) a 64×64 matrix-addressable micro-LED array, and (b) a 16×16 individually-addressable micro-LED array.

In terms of the pixel addressing, micro-LED array devices can be classified as matrix-addressable devices or individually-addressable devices. As shown in Figure 2.7 (a), each row of pixels in a matrix-addressable micro-LED device shares a common n-contact, while each of its column shares a common p-contact. Therefore, any individual pixel in the micro-LED array can be driven by the corresponding column and row electrodes. A big advantage of such design is that the number of electrical contacts can be significantly reduced compared with the device that requires separate contacts for each LED pixel, which greatly simplifies the device design and the complexity of the driving circuit, especially for a micro-LED array consisting of many pixels. Another approach of micro-LED array design which allows each pixel to be individually addressed is to fabricate separate metal contacts for each micro-LED pixel. In our work, such individually-addressable micro-LED devices normally have separate p-contacts but share a common n-contact, as shown in Figure 2.7 (b). Therefore, each of the micro-LED pixel can be individually addressed via applying voltage between the specific p-contact and the common n-contact.

In order to drive and test the micro-LED device, several approaches are also developed. Firstly, individual micro-LED pixel can be driven by probes, via directly making contact between probe tips and the contacts of micro-LED pixels, as shown in Figure 2.8 (a). Secondly, using a wire-bonding machine, micro-LED pixels can be wire-bonded to a printed circuit board (PCB) with easily-accessible electrodes soldered on it, as shown in Figure 2.8 (b). The electrodes are connected with the contacts of micro-LED pixels by bonding wires, which makes it possible to drive the pixel individually through specific

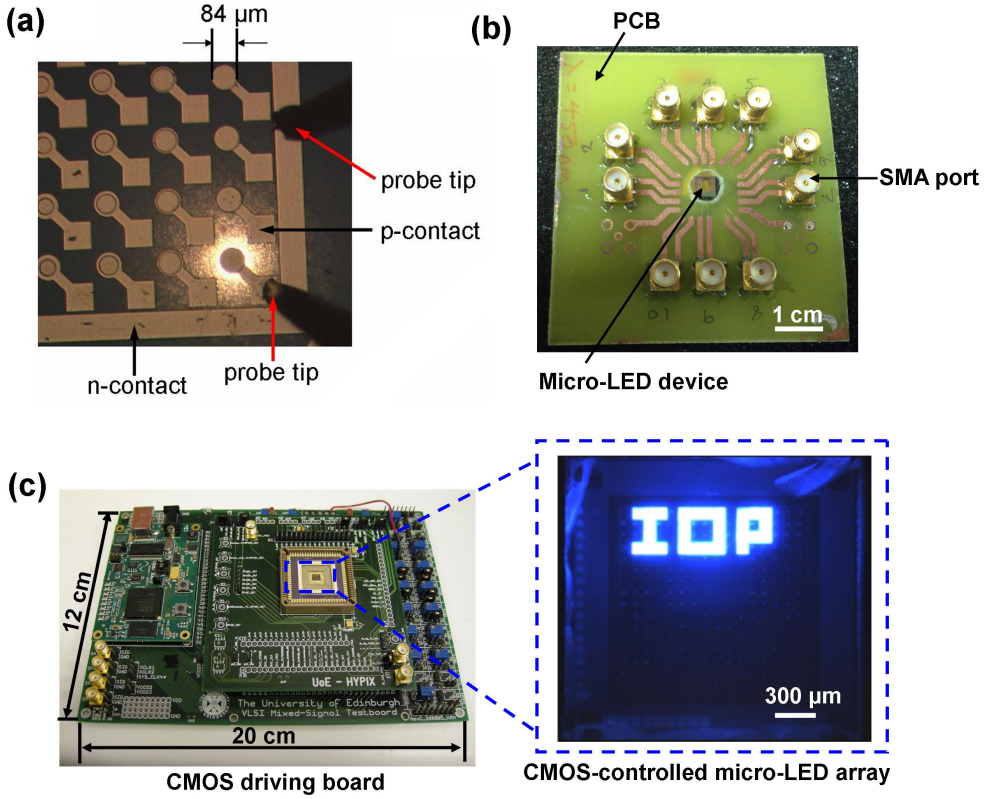

FIGURE 2.8: Image of (a) an 8×8 micro-LED array driven by probes, (b) a micro-LED device bonded on PCB with soldered SMA ports, and (c) controllable emission pattern 'IOP' (abbreviation for the Institute of Photonics) generated by the CMOS-controlled micro-LED array. The CMOS driving board is shown in the same figure as well.

electrodes or input port. Furthermore, to achieve a more easily-controllable micro-LED device, a corresponding electronic driver chip, driver board and computer-controllable interface were also developed to match the micro-LED array device. In this case, each of the micro-LED pixel or several of them can be easily addressed individually or simultaneously via a simple computer interface, which sends instructions to the driver board and circuitry to control the micro-LED device. In this work, driver circuitry based on complementary metal-oxide-semiconductor (CMOS) electronics is mainly used, which gives a convenient control to the micro-LED device [85]. More importantly, with years of development, CMOS-controlled micro-LED devices have been greatly improved and implemented for many applications, such as bioengineering, chemical sensing, optical communications and micro-displays [35, 64, 86, 87]. Figure 2.8 (c) shows the CMOS driving board (developed by University of Edinburgh as part of our collaboration) and the CMOS-controlled micro-LED device with a controllable emission pattern. Details of the CMOS-controlled micro-LED devices and their applications will be presented in chapter 3 and chapter 4.

2.2.2 Electrical characteristics of micro-LEDs

In this work, the electrical characteristics of micro-LEDs mainly focus on investigating the current-voltage and capacitance-voltage characteristics of micro-LED devices. The current-voltage characteristics of micro-LED devices are presented here while the capacitance-voltage characteristics of micro-LED devices will be presented in chapter 6. The relationship between the current (I) passing through an LED and the applied bias voltage (V) is defined as the current-voltage (I-V) characteristic of the device. The fundamental principles of the I-V characteristic of an LED are based on the classic semiconductor theory of a p-n diode as shown in chapter 1, section 1.2. For practical LED devices, their I-V characteristics are highly correlated with the properties of each specific device design, such as the device geometry and wafer material [26]. Besides, the I-V characteristic of an LED device can also be significantly influenced by the device fabrication process. Taking the micro-LED devices presented in this thesis into consideration, some unintentional variations of device-to-device performance are expected due to the variations between each device fabrication process.

To further explore the I-V characteristics of micro-LEDs, a specifically-designed micro-LED device was fabricated and given I-V measurement using a probe station and a current source (YOGOKAWA GS610). This 450 nm blue-emitting micro-LED device was fabricated from a standard commercially available MQW LED wafer grown on a *c*-plane sapphire substrate. The device consists of an 8×8 array of individually-addressable micro-disk pixels on a 200 μm centre-to-centre pitch, with each row consisting of pixels of identical size, but columns containing pixels with different diameters ranging from 14 to 84 μm in 10 μm intervals. The disk-shaped pixel mesa was defined using photolithography and inductively plasma etching, and other details of the device fabrication can be found in section 2.1. Due to the flip-chip format, this micro-LED device is designed to be operated inverted, with the light emission extracted from the polished sapphire substrate. Figure 2.9 (a) shows the I-V characteristics of individual micro-LED pixels with different diameters. Here it can be seen that the threshold voltage, which is defined as the voltage at which the injection current reaches 5 mA, increases as the pixel size decreases. The series resistance, which can be approximately determined by taking the slope of the linear part of the I-V curve, also increases as the pixel size decreases. These effects are attributed to a smaller surface area of the micro-LED pixel as it size

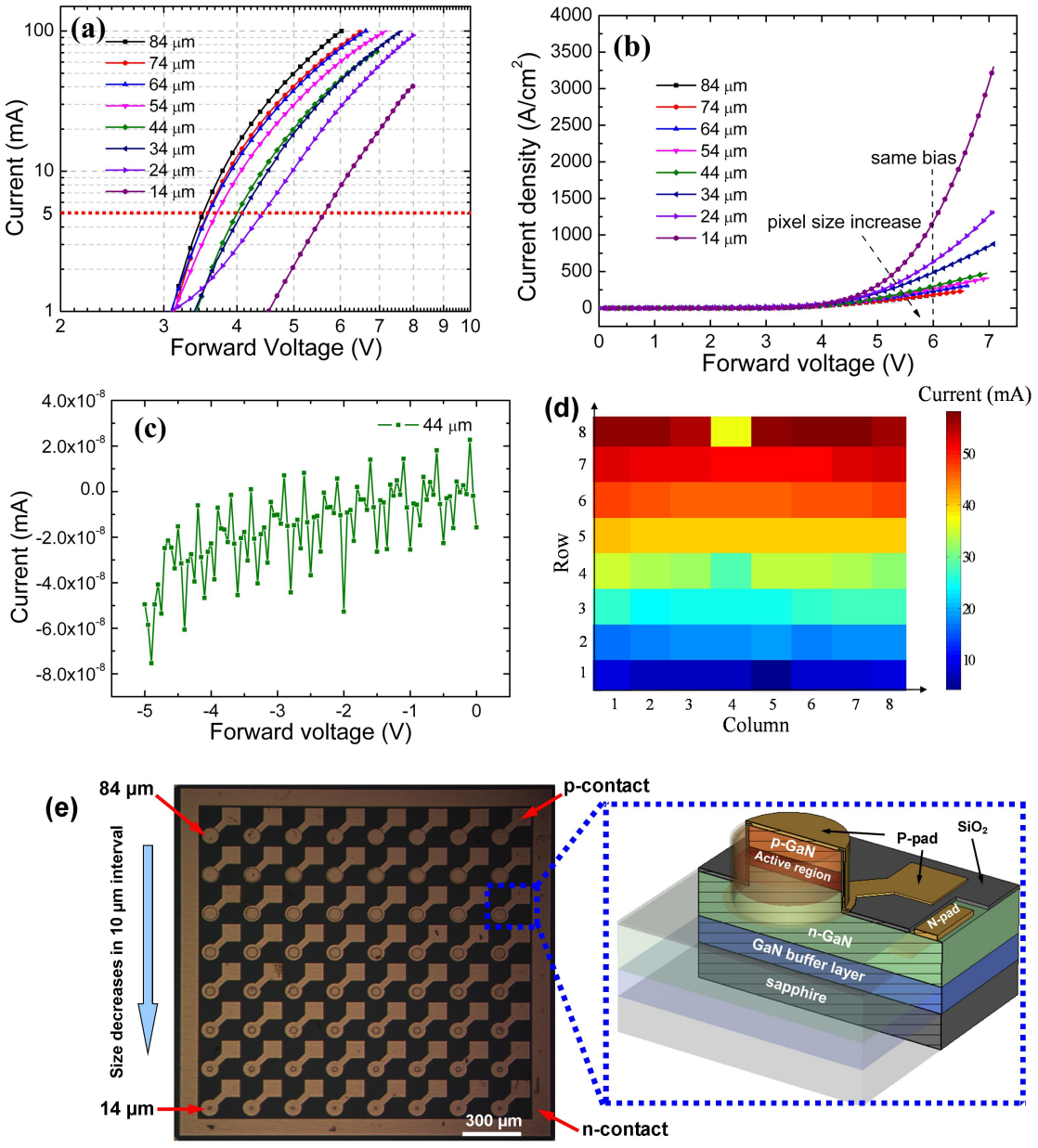

FIGURE 2.9: (a) I-V curves of representative micro-LED pixels with different diameters; (b) currenst density versus forward bias voltage of representative micro-LED pixels with different diameters; (c) I-V curve of a representative 44 μm diameter micro-LED pixel under reverse bias voltage; (d) injection current across different micro-LED pixels under 5.5 V applied bias; (e) microscope image of the 8×8 micro-LED array and a 3D schematic structure of a representative micro-LED pixel with cross-sectional view.

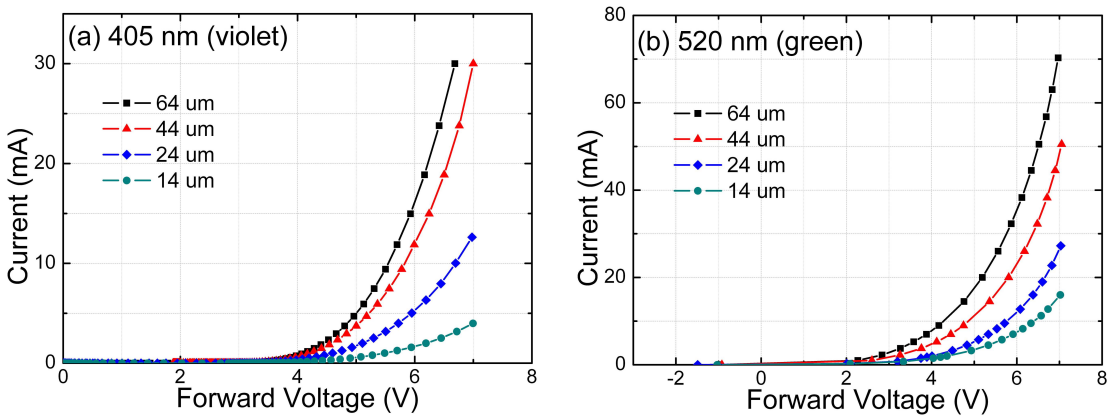

FIGURE 2.10: I-V curves of selective pixels from two 8×8 micro-LED array with emission wavelengths at (a) 405 nm (violent-emitting device) and (b) 520 nm (green-emitting device).

decreases [88]. It is worth noting that Figure 2.9 (a) plots the data in logarithmic scale instead of linear scale and the linear part of the I-V curve can be more directly viewed when the data is plotted in linear scale. Figure 2.9 (b) shows the current density versus forward bias voltage for micro-LED pixels with different diameters. Under the same bias voltage, the current density is higher for the pixel with smaller size, which is due to reduced current crowding effect and uniform current spreading of the micro-LED pixel with smaller size [26, 88]. Figure 2.9 (c) shows the I-V curve of a representative 44 μm diameter pixel under reverse bias conditions. The reverse current is very small, indicating the leakage current is very small for this pixel. In addition, the I-V curves of other micro-LED pixels with different sizes were also measured under reverse bias conditions and they are very similar to the I-V curve shown in Figure 2.9 (c). Figure 2.9 (d) shows the result of injection current uniformity of the whole micro-LED array under an applied bias of 5.5 V. The good electrical uniformity within each row of pixels shows that the testing results achieved from a selected pixel can be used as good references for most other pixels with the same size. Figure 2.9 (e) shows a top-view microscope image of the whole micro-LED array and a 3D schematic structure of a typical micro-LED pixel from the array.

Micro-LED devices with the same design and configuration as the 8×8 450 nm blue-emitting device but with different emission wavelengths were also fabricated and measured. Figure 2.10 (a) and (b) show the I-V characteristics of the selective pixels from two other 8×8 micro-LED devices with peak emission wavelengths at 405 nm (violet) and 520 nm (green), respectively. As shown in Figure 2.10, for micro-LED pixels with

the same size, their threshold voltages and series resistances normally increase for the shorter wavelength devices (when turned on, a micro-LED device with smaller series resistance normally has larger injection current as the series resistance (R_s) under specific applied bias can be approximately calculated via ohm's law: $R_s = dV/dI$, i.e. the ratio of applied bias and injection current). According to the classic LED theory shown in chapter 1, section 1.2, the threshold voltage of an ideal LED device should increase with the increase of bandgap energy. Therefore, a micro-LED device with a shorter wavelength is expected to have a higher threshold voltage. In addition, for violet and ultraviolet micro-LED devices, the relatively higher Al concentration in p-type GaN and poorer crystal quality of LED wafer materials also contribute to higher series resistances. The series resistance of LED is mainly from p-type GaN as the hole concentration is very low under room temperature, resulting in high resistivity of p-type GaN layer [26]. Excess Al concentration in p-type GaN makes the Mg acceptor even more difficult to generate holes as AlN is relatively easy to form compared with $Mg^{+}N$. As a result, the hole concentration drops and the series resistance increases.

2.2.3 Optical characteristics of micro-LEDs

For LED devices, one of the most important and fundamental optical characteristics is their optical output power, which normally depends on many factors, such as device design, fabrication process, epitaxial structure and packaging. In this sub-section, the output power versus current (L-I) characteristics of three micro-LED devices with different emission wavelengths are investigated.

Figure 2.11 shows electroluminescence (EL) spectra of three test micro-LED devices fabricated from different wafer materials, with peak emission wavelengths at 405 nm, 450 nm and 520 nm, respectively. These micro-LED devices are the same 8×8 micro-LED array devices presented in the last sub-section and they feature in the following L-I measurements as well. Each spectrum shown in Figure 2.11 is measured from an 84 μm diameter pixel at an injection current of 20 mA. Figure 2.12 (a) shows the L-I characteristics of the micro-LED pixels with different diameters from the 450 nm blue-emitting 8×8 micro-LED array. The output power of each micro-LED pixel is measured by a power-meter (Melles Griot) with its calibrated photodetector placed closely on top of the light-emitting surface of the device. The photodetector has a silicon photodiode with

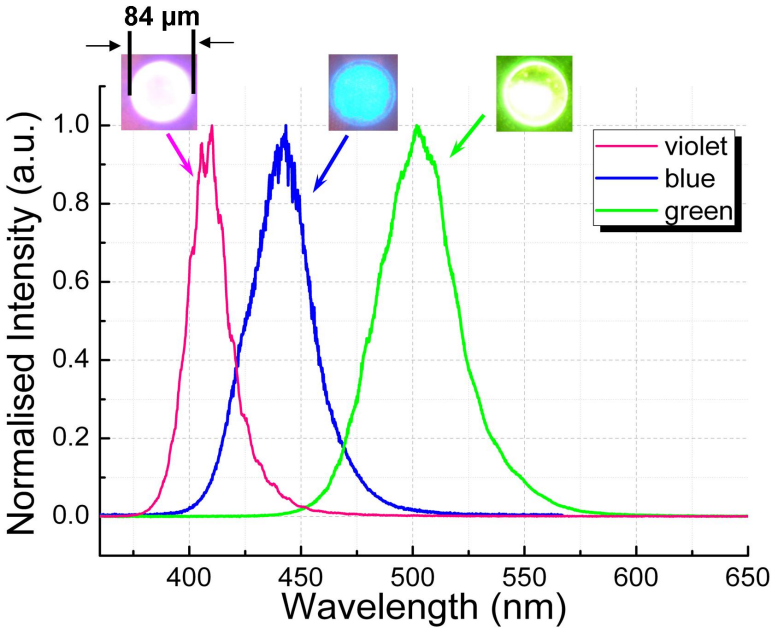

FIGURE 2.11: EL spectra of three 84 μm diameter pixels fabricated from different wafer materials. The pixels are in operation under a DC current of 20 mA.

a surface area of around 0.5 cm^2, which is 600 times larger than the surface area of the largest micro-LED pixel. In this case, most of the output power of micro-LED from its emitting surface can be collected by the photodetector. In addition, the output power of micro-LED were also measured in an integrating sphere, which collects the light emission from micro-LED device in all directions. The results show that the output power of the flip-chip micro-LED device measured by the integrating sphere are quite similar to that measured by the power-meter. Therefore, the coupling efficiency in the measurement using power-meter for different size micro-LEDs is the same and the measured optical power can be used to represent the overall output power from the micro-LED device. The injection current is measured by connecting an ammeter in series with the device under test. As shown in Figure 2.12 (a), the maximum output power of micro-LED pixel increases with the increase of pixel size, as would be expected. Figure 2.12 (b) shows the result of output uniformity of the whole micro-LED array under an applied bias of 5.5 V. The good output uniformity across the whole array indicates that the results achieved from selected pixels can be used as good references for most other pixels with the same size.

Figure 2.13 shows the relations between optical output power density (output power from the pixel divided by its active area) and injection current density (injection current of the pixel divided by its active area) for 450 nm micro-LED pixels with different

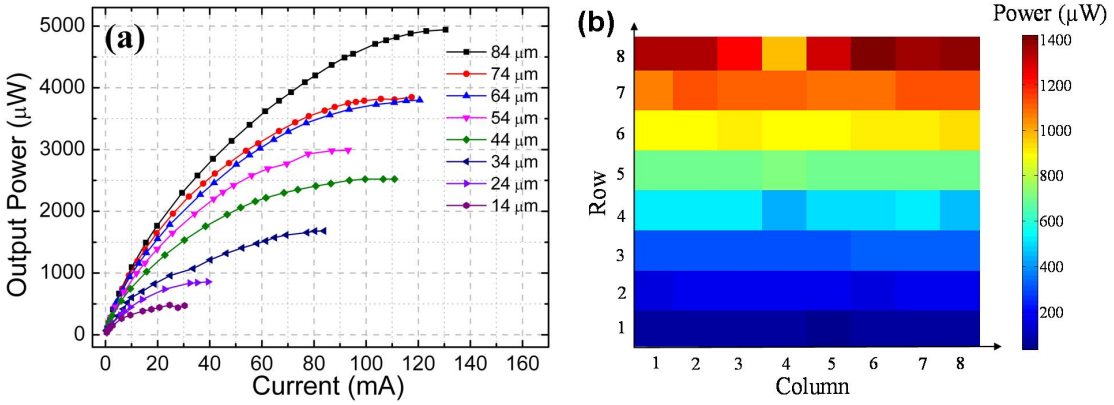

FIGURE 2.12: (a) L-I characteristics of the 450 nm micro-LED pixels with different diameters; (b) optical output mapping across the whole 450 nm 8×8 micro-LED array under 5.5 V applied bias.

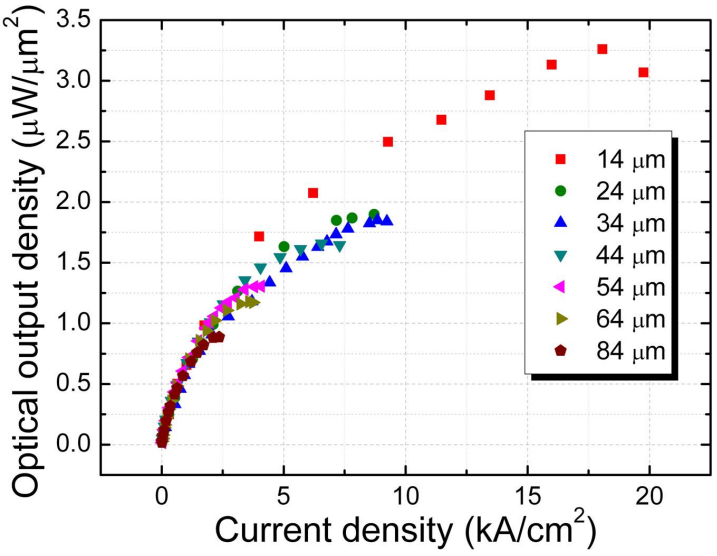

FIGURE 2.13: Characteristics of output power density versus injection current density of individual micro-LED pixels with different sizes, from the 450 nm 8×8 micro-LED array.

diameters. As shown in Figure 2.13, the output power density of the 84 μm diameter pixel (largest pixel) saturates at 0.88 μW/μm^2 (88 W/cm^2) under an injection current density of 2.3 kA/cm^2 while the output power density of the 14 μm diameter pixel (smallest pixel) reaches 3.25 μW/μm^2 (325 W/cm^2) under an injection current density of 19.75 kA/cm^2. A clear trend is observed that micro-LED pixels with smaller sizes can be operated at larger injection current densities and have higher maximum output power densities compared with micro-LED pixels with larger sizes. An explanation for this observation is that the smaller-size micro-LED pixels have superior thermal management capabilities compared with the larger-size pixels, which enables them to be operated at higher current densities before power saturation caused by the self-heating

effect. Figure 2.14 (a) shows the junction temperatures of size-dependent micro-LEDs under different current densities [88]. These size-dependent micro-LEDs have similar designs as the micro-LEDs reported here. The junction temperatures of the micro-LEDs were measured using a spectral-shift method [26] and the smaller micro-LED pixel has lower junction temperature compared with the larger micro-LED pixel under the same current density. Due to larger sidewall to volume ratios, smaller micro-LED pixels have stronger sidewall heat radiation/conduction capabilities compared with larger micro-LED pixels. The current crowding effect, which is believed to be a main reason for generating heat in the device, is also greatly minimised in the smaller-size pixels. Shown in Figure 2.14 (b) and (c) are simulated junction-temperature distribution for a 40 μm and a 150 μm micro-LED pixel under the same average current density of 500 A/cm^2 [88]. As shown, the average junction temperature for the 40 μm pixel is much lower than the 150 μm pixel, indicating that the self-heating effect in a smaller mesa structure is reduced. In addition, simulated junction-temperature distribution is quite uniform for the 40 μm pixel, while relatively large variation in the junction temperature across the active area is observed for the 150 μm pixel. The left edge of the 150 μm pixel close to n-contact is overheated, which is attributed to serious current crowding effect at the edge of the mesa structure. Figure 2.14 (d) shows the simulated average junction temperature against current density for the 40 μm and the 150 μm micro-LED pixel. More details of the work can be found in [88]. As indicated by these measured and simulation results, the current distribution is not uniform across large micro-LED pixels and some areas may have excessive current densities. In contrast, smaller micro-LEDs have uniform current distribution and can work in high-current-density regimes not accessible by larger micro-LEDs. In addition, it is meaningless to use the current density of a region with serious current crowding to represent the current density of the device. Therefore, average current density, i.e. current divided by device size, is used to characterise the micro-LED device in this work. It is worth mentioning that infared pictures have also been taken to characterise the thermal effect in size-dependent micro-LEDs. However, due to the small size of micro-LED and the limitation of the resolution of infared camera, persuasive results have not been achieved. The relevant work is still ongoing.

The current-dependent self-heating effect in the device can significantly reduce its light output since an increased junction temperature results in more carrier leakage and

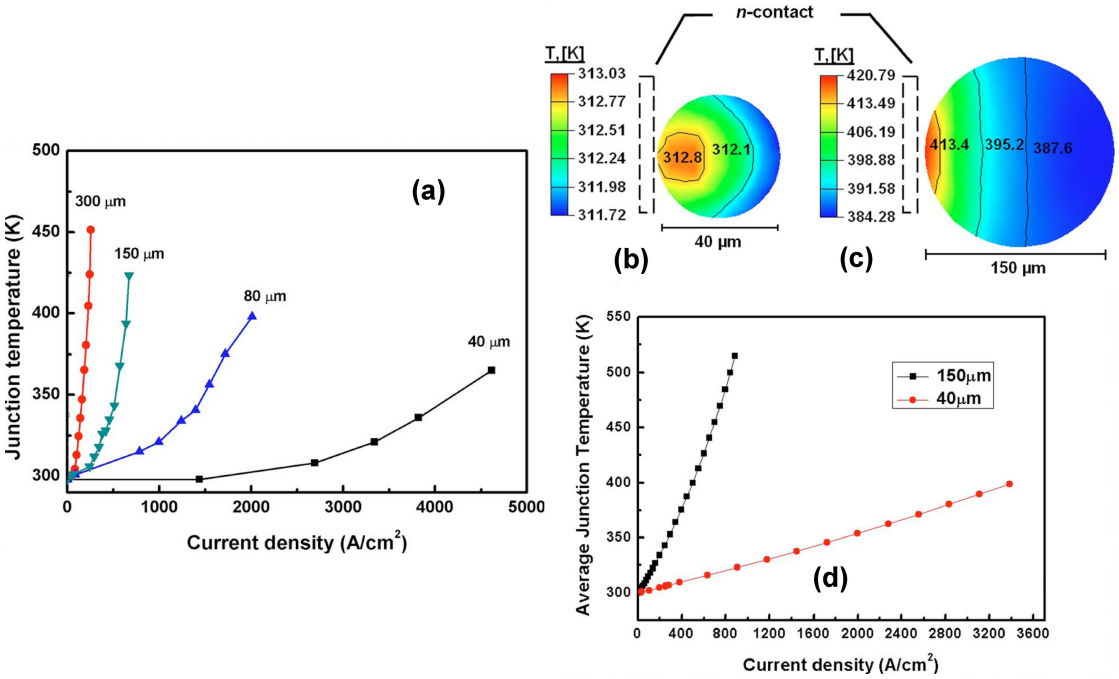

FIGURE 2.14: (a) Measured junction temperature as a function of the current density for different pixel sizes; simulated junction-temperature distribution in the active area of (b) the 40 μm pixel and (c) the 150 μm pixel under the same current density of 500 A/cm^2; (d) simulated average junction temperature against current density for the 40 μm pixel and the 150 μm pixel [88].

stronger non-radiative recombination in the active region [26]. Additionally, the ohmic contact and p-n junction can also be damaged by overheating, which has a destructive effect on device performance and may result in device failure. Therefore, the superior thermal management capabilities of smaller-size micro-LEDs are very important for their practical applications. We will show later on that such capabilities also increase the device modulation bandwidth and improve the device performance for VLC. It is also worth noting that the conventional broad-area LEDs for high-power illumination normally operate at current densities of 0.1-1 kA/cm^2 whist the micro-LEDs presented here can operate at current densities of up to 20 kA/cm^2, proving that the micro-LED format is a more suitable approach towards some applications requiring the device to be operated under large current densities and with high output power densities, such as organic laser photo-pumping [89].

The L-I characteristics of selected pixels from 405 nm and 520 nm 8×8 micro-LED arrays are shown in Figure 2.15 (a) and (b), respectively. Compared with the output power of the 450 nm micro-LED pixels shown in Figure 2.12 (a), 405 nm and 520 nm micro-LED pixels have lower output power at the same injection current for a pixel of

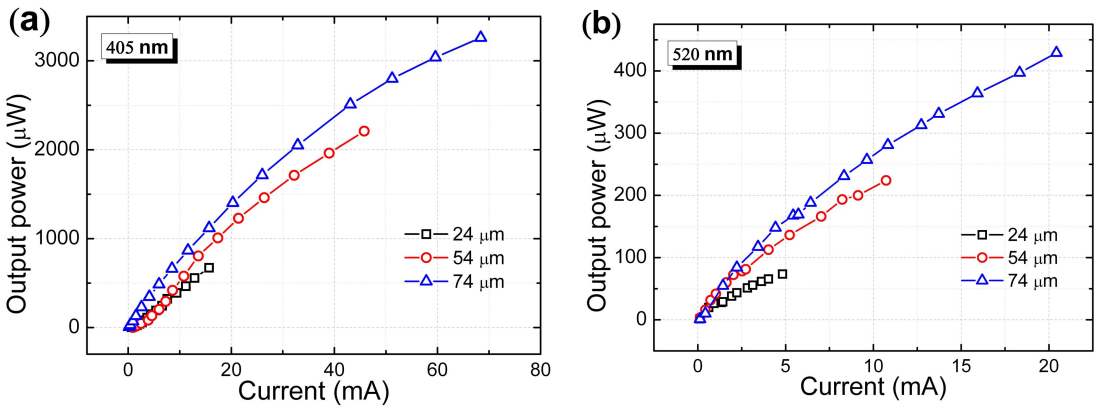

FIGURE 2.15: L-I characteristics of selective pixels from (a) a 405 nm 8×8 micro-LED array, and (b) a 520 nm 8×8 micro-LED array.

the same size. For the shorter wavelength device, this observation is probably due to a reduced carrier localisation effect in the wafer material [90]. The indium content in the LED wafer material is capable of localising the injected carriers. In other words, the injected carriers are confined in the indium-rich clusters of the active region and are prevented from diffusing towards non-radiative recombination defects. However, there is less indium content in the shorter wavelength epitaxial wafer, which means the localising effect of indium content is weakened and the carriers are more sensitive to non-radiative recombination defects. Therefore, the 405 nm micro-LED devices are less efficient and powerful compared with the 450 nm ones. For the 520 nm device, the observation of less output power is probably due to reduced radiative recombination caused by a stronger piezo-electric field in the active region [91]. There is more indium content in the longer wavelength wafer material, which results in a stronger piezo-electric field in the quantum wells. The piezo-electric field minimises the overlap of electron wave function and hole wave function in the quantum wells, resulting in lower radiative efficiency and less output power from the device. This drop of efficiency and output power in green LEDs, also known as the 'green gap', is regarded as a limitation of the high-power green LEDs (see chapter 1, Figure 1.17). A lot of effort has been made to tackle this issue, such as using non-polar and semi-polar wafer materials grown on thick GaN bulk substrates [92–94]. Details about the influence of piezo-electric field on LED performance can be found in chapter 1, section 1.3.

2.3 Modulation characteristics of micro-LED devices

Modulation characteristics of micro-LED devices are very important for their applications for VLC as such characteristics represent how fast a device can be modulated to transmit data. Before presenting the performance of micro-LED devices for VLC, we will first analyse the modulation characteristics of micro-LED devices by measuring their frequency responses. The advantages of using micro-LED devices for VLC will also be discussed and presented in this section.

The frequency response of an LED device represents the relationship between modulation frequency and the output power from the device transmitted at this frequency. An AC-modulated LED device normally has higher output power at lower modulation frequency and lower output power at higher modulation frequency. Because the injected carriers in LED device cannot recombine fast enough to respond and follow the applied modulation signal at high frequency, resulting in a drop of output power at high frequency. The power transfer function of an LED device is given by:

$$P(f) = \frac{1}{\sqrt{1 + (2\pi f\tau)^2}} \tag{2.1}$$

where $P(f)$ is the frequency response, f is the modulation frequency and $\tau \approx RC$, is the RC time constant of the LED [26]. Denoting the diode geometric capacitance as C and the overall series resistance as R, the frequency response of an LED device is determined by its RC time constant. The series resistance R includes both the series resistance of LED and the electrical contact resistance. It is also worth noting that the geometric capacitance of LED is essentially different from the capacitive response of LED which will be introduced in chapter 6. The geometric capacitance of LED is a function only of its geometry and the permittivity of the dielectric while the capacitive response of LED is a current-dependent phenomenon determined by the carrier dynamics. For a micro-LED device, its geometric capacitance and the current-injected active region are much smaller compared with its conventional broad-area counterpart, so that the carrier differential lifetime rather than the diode capacitance limits the maximum modulation frequency [64]. Therefore, τ in Equation 2.1 can be approximately regarded as the differential lifetime of injected carriers of micro-LED devices. The bandwidth of the

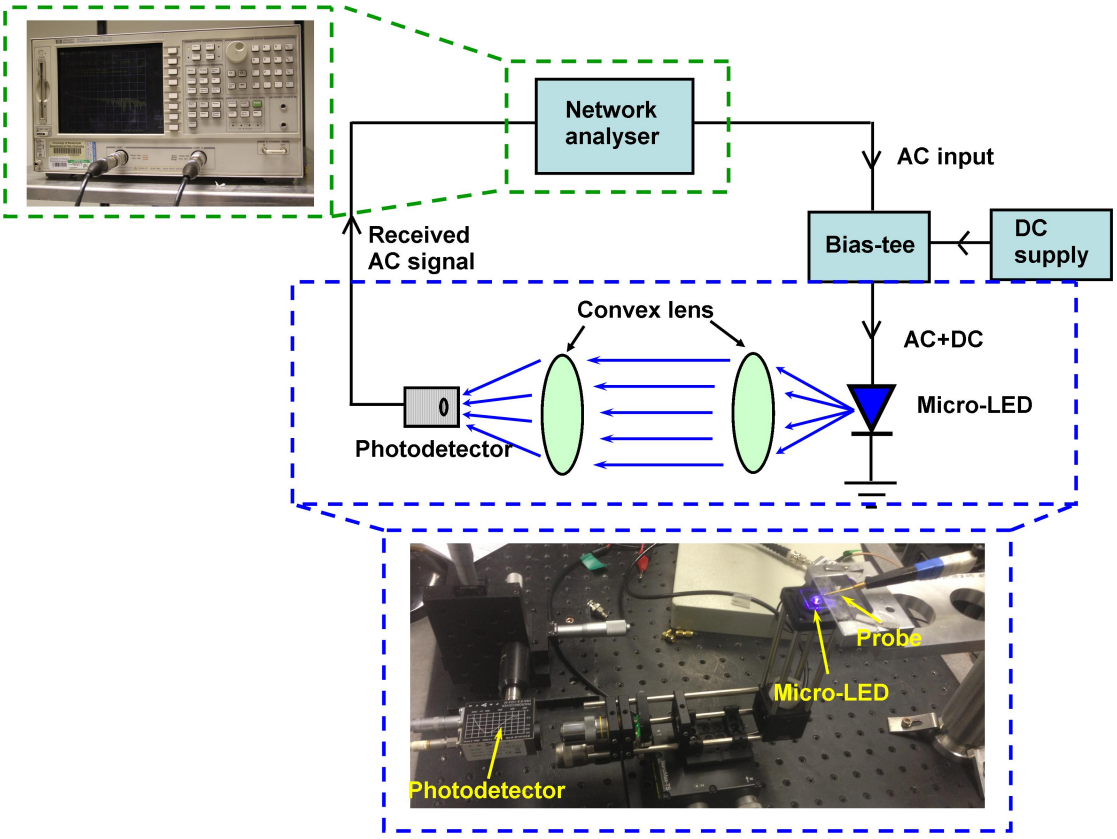

FIGURE 2.16: Setup of the micro-LED frequency response measurement and images of the experimental setup and equipment.

system, Δf, corresponds to the frequency at which the power transmitted through the system is reduced to one-half of its low-frequency value. This bandwidth is also called the -3 dB frequency/bandwidth, since the power transmitted at this frequency is reduced by 3 dB compared with the low-frequency value. The -3 dB bandwidth of an LED is given by:

$$\Delta f = f_{-3dB} = \frac{\sqrt{3}}{2\pi\tau} \tag{2.2}$$

Figure 2.16 shows the setup for frequency response measurement of micro-LED devices. As shown in Figure 2.16, a probe was used to address the micro-LED pixels. By placing the probe signal tip on the p-contact area and the probe ground tip on the n-contact area, individual micro-LED pixels can be electrically driven and modulated. It is also worth noting that there are a wide range of probes with different tip pitches available for this measurement, providing flexibility in choosing and addressing individual pixels from micro-LED devices with different designs. In order to measure the frequency response

characteristics of the micro-LED pixels, a small AC modulation signal was first combined with a DC bias by a bias-tee and then applied to the micro-LED pixels under test. The DC bias was supplied from a DC power supply and the small AC modulation component was generated by a network analyser (Hewlett Packard 8753ES). The small AC modulation component mainly consisted of a chirped sine wave, which is a fixed-amplitude sine wave with its frequency sweeping from low frequency to high frequency (75 KHz to 1 GHz). After being modulated, the optical output from the micro-LED was imaged onto the active area of a fast AC-coupled photodetector with a cut-off bandwidth of 1.4 GHz (FEMTO HAS-X-S-1G4-SI-FS). Then the received optical signal was returned to the input port of the network analyser for measuring the frequency response. Since the photodetector is an AC-coupled photodetector, only the AC optical component modulated by the small AC modulation signal was received by the network analyser. Finally, the network analyser recorded the optical responses of micro-LEDs under different modulation frequencies and presented the overall frequency response of the device under test. In other words, the network analyser is a two-port instrument, which sends frequency-dependent signal to modulate the micro-LED through the output port and receives the response signal from the micro-LED via a photodetector connected to the input port. The intensity of the micro-LED under specific modulation frequency is recorded by the network analyser, which further presents the frequency response of the micro-LED after finishing a complete frequency sweep.

Using the experimental setup mentioned above, frequency responses of different-size pixels from a wide range of different LED devices were measured and analysed. These devices were all fabricated by Dr David Massoubre. Figure 2.17 (a) shows a frequency response curve of a typical 60 μm micro-LED pixel from a 450 nm array with an injection current of 100 mA. The device consists of a 16×16 array of individually-addressable micro-disk pixels on a 100 μm centre-to-centre pitch, with each row consisting of pixels of identical size, but columns containing pixels with different diameters (micro-LED pillar) at 5 μm, 10 μm, 15 μm, 20 μm, 30 μm, 40 μm, 50 μm and 60 μm, respectively. Pixels from every two columns have the same sizes so that the whole 16×16 micro-LED array consists of 256 pixels with eight different sizes. Figure 2.17 (b) shows a microscope image of a section of the 450 nm 16×16 micro-LED device. As shown in Figure 2.17 (a), the bandwidth of a 60 μm micro-LED pixel reaches 134.7 MHz under a DC injection current of 100 mA, which is high enough for data transmission of up to several hundred

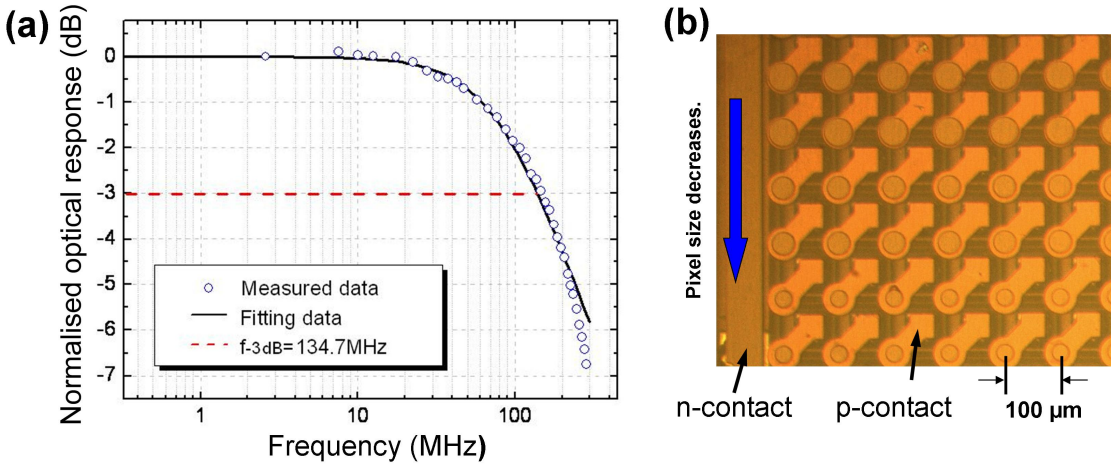

FIGURE 2.17: (a) Frequency response of a typical 60 μm micro-LED pixel from a 450 nm 16×16 micro-LED array with an injection current of 100 mA. (b) Microscope image of a section of the 16×16 micro-LED array device.

Mbit/s. The fitting method is based on the frequency-dependent power transfer function shown in Equation 2.1.

More bandwidth versus current characteristics from different LED devices are shown in Figure 2.18. Figure 2.18 (a) shows the bandwidths of different-size pixels from a 450 nm blue-emitting 16×16 micro-LED array under different injection currents and Figure 2.18 (b) shows the bandwidths of different-size pixels from a 520 nm green-emitting 16×16 micro-LED array under different injection currents. The 520 nm micro-LED array has the same format as the 450 nm 16×16 micro-LED device. Figure 2.18 (c) shows the bandwidth versus current characteristics of LED pixels from two 16×16 'Tessellated' LED array devices with different peak emission wavelengths. The 450 nm blue-emitting 'Tessellated' device and the 520 nm green-emitting 'Tessellated' device have the same array design, which consists of 16×16 individually-addressable uniform-sized square LED pixels on a 100 μm centre-to-centre pitch and each pixel is 99×99 μm^2 in area with a 1 μm separation. Figure 2.18 (d) shows the bandwidths of LED pixel from a 450 nm 8×8 'Tessellated' LED array under different injection currents. This 450 nm 'Tessellated' LED device consists of 8×8 individually-addressable square LED pixels with a uniform size of 198×198 μm^2 on a 200-μm centre-to-centre pitch. The separation between two adjacent pixels is 2 μm.

As shown in Figure 2.18, for all the LED pixels, their modulation bandwidths increase significantly with the increase of injection current. Similar bandwidth results of micro-LED devices were reported previously [64, 85, 95]. This observation is not due to the

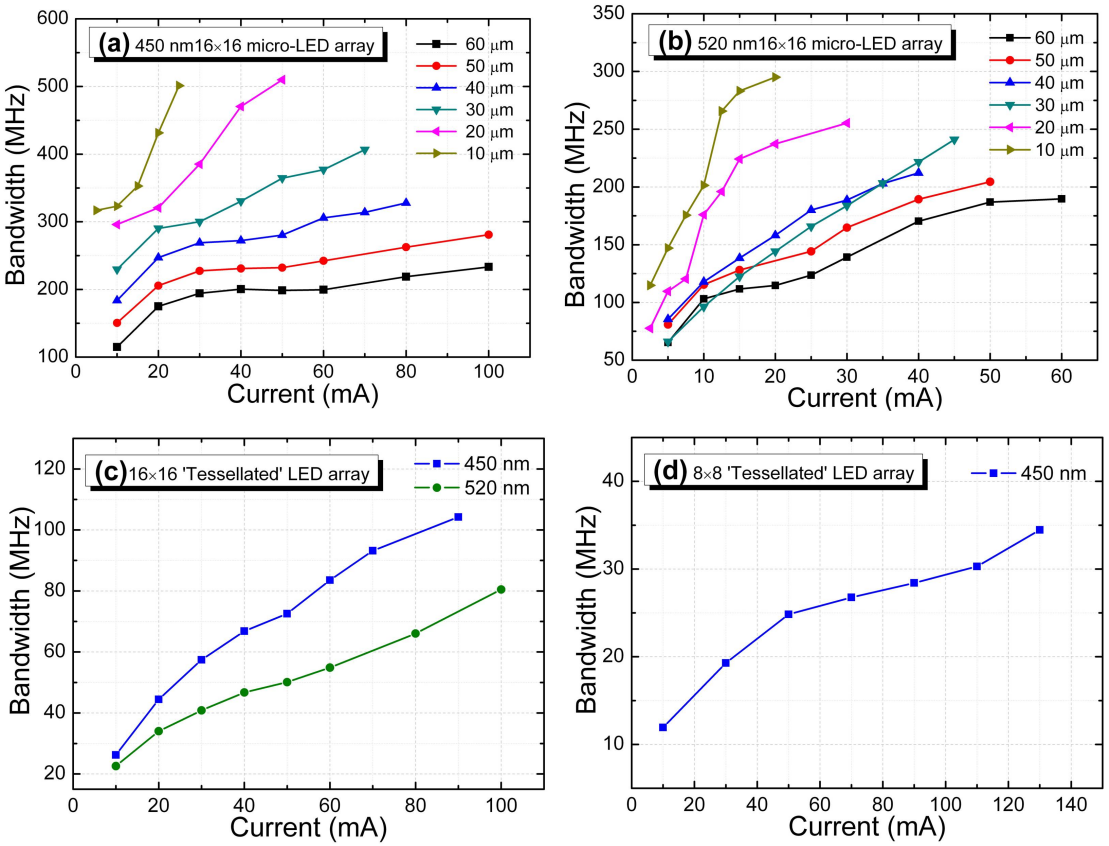

FIGURE 2.18: (a) Bandwidth versus current for micro-LED pixels with different sizes from a 450 nm blue-emitting 16×16 micro-LED array; (b) bandwidth versus current for micro-LED pixels with different sizes from a 520 nm green-emitting 16×16 micro-LED array; (c) bandwidth versus current for LED pixels from two 16×16 'Tessellated' LED array devices with peak emission wavelengths at 450 nm and 520 nm; (d) bandwidth versus current for an LED pixel from an 8×8 'Tessellated' LED array device with a peak emission wavelength at 450 nm.

influence of RC time constant of the LED as the RC time constant is not a current-dependent parameter. This observation is probably due to the shortened carrier lifetime (ns regime) as the injection carrier density increases with the increase of injection current. To clarify this explanation, a classic ABC model is used, which considers that the current through the device is made up of three contributions, i.e. a non-radiative current due to Shockley-Read-Hall (SRH) recombination at defects, a current due to radiativere recombination of electrons and holes, and an Auger recombination current [28]. Thus, the total current I can be denoted as:

$$I = e \cdot a \cdot d \left(AN + BN^2 + CN^3 \right) \tag{2.3}$$

where N is the carrier density within the active region and A, B, C represent the

SRH, radiative and Auger coefficients, respectively. The elementary charge is denoted as e while a and d are the active area of the device and the thickness of active region, respectively. As shown in Equation 2.2, the modulation bandwidth is determined by the differential carrier lifetime. Under small signal modulation, i.e. a large DC bias is combined with a small AC signal to modulate the device, the modulation bandwidth is determined by the differential carrier lifetime [28], which can be described by the following equation:

$$\tau = \frac{1}{A + 2BN + 3CN^2} \tag{2.4}$$

An increase of injection current normally increases the amount of injected carriers in the active region of the device, which not only results in a higher carrier density but also a shorter differential carrier lifetime. Therefore, under large injection current, a high modulation bandwidth of LED device is expected due to an increase of carrier density and a decrease of differential carrier lifetime in the active region. This is the crucial and fundamental observation which facilitates the use of micro-LED devices in high-bandwidth data communications.

Equation 2.4 has also been used to study the recombination processes of III-nitride micro-LEDs and fit the A, B, C coefficients. The carrier density of the active region of LED under specific injection current can be calculated using the differential carrier lifetime while the differential carrier lifetime can be caculated from the measured modulation bandwidth according to Equation 2.2 [96]. According to Equation 2.4, A coefficient can be fitted by using the differential carrier lifetime at very low current density as the terms in Equation 2.4 containing differential carrier density are negligible in this case. B coefficient can be fitted by measuring the output power of the LED device and the light extraction efficiency of the device [28]. After getting the carrier density, A and B coefficients, C coefficient can be fitted. For 450 nm III-nitride micro-LED devices, the A coefficient was fitted in the range $1.2\times10^{-8}\mathrm{s}^{-1}$—$3.2\times10^{-8}\mathrm{s}^{-1}$, the B coefficient was fitted in the range $0.5\times10^{-11}\mathrm{cm}^3\mathrm{s}^{-1}$—$4\times10^{-11}\mathrm{cm}^3\mathrm{s}^{-1}$, the C coefficient was fitted in the range $0.7\times10^{-29}\mathrm{cm}^6\mathrm{s}^{-1}$—$1.3\times10^{-29}\mathrm{cm}^6\mathrm{s}^{-1}$. For 520 nm III-nitride micro-LED devices, the A coefficient was fitted in the range $0.8\times10^{-8}\mathrm{s}^{-1}$—$1.8\times10^{-8}\mathrm{s}^{-1}$, the B coefficient was fitted in the range $0.5\times10^{-11}\mathrm{cm}^3\mathrm{s}^{-1}$—$5\times10^{-11}\mathrm{cm}^3\mathrm{s}^{-1}$, the C coefficient was fitted in the range $2\times10^{-30}\mathrm{cm}^6\mathrm{s}^{-1}$—$4\times10^{-30}\mathrm{cm}^6\mathrm{s}^{-1}$. These fitted parameters are comparable

to the values reported by other groups and the theoretical values [97–101]. Detailed fitting processes can be found in [28].

The 520 nm green-emitting device shows lower modulation bandwidth compared with the 450 nm blue-emitting device for the same size pixels under the same injection current. This phenomenon is probably caused by the strong piezo-electric polarisation effect in the quantum wells of green-emitting materials. The piezo-electric field distorts the energy band of quantum wells so that the confining capability of quantum wells to injected carriers is weakened. Therefore, instead of being confined in the active region, more injected carriers overflow from the quantum wells, causing a significant loss of carriers in the active region [26, 91]. The loss of injected carriers in the active region influences the carrier concentration, which results in longer carrier differential lifetimes and lower modulation bandwidths accordingly.

As shown in Figure 2.18, for the micro-LED pixels fabricated from same wafer materials but with different sizes, smaller-size pixels normally have larger modulation bandwidths compared with the larger-size pixels under the same injection current. In addition, for a 10 μm diameter micro-LED pixel, its 'maximum' modulation bandwidth exceeds 500 MHz at 25 mA, while an LED pixel with an area of 198×198 μm^2 from an 8×8 'Tessellated' LED device only has a 'maximum' modulation bandwidth of less than 35 MHz at 130 mA. This 'maximum' modulation bandwidth is defined as the max value of modulation bandwidths of an LED device operating under a certain range of injection current before its power rolls over. The following analysis indicates that the superior modulation performance of smaller-size LED pixels is due to their capabilities to operate in a high carrier-density regime. Figure 2.19 shows the bandwidth versus current density (injection current divided by the active area) of LEDs with different pixel sizes from the 450 nm blue-emitting 16×16 micro-LED device. Under the same current density, different sized LEDs from the same micro-LED device show similar modulation bandwidths regardless of the pixel size. However, smaller-size micro-LED pixels show higher maximum modulation bandwidths because they are able to operate/withstand higher injection current densities while the larger-size micro-LEDs cannot. The physical origin for dependence of bandwidth versus device size is the different current crowding effect in the size-dependent micro-LEDs. Due to reduce current crowding and uniform current spreading, smaller-size micro-LED pixel is able to operate in high-current-density

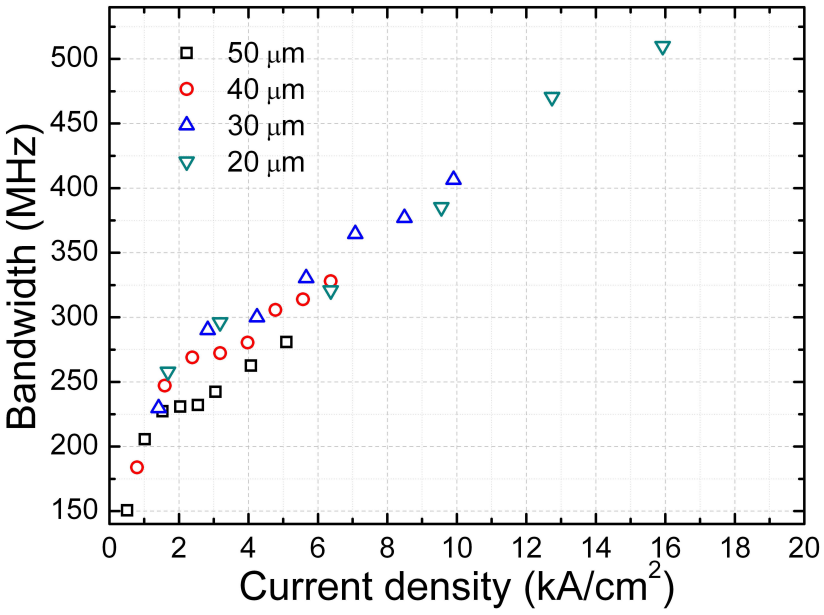

FIGURE 2.19: Bandwidth versus current density for different sized micro-LED pixels from the same 450 nm blue-emitting 16×16 micro-LED array.

regime, leading to reduced differential carrier lifetimes and higher modulation bandwidths [64, 88, 102].

The modulation bandwidth of the 20 μm micro-LED pixel reported here is over 500 MHz, which is believed to be the highest modulation bandwidth for GaN-based LED devices. Compared with conventional high-power broad LEDs for illumination, which usually have a modulation bandwidth of 20 to 30 MHz, micro-LEDs have thus shown superior modulation characteristics and great potential for VLC. In general, to improve the modulation bandwidths of LED devices, optimised packaging and efficient heat-sinking design are also very important since such improvement will enable LED devices to withstand higher operating current densities and achieve better modulation characteristics. Details of the application of micro-LEDs for VLC will be presented in the next chapter.

2.4 Summary

In summary, this chapter provides an overview of the fabrication of III-nitride micro-LED devices, the electrical and optical properties of micro-LED devices, and the modulation characteristics of micro-LED devices. The experimental part mainly focuses on investigating the electrical and optical characteristics of these micro-LED devices. The electrical and optical properties of the micro-LED devices are determined by many

factors, such as device configuration, device fabrication, LED wafer material, etc. In addition, the modulation bandwidths of some of the micro-LED pixels exceed 500 MHz, which is believed to be the highest modulation bandwidth for GaN-based LED devices. It is also found that the smaller-size micro-LED pixels have larger modulation bandwidths due to their superior performance in thermal management and the capabilities to operate in high-current-density regime. These results demonstrate the great potential of using micro-LED devices for VLC and lay the foundation for further investigating the multi-emitter nature of micro-LED array devices for high-speed parallel data transmission.

Chapter 3

CMOS-controlled micro-LED arrays and their applications in visible light communications

III-nitride micro-LED arrays provide a direct approach for efficiently generating micro-scale spatio-temporal light patterns which can be used for many applications. In order to fully utilise the 'multi-emitter' nature of the micro-LED array, it is desirable to integrate suitable controlling electronics onto the micro-LED device, allowing individual pixels from the micro-LED device to be conveniently addressed. Therefore, complementary metal-oxide-semiconductor (CMOS) controlled driver arrays suitable for being integrated with micro-LED arrays have been developed. This chapter mainly presents the performance of such CMOS-controlled micro-LED devices and their related applications for visible light communications (VLC). In section 3.1, the background of general CMOS technology is introduced. In section 3.2, the development of CMOS-controlled micro-LED arrays is presented. The CMOS driver chip was designed by our collaborator Dr Robert Henderson's group in the Institute for Integrated Micro and Nano Systems, School of Engineering, University of Edinburgh. However, the design parameters were determined in full collaboration with our group according to the configuration of our micro-LED devices, the compatibility of CMOS chip to the micro-LED devices, and the requirements of different applications. The CMOS-controlled micro-LED arrays

which will be shown contain 256 individually-addressable micro-LED pixels. In section 3.3, use of a single pixel from a 'bare' micro-LED array (without being integrated with CMOS electronics) for VLC is demonstrated. In section 3.4, single-channel and multiple-channel data transmissions are demonstrated for the CMOS-controlled micro-LED devices. Compared with the 'bare' micro-LEDs driven by a high-speed probe for VLC, the CMOS-controlled micro-LED devices have clear advantages including convenient computer control of each pixel within the array and the capability for high-throughput parallel data transmission by independently modulating up to 16 columns of micro-LEDs. Finally, a summary of the work present in this chapter is given in section 3.5.

3.1 Background of CMOS technology

For the last 25 years, CMOS (complementary metal-oxide-semiconductor) technology has been the dominant technology for constructing electronic integrated circuits on silicon wafers [103]. CMOS technology has the advantages of being cost-effective, reliable, manufacturable, of low power consumption and very importantly, scalable. The feature sizes of early CMOS transistors were in the micrometre range while the feature sizes of current CMOS devices are scaled down to the nanometre range, allowing a high density of logic functions to be integrated on a single chip. It was primarily for this reason that CMOS became the technology most used in very-large-scale integrated or ultra-large-scale integrated circuits. Nowadays, CMOS is regarded as the key technology in semiconductor-related microelectronics and is widely used in microprocessors, microcontrollers, image sensors, data converters, and various digital logic circuits. The term 'CMOS' not only refers to a particular style of digital circuitry design but also the family of processes used to fabricate the circuitry. Normally, the feature size of the smallest transistor that a CMOS fabrication process can produce and the standard voltage supplying to the CMOS are used to name a specific CMOS process [103]. For example, a '5 volt, 0.35 μm CMOS process' refers to the CMOS circuitry with minimum feature size of 0.35 μm and a voltage supply of 5V.

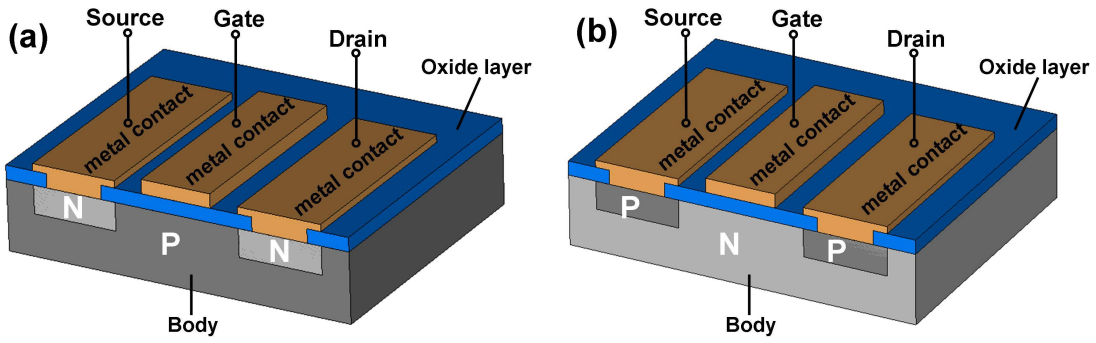

FIGURE 3.1: Schematic structures of (a) NMOS and (b) PMOS.

3.1.1 Metal-Oxide-Semiconductor Field Effect Transistor

The basic unit of CMOS circuitry is the Metal-Oxide-Semiconductor Field Effect Transistor (MOSFET). The term 'metal-oxide-semiconductor' is a reference to the physical structure of certain field-effect transistors, with a metal gate electrode placed on top of an oxide insulator, which in turn is on top of a semiconductor material. MOSFET contains two types of transistors, i.e. n-type MOSFET (NMOS) and p-type MOSFET (PMOS). Since NMOS and PMOS are usually used together to implement digital logic circuitry, the term 'complementary metal-oxide-semiconductor' is used to name the circuitry and relevant technology. 3D schematic structures of the NMOS and PMOS transistors are shown in Figure 3.1 (a) and (b), respectively. The operation principle of NMOS transistor will first be presented. As shown in Figure 3.1 (a), the body of NMOS consists of a p-type Si region and two n-type Si regions. The two n-type regions are known respectively as the source region and drain region, and are formed by doping using ion implantation [104]. Metal electrodes are formed on top of the two n-type regions and the two electrodes are denoted respectively as the terminal Source (S) and terminal Drain (D). An isolation layer of SiO_2, typically 0.05 μm to 0.1 μm thick, is grown on top of the p-type region in between the two n-type regions [104]. Another metal electrode is formed on top of this SiO_2 layer and denoted as the terminal Gate (G).

Depending on the applied voltage between gate and source (U_{GS}) and the applied voltage between drain and source (U_{DS}), NMOS is operated in one of the three working regions. The first region is known as the 'cutoff region'. In this region, the voltage between the gate and source, U_{GS}, is 0 V or remains below a certain threshold/turn-on voltage, U_T. In this case, very little current can flow throw from drain to source even if a positive voltage, U_{DS}, is applied between them. This is due to the p-n junction formed between

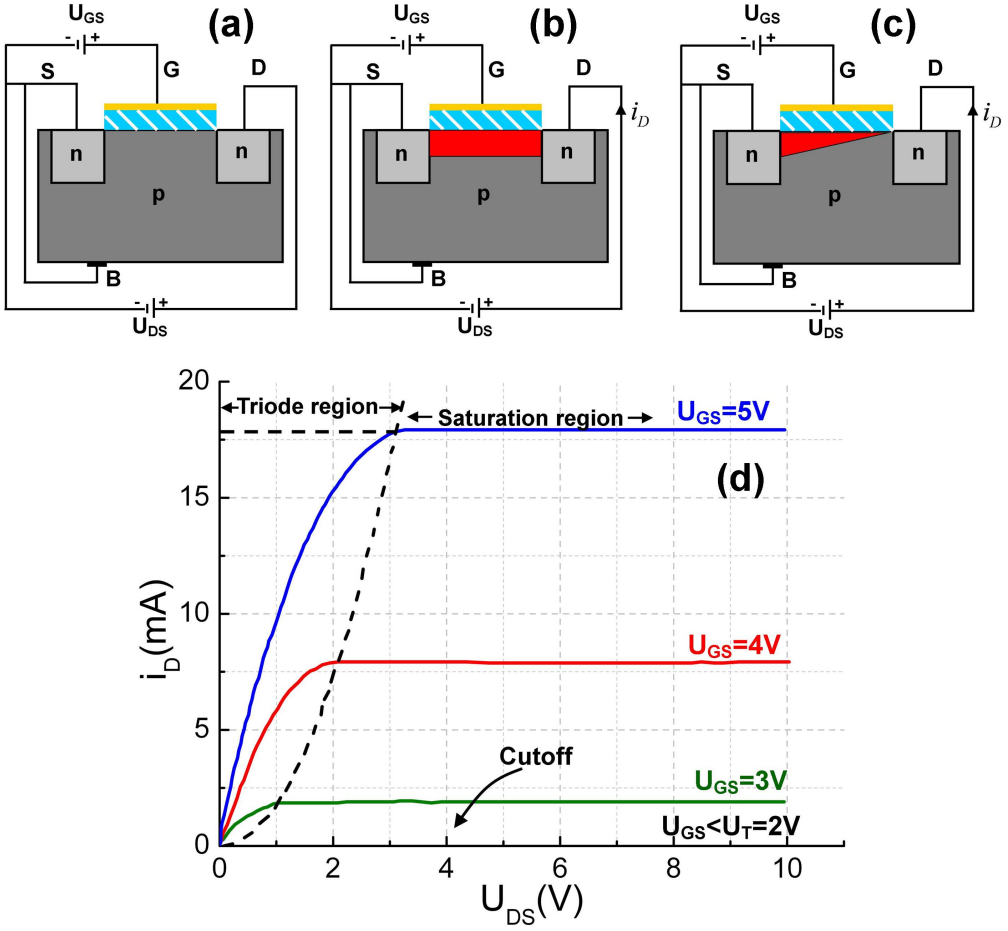

FIGURE 3.2: Schematic structures of an NMOS transistor working in (a) cutoff (b) triode and (c) saturation regions. (d) Characteristic I-V curves of an NMOS transistor, the data is from [104].

the NMOS body and drain region, which is reverse-biased by the U_{DS}. Figure 3.2 (a) illustrates a schematic of an NMOS transistor operating in the cutoff region. When $U_{GS} \geq U_T$ and $0 < U_{DS} < U_{GS} - U_T$, the transistor is operating in the 'triode region'. In this region, a large enough voltage is applied between the gate and source. Since the terminal source and the body of NMOS are connected together, then an electrical field that repels holes and attracts electrons is formed directly underneath the gate terminal. Influenced by this electric field, a thin layer underneath the gate terminal is formed where the electron density exceeds the hole density. This layer, which can be said to be inverted, is also known as the 'inversion channel' for NMOS, as it establishes an n-type channel bridging two n-type regions, i.e. the drain region and source region. If a positive bias, U_{DS}, is applied between the drain and source, a current, i_D, will flow from the drain to source via this channel. For small values of U_{DS}, i_D is proportional to the product of U_{DS} and the excess gate voltage ($U_{GS} - U_T$). Figure 3.2 (b) illustrates

a schematic of an NMOS transistor operating in the triode region, with the inversion channel highlighted in red. As the voltage U_{DS} continues to increase, the electrons which form inversion channel are attracted to the drain. This effect results in a narrowing of the inversion channel adjacent to drain and subsequently increases the resistance of the inversion channel. In this case, the current i_D is no longer proportional to U_{DS}. When U_{DS} is increased to a value causing complete depletion of the inversion channel, i_D will no longer increase at all due to the 'pinch-off' of the inversion channel. Therefore, NMOS is operating in the 'saturation region'. Figure 3.2 (c) illustrates a schematic of an NMOS transistor operating in saturation, with the tapering of the channel highlighted in red. Figure 3.2 (d) shows the characteristic current-voltage (I-V) curves of an NMOS transistor operating in cutoff, triode and saturation regions.

As shown in Figure 3.1 (b), the device structure of a PMOS transistor is similar to an NMOS transistor, except that the p-type and n-type regions are reversed in comparison to NMOS. In NMOS, an n-type inversion channel is formed when the device is operated in triode region and the current flows through NMOS transistor when $U_{GS} \geq U_T$; in PMOS, a p-type inversion channel is formed when the device is operated in triode region and the current flows through PMOS transistor when $U_{GS} \leq U_T$. It can be seen that the operating principles of the two devices are very similar, but the polarities of gate-source voltage (U_{GS}) are different, determined by the conditions required for forming inversion channels. A positive voltage is normally added between source and drain in PMOS and the current subsequently flows through source to drain. This is different from NMOS in which the current flows in a reverse direction from drain to source. In addition, the mobility of electrons, which are the carriers in the NMOS, is about two times greater than that of holes, which are the carriers in PMOS. For this reason, an NMOS device will have one-half the resistance or impedance of an equivalent PMOS device with the same geometry and under the same operating conditions. Therefore, integrated circuits based on NMOS can be smaller for the same complexity or, even more importantly, they can be more complex with no increase in device area. Compared with NMOS, PMOS technology has advantages such as low cost and high noise immunity [103]. It is worth noting that both NMOS and PMOS transistors function as a digital 'switch', which controls the current flowing through the drain region to source region or reversely via controlling the magnitude of gate voltage. This 'switch' nature is the key feature of CMOS technology, which makes it possible to realise digital logic circuits for a variety

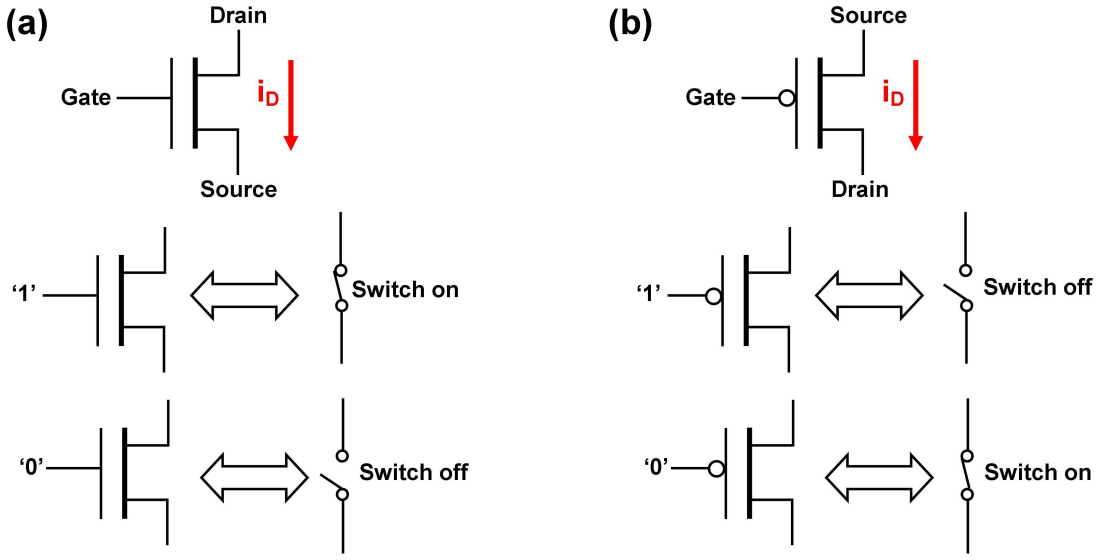

FIGURE 3.3: Circuit diagram symbols of (a) NMOS and (b) PMOS. The schematic logic operation process of NMOS and PMOS in response to different logic inputs are plotted in (a) and (b), respectively.

of applications.

3.1.2 Basic CMOS logic circuitry

A CMOS control chip with complex functions, such as the one used to control micro-LED devices, is formed by basic CMOS logic circuitry with the functionality for specific logic operation. Here, we will briefly introduce how a basic CMOS logic circuitry is constructed via a combination of NMOS and PMOS transistors and its relevant logic operation process according to different inputs. The circuit diagram symbols of NMOS and PMOS are shown in Figure 3.3 (a) and (b), respectively. For NMOS, if the voltage applied between gate and source is higher than the turn-on voltage, i.e. $U_{GS} \geq U_T$, current can flow through the drain to source under a positive drain-to-source voltage U_{DS}. In this case, the NMOS 'switch' is turned on by the gate voltage U_{DS}. In a digital logic circuit, logic 1 is normally defined as the voltage above the threshold voltage to turn on an NMOS transistor while logic 0 is defined as the voltage below the threshold voltage to turn off an NMOS transistor. For PMOS transistors, the logic operation process is opposite to NMOS, i.e. logic 1 turns off the PMOS and logic 0 turns on the PMOS. The schematics of PMOS and NMOS in response to different logic inputs are also plotted in Figure 3.3 (a) and (b), respectively.

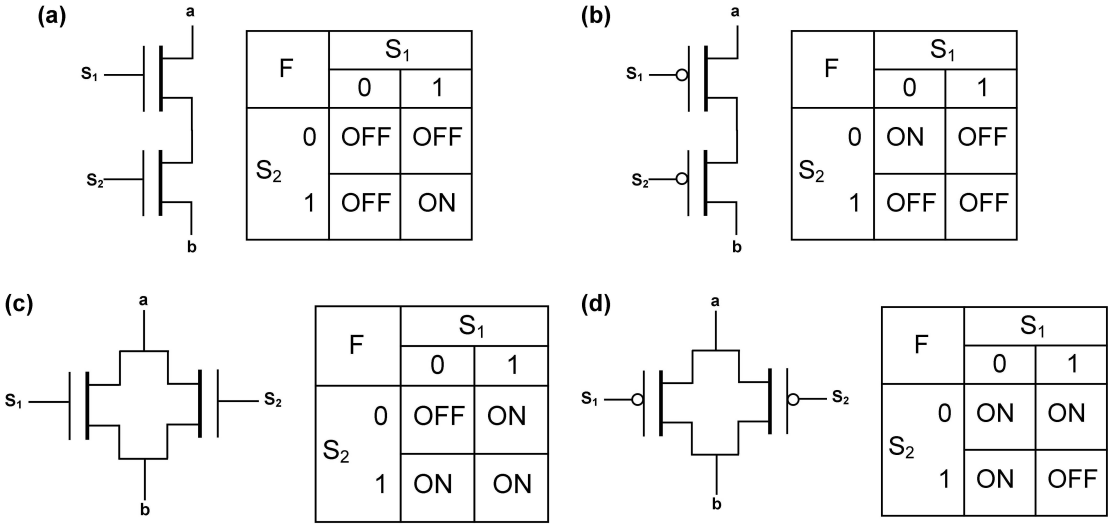

FIGURE 3.4: Circuit diagram and truth table of (a) two NMOS transistors connected in series, (b) two PMOS transistors connected in series, (c) two NMOS transistors connected in parallel, and (d) two PMOS transistors connected in parallel.

Figure 3.4 shows the circuit diagrams of two MOS transistors, either p-type or n-type, connected in parallel or series. These four combinations of MOS transistors lay the foundation of logic operation of the CMOS circuitry, as any CMOS circuitry, no matter how complex or simple, is formed by connecting MOS transistors in parallel or series. As shown in Figure 3.4 (a), when two NMOS transistors are connected in series, a logic relation 'AND' is formed and $F = S_1 \bullet S_2$, where S represents the state of input signal and F represents the transfer function. When two PMOS transistors are connected in series, $F = \overline{S_1} \bullet \overline{S_2}$, as shown in Figure 3.4 (b). Figure 3.4 (c) shows the situation when two NMOS transistors are connected in parallel. If any of the two NMOS transistors is turned on, the combination switch is turned on. Thus, a logic relation 'OR' is formed and $F = S_1 + S_2$. If two PMOS transistors are connected in parallel, $F = \overline{S_1} + \overline{S_2}$, as shown in Figure 3.4 (d). Since the function of different combinations of MOS transistors is to transfer the state of an input signal to the output terminals according to a specific logic operation process, CMOS basic circuitry is also known as the transfer gate.

One of the most important transfer gates used to build CMOS digital logic circuits is the CMOS inverter (NOT gate), which can be constructed using one PMOS transistor and one NMOS transistor. Figure 3.5 (a) shows the circuit diagram and symbol of a CMOS inverter. U_{DD} is the positive voltage supply, U_{SS} is the ground, A is the logic input and F is the logic output. If A='1', the upper PMOS transistor is off and the lower NMOS transistor is on. In this case, there is a conductive link between F and

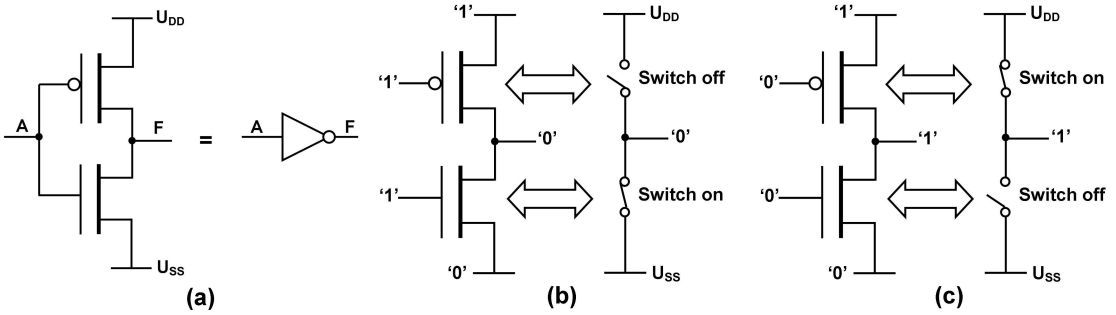

FIGURE 3.5: (a) Circuit diagram and symbol of a CMOS inverter (NOT gate) with logic input A and logic output F; (b) schematic logic operation process of a CMOS inverter in response to logic input '1'; (c) schematic logic operation process of a CMOS inverter in response to logic input '0'.

U_{SS}, and F=U_{SS}='0'. If A='0', the upper PMOS transistor is on and the lower NMOS transistor is off. Therefore, there is a link between F and U_{DD}, and F=U_{DD}='1'. It is obvious that the logic output F always has an inverse logic state to the logic input A, i.e. $F = \overline{A}$. Figure 3.5 (b) and (c) illustrate the logic operation processes of a CMOS inverter in response to different logic inputs. Figure 3.5 also shows why PMOS transistor and NMOS transistor are regarded as 'complementary' to each other in CMOS circuitry. As shown, the upper PMOS transistor controls whether the output is connected to logic 1, while the lower NMOS transistor controls whether the output is connected to logic 0. Under the same input, when the PMOS transistor is off, the NMOS transistor is always on; when the PMOS transistor is on, the NMOS transistor is always off. The two transistors work together to realise the logic operation of the circuitry, but complement the functionality of each other.

In addition to the NOT gate, the CMOS NAND gate and NOR gate are also very important logic gates which are widely used to construct CMOS digital logic circuits. The circuit diagrams of the CMOS NAND gate and NOR gate are shown in Figure 3.6 (a) and (b), respectively. The basic NAND gate and NOR gate consist of two PMOS transistors and two NMOS transistors. For the NAND gate, the upper PMOS transistors are connected in parallel and the lower NMOS transistors are connected in series. If one of the two inputs, either A or B, is logic 0, then there will be a conductive path existing between U_{DD} and the output F. Therefore, F=1. When A and B are both logic 1, the upper PMOS transistors are both in off states and the lower NMOS transistors are both on. In this case, there will be a path existing between U_{SS} and the output F, so F=0. The logic relation, $F = \overline{A \bullet B}$ (NAND), is formed. For the NOR gate, the upper

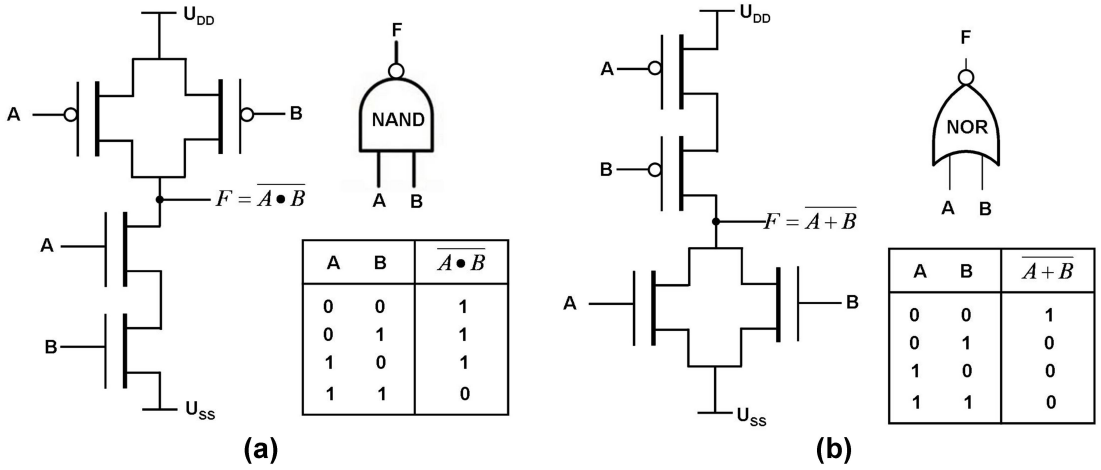

FIGURE 3.6: (a) Circuit diagram, symbol and truth table of a CMOS NAND gate with logic inputs A, B and a logic output F; (b) circuit diagram, symbol and truth table of a CMOS NOR gate with logic inputs A, B and a logic output F.

PMOS transistors are connected in series and the lower NMOS transistors are connected in parallel. The output F is equal to 0 except when A and B are both 0. Therefore, the logic relation, $F = \overline{A + B}$ (NOR), is formed. The corresponding truth tables and symbols of the CMOS NAND gate and NOR gate are also shown in Figure 3.6 (a) and (b), respectively.

The basic CMOS circuitry (logic gates) can be used to construct circuits with different logic functions. For example, by combining one NAND gate and one NOT gate together with the logic output of the NAND gate connecting to the logic input of the NOT gate, an AND gate can be realised. Clearly, by using basic CMOS logic gates, much more complex digital circuits can be built, such as the control circuit to drive micro-LEDs. The specific functionality of the CMOS control chips will be discussed in more detail in the following section.

3.2 CMOS/micro-LED integration and CMOS-controlled micro-LED devices

The work in our research group of designing and subsequently using CMOS driver chips to control micro-LED devices started in 2007. Since then, modifications to the CMOS driver chip have been made by to improve its performance and meet the requirements of different applications. The first CMOS driver chip for fully operating the integrated

micro-LED array was implemented in 2008 and it was named the 'first-generation' device [95, 105]. For clarity, subsequent CMOS designs following the 'first-generation' were named 'second-generation', 'third-generation', etc. These CMOS chips were all designed (under jointly agreed specifications) by our collaborator Dr Robert Henderson's group in the Institute for Integrated Micro and Nano Systems, School of Engineering, University of Edinburgh. While my work mainly focuses on the characterisation of the CMOS-controlled micro-LED devices and their high-end applications. These high-performance CMOS-controlled micro-LED devices have now been used for a variety of applications such as self-emissive micro-displays, optoelectronic tweezers, chemical explosives sensors, time-resolved fluorescence measurement systems, mask-less photolithography and VLC [35, 64, 87, 95, 106–109].

3.2.1 Layout of CMOS driver chip

In terms of VLC, all the experimental results presented in this chapter are based on the 'fourth-generation' CMOS-controlled micro-LED device, whose design was improved based on the experience with the previous CMOS designs. Since the previous CMOS designs ('first-generation', 'second-generation', 'third-generation') were reported in detail elsewhere [95, 105], only the 'fourth-generation' CMOS device will be introduced and discussed here. Figure 3.7 (a) shows a microscope image of a bare 'fourth-generation' CMOS chip (not bonded to a micro-LED array), which was implemented in a standard 0.35 μm 3.3 V CMOS technology by Austria Microsystems. Each chip consists of a 16×16 array of CMOS drivers. The size of each driver is 100×100 μm^2, and contains a 50×50 μm^2 electrode (bonding pad) and dedicated driver circuitry. Four metal layers were used to realise the full operation of the CMOS device, the bottom two layers being used for routing signals of the CMOS transistors, the third layer acting as a protection layer to prevent the bottom layers being applied with high-voltage signals from above, and the uppermost layer being patterned into an array of electrodes to interface to the micro-LED device. A bump-bonding process, which will be introduced later, was used to provide electrical and physical contact between the micro-LED electrodes and CMOS electrodes. However, based on our previous experience, the bonding process may damage the CMOS control circuitry if it is placed right beneath the electrode (bonding pad). Therefore, in the 'fourth-generation' CMOS chip, its driver circuitry is designed to surround the electrode, as shown in Figure 3.7 (b). In addition, each CMOS electrode

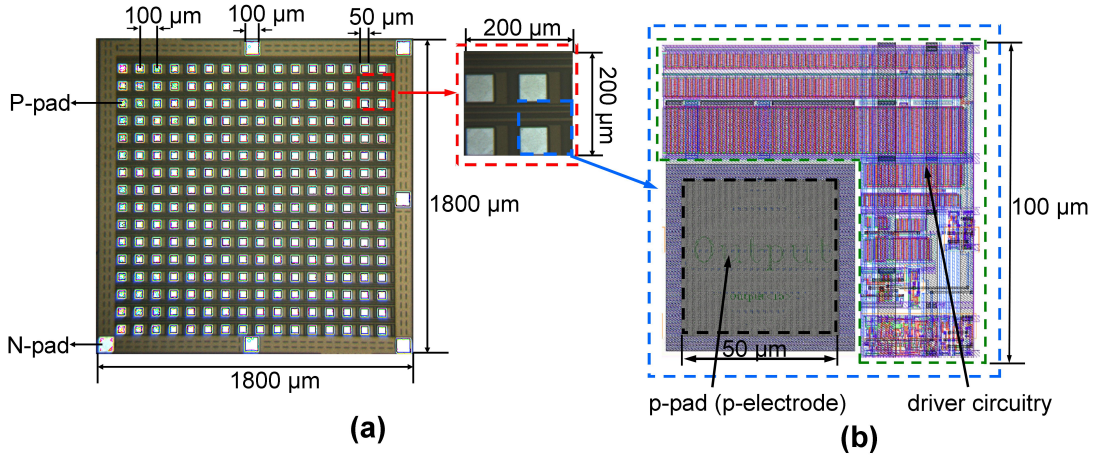

FIGURE 3.7: (a) A top-view optical microscope image of a 'fourth-generation' CMOS chip; (b) the design of a single CMOS driver.

is placed on the top surface of a tungsten column, which propagated vertically through the entire chip (four metal layers) and provided excellent mechanical stability for the chip.

3.2.2 Logic circuitry of CMOS driver

The logic circuitry contained within each CMOS driver is shown in Figure 3.8. The input *ROW* and input *COL* determine which driver from the CMOS chip is addressed and the input *CLK* is the clock signal of the CMOS driver. When a particular driver is addressed (when its input *ROW* and input *COL* are high) and the clock signal is on the rising clock edge (*CLK* is high), the output of the *D*-type flip-flop will match the state of the input *DIN* (driver input), which is the state that is intended to be sent to the particular CMOS driver. The input *MODE_CONTROL* controls the output mode of the driver. When *MODE_CONTROL* is high, the driver will respond according to the state of *INPUT_SIG* (driver input signal), which can be a DC signal from the CMOS driver board, an on-chip voltage-controlled oscillator (*VCO*) or an off-chip external signal. When *INPUT_SIG* is also high, the output of the *D*-type flip-flop, i.e. the state of *DIN*, is sent to the particular CMOS driver. Depending on the state of *DIN*, the CMOS driver can be either turned on or turned off. If the CMOS driver is turned on, a positive bias (*LED_VDD*) will be applied to the micro-LED pixel and the corresponding micro-LED pixel will respond depending on *LED_VDD* and its L-I and I-V characteristics. In addition, the CMOS driver can also operate in pulse mode if the *MODE_CONTROL* is low. In this

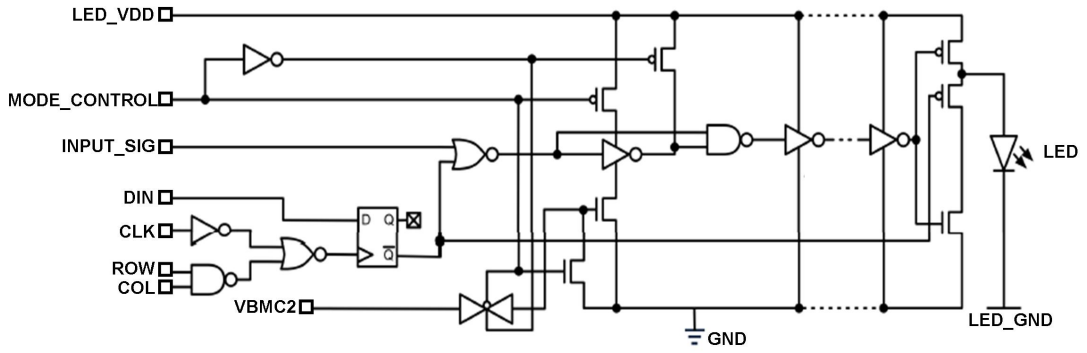

FIGURE 3.8: Logic circuitry of each CMOS driver.

case, a short electrical pulse will be sent to the CMOS driver. The functionality of the pulse mode is realised by *VCO* circuitry and relevant pulse generation circuitry, and the main application of operating a CMOS driver in pulse mode is for time-resolved fluorescent measurements and organic laser photo-pumping [89, 107, 108]. However, the pulse mode has not been used for the work presented in this thesis and details of similar *VCO* circuitry and pulse generation circuitry have been presented before [95, 105, 110]. Therefore, the operation of a CMOS driver under pulse mode will not be discussed here. The CMOS chip is implemented using a 3.3 V logic level. In this case, the voltage applied to the source and drain of CMOS transistors cannot go beyond 3.3 V, i.e. the maximum value of *LED_VDD* is limited to 3.3 V. Given the relatively high turn-on voltages of GaN-based LEDs, 3.3 V is not enough to operate these LED devices for practical applications. To solve this problem, one key design of the CMOS chip is to physically separate the ground terminal of the micro-LED (*LED_GND*) from the ground terminal of the main CMOS logic circuit (*GND*). This means that by adding a positive voltage between *GND* and *LED_GND*, *LED_GND* can be relatively pulled down to negative compared with *GND*. Such feature allows the *LED_VDD* to supply forward voltages higher than 3.3 V to CMOS-controlled micro-LEDs without causing any damage to the CMOS transistors. For example, if *LED_VDD* is 3.3 V and *LED_GND* is biased with -3 V with respect to *GND*, then a total forward bias of 6.3 V (3.3 V+3 V=6.3 V) will be applied to the micro-LED pixel. Hence, micro-LEDs can be operated to produce enough output power for practical applications, such as micro-displays and VLC.

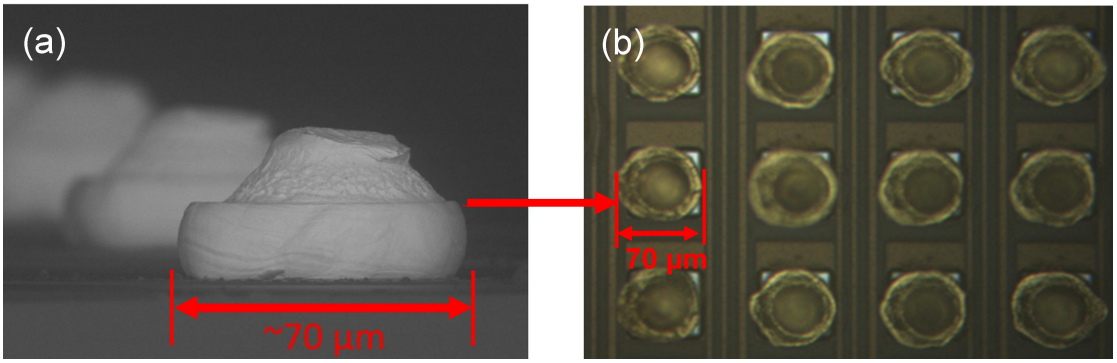

FIGURE 3.9: (a) SEM image showing that the gold bumps have 'up-turned mushroom' shapes; (b) top-down microscope image of a gold-bump deposited CMOS chip.

3.2.3 Flip-chip bonding

The CMOS driver chips are electrically and physically integrated with micro-LED array devices via a flip-chip bonding process, which is very important to functionalise the CMOS-controlled micro-LED devices. Each CMOS bonding pad/electrode is connected to the electrode of a micro-LED pixel by a gold bump, which effectively provides good connection between the micro-LED pixel and its control circuitry. The gold bumps were first deposited onto the CMOS chips using an automatic wire-bonder machine (Palomar Technologies Inc., Palomar 8000), whose tip was fed with gold wire with a diameter of 20 μm via a capillary. As the tip came into contact with a CMOS bonding pad, a combination of thermal and ultrasonic energy was applied at the bonding tip to melt the gold wire, which subsequently formed a gold bump on the CMOS bonding pad. Figure 3.9 (a) shows a scanning electron microscope (SEM) image of typical gold bumps formed on the CMOS bonding pad. The gold bumps have 'up-turned mushroom' shapes and approximate diameters of 70 μm. Figure 3.9 (b) shows a top-down optical microscope image of a section of a CMOS chip deposited with gold bumps. Once the CMOS chip was fully deposited with gold bumps, it was transferred to another machine, a flip-chip bonder (Finetech Fineplacer; Finetech, GmbH and Co. KG). In this machine, the micro-LED array device was firstly aligned above the CMOS chip with its metal electrodes facing down to the CMOS chip. Then, the two chips were mechanically pressed together along with ultrasonic energy and thermal energy being applied during the whole pressing process. As a result, the gold bumps were sandwiched between CMOS chip and micro-LED device, and with its upper surface and lower surface firmly adhered to the electrodes of micro-LED and bonding pads of CMOS chip, creating good signal path between the micro-LED array device and the CMOS chip.

Chip dimensions	3.2×3.2 mm^2
Fabrication process	0.35 μm
Array size	16×16, 256 drivers
Driver pitch	100 μm
Pad size	60×60 μm^2
Maximum current (per driver)	250 mA
Maximum voltage provided by driver board	3.3 V

TABLE 3.1: Design parameters of CMOS driver chip.

3.2.4 CMOS driver board

In order to operate the CMOS-controlled micro-LED device, a CMOS driver board was developed by the University of Edinburgh, as shown in Figure 3.10. There are a group of variable resistors on the right side of the main driver board and these resistors can be adjusted manually to control the micro-LED forward bias (*LED_VDD*), *VCO* clock frequency and optical pulse duration. A field-programmable gate array (FPGA) unit (Opal Kelly, XEM3010-1500P) is attached to the main driver board (blue dashes in Figure 3.10). The FPGA unit interfaces with a computer via a universal serial bus (USB) interface in order to receive instructions from the operating software. The operating software allows the user to control individual LED units and the operating mode of the array (DC, pulse, etc.) via a user-friendly graphical computer interface. In addition, the FPGA board powers the CMOS-controlled micro-LED device using the power supplied from the computer USB port. The maximum voltage supplied by the FPGA board is 3.3 V. In order to drive the micro-LED with more than 3.3 V, the ground terminal of the micro-LED should be biased below 0 V by adding a positive voltage between *GND* and *LED_GND*. The daughter card, shown by red dashes in Figure 3.10, maps the input signals from the main driver board to appropriate pins on the CMOS chip, and also provides several SubMiniature Version A (SMA) input/output ports which can be used for purposes such as trigger inputs/outputs to/from the CMOS-controlled micro-LED device. A summary of the CMOS chip is shown in Table 3.1, which overviews its design parameters.

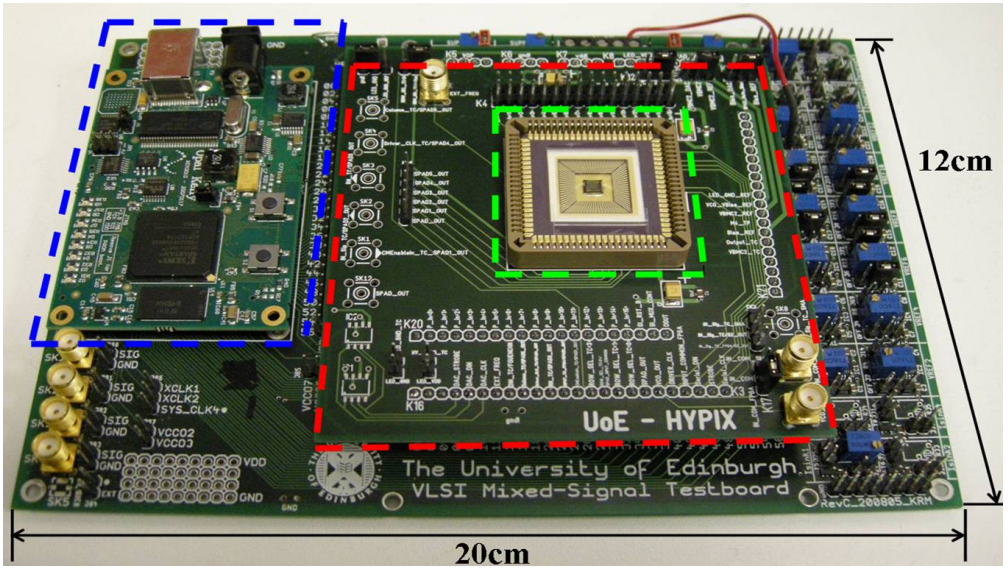

FIGURE 3.10: Photograph of the CMOS driver board used for operating the CMOS-controlled micro-LED array. Attached to the motherboard is a FPGA board (blue dashes), the daughter card (red dashes) and a packaged CMOS-controlled micro-LED device (green dashes).

3.3 Micro-LED device for single-channel data transmission

Before presenting the results of using CMOS-controlled micro-LEDs for VLC, proof-of-concept experiments were carried out to demonstrate optical data transmission using 'bare' micro-LED pixels (without being integrated with CMOS electronics). This works lays the foundation for presenting the VLC results based on CMOS-controlled micro-LEDs.

Figure 3.11 shows the schematic experimental setup for testing the performance of micro-LED pixels for optical communications. This setup is similar to that used for the frequency response measurements, but the measuring instruments are different. As shown in Figure 3.11, an AC data signal was first generated from a data pattern generator (Anritsu Pulse Pattern Generator MP1763C) and then combined with a DC bias to reach above the threshold voltage of the LED device. Since the data pattern generator does not have an internal synchroniser, it was clocked using the output from a network analyser. After being combined with a DC bias, the overall modulation signal was applied to individual micro-LED pixels using a probe system, similar to that used in the frequency response measurement shown in chapter 2, section 2.3. The modulated optical emission was imaged onto a fast AC-coupled photodetector (FEMTO HAS-X-S-1G4-SI-FS)

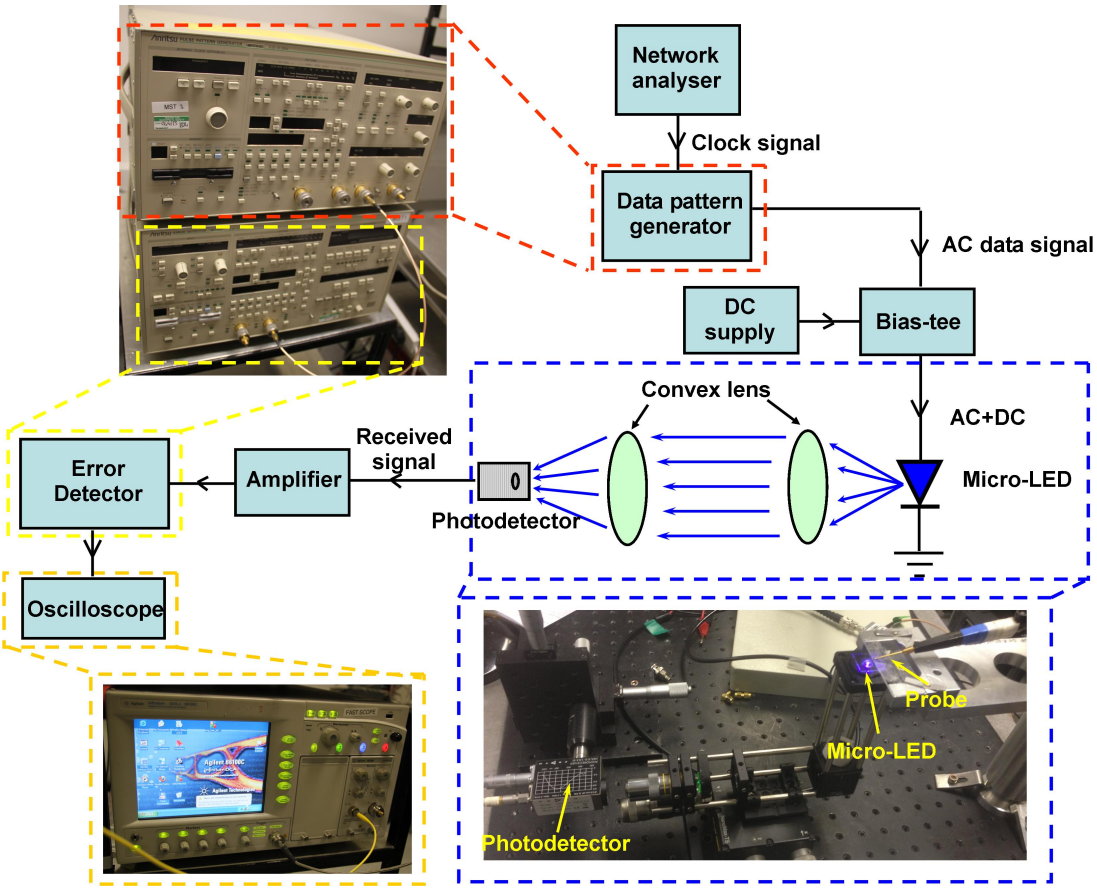

FIGURE 3.11: Schematic setup of the optical communication system using micro-LEDs.

and the received optical signal was transformed into an electrical signal by the photodetector. After being amplified by an external amplifier (HP8477D, dual stage 50dB electrical amplifier), the electrical signal was sent to an error detector (Anritsu Error Detector MP1764C) for further bit-error ratio (BER) measurement. BER refers to the ratio of incorrectly transmitted data bits to the total number of transmitted bits, so a BER of 1×10^{-4} indicates that there is one incorrectly transmitted bit out of every 10000 bits that were transmitted. BER measurement is performed by comparing the original transmitted data bits with the received data bits by the error detector. In this case, the received data bits need to be synchronised with the reference data bits, allowing each specific data bit that was received to be compared with the same bit that was transmitted. The data pattern generator and the error detector are the main instruments used for BER measurement and they together form a bit-error ratio test (BERT) system. Normally, an oscilloscope is connected to the error detector to monitor the received data signal. The received data signal can be directly viewed on the screen of the oscilloscope and such feedback is important for adjusting optics to achieve a better collection of the

optical signal at the photodetector.

The data signal used for data transmission was in a format of an non-return-to-zero (NRZ) pseudo-random bit sequence (PRBS) instead of an NRZ random data sequence. As for an NRZ random data sequence, each bit in the sequence has a 50% probability of being either 1 or 0, regardless of the state of the adjacent bits. Therefore, it is possible to have a long sequence of consecutive identical digits (CIDs), which contains a low frequency component and makes it difficult for the high-speed system to 'recognise' the data bits correctly. In addition, after transmitting CIDs, the sudden change of the state of a data bit makes it difficult for the system to respond and causes more error bits to the system. Therefore, data are usually encoded in specific bit patterns, which aim to reduce the length of CIDs and map the data in an easily-distinguishable format so that the system can differentiate the date bits precisely. Since data encoding can significantly improve the BER, different PRBS lengths are used to mimic data encoded using different schemes. In this work, short pattern lengths, i.e. 2^7-1 and 2^9-1 bits, were used to frame the data signal and test the capability of micro-LEDs for data transmission. Such schemes provide good approximation to actual Gigabit Ethernet and Fibre Channel which require data encoded into 10 bit long 'packages' using 8B/10B encoding [111]. It is also worth indicating that there are various encoding schemes developed for optical communications aiming to tackle specific issues and they are much more complex and powerful than the PRBS encoding schemes used here. For example, forward error correction, which refers to the encoding schemes allowing for errors in the transmitted data to be detected and corrected, is often implemented in optical communication systems to decrease the BERs [70]. Since the work here mainly focuses on initial VLC demonstration based on micro-LED devices, advanced encoding schemes will not be discussed in detail.

The peak-to-peak voltage of the NRZ PRBS data signal from BERT is from 0 V to 2 V, which is below the turn-on voltage of a micro-LED device and cannot be used to modulate the micro-LED device directly. Therefore, the voltage of data signal was level-shifted by combining a DC offset voltage before being applied to operate the device. An illustration of the NRZ data signal to drive the micro-LED device is shown in Figure 3.12. The micro-LED device is modulated under a binary pulse amplitude modulation scheme and the high level and low level of the modulation signal represent the logic 1 and logic 0, respectively. The modulation depth of the system is defined by the ratio

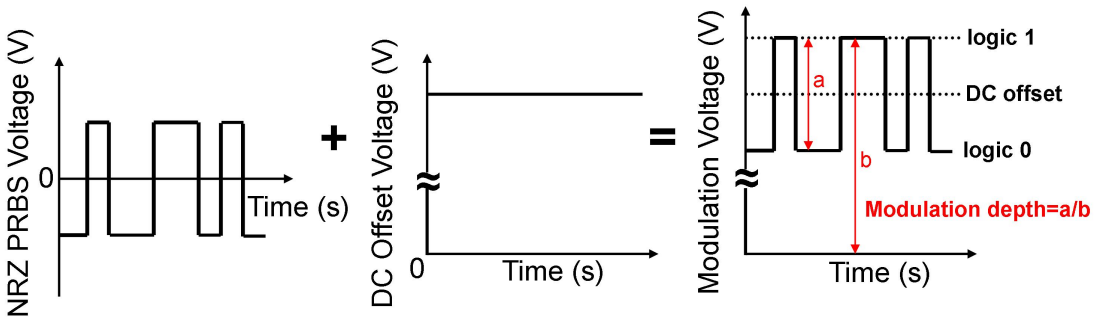

FIGURE 3.12: Illustration of the NRZ PRBS data signal combined with a DC offset and applied to a micro-LED.

between peak-to-peak amplitude of the BERT output and the combined amplitude of BERT output and DC bias voltage.

Demonstration of optical data transmission was carried out using a 44 μm diameter micro-LED pixel from an 8×8 array with a peak emission wavelength of 450 nm. I-V, L-I and modulation characteristics of similar micro-LED pixels have been investigated and were presented in chapter 2, section 2.2. An NRZ PRBS (2^7-1 bits) data stream from the BERT is used to modulate the micro-LED pixel directly by using a high-speed probe. In this case, the amplitude of the output signal from the micro-LED pixel is modulated. Details of the amplitude modulation scheme can be found in chapter 1, section 1.4. The BERs are measured as a function of the received optical power at the photodetector. A neutral density filter wheel is used to control the optical power received by the photodetector while the DC bias of the device is kept in constant in the measurement. The DC bias current provided to the 44 μm diameter micro-LED pixel is 40 mA. As low currents inhibit the data transmission rate due to reduced modulation bandwidth and high currents may cause device failure due to self-heating effect, a bias current of 40 mA provides an appropriate trade off between the modulation performance and device reliability. Figure 3.13 shows the measured BERs versus received optical power at different data rates. As shown, for a given BER, lower optical power is required for lower data rates. At low data rates, micro-LED is able to follow the input data signal and only very small optical power is needed to distinguish the data. When the data rate increases, micro-LED can not respond fast enough to match up with the high-frequency input data signal. Therefore, the micro-LED device is required to operate in larger current-density regime so that the modulation capability of micro-LED can be improved and more optical power can be used to distinguish the data. Error-free data

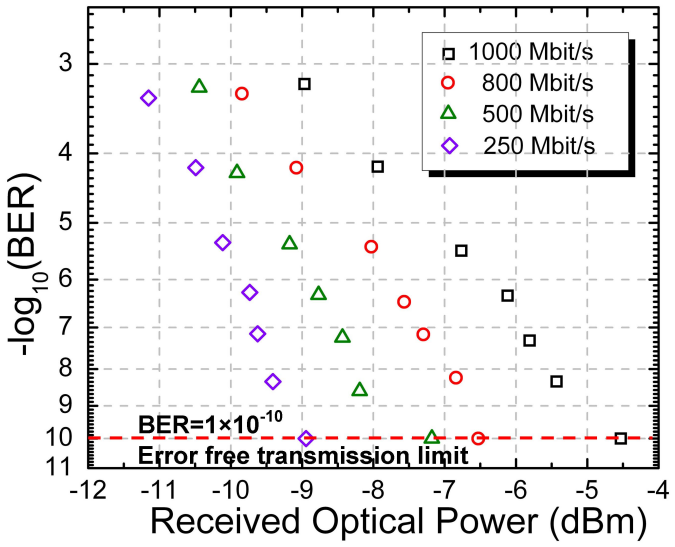

FIGURE 3.13: BERs measured from a 44 μm diameter micro-LED pixel with data transmission rate at 250 Mbit/s, 500 Mbit/s, 800 Mbit/s and 1000 Mbit/s (1 Gbit/s), as a function of the received power at the photodetector. The bias current of the micro-LED pixel is 40 mA.

transmission, defined as a BER of less than 1×10^{-10}, is achieved at a data rate of up to 1 Gbit/s (1000 Mbit/s). A further increase of power can not increase the error-free transmission rate, indicating that this data transmission rate is probably limited by the modulation capability of the micro-LED pixel. In this case, the micro-LED pixel can not respond fast enough to follow the input data signal due to the limitation of its modulation capability. Even if more optical power is transmitted, the received data signal still can not be distinguished and decoded.

In an optical communication system, an 'eye diagram', also known as an 'eye pattern', is an oscilloscope display constructed by repeatedly sampling the received signal over a period of several clock cycles at an interval of one clock cycle, and overlaying the received data [26]. An eye diagram is regarded as an experimental tool for the evaluation of the combined effects of channel noise and inter-symbol interference on the performance of a baseband pulse-transmission system under amplitude modulation (see chapter 1, section 1.4). Normally, distortion of the signal waveform due to inter-symbol interference and noise appears as the closure of the eye diagram, while an open eye diagram corresponds to minimal signal distortion and better signal quality. Therefore, the eye diagram allows us to estimate the overall performance of an optical communication system based on micro-LED devices. Although the closure of an eye diagram can be directly viewed, there is no strict universal standard to define the closure of an eye diagram. Normally,

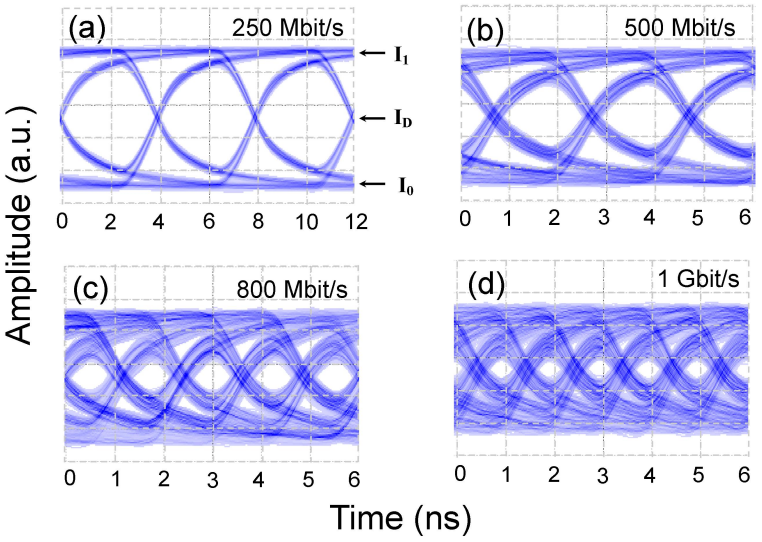

FIGURE 3.14: Eye diagrams of the 44 μm diameter micro-LED pixel modulated at (a) 250 Mbit/s, (b) 500 Mbit/s, (c) 800 Mbit/s and (d) 1 Gbit/s, respectively. Also indicated in Figure 3.14 (a) are the three state levels for '0' state (I_0), '1' state (I_1) and decision state (I_D).

a closed eye diagram can be defined as the eye diagram formed by data which can not meet the BER standard of a communication system. For Figure 3.13, the closure of an eye diagram can be defined as the eye diagram formed by data with BER larger than 1×10^{-10}. Figure 3.14 shows the eye diagrams of the 44 μm diameter micro-LED pixel at different data rates and with a bias current of 40 mA, which were measured by sending the received optical data signal to a real-time oscilloscope (ROHDE&SCHWARZ-RTO-1022). In Figure 3.14 (a), the level of the '1' state (I_1) and of the '0' state (I_0) and of the decision level (I_D) are indicated by the black arrows. The decision level, i.e. the boundary between what is interpreted by the receiver as '0' and '1', normally lies in the middle between the '0' state and '1' state. The 'eye' shown in Figure 3.14 (a) is wide open, indicating that error-free data transmission is easily achievable at this data rate using micro-LED device. However, as the data rate increases to 1 Gbit/s, the eye diagram closes and the state of the '0' and '1' level cannot be clearly distinguished, resulting in an increase of BER. Therefore, in order to achieve a given BER, more received power is required to distinguish the state of transmitted data for higher data rates than for lower data rates. These conclusions are consistent with the data of BERs versus received power provided in Figure 3.13.

If the data rate is increased beyond the modulation capabilities of the micro-LED devices, the eye diagrams will close completely and the distorted data signal can no longer be

distinguished and recovered. In this case, error-free data transmission can no longer be achieved. Since micro-LED devices have much higher maxmium modulation bandwidths compared with broad-area LED devices, they also show superior performance over broad-area LED devices in optical communications. The maxmium modulation bandwidth of a micro-LED device is defined as the modulation bandwidth at the specific current density which the thermal roll-over of optical power appears. Ideally, if the injection current density can always be increased, there will be no limitation of the maxmium modulation bandwidth of micro-LED. However, in practise, the thermal effect can cause the failure of micro-LED if the device is driven under very high injection current densities. Therefore, in this work, the micro-LED devices were not driven at extreme high-current conditions to get the best possible results. In addition, CMOS drivers with low switching speeds can also influence the performance of CMOS-controlled micro-LEDs for VLC. In order to improve the performance of micro-LED for VLC, factors such as device thermal management and control electronics need to be taken into careful consideration.

As shown in this work, 1 Gbit/s error-free data transmission is achieved using a single 44 μm diameter micro-LED pixel under basic binary pulse amplitude modulation scheme. For a single broad-area LED device with lower modulation bandwidth, such high data transmission rate is unimaginable if it is modulated under a basic binary pulse amplitude modulation scheme. Therefore, in order to increase the date rate of broad LED device for VLC, much effort has been made to develop advanced encoding techniques and highly efficient modulation schemes [60, 63, 72, 74, 112]. For example, orthogonal frequency division multiplexing (OFDM) has been proved to be an appropriate modulation scheme for VLC due to its high spectral efficiency. An over 1 Gbit/s single-channel VLC link has been reported using a broad-area LED device under OFDM modulation and demodulation schemes [74]. However, if a micro-LED device is implemented for VLC under OFDM modulation scheme, much higher data rates can again be achieved compared with broad-area LED devices. Recently, a 3-Gb/s single-LED OFDM-based VLC link was realised using a 50 μm diameter Gallium Nitride micro-LED in collaboration with our colleagues at the University of Edinburgh [65]. To date, this is the fastest VLC system using a single LED, showing the great potential of using micro-LED devices for high-speed optical data transmission. This micro-LED device was fabricated by our group and the pixels have a similar design to the 44 μm diameter micro-LEDs used for the 1 Gbit/s VLC demonstration reported here.

It is worth noting that the work on applying OFDM modulation schemes to micro-LED devices has just started. Future work in this area will focus on further developing advanced encoding and modulation schemes and applying such schemes on micro-LED devices to improve their performance in VLC. In addition, since the modulation characteristic of micro-LEDs is crucial for high-speed data transmission, improving the device modulation capability through optimising device design and using better wafer materials is definitely worth further attention and investigation. Last but not least, there are hundreds of micro-LED pixels on a single micro-LED array device. After being integrated with a CMOS driver array, each micro-LED pixel in the array can be individually addressed via an easily-controllable interface, which allows many micro-LED pixels to be modulated simultaneously to deliver high-speed parallel data streams for VLC. In this case, a single on-chip multiple-channel VLC system is realised and such VLC system should have much larger data-transmission capacity compared with a single-channel VLC system. More details about the multi-emitter nature of CMOS-controlled micro-LED array and on-chip multiple-channel VLC system will be presented in the following section.

3.4 VLC based on CMOS-controlled micro-LED devices

3.4.1 Single-channel VLC implementation

CMOS electronics allow convenient control of individual pixels from micro-LED arrays via a simple computer interface, making micro-LED devices much more controllable for practical applications. As shown above, CMOS drivers function as a digital switch to control the output state of micro-LED devices according to the state of the driver input signal, i.e. *INPUT_SIG*. When *INPUT_SIG* is logic 0, the CMOS driver is switched off and the corresponding micro-LED pixel will be off. When *INPUT_SIG* is logic 1, the CMOS driver is switched on and a bias is then applied to the corresponding micro-LED pixel. The optical output of the micro-LED is determined by the applied bias and its I-V and L-I characteristics. In this way, the output state of the CMOS-controlled micro-LEDs can vary between two levels, i.e. are on-off-keying (OOK) modulated according to the state of the *INPUT_SIG*. Therefore, the LED pixel in the micro-LED array can be used as a visible-light point-to-point data transmitter and the CMOS driver is used

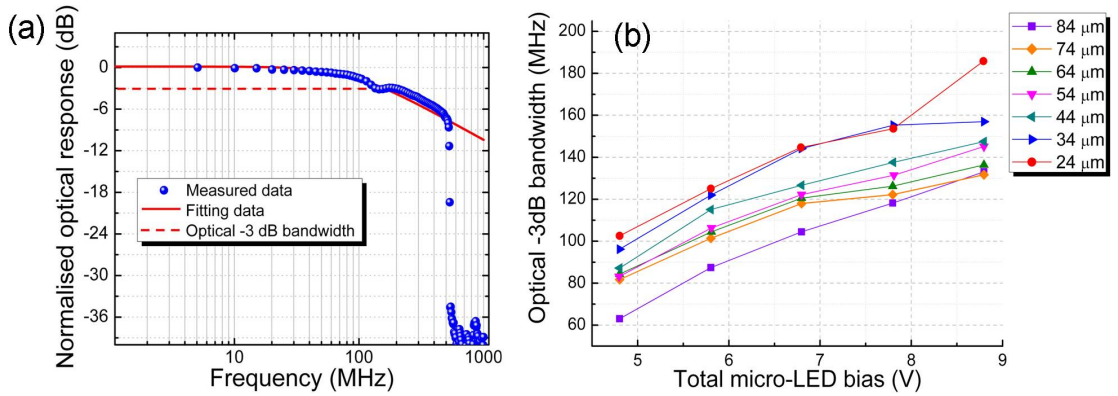

FIGURE 3.15: (a) Frequency response of a 34 μm diameter CMOS-controlled micro-LED pixel, with a forward bias of 7.8 V. The optical -3 dB bandwidth is 155.3 MHz. A sudden drop in the amplitude of the measured data can be seen occurring at 550 MHz; (b) bandwidth versus forward bias for micro-LEDs with different pixel diameters from the same CMOS-controlled 450 nm blue-emitting micro-LED array.

as a corresponding modulator. By identifying the intensity change of the optical signal, a VLC link can be realised based on CMOS-controlled micro-LED devices.

The frequency response of a single CMOS/micro-LED pixel was measured using a high-speed silicon photodetector (Newport 818-BB21A) and a network analyser (Hewlett Packard 8753ES). The output from the network analyser was first combined with a DC offset to reach the logic threshold of the CMOS electronics and then sent to the CMOS chip to trigger *INPUT_SIG* and modulate the micro-LED pixel. The optical response of the pixel was then detected by the fast photodetector and the electrical output of the detector was fed back to the network analyser. Figure 3.15 (a) shows the frequency response of a representative 34 μm diameter pixel from an 8×8 CMOS-controlled micro-LED array with a peak emission of 450 nm. Details of the 'bare' 8×8 micro-LED array (without being integrated with CMOS driver chip) can be found in chapter 2, section 2.2. The layout of the 8×8 micro-LED array matches the layout of the 16×16 CMOS driver array, in which 64 of the CMOS drivers are bonded with the pixels from the 8×8 micro-LED array. The -3 dB bandwidth of the tested pixel is around 155 MHz at an LED forward bias of 7.8 V. As shown in the Figure 3.15 (a), up until approximately 550 MHz, the frequency response of this CMOS-controlled micro-LED can be reasonably well fitted to the expression given in chapter 2 (Equation 2.1), where τ represents the differential carrier lifetime. In this case, the τ of the test pixel is 1.8 ns under 7.8 V applied bias, slightly larger than the expected carrier lifetime [26, 64]. This effect is due to the smaller modulation bandwidth of the CMOS-controlled micro-LED compared with 'bare' micro-LED and the reasons will be discussed at the end of this paragraphy.

As shown in Figure 3.15 (a), there is a sudden drop in the frequency response at around 550 MHz, which is due to the digital characteristics of the CMOS circuit. The present CMOS drivers ('fourth-generation') are not able to be switched on and off in response to very high-frequency signals. Therefore, they are effectively in the off state above 550 MHz. The frequency at which this drop-off occurs may be increased in future driver designs by, for example, using lower voltage CMOS transistors with faster switching speeds. As shown in Figure 3.15 (a), there is another drop in the frequency response at around 150 MHz, which is probably due to the influence of signal reflection. The signal reflection may be caused by the resonance of the CMOS driver board when an input signal with specific frequencies is sent to it. However, further research is needed to confirm the origin of this response drop. It is worth noting that this response drop at around 150 MHz will not influence the performance of CMOS-controlled micro-LED device significantly as the magnitude of the response drop is fairly small. Figure 3.15 (b) shows the optical -3 dB bandwidth versus applied bias characteristics of representative micro-LEDs with different pixel diameters from the 8×8 CMOS-controlled micro-LED array. The modulation bandwidths of the CMOS-controlled micro-LEDs were found to be up to 185 MHz. In a similar fashion to the measurements obtained from the 'bare' micro-LEDs, the optical -3 dB bandwidths of different pixels all show a dependence on the applied bias (the injection current) [64, 111]. Analysis of the data suggests that the injection current increases with the increment of applied bias and for high injection current, the increase of -3 dB bandwidth of the device is related to the increase of carrier density and the decrease in carrier lifetime (see chapter 2). The smaller LED pixels show higher optical -3 dB bandwidths than the larger ones under the same applied bias. This is attributed to the higher current/carrier density within the smaller pixel compared with the larger pixel under the same applied bias. The -3 dB bandwidths of the CMOS-controlled micro-LEDs are lower compared to the measurements shown earlier from the 'bare' micro-LEDs directly driven by a high-speed probe. This effect is largely due to the high modulation depth of the CMOS driver output, combined with the frequency response of the CMOS driver itself. The frequency response (switching speed) of the CMOS driver is mainly determined by the RC components of the transistors, which also influence the overall performance of the CMOS-controlled micro-LED device [64]. For 'bare' micro-LEDs, they are modulated under a small-signal modulation scheme, in which the device is kept in 'on' state by the DC component of the modulation signal. For CMOS-controlled micro-LEDs, they are modulated under OOK modulation scheme,

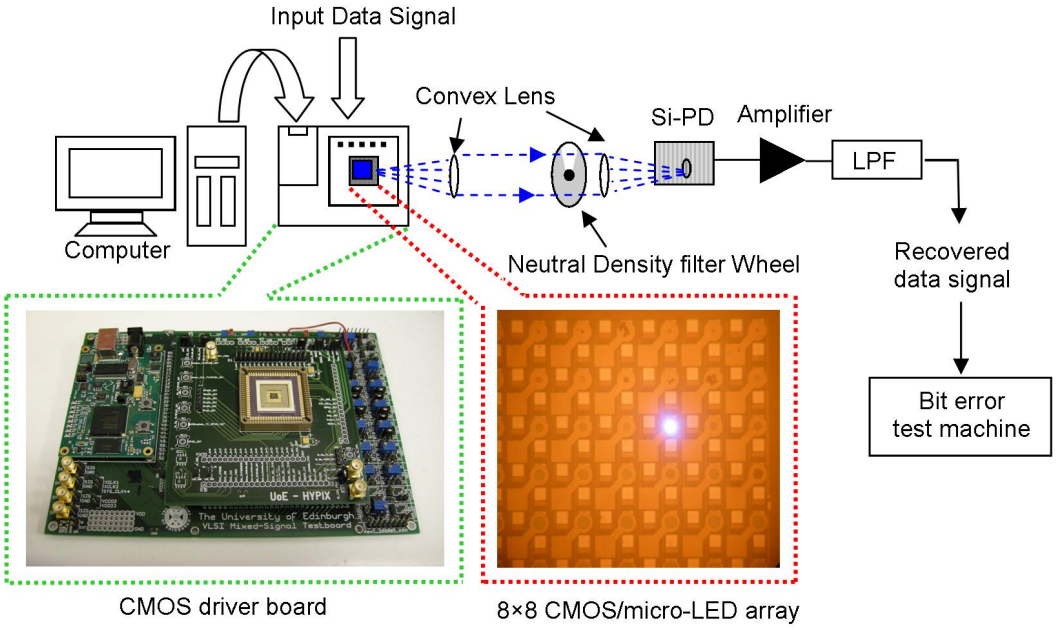

FIGURE 3.16: Schematic diagram of the experimental setup of the single-channel VLC system.

in which the micro-LEDs are turned on and off. Under same applied bias, the average carrier density of micro-LEDs under OOK modulation is smaller than that of micro-LEDs under small-signal modulation. Therefore, the high modulation depth of the OOK modulation scheme reduces the modulation bandwidths of the micro-LEDs driven by CMOS. However, it is expected that an optimised design of the CMOS driver, which allows analog small-signal modulation, would enable much higher bandwidth, similar to the 'bare' micro-LEDs modulated by a high-speed probe.

Figure 3.16 shows a schematic diagram of the experimental setup of a single-channel VLC system based on the 8×8 CMOS-controlled micro-LED array with a peak emission wavelength of 450 nm. Data transmission was performed using a 24 μm diameter LED pixel from the 8×8 CMOS-controlled micro-LED array on a bit-error ratio test (BERT) system, which contains a data-pattern generator (Anritsu Pulse Pattern Generator MP1763C) and a bit-error detector (Anritsu Error Detector MP1764C). The data signal was generated by the data-pattern generator and sent to the CMOS chip via an SMA input port to directly trigger *INPUT_SIG*. The data signal consists of NRZ PRBS with a peak-to-peak amplitude of 2 V. A short pattern length, i.e. 2^7-1 bits, was used to frame the PRBS data signal as this scheme is appropriate to 8B/10B encoding used in Gigabit Ethernet and Wireless Local Area Network. The optical output from the LED

pixel was collected by a 0.68 numerical aperture lens and imaged onto a high-speed silicon photodetector, which transformed the received optical signal into an electrical signal. The electrical signal was subsequently passed to a 50 dB electrical amplifier and a 1200 MHz low pass filter (LPF) before being sent to the bit-error detector, which compared the received electrical signal with the original data signal sent to the CMOS/micro-LED chip and presented the BERs. Figure 3.17 (a) shows the BERs versus received optical power of the 24 μm pixel at different bit rates. The forward bias across the micro-LED was 7.5 V and the received optical power at the detector was adjusted by a neutral density filter wheel placed between the micro-LED and detector. The neutral density filter wheel allows the BER to be measured as a function of received optical power at the detector and ensures the detector is not saturated. As shown in Figure 3.17 (a), bit rates from 155 Mbit/s to 512 Mbit/s were investigated and error-free data transmission, in this case indicated by observing no errors after transmitting 1×10^{10} bits, could be achieved for bit rates of up to 512 Mbit/s. Corresponding eye diagrams taken at 155, 300 and 512 Mbit/s are shown in Figure 3.17 (b), (c) and (d), respectively. Up to 300 Mbit/s, clear open eye diagrams can be observed, but at 512 Mbit/s, the eye diagram is beginning to close. Transmission of the same PRBS data was also performed using 44 μm and 84 μm diameter LED pixels from this device, with error-free data being obtained at 400 and 300 Mbit/s, respectively. These results are consistent with the bandwidth data shown in Figure 3.15 (b).

Compared with the optical data transmission results based on 'bare' micro-LEDs, the modulation bandwidths and error-free data transmission rates of CMOS-controlled micro-LEDs are lower due to the limitation of the OOK modulation scheme. However, benefit is achieved by the additional functionality available from the CMOS-controlled micro-LEDs, including convenient computer control of each pixel within the array and the potential for multiple-channel data transmission by independently modulating (with this CMOS chip) up to 16 columns of micro-LEDs. Characterisation of the device under multi-data input operation using a 16×16 CMOS-controlled micro-LED array, including the issues such as electrical and optical crosstalk between channels, will be presented in the following sub-section.

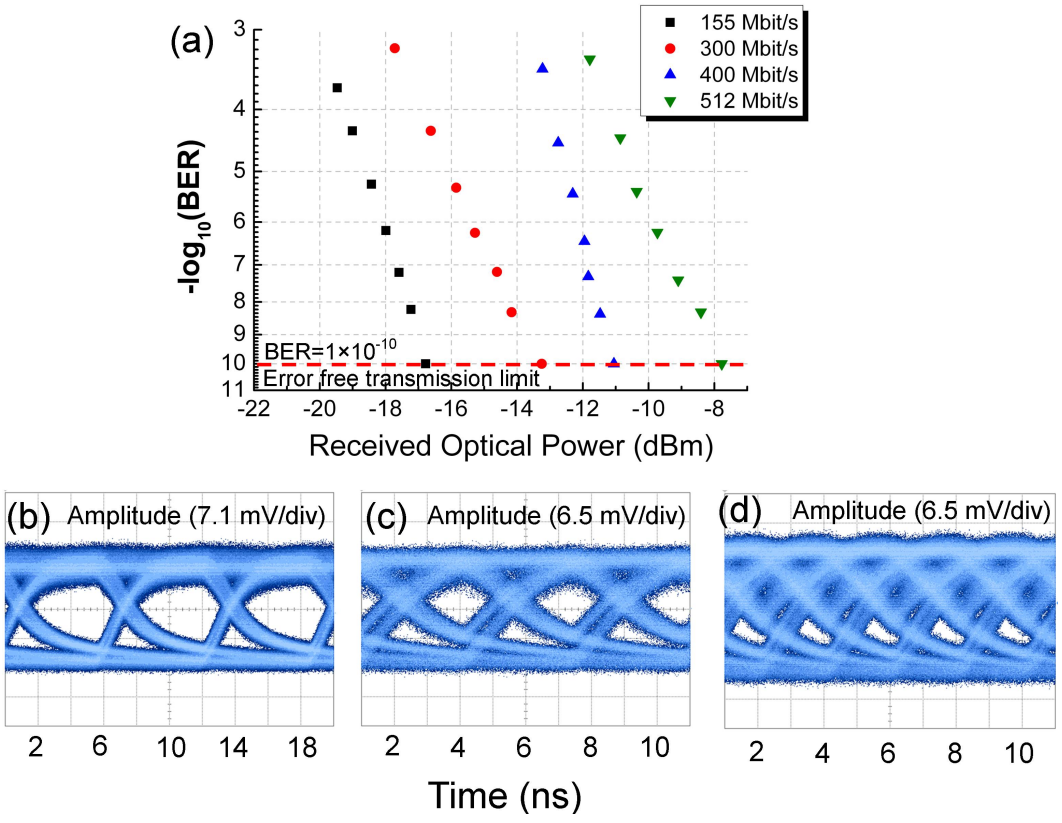

FIGURE 3.17: (a) BERs at various bit rates measured from a 24 μm diameter pixel with a peak emission wavelength of 450 nm, a forward bias of 7.5 V, and a PRBS length of 2^7-1 bits. Corresponding eye diagrams were taken at (b) 155, (c) 300 and (d) 512 Mbit/s.

3.4.2 Multiple-channel VLC implementation and crosstalk issue

To significantly increase VLC data transmission capacity, optical wireless multiple-input multiple-output (MIMO) systems have been developed [113–115]. The idea of optical wireless MIMO is to modulate a number of individual light sources simultaneously for data transmission, thus realising high-speed parallel data streams for communications. An optical MIMO system could greatly enhance the system data transmission capacity compared with a single-input/single-output system, and thus has drawn much attention recently [116, 117]. However, most optical MIMO systems are currently based on separate LED devices. In the last sub-section, we introduced a CMOS-controlled array, allowing individual pixels from the array to be readily controlled via a simple computer interface while retaining high modulation bandwidths. A 512 Mbit/s data transmission rate using a single pixel from such a CMOS-controlled micro-LED array was demonstrated. In this part, we will further investigate the modulation capability of multiple CMOS-controlled LED pixels in parallel with independent data input per pixel and

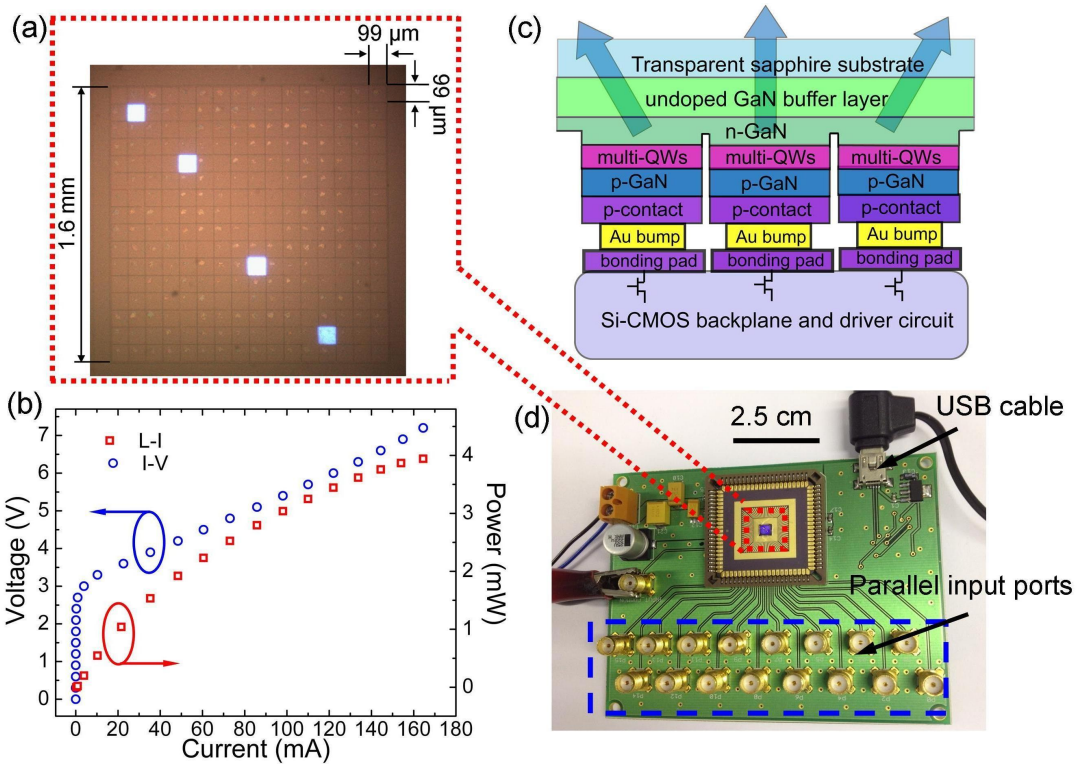

FIGURE 3.18: (a) Microscope image of the whole CMOS-bonded micro-LED array with four individual pixels in operation; (b) characteristic I-V and L-I curves of a standard CMOS-bonded micro-LED pixel; (c) illustration of the flip-chip bonding between micro-LED array and CMOS driver array using Au bumps; (d) image of the CMOS driving board with the parallel data input ports highlighted by the blue dash.

demonstrate an easily-controllable on-chip optical MIMO system. By simultaneously modulating four 450 nm blue-emitting 99×99 μm^2 CMOS-controlled LED pixels using an on-off key (OOK) modulation scheme, non-return-to-zero (NRZ) data streams at bit rates of up to 375 Mbit/s per pixel have been achieved. Error-free operation, defined as a BER of less than 1×10^{-10}, is confirmed for all of the data channels, giving a total bit rate of 1.5 Gbit/s. This establishes a baseline demonstration of the parallelism of these arrays and opens the way to further multiple-channel scaling.

The 450 nm micro-LED array device used here was fabricated from a commercially available multi-quantum-well (MQW) LED wafer grown on a *c*-plane patterned sapphire substrate. It has a similar epitaxial structure and processing steps to those reported previously (chapter 2, section 2.1). The array device consists of 16×16 individually-addressable uniform-sized square LED pixels on a 100 μm centre-to-centre pitch and each pixel is 99×99 μm^2 in area with a 1 μm separation [Figure 3.18 (a)]. Every pixel in the array shares a common n-contact, and can be individually addressed through their independent p-contacts. Due to the flip-chip format of the device, light is extracted from

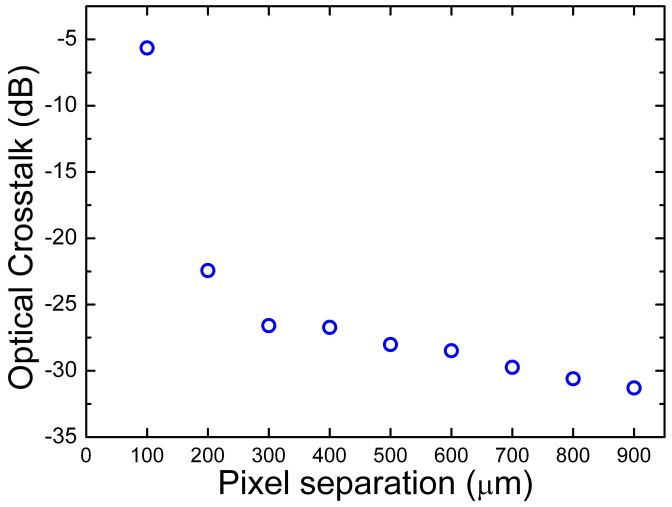

FIGURE 3.19: Optical crosstalk as a function of pixel separation between the aligned pixel and other non-aligned pixels.

the transparent and polished sapphire substrate. Figure 3.18 (b) shows the I-V and L-I curves of a typical LED pixel driven by the CMOS under direct current (DC) operation at room temperature. The CMOS driver chip used here, as presented above, is a 16×16 array of individually-controllable 100×100 μm^2 driver cells on a centre-to-centre pitch of 100 μm. The CMOS driver chip matches the layout of the 16×16 micro-LED array precisely and each micro-LED pixel is flip-chip bonded onto a corresponding CMOS cell [Figure 3.18 (c)]. In this case, the CMOS driver chip can be used to drive 256 micro-LED pixels. A new CMOS driver board was developed specifically for the purpose of VLC (in collaboration with the University of Edinburgh). Figure 3.18 (d) shows the layout of the CMOS driving board and corresponding data input ports. Compared with the previous design (see Figure 3.10), the new board design also allows each CMOS/micro-LED unit to be easily controllable via a simple computer interface but is much more compact in format, leaving out the unnecessary parts for VLC, such as FPGA unit, VCO circuitry, pulse generation circuitry, etc. In addition, the new board design is beneficial for reducing the interference from undesirable capacitive and inductive components to CMOS drivers [103], especially under high-speed modulation. As show in Figure 3.18 (d), there are sixteen independent SMA input ports on the CMOS driving board, allowing each column in the array to be modulated simultaneously but with independent data patterns.

The modulated light beams from the micro-LED pixels were focused onto a high-speed alternating current (AC)-coupled silicon photodetector using a 0.68 numerical aperture

lens. By adjusting the positions of the lens and photodetector, the micro-LED pixels were separately aligned with the detector for light output measurement. In the present system, although only one micro-LED pixel is aligned to the photodetector at one time, the detector could also receive undesired optical signals from other active micro-LED pixels. This causes optical crosstalk and this was measured using the method described as follows. With one micro-LED pixel turned on, its emission beam was aligned to the photodetector and its optical output power was measured. The pixel was then turned off and without changing the alignment of the photodetector, adjacent non-aligned pixels were switched on individually and the optical power coupled to the photodetector was recorded. The optical power from the aligned micro-LED pixel was then compared with the optical power received from other non-aligned micro-LED pixels, and thus the optical crosstalk could be quantified. Figure 3.19 shows the optical crosstalk (in dB) as a function of the centre-to-centre pixel separation between the aligned micro-LED pixel and other non-aligned micro-LED pixels. As shown in Figure 3.19, when using the pixels next to each other (pixel separation 100 μm) for parallel data transmission, the optical crosstalk is approximately -6 dB, which could influence the system performance. However, when the pixel separation reaches 300 μm and above, the optical crosstalk is less than -25 dB. Therefore, in our current system we can effectively neglect optical crosstalk by selecting active micro-LED pixels with a minimum spatial separation of 300 μm. The optics used in the current system was chosen for characterising the performance of the CMOS/micro-LED pixels, and it is noted that the optical crosstalk will vary depending on how the light is collected at the detector. By using specifically-designed optics, such as integrated micro-lenses [30], it should be possible to modify the beam profiles from the micro-LEDs and thus reduce the optical crosstalk between two adjacent pixels.

The frequency response of a single 99×99 μm^2 CMOS/micro-LED pixel was measured using the same method as presented before. At an applied bias of 6.5 V, the optical -3 dB bandwidth of the CMOS-controlled micro-LED pixel was found to be approximately 150 MHz. To test the bandwidth uniformity of the micro-LED array, fourteen pixels along the diagonal of the array were measured and the optical -3 dB modulation bandwidths were found to be 145 MHz±10MHz for all of the pixels. Data transmission was carried out using four individual micro-LED pixels. The reason that four micro-LED pixels were chosen to carry out the data transmission measurement is that we believe this to be

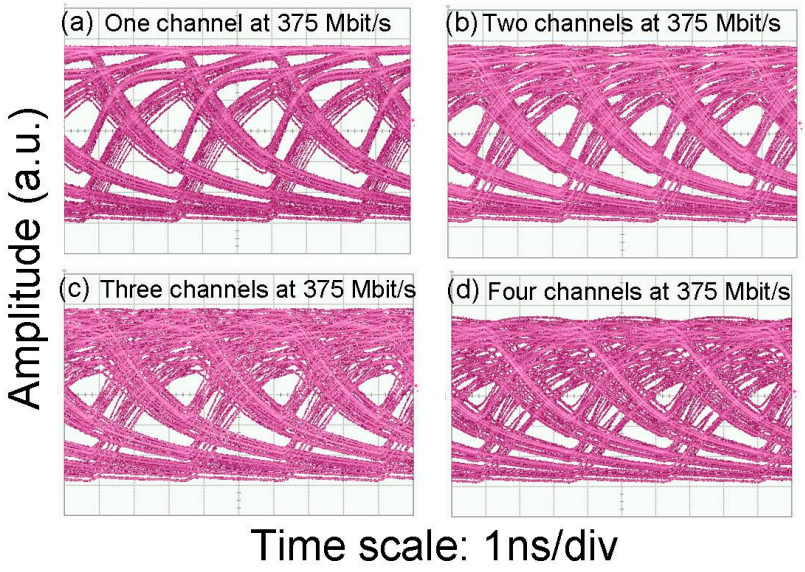

FIGURE 3.20: Eye diagrams of a typical CMOS/micro-LED pixel when it is modulated at 375 Mbit/s in (a) one channel, (b) two channels, (c) three channels and (d) four channels. The applied bias is 6.5 V.

enough to prove the concept of parallel data transmission using this CMOS/micro-LED device and it allows issues such as crosstalk to be examined. In this data transmission measurement, four separate data sources with a common clock frequency were used. The four data signals were all OOK-NRZ PRBS with a standard pattern length of 2^7-1 bits and a peak-to-peak voltage from 0 to 2 V, which is above the logic threshold of the CMOS electronics (1.0 V). The data signals were sent to the CMOS chip through four parallel inputs to trigger four independently-addressable CMOS drivers directly, and in this way, the four corresponding micro-LED pixels could be modulated simultaneously with different data patterns. The spatial separation between the modulated micro-LED pixels was kept above 600 μm, and in this case the optical crosstalk in this multiple-channel system is less than -25 dB (Figure 3.19) and thus negligible.

A typical eye diagram from an individual pixel (aligned to the detector) modulated at 375 Mbit/s and with a 6.5 V applied bias is shown in Figure 3.20 (a). The eye diagrams recorded from this aligned pixel when two, three and four micro-LED pixels were modulated simultaneously at 375 Mbit/s with a 6.5 V applied bias are shown in Figure 3.20 (b)-(d), respectively. It can be noted that the eye diagram quality degrades with an increasing number of modulated pixels (channels), indicating the presence of electrical crosstalk, as the optical crosstalk is negligible in this configuration. The BERs were measured as a function of received optical power for the cases of one, two, three and

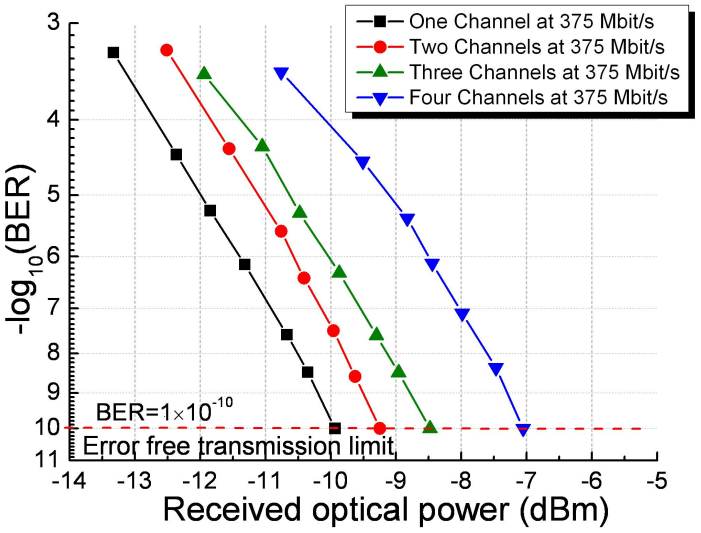

FIGURE 3.21: BERs measured from the CMOS/micro-LED pixel at 375 Mbit/s, with one channel, two channels, three channels and four channels in operation, as a function of the received optical power at the detector.

four active micro-LED pixels. For our system, error-free transmission could be achieved for a bit rate of up to 375 Mbit/s per pixel with four pixels modulated simultaneously, giving a total bit rate of 1.5 Gbit/s from the whole device. Figure 3.21 shows the BERs versus received power under different modulation conditions. To achieve the same BER at the same bit rates, higher received optical powers were required as the number of modulated pixels was increased, as anticipated from the eye diagrams. Compared to the case of one modulated pixel under error-free transmission, there was a power penalty of 0.69 dBm, 1.46 dBm and 2.88 dBm for two, three and four pixels being modulated, respectively. This power penalty is largely attributed to the electrical crosstalk in the CMOS drivers, which will be discussed in detail in the following. By aligning the detector to other micro-LED pixels, our measurement showed that the BER characteristics of other pixels were very similar to the investigated micro-LED pixel, as would be expected.

Inter-channel crosstalk is an important issue in MIMO systems as the unwanted interference between channels can degrade the overall system performance. As such, the magnitude and origin of the electrical crosstalk of our CMOS-controlled micro-LED device were investigated. It was found that the isolation resistance between two pixels on a 'bare' micro-LED array (without being integrated with a CMOS chip) is very high, suggesting that the electrical crosstalk comes from the integration with the CMOS electronics and the driver board. To investigate the electrical crosstalk occurring during multiple-channel operation, two representative pixels with a spatial separation of more

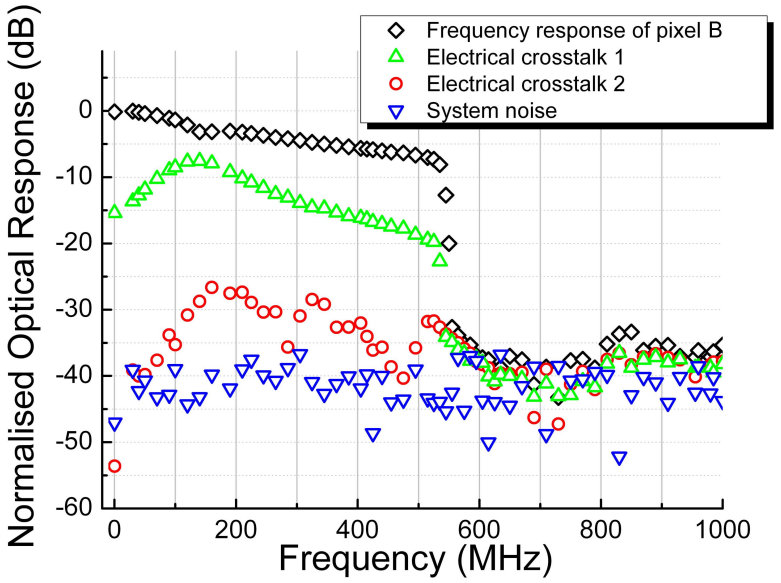

FIGURE 3.22: Frequency response curves of a typical CMOS/micro-LED pixel under different operating conditions. The blue data points represent the system noise. The red data points represent the frequency response with the influence of electrical crosstalk caused by mutual inductance/capacitance. The green data points represent the frequency response with the influence of electrical crosstalk caused by 'Ground Bounce' effect. The black data points represent the frequency response of the micro-LED pixel under 6.5 V applied bias voltage.

than 600 μm from the CMOS/micro-LED array, denoted hereafter as 'pixel A' and 'pixel B', were chosen. Figure 3.22 shows the frequency response of the CMOS/micro-LED system under a number of different drive conditions. For all these measurements, pixel B was always aligned to the AC-coupled photodetector. The blue data points (inverted triangles) shown in Figure 3.22 represent the system noise floor, which was measured by only turning on pixel B in DC and aligning its output to the AC-coupled photodetector. The black data points (diamonds), which are approximately 40 dB above the system noise floor, show the normalised frequency response of pixel B when it is modulated alone by sending signals from the network analyser to data input port B. It is very similar to the normal frequency response curve shown in 3.15 (a), as would be expected. The red data points (circles) shown in Figure 3.22 are the frequency response of pixel B when operated in DC mode alone, when the network analyser is connected to data input port A but pixel A is not turned on. There is a slight increase in the system response above the noise floor, possibly caused by the mutual capacitance/inductance between driver electronics, which could give rise to signal feed through from one channel to another [103]. However, this level of crosstalk (-25 dB) is not large enough to explain the power penalties shown in Figure 3.21. The green data points (triangles) shown in Figure

3.22 represent the frequency response of pixel B when it is in DC operation and pixel A is turned on and modulated. In principle, if there is no electrical crosstalk between the two pixels, the frequency response of pixel B should always be on the same scale as the system noise floor (blue data points) no matter the state of pixel A, since the AC-coupled photodetector will not respond to the DC output from pixel B. The observed rise of the frequency response from the AC-coupled detector indicates that pixel B has been modulated by the electrical crosstalk brought by modulating pixel A. As shown by the green data points, this electrical crosstalk causes pixel B to be modulated to a magnitude (-10 dB) which could influence the data transmission process. Analysis indicates that this electrical crosstalk is caused by the power routing resistance between CMOS drivers. When one pixel is in operation, turning on another pixel will induce a small global voltage drop due to the power routing resistance, leading to a lower bias to the first pixel. By turning off the second pixel, the first pixel will recover to its initial bias and output power. Thus, when the second pixel is OOK modulated, the absolute bias applied to the first pixel will fluctuate and this gives rise to the electrical crosstalk. This effect is known as the 'Ground Bounce' effect in the CMOS industry [103]. To minimise the electrical crosstalk in high data rate CMOS driver circuits, it is therefore essential to reduce the power routing resistance (the metal track resistance of the current CMOS driver is estimated to be 0.43 Ohm). By using thicker and wider metal power tracks in the future CMOS chip, we believe the power routing resistance in CMOS drivers can be reduced and the influence of electrical crosstalk can be minimised accordingly. Assuming that the electrical crosstalk could be greatly reduced and 375 Mbit/s error-free data transmission per channel with 16 simultaneous data inputs, an overall data rate of 6 Gbit/s could in principle be achieved by the whole array.

3.5 Summary

In summary, this chapter introduces the background of CMOS technology, the implementation of CMOS-controlled micro-LED arrays, and the application of the CMOS-controlled micro-LEDs for high-speed data transmission. In section 3.1, the background of CMOS technology is presented, including the operating principles of NMOS and PMOS, and the construction of basic CMOS logic circuitry. The logical operation processes and functionalities of different CMOS logic gates are also presented in the same

section. In section 3.2, a CMOS driver chip is developed to be integrated with micro-LED arrays and individually control each micro-LED pixel. The layout of the CMOS driver chip and the driver circuitry are presented in detail. In addition, a CMOS driver board is developed to drive the CMOS-controlled micro-LEDs, allowing micro-LED pixels to be conveniently controlled via a simple computer interface. The experimental part starts from section 3.3. In this section, a proof-of-concept VLC link with data transmission rate of up to 1 Gbit/s is realised using a 'bare' 44 μm micro-LED pixel driven by a high-speed probe. It is worth noting this data transmission is achieved using a single micro-LED pixel under binary pulse amplitude modulation scheme. These results demonstrate the great potential of using micro-LED devices for VLC and lay the foundation of further investigating the multi-emitter nature of micro-LED array devices for high-speed parallel multiple-channel data transmission. In section 3.4, the applications of CMOS-controlled micro-LEDs for single-channel and multiple-channel VLC are presented. The modulation bandwidths of the micro-LEDs under CMOS control were found to be up to 185 MHz, with error-free data transmission using OOK scheme being demonstrated at bit rates of up to 512 Mbit/s under single-channel operation. To make a further step, we also reported the characterisation of a single on-chip multi-transmitter VLC demonstrator system based on four pixels in a CMOS-controlled micro-LED array. When four pixels are modulated simultaneously, error-free data transmission of up to 375 Mbit/s per pixel can be achieved, giving an aggregate parallel data transmission rate of 1.5 Gbit/s. Analysis suggests that on-chip crosstalk, brought by modulating multiple pixels simultaneously, induces the reduction of signal quality in the multiple-channel system, such that more optical power (power penalty) is required to be received by the detector to compensate. We have identified the origins of electrical crosstalk, in particular the 'Ground Bounce' effect caused by a relatively high power routing resistance, and proposed ways to reduce these issues in future CMOS driver designs. The results reported here highlight the potential of using such a device as an easily-controlled and highly-integrated multiple-channel optical data transmitter, allowing (in this case) up to 16 channels, each capable of transmitting data at hundreds of Mbit/s, for parallel data transmission.

Chapter 4

Micro-display systems based on III-nitride micro-LED arrays

This chapter contains four separate but closely related sections, which present the development of monochromatic and colour-tunable micro-display systems based on III-nitride micro-LED devices. Previous research has demonstrated some micro-display systems based on conventional display technologies, as summarised in section 4.1. Compared with conventional micro-display systems, a micro-display based on III-nitride materials would be more attractive and desirable for practical applications requiring high brightness, strong reliability and low-voltage-operation characteristics. In this case, micro-display systems based on III-nitride micro-LED arrays are demonstrated in section 4.2. Such monochromatic micro-display systems could deliver programmable high-resolution micro-scale images. In section 4.3, to make a further step, we demonstrate a multi-colour micro-display system based on a micro-LED array made from one InGaN epitaxial structure. Finally, section 4.4 summarises the work presented in this chapter.

4.1 Background of micro-display systems

As illustrated in Figure 4.1 (a), a micro-display refers to a compact display system with small size and high resolution, which is normally magnified by optics to deliver enlarged virtual images or projected images and can be used for many applications such as head-mounted displays, video headsets, contact lens display, camcorder viewfinder and

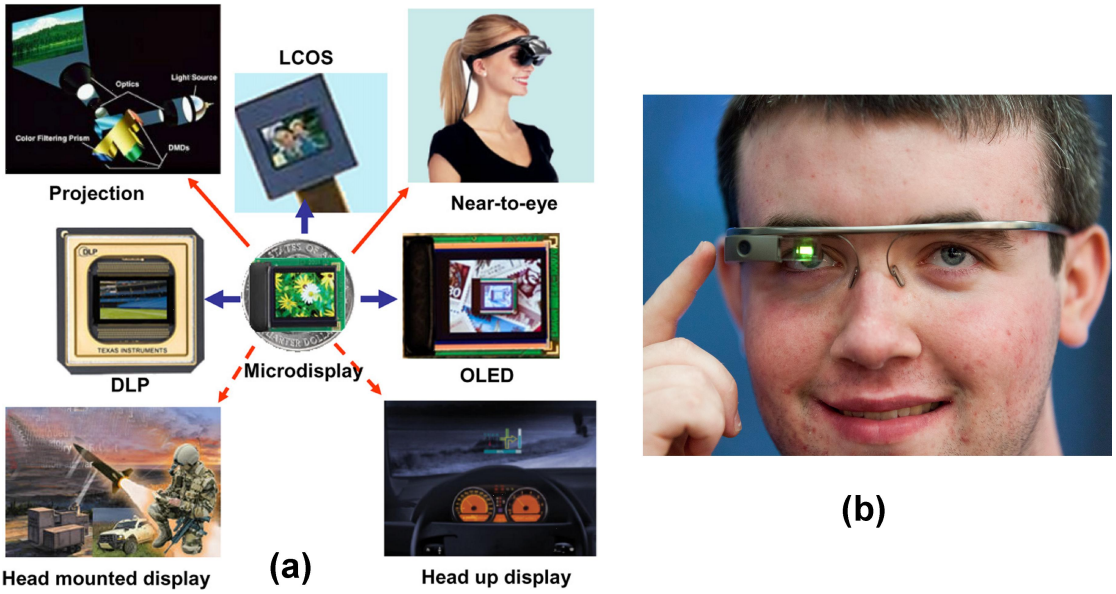

FIGURE 4.1: (a) Micro-display has been widely used for many applications [118]. (b) An image of Google Glass^{TM} in operation and the integrated micro-display system is one of its key components [119].

projection TV [118, 120–122]. More recently, search engine giant Google has launched its new product Google Glass^{TM} to the market, which is a new-concept of camcorder viewfinders integrated on spectacles with a high-resolution micro-display system. Google Glass^{TM} has attracted a lot of market interest since its inception and an image of Google Glass^{TM} is shown in Figure 4.1 (b). To implement the electrically driven micro-display systems for high-end applications such as Google Glass^{TM}, properties like high resolution, brightness, reliability and other merits must be taken into careful consideration. In general, micro-display systems can be divided into two categories, i.e. modulated micro-displays and self-emissive micro-displays. For modulated micro-displays, liquid crystal on silicon (LCOS) and digital micro-mirror display (DMD, also known as a Digital Light Processor, DLP) are relatively mature technologies commonly found in commercial television and image projectors. These modulated micro-displays are blanket-illuminated by one or several light sources and the images are formed by filtering out the undesired light at the display screen. For example, the fundamental working principle of LCOS is to utilise the electrochemical properties of liquid crystal material to form an optical polariser, which modulates the light incident on the display screen by controlling the polarisation direction of liquid crystal material under different applied bias voltages. The power efficiency of modulated micro-displays is low as a certain amount of power is filtered out and wasted. In addition, the reliability, brightness and contrast of these

modulated micro-displays are lower than those required for applications such as under direct sunlight or extreme conditions [84, 118, 120, 121]. For a self-emissive micro-display, colour-filtered organic LEDs (OLEDs) is a mature technology, which is similar to a III-nitride micro-LED array in the sense that they are both emissive displays consisting of arrays of individual light-emitting pixels, with the key difference being that the material that emits light in an OLED display is organic semiconductor light-emitting molecule or polymer. A key advantage of OLED is that the organic light-emitting materials can be processed in a more straightforward and cost-effectively way than inorganic materials, which is crucial for the commercialisation of OLED-based products [123]. However, the electro-optical performance, power efficiency, reliability, robustness and lifetime of the OLED itself are still far inferior to its inorganic counterpart [83, 124]. These shortcomings influence the performance of OLED-based products and limit the further application of OLED technology to high-performance micro-display systems.

4.2 Monochromatic micro-display systems based on III-nitride micro-LEDs

High-power LEDs based on III-nitride materials have achieved dramatic development within the last twenty years. InGaN-based LEDs have the capability to efficiently generate light across ultraviolet-blue-green part of the spectrum, allowing solid-state visible light sources to be commercialised for wide applications [23, 24, 26]. The power efficiency of InGaN emitters is several times higher than OLEDs and other electroluminescent emitters. In addition, with their multi-quantum-well (MQW) structures, InGaN-based LEDs normally have a narrow emission band, which provides an important basis for high colour purity and chromatic reliability. Due to their intrinsic material properties, InGaN-based LEDs have much longer operational lifetimes (>100 000 h) and can be operated under harsh conditions such as high or low temperature (-50 °C to 120 °C) and humidity. More importantly, they can provide a viewing angle of more than 120° and be easily driven by compact electronic drivers without high voltage requirement. All these superior properties make the III-nitride based micro-LED emitter array an attractive candidate for high-performance micro-display systems compared with other technologies [83]. A detailed comparison of various technologies for micro-displays is

Technology	Liquid crystal	Organic LED	III-nitride LED
Mechanism	Backlighting	Self-emissive	Self-emissive
Typical luminance	10^3 cd/m^2	10^3 cd/m^2	10^6 cd/m^2
Luminous efficacy	Medium	Low	High
Contrast ratio	Low (>200:1)	high (>10000:1)	high (>10000:1)
Response time	ms	μs	ns
Operating temperature	0 °C to 60 °C	-50 °C to 70 °C	-100 °C to 120 °C
Lifetime	Medium	Medium	Long
Cost	Low	Low	Low

TABLE 4.1: Comparison of various technologies for micro-displays [26, 83].

shown in Table 4.1. Details of the development of III-nitride materials and LEDs can be found in chapter 1, section 1.1 and section 1.3.

4.2.1 Addressing schemes of III-nitride micro-displays

III-nitride micro-displays reported in this thesis are based on III-nitride micro-LED emitter arrays, in which micro-LED pixels can be individually controlled to generate micro-scale light patterns. In terms of the addressing schemes, III-nitride micro-LED arrays can be classified in to two types, i.e. individually-addressable devices and matrix-addressable devices (see chapter 2, section 2.2.1). Individually-addressable micro-LED arrays have separate metal contacts for each micro-LED pixel, as was first developed by H. X. Jiang's group then at Kansas State University in 2000 [125]. Micro-LED pixels of 12 μm diameter with peak emission wavelength at 408 nm were fabricated from an AlInGaN LED wafer by photolithographic patterning, ICP etching and Ohmic contact metalisation. Since no integrated electronic circuitry was developed during that time, each pixel was addressed using a probe and the applications based on this micro-LED device were very limited. In 2001, the same group reported a prototype blue micro-display system based on a similar micro-LED array device but with specifically-designed contact pads for each micro-LED pixel [84]. As shown in Figure 4.2, this device has a dimension of 0.5×0.5 mm^2 and consists of 10×10 individually-addressable micro-LED pixels with a pixel diameter of 12 μm. Emission properties of the micro-LED array such as electroluminescence spectra, L-I characteristics, viewing angle, and uniformity were also investigated. Each pixel from the micro-LED array device could be addressed via separate p and n contacts at the edge of the array, which is easier for driving and packaging the device compared with the previous design.

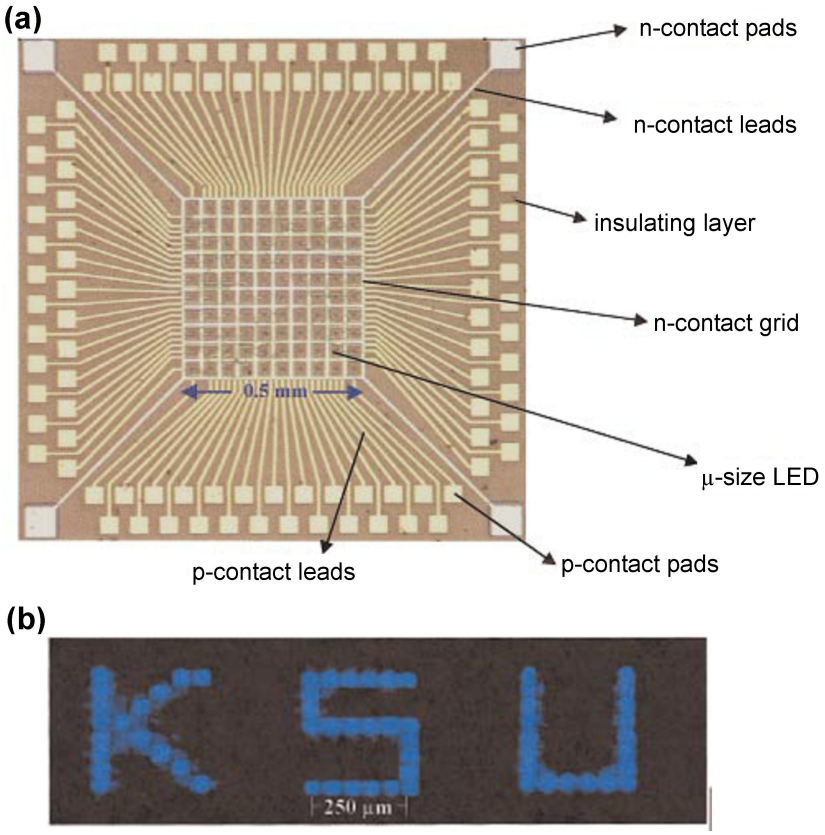

FIGURE 4.2: (a) Microscope image (top view) of the individually-addressable micro-disk LED array developed by H. X Jiang's group at Kansas State University. (b) Controllable emission pattern "KSU" from the micro-LED array device, demonstrating the operation of a prototype III-nitride micro-display [84].

To simplify the individually-addressing scheme of the micro-LED array, a matrix-addressing scheme was developed, whereby each row of pixels shares a common p-contact and each column shares a common n-contact (see chapter 2, section 2.2.1). In this case, any individual pixel in the micro-LED array can be driven by electrically addressing the corresponding column and row simultaneously. The first matrix-addressable micro-LED array from our Institute was demonstrated in 2002 and significant progress has been made since then to optimise the device design and improve the device performance [126]. A matrix-addressable micro-LED device is normally fabricated following the standard micro-LED fabrication procedures reported in chapter 2, section 2.1. However, specific fabrication techniques were also developed to improve the performance of matrix-addressable micro-LED device. For example, early matrix-addressable micro-LED devices used an anisotropic etch to define mesas which have nearly vertical side walls and it is thus difficult to achieve continuous metal tracks for electrical connection. To overcome this, a less anisotropic etch technique was developed to form mesas with

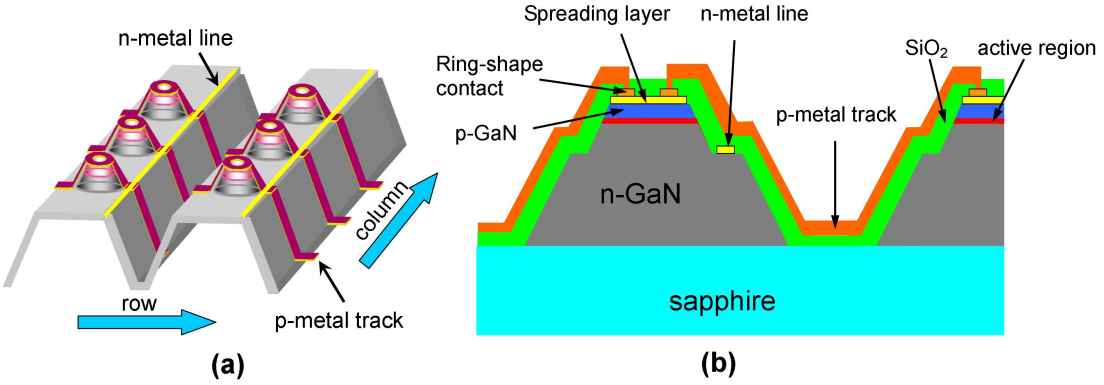

FIGURE 4.3: (a) 3D schematic of a matrix-addressable micro-LED device. Each row of the pixels shares a common p-contact and each column of the pixels shares a common n-contact. (b) Cross-sectional schematic of a matrix-addressable micro-LED device.

side walls sloped at 20-45°, allowing metal tracks to be deposited along and across the mesa slopes. In addition, a scheme of depositing parallel n-metal lines along each column of n-GaN mesa has been developed so that the series resistance variation between each pixel is significantly reduced and good emission uniformity across the whole device can be achieved. More details about the fabrication techniques to improve the performance of matrix-addressable micro-LED devices can be found in the relevant literatures [127–129]. 3D and cross-sectional schematics of the matrix-addressable micro-LED device are illustrated in Figure 4.3 (a) and (b), respectively, providing more information about the structure of the matrix-addressable micro-LED array.

4.2.2 Top-emission and flip-chip configurations of III-nitride micro-displays

In terms of the direction of light extraction, micro-LED devices can be classified into top-emission devices and flip-chip devices. Micro-LED devices with a top-emission configuration normally have a thin p-contact metal with low absorption and reflection. The light is then extracted from the top side of the micro-LED pixel. However, a micro-LED device with a flip-chip configuration is operated inverted, with the light extracted from the backside of the device. On top of its p-contact metal, an additional reflective mirror is usually deposited to enhance the light output from the device. The schematic structure of a flip-chip micro-LED device is shown in Figure 4.4 (a). It is worth noting that the micro-LED devices reported in this chapter were fabricated by Dr Zheng Gong

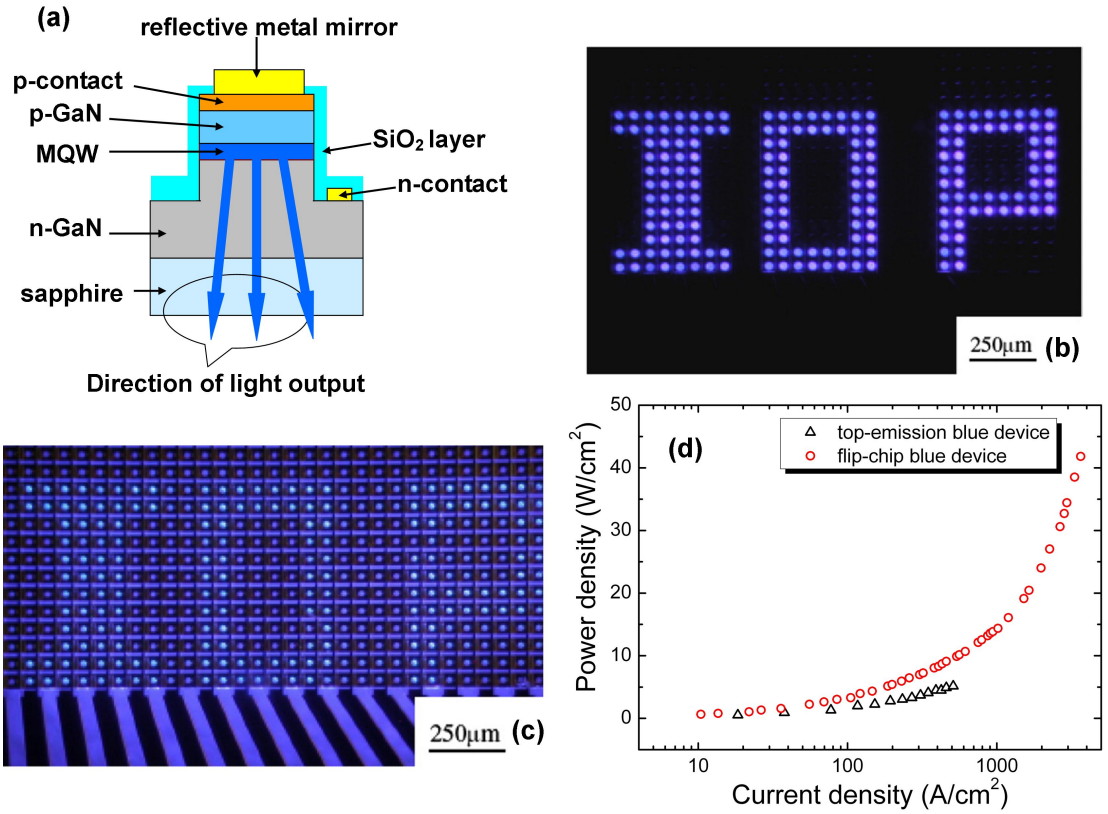

FIGURE 4.4: (a) Schematic structure of a flip-chip micro-LED device; controllable emission pattern 'IOP' from (b) a flip-chip blue-emitting matrix-addressable micro-LED array and (c) a top-emission blue-emitting matrix-addressable micro-LED array; (d) power density versus current density characteristics of the flip-chip device and the top-emission device [77].

and Dr David Massourble, and my work mainly focused on the characterisation and applications of these micro-LED devices.

For the purpose of micro-displays, the flip-chip format of the micro-LED devices has been proved to be a better choice compared with the top-emission format. Representative micro-display images generated by a flip-chip blue-emitting matrix-addressable micro-LED array and the top-emission blue-emitting matrix-addressable micro-LED array are shown in Figure 4.4 (b) and (c), respectively. Both the devices are fabricated from the same LED wafer material following similar processing steps and share the same device layout, i.e. a 64×64 micro-LED array with a uniform pixel size of 20 μm on a 50 μm pitch. As shown in Figure 4.4 (b), a clear micro-display image with good emission uniformity, high brightness, high contrast and low light scattering is demonstrated for the flip-chip device. This image contrasts with the micro-display image generated by the top-emission device shown in Figure 4.4 (c), where the brightness and the contrast are poorer under the same operating current. Due to optical micro-cavity effects [77], the

light scattering (optical crosstalk) for the top-emission device was so strong that even the non-emitting pixels were lightened up. The optical resolution of a flip-chip device, defined as the smallest distinguishable light pattern imaged on the sapphire substrate, is mainly determined by the thickness d of the p-GaN layer. A spatial resolution of $1.59d$ can in principle be achieved, corresponding to about 300 nm in typical epitaxial structures [130]. Figure 4.4 (d) shows the power density as a function of current density for both the flip-chip device and the top-emission device. Under the same injection current density, the flip-chip device can provide a much larger output power density than the top-emission device. For example, at a current density of 500 A/cm^2, the power density of flip-chip device reaches 10 W/cm^2, which is two times larger than that from the top-emission device. The enhancement of power output of flip-chip device is due to the following reasons. First, light in the flip-chip micro-LED device is emitted through the transparent sapphire substrate instead of the semi-transparent spreading layer. Hence, more light can be extracted due to the reduced light absorption and the smaller refractive index difference between sapphire and air. Second, with a thick, reflective p-pad, the current spreading is more uniform for the flip-chip device and the current crowding effect is subsequently minimised. It should be noted that the flip-chip micro-LED device can sustain an extremely high injection current density and thus provide a surprisingly large absolute output power. This is attributed to the improved thermal management of the flip-chip device after it was packaged. For our flip-chip matrix-addressable micro-LED array, a silicon mount with Ti/Au metal tracks is normally fabricated to match the layout of the device, as shown in Figure 4.5 (a). The inner pads of the silicon mount match the corresponding p-pads and n-pads of the device precisely while the outer pads of silicon mount are used for wire bonding. After the device is flip-chip bonded onto the silicon mount via a Au-bump bonding process, it is then adhered onto a 144-pin device package. Finally, the outer metal pads on the silicon mount are connected with the metal pads on the package via wire bonding and the whole packaging process is completed. An image of the fully packaged device is shown in Figure 4.5 (b). Since most of the heat is generated in the active region adjacent to the p-layer of GaN, the Au-bump connecting the p-pad and the silicon mount will help the flip-chip device to dissipate heat effectively. In this case, the thermal management of the flip-chip device is improved after device packaging.

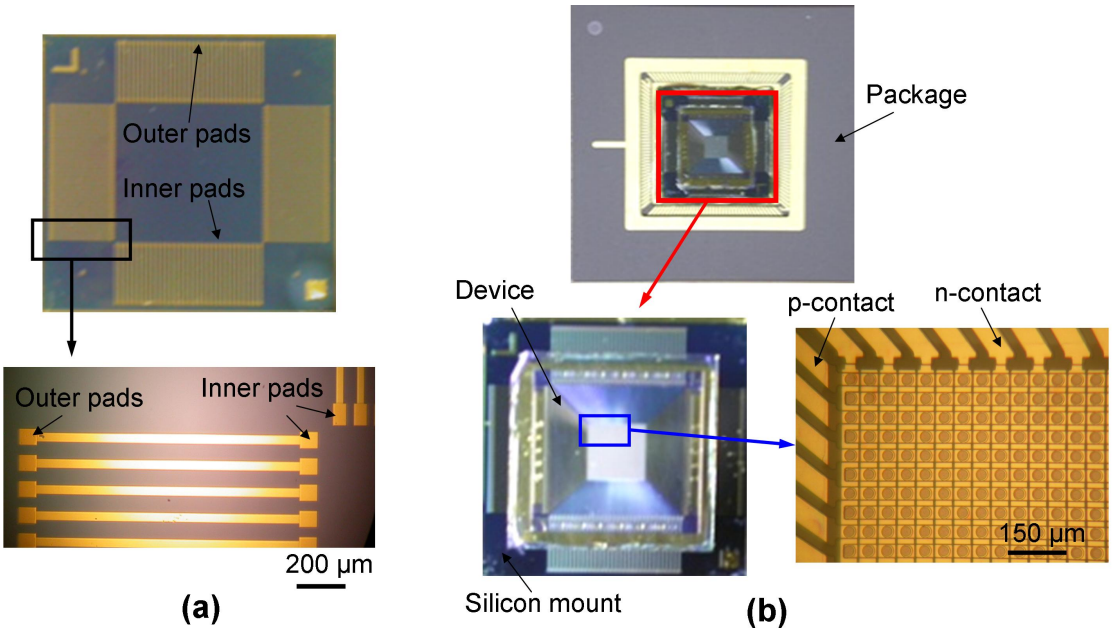

FIGURE 4.5: (a) Optical images of the silicon mount with 128 metal tracks; (b) optical images of the fully packaged device.

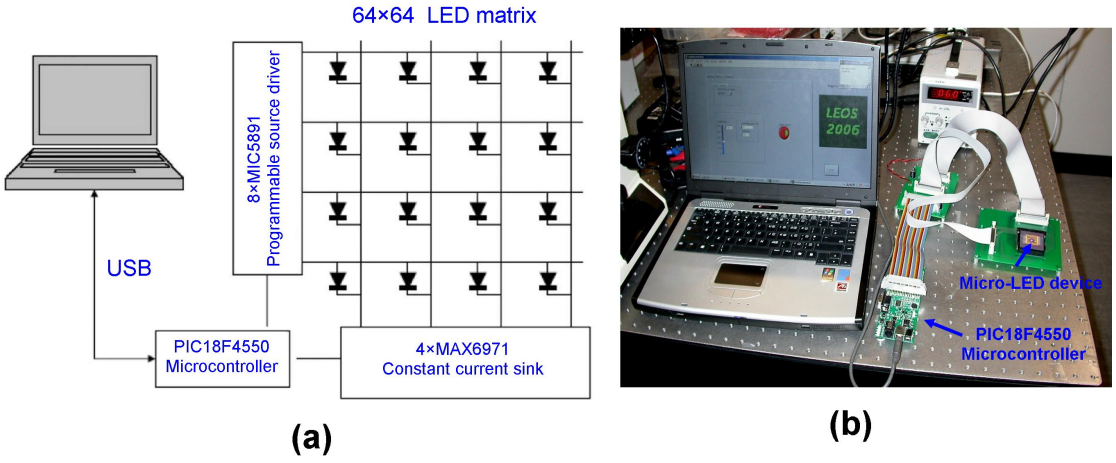

FIGURE 4.6: (a) Schematic driver circuit for the 64×64 matrix-addressable micro-LED arrays; (b) actual setup of the micro-display system.

4.2.3 Matrix-addressable micro-display systems

To demonstrate the use of 64×64 matrix-addressable micro-LED devices as micro-display systems, suitable electronic circuitry and driver board were developed by V. Poher from Imperial College London [131], allowing users to easily control the emission patterns via a simple computer interface. To build up an image, the driver circuitry raster-scans each row of the micro-LED array in a very quick succession, constructing images with refreshing rates fast enough for the human eye not to be able to distinguish each individual frame. A schematic diagram of the electronic circuitry and an image of

the actual micro-display setup are shown in Figure 4.6 (a) and (b), respectively. As shown in Figure 4.6 (a), a PIC (Programmable Interface Controller) microcontroller (PIC18F4550) is connected to the host computer to receive instructions via a USB port. The PIC interprets the received information from computer and implements the users' commands. In this way, appropriate row and column addressing information can be sent to the driver circuitry depending on the desired output image set by the user. For the matrix-addressable device, the p-contact rows of the array are controlled by MIC5891 programmable voltage sources. A MIC5891 programmable voltage source has eight parallel outputs and each output is connected to a p-contact row. Therefore, eight MIC5891 programmable voltage sources are used to control the 64×64 micro-LED array. MIC5891 programmable voltage source is capable of sourcing 500 mA at up to 35 V for each row, enough to turn on the micro-LED pixels for micro-display applications. Since the MIC5891 programmable voltage source is capable of applying bias voltage to a single row at a rate of up to 38000 times per second, such matrix-addressable micro-display system can deliver images that appear continuous and flicker-free. In order to compensate for the small variations among the micro-LED pixels and ensure uniformity in performance across the array, n-contact columns of the array are driven by MAX6971 constant-current sink drivers in a constant-current mode, which ensures the same current flowing through each column even if it has different turn-on voltage and series resistance characteristics. A MAX6971 constant-current sink driver has sixteen parallel inputs and each input is connected to an n-contact column. Therefore, four MAX6971 constant-current sink drivers are used to drive the 64×64 micro-LED array. The brightness of the LEDs can be adjusted by changing the current flowing through the device externally or through a pulse-width modulation scheme under the control of MAX6971 drivers. Under pulse-width modulation scheme, the operating micro-LED pixels are on and off modulated and the brightness of the pixels can be tuned by adjusting the duty cycle, i.e. the ratio of the pulse duration to the flashing period. Finally, graphical user interfaces (GUIs) are developed based on Matlab^{TM} using data acquisition toolbox 8.1. GUIs allow the user to conveniently control the optical characteristics of the micro-display system, such as brightness, emission pattern, raster-scan speed, etc. The GUI and micro-display patterns generated by different micro-LED devices are shown in Figure 4.7 (a) and (b)-(e), respectively.

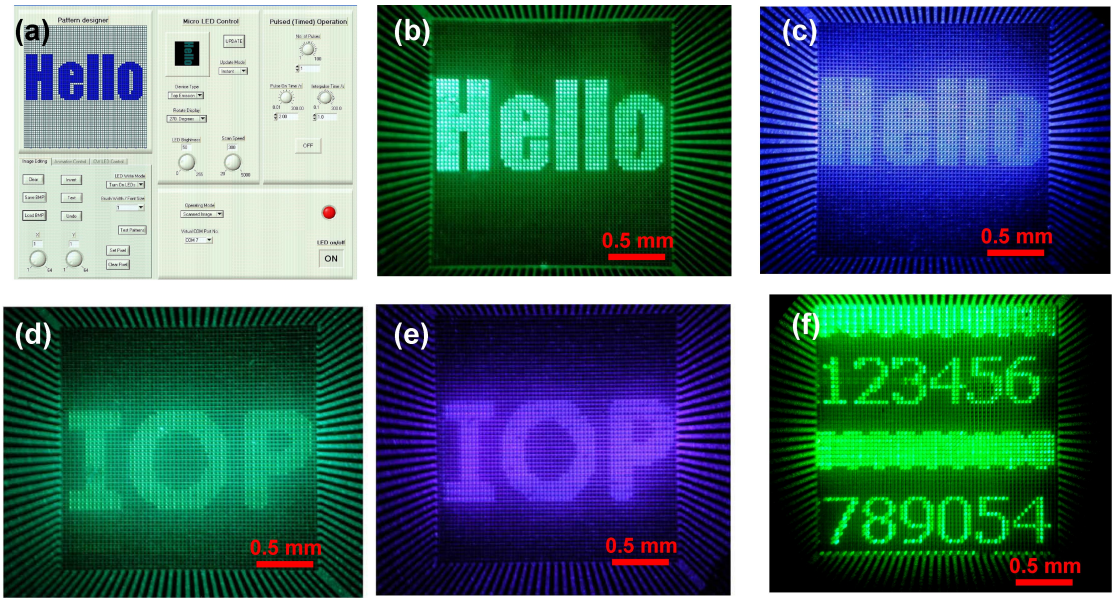

FIGURE 4.7: (a) 64×64 matrix-addressable micro-LED GUI and (b)-(f) optical microscope images of programmable micro-display emission patterns.

Although matrix-addressable micro-LED devices have been proved to be a good candidate for high-performance III-nitride micro-display system, the disadvantages and shortcomings of this approach should not be ignored. Firstly, the emission patterns generated by a matrix-addressable micro-LED device are based on raster-scanning the array and each row is only active for a faction of the time. Hence, the average output power of each pixel and of the emission patterns is greatly reduced. Secondly, the pixels from a matrix-addressable device are interconnected with each other by metal tracks, whereby each row of the pixels shares a common p-contact and each column shares a common n-contact. Therefore, single damage to the pixel will not only influence the pixel itself but also the pixels interconnected to the damaged pixel, causing the failure of the pixels in the same row and column. Furthermore, damage to the metal tracks interconnecting the pixels will also disconnect the pixels in a row/column fashion. Taking all these factors into consideration, it is desirable to be able to individually address each pixel, increasing the average output power of the micro-display system and improving the device reliability. In this case, individually-addressable micro-LED arrays suitable for integration with CMOS driver arrays were first designed by the Institute of Photonics in 2008 and have been optimised and developed for various applications since then. Details about the CMOS driver circuitry, CMOS-controlled micro-LED array and its application for VLC have been presented in chapter 3. In the following section, we will mainly discuss the realisation of micro-display systems based on CMOS-controlled micro-LED arrays.

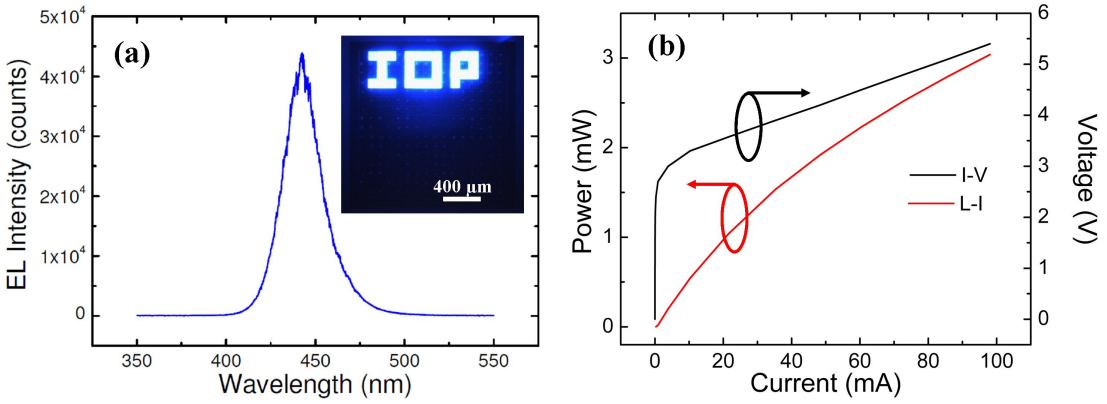

FIGURE 4.8: (a) EL spectrum of a CMOS-controlled micro-LED pixel under an injection current of 40 mA. Inset: Emission pattern 'IOP' generated by the CMOS-controlled micro-LED array. (b) I-V and L-I characteristics of a typical CMOS-controlled micro-LED pixel.

4.2.4 Individually-addressable micro-display systems

As presented in chapter 3, CMOS technology not only offers an efficient approach to individually control the micro-LED pixels but also is capable of modulating each pixel up to several hundred MHz. Therefore, such capabilities make it possible for a CMOS-controlled micro-LED array to deliver high-brightness video graphics images that appear continuous to the human eye. Figure 4.8 (a) shows the EL spectrum of a blue-emitting CMOS-controlled micro-LED pixel with a DC operating current of 40 mA. This CMOS-controlled micro-LED array consists of 16×16 individually-addressable tessellated (sqaure area) micro-LED pixels with a same pixel size of 99 μm. A microscope image of the emission pattern 'IOP' (abbreviation for the Institute of Photonics) generated by this CMOS-controlled micro-LED device is shown in the inset of Figure 4.8 (a). Figure 4.8 (b) shows the I-V and L-I characteristics of the CMOS-controlled micro-LED pixel. At an injection current of 98 mA, the output power of a single pixel reaches 3 mW and the power density reaches 30.6 W/cm^2, yielding brightness in excess of 2×10^6 cd/m^2. This is already several orders of magnitude higher than those achieved by alternative technologies such as OLED displays. Apart from our group, other groups have also reported the III-nitride high-resolution micro-display systems based on CMOS-controlled micro-LED devices [83], such as is shown in Figure 4.9.

The III-nitride micro-display systems reported above are monolithic and not capable of delivering multi-colour images. For micro-display systems, it is desirable to have light emitters capable of emitting different colours instead of single ones. To achieve this,

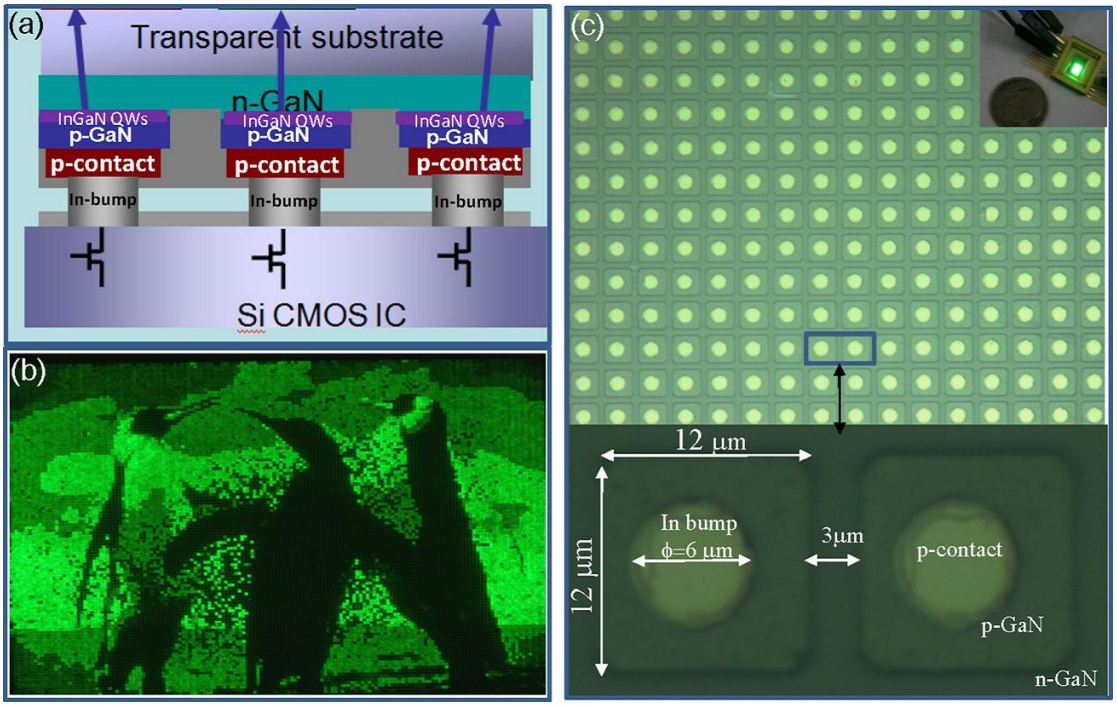

FIGURE 4.9: (a) Illustration of the flip-chip bonding between micro-LED array and CMOS driver array via indium bumps; (b) a projected image of penguins from a green (517 nm) InGaN micro-display (having a pixel size of 12 μm and a pitch distance of 15 μm) operating at a driving current of 1 μA per pixel; (c) the zoom-in image of a segment of an InGaN micro-LED array chip showing its pixels and indium bumps viewed from the transparent sapphire side. The top inset shows a fully assembled green InGaN micro-display (160×120 pixels) in operation (1 μA per pixel) [83].

several approaches have been proposed and details of realising a colour-tunable micro-display system based on a CMOS-controlled micro-LED device will be reported in the following section.

4.3 CMOS-controlled smart colour-tunable micro-display system

4.3.1 Development of colour-tunable materials and micro-displays

Compared to liquid crystal technology and OLEDs [132, 133], conventional thin-film III-nitride LEDs fabricated from the same epilayer usually emit light at a single colour determined by the specific quantum-well (QW) structure used. Such monochromatic emission limits the multi-colour applications of these LEDs. Recent progress toward multi-colour applications of inorganic LEDs, such as flat panel screens for television, computer, and mobile devices, therefore mainly relies on the mechanical packaging together of separate

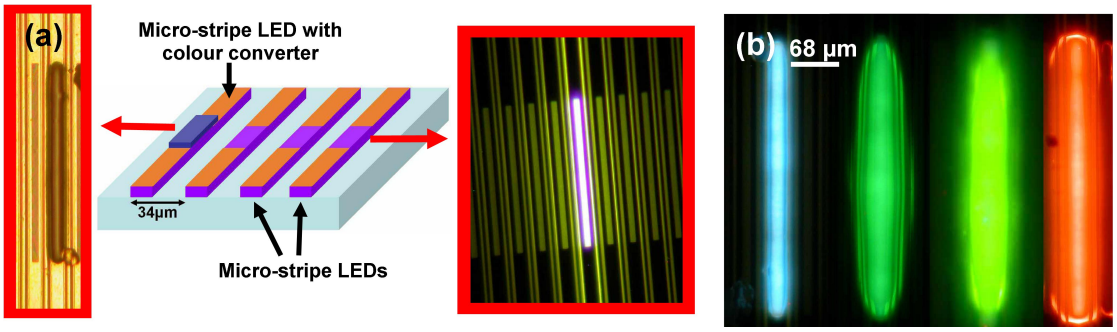

FIGURE 4.10: (a) A schematic of the micro-stripe LED integrated with colour converter (centre) and microscope images of the integrated device under white-light illumination (left) and a UV micro-stripe LED in operation (right); (b) blue, green, yellow and red colour emission from UV-emitting micro-stripe LEDs integrated with nanocrystal/epoxy colour-converters [136].

LED devices emitting at different colours to form a multi-colour unit. However, this method imposes a major limitation for the scalability and the resolution of the display as a result of the limited packaging placement accuracy (a few hundred microns). It is expected that the packaging approach will become increasingly difficult with decreasing LED die size and increased packaging density. A multi-colour micro-display system based on micro-LEDs with typical pixel sizes of 20 μm, for example, would therefore be very difficult to achieve by this technology. Alternatively, the integration of monochromatic LEDs with different colour converters such as organic polymer blends and semiconductor nanocrystals has also been reported [134–136]. This approach is through luminescence down conversion, in which III-nitride ultraviolet (UV) or blue LED emitters pump one or more colour converters to generate secondary (longer-wavelength) emission. Figure 4.10 shows a typical result of colour down conversion achieved in our group. Blue, green, yellow and red nanocrystal/epoxy colour converters have been successfully integrated with micro-LEDs, resulting in a multi-colour emission from a single LED chip [136]. However, it is worth mentioning that the addition of colour converters complicates the device fabrication and may reduce the device reliability due to the degradation of integrated colour converters. Therefore, to simplify the fabrication complexity associated with the aforementioned techniques, it is extremely important to explore simpler approaches for multi-colour displays.

Recently, there were several reports on the development of III-nitride LEDs with tunable colour emission and their potential in multi-colour display and phosphor-free white lighting [36, 37, 137–139]. In that work, by controlling the growth conditions, indium-rich quantum wells (QWs) were achieved in III-nitride LED wafer structures containing

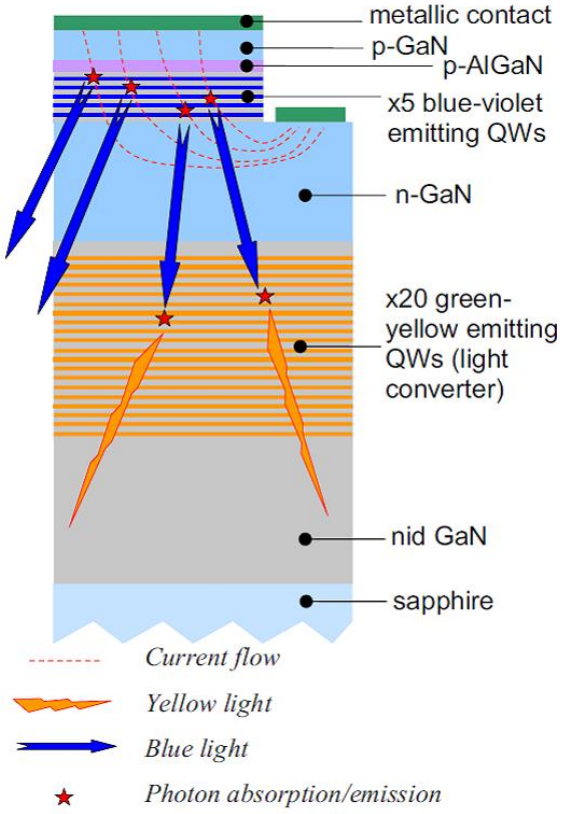

FIGURE 4.11: Schematic structure of a colour-tunable device, consisting of blue-violet emitting QWs grown on top of the green-yellow emitting QWs [36].

blue or UV InGaN QWs, leading to another longer-wavelength green or amber emission together with shorter-wavelength emission. The longer-wavelength emission is generated by the indium-rich QWs, which can be photo-pumped by shorter-wavelength structures or electrically-pumped via carrier injection, depending on the specific wafer structures and related carrier dynamics. Figure 4.11 shows a schematic structure of the colour-tunable device reported in [37]. As shown, blue-violet emitting QWs are used to photo-pump green-yellow emitting QWs (colour-converter), resulting in a mixed emission from the two sets of QWs. Under different injection currents, the ratio of the output power from the two sets of QWs is different. Therefore, the colour of the light emission is different under different injection currents.

Another approach toward colour-tuanble LED device is to fabricate a three-terminal LED device with two sets of QWs seperated by a tunnel junction, as shown in Figure 4.12 [140]. The first terminal functions as a p-contact for the top QWs; the second terminal functions as a n-contact for the top QWs and a p-contact for the bottom QWs; the third terminal functions as a n-contact for the bottom QWs. In this case, carriers

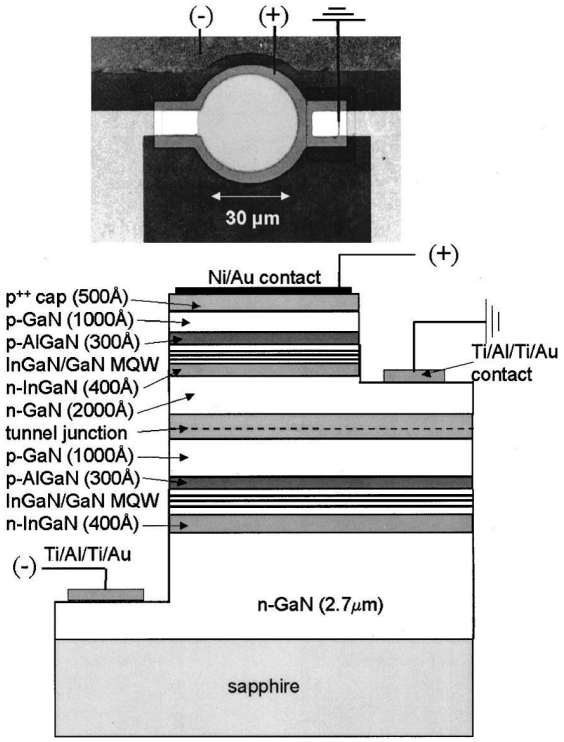

FIGURE 4.12: Schematic view of the three-terminal dual-wavelength LED, indicating the active regions, the tunnel junction, and the bias arrangement. A plan view image of the device is shown at the top [140].

can be injected into the two sets of QWs simultaneously, leading to two different light emissions with different colours from the two sets of QWs. By adjusting the emission intensity of each set of QWs, a colour-tunable emission can be generated. In addition, GaN nanorod arrays with InGaN QWs anisotropically formed on the nanorod tips and sidewalls have been developed to achieve colour-tunable LEDs [36]. Figure 4.13 (a) shows a transmission electron microscope (TEM) image of a colour-tunable GaN nanorod with $In_xGa_{1-x}N$/GaN MQWs grown on two different facets, i.e. the nanorod tip and sidewall. High-magnification TEM images of QWs grown on tip and sidewall of this GaN nanorod are shown in Figure 4.13 (b) and (c), respectively. Figure 4.13 (d) illustrates the energy-dispersive X-ray (EDX) line profiles of indium content in these QWs. The indium contents are estimated to be 0.60 and 0.15 for the QWs formed on the tip and sidewall of this GaN nanorod, which correspond to red and blue emission, respectively. At low bias voltage, carriers are only injected into the tips of GaN nanorods due to locally enhanced potential drop around the nanorod tips. When the bias voltage increases, equipotential plane is uniformly distributed from the tip to the sidewall surface of the nanorod, leading to effective carrier injection into both the nanorod tips and sidewalls. As a result, the nanorod tips emit red light and the nanorod sidewalls emit blue light,

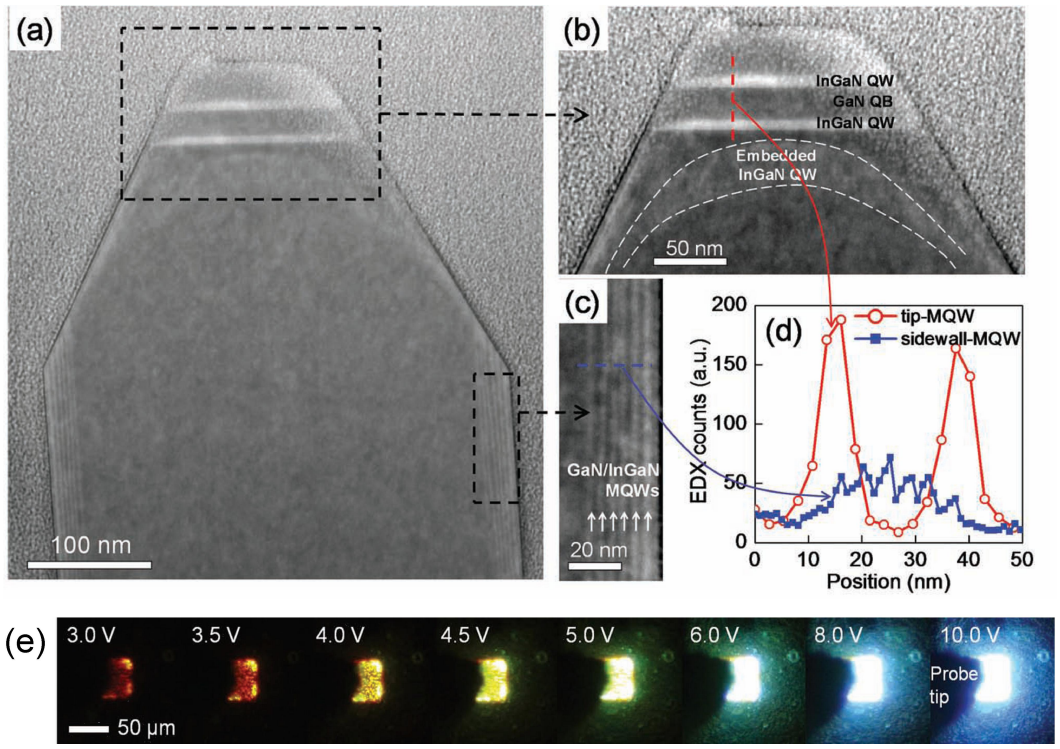

FIGURE 4.13: (a) TEM image of a typical colour-tunable GaN nanorod; high-magnification TEM images of QWs formed on (b) tip and (c) sidewall of this GaN nanorod; (d) EDX line profiles of the indium content of QWs formed on the nanorod tip and sidewall; (e) light emission photographs of an LED fabricated from this GaN nanorod wafer under different applied bias voltages [36].

and a mix of the red emission with the blue emission leads to a colour-tunable emission from the GaN nanorods. As the voltage further increases, the red emission saturates and the colour of light emission changes from amber to blue with the increase of bias voltage. In addition, more carriers are injected into the active regions of GaN nanorods with the increase of bias voltage, leading to an increase of the emission intensity. Figure 4.13 (e) shows a series of EL images taken at various bias voltage levels for the LED fabricated from this GaN nanorod wafer, exhibiting the gradual change in the emission colour with increasing bias voltage [36].

Although the above colour-tunable LED wafer materials have been widely reported, their applications are limited due to the low repeatability of these growth processes. Besides, these LED wafer materials have never been used to realise any multi-colour inorganic display systems, which are believed to be one of the most important and key motivations for growing such wafer materials. To make a further step in this area, we demonstrate below a CMOS-controlled inorganic micro-display system capable of delivering programmable animated images while showing direct colour tuning from red to green at comparable

output power, all based on one InGaN structure. To implement such a micro-display system, we fabricated a dedicated micro-LED array from this InGaN structure, interfaced it to a CMOS driver array, and showed direct display performance and colour tuning under the CMOS control. Our InGaN QW material contains high (0.4) indium mole-fraction, and the principle of colour tuning of this QW structure has been previously reported [51]. Our further measurement shows that the modulation bandwidths of these integrated CMOS/micro-LED colour-tunable pixels reach beyond 100 MHz, thus also providing a wavelength-agile source for high-speed visible light communications (VLC). For such a colour-tunable micro-display, error-free data transmission at bit rates of up to 250 Mbit/s per pixel has been achieved using on-off-keying (OOK) non-return-to-zero (NRZ) modulation.

4.3.2 System design and fabrication

The LED wafer used for the micro-display fabrication was grown at Peking University on a *c*-plane sapphire substrate by metal organic chemical vapour deposition. Shown in Figure 4.14 (a) is the epitaxial structure of the LED wafer, which consists of a 1.5 μm thick GaN buffer layer, a 4 μm thick n-doped GaN layer, a five-period $In_{0.18}Ga_{0.82}N$ (3 nm)/GaN (10 nm) multiple-quantum-well (MQW) layer emitting at 460 nm, a seven-period $In_{0.40}Ga_{0.60}N$ (4 nm)/GaN (13 nm) MQW layer emitting at 600 nm (main QWs), and a 210 nm thick p-GaN cap layer. Figure 4.14 (b) shows a schematic diagram of the conduction energy band in the active region of the LED wafer material. The low-indium-content blue QWs function as an electron reservoir and pre-strain-relaxation layer for improving the radiative efficiency of the main QWs [141, 142]. The micro-LED device used for the micro-display demonstration was fabricated by using a similar process to that reported previously [76]. It is a 16×16 array of individually-addressable micro-disk LED pixels with a diameter of 72 μm on a 100-μm centre-to-centre pitch [see Figure 4.15 (a)]. Each pixel within the micro-LED array shares a common n-contact and is addressed via an individual p-contact. Due to the flip-chip design, light is extracted from the polished sapphire substrate of the device. Figure 4.15 (b) shows the current-voltage (I-V) and corresponding optical power versus driving current (L-I) curves of a typical such LED pixel, driven by CMOS under DC conditions at room temperature.

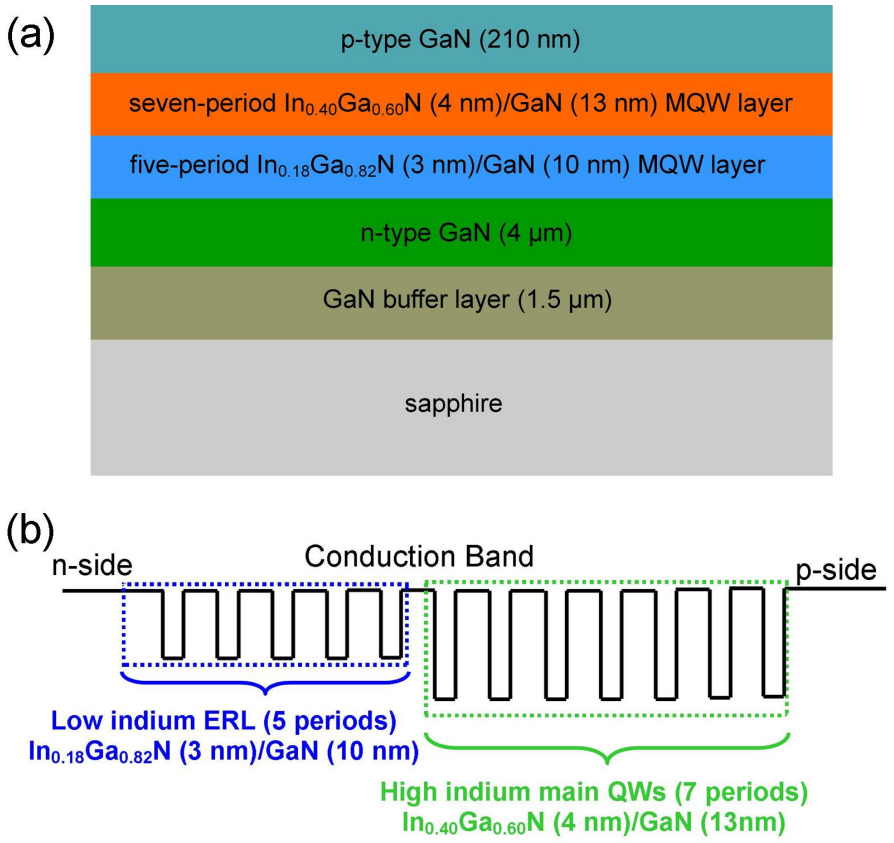

FIGURE 4.14: (a) Epitaxial structure of the LED wafer used for fabricating the colour-tunable micro-LED device. (b) A schematic diagram of the conduction energy band in the active region of the colour-tunable LED wafer material.

The CMOS driver chip, which consists of a 16×16 array of individually-controllable 100×100 μm^2 driver cells on a centre-to-centre pitch of 100 μm, was designed to match the 16×16 micro-LED array. To achieve electrical connection between the entire micro-LED array and the CMOS driver chip, each micro-LED pixel's p-pad is Au-bump bonded onto a corresponding CMOS driver cell, which contains a 60×60 μm^2 bonding pad and dedicated logic circuit. Each bonded CMOS driver functions as a high-speed switch to control the output of each micro-LED pixel according to the state of input trigger signal. When the input trigger signal of a CMOS cell is logic 1, the CMOS driver is turned on and the output of the corresponding micro-LED is determined by the applied voltage and the I-V and L-I characteristics of the micro-LED itself. Thus, by programming the input trigger signals for each CMOS driver cell, this CMOS/micro-LED micro-display system is capable of delivering dynamic images. To implement this, a CMOS driving board [as shown in Figure 4.15 (c)] with a field-programmable gate array (FPGA) unit and a simple computer interface was developed. The FPGA unit allows the micro-LED

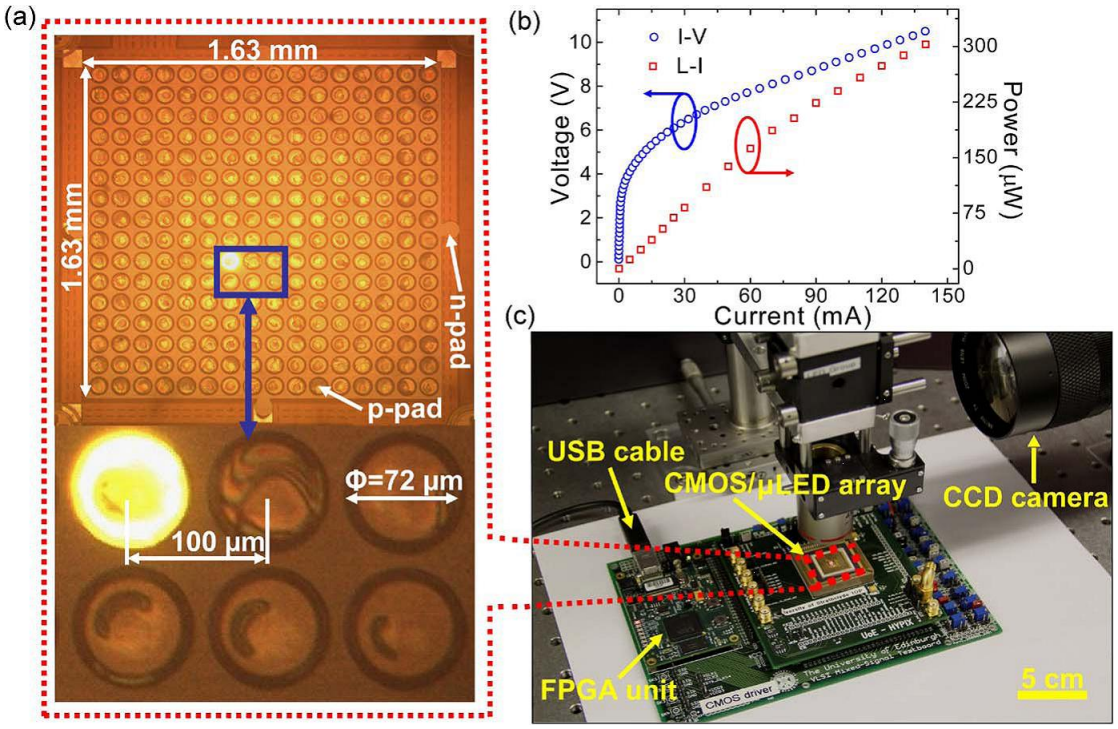

FIGURE 4.15: (a) Microscope image of the whole CMOS-bonded micro-LED array with an individual pixel in operation. (b) Characteristic I-V and L-I curves of a 72 μm diameter CMOS-bonded micro-LED pixel. (c) Image of the CMOS driving board and relevant microscope/CCD-camera setup for the micro-display demonstration.

array to deliver video images by distributing input signals for CMOS drivers according to the computer instructions programmed by hardware description language and the whole micro-display system is powered by a computer USB port. More details about the design, function, and operation procedures of the CMOS electronics used here can be found in chapter 3 and our previous reports [64, 110]. In this work, dynamic images at a frame rate of 1.67 Hz (0.6 s per frame) are shown. The current CMOS chip can only update the micro-LED pixels one by one, which limits the frame rate. But we anticipate that, with a suitable software interface and a specifically-designed CMOS chip, which could update pixels in an entire array at a time, dynamic videos could be displayed at high frame rates for this micro-display system.

4.3.3 General performance of the colour-tunable micro-display system

Figure 4.16 shows the current-dependent electroluminescence (EL) spectra of a typical CMOS-controlled micro-LED pixel, under different DC injection currents at room temperature. A significant blueshift of the emission wavelength of the main QWs [as indicated by the arrow of Figure 4.16] appears as the injection current increases, resulting in

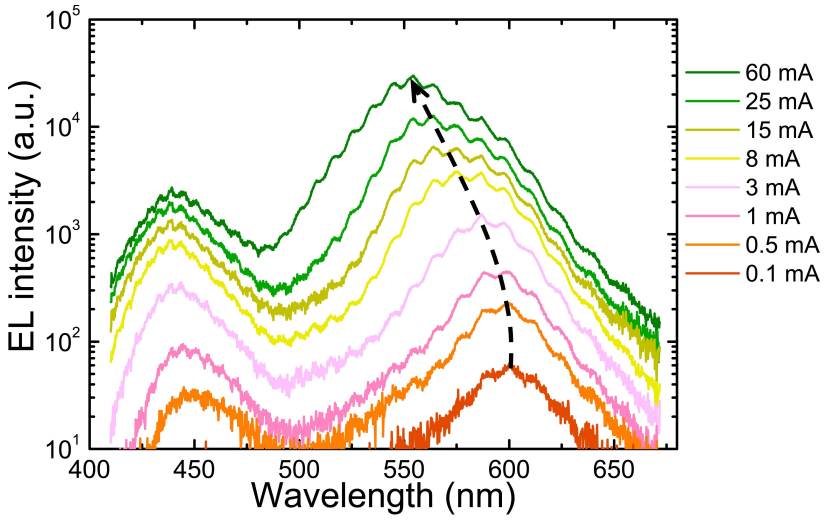

FIGURE 4.16: EL spectra of the colour-tunable CMOS/micro-LED pixel taken at various injection currents from 0.1 to 60 mA.

the tunable emission from the micro-LEDs. Both the screening of the quantum-confined Stark effect (QCSE) in polar QWs (see chapter 1, section 1.3) and the band-filling effect can lead to this blueshift. Based on the numerical stimulation results reported previously [51], in the relatively low-current-density regime (<3.5 kA/cm^2), the main contribution to the blueshift of the main QWs is due to both the band filling effect and the screening of the QCSE, whereas in the high-current-density regime, the blueshift of the spectra is mainly caused by the band filling effect, since the piezo-electric field is almost completely screened in the high-current-density regime. Shown in the inset of Figure 4.16 is a detailed current-dependent normalised EL spectral mapping. It can be seen that the main emission peak wavelength of the micro-LED shifts from 600 nm to 550 nm when increasing the injection current from 0.1 mA to 80 mA and saturates at 550 nm. The dominant emission of the micro-LED is from the main QWs, whereas the emission from the blue QWs is (as it is designed to be) much weaker, which is probably due to the low mobility of hole and the long hole-migration distance between the blue QWs and the p-GaN layer [143]. Figure 4.17 shows the calculated CIE (1931) coordinate curve according to the current-dependent normalised EL spectra. As shown in Figure 4.17, the CIE coordinate curve shifts from the red region to the green region with increased injection current, indicating a distinct and direct colour change of the light emitted by the micro-LED device. Three images of micro-LED pixels with different colours, corresponding to the three CIE coordinates highlighted in Figure 4.17, are shown in the same figure as well. It is also worth highlighting that the small pixel size and associated

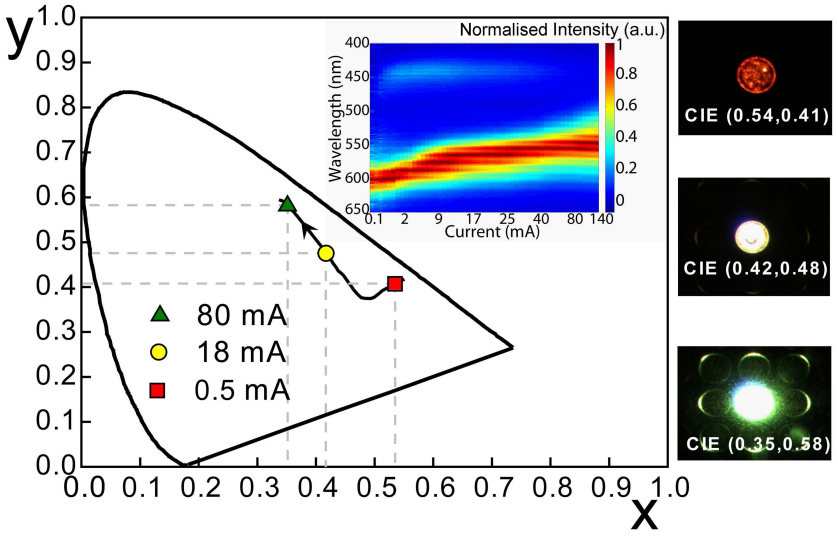

FIGURE 4.17: Chromatic coordinate curve corresponding to the normalised EL spectra shown in the inset, with three specific chromatic coordinates highlighted. The three micro-LED images are related to the highlighted chromatic coordinates. Inset: current-dependent (from 0.1 mA to 140 mA) normalised EL spectral mapping of the micro-LED pixel.

large dynamic range of current density enable the broad tuning of colour. The change of the colour with the increase of injection current is mainly due to the spectral shift of main QWs caused by the screening of QCSE and the band-filling effect. The emission of blue QWs is much weaker compared with the emission from main QWs, thus does not contribute to the colour-tunability of the device significantly. In addition, due to very low blue emission from the device, white light emission has not been achieved at the current stage.

A current-dependent spectral shift is generally undesirable for applications where a constant emission wavelength is required. However, utilising this characteristic of the micro-LEDs, it is feasible to demonstrate a colour-tunable or multi-colour micro-display system based on a single LED array made from the same wafer material. Such a multi-colour display system has many advantages such as the elimination of using inorganic/organic colour converters and LED dies emitting at other colours, thereby reducing the production cost and enabling a more compact design. Furthermore, there is a possibility to use colour mixing to increase the colour gamut of the micro-display, by cycling individual pixels through different colours at fast rates. However, one should note that, to achieve this multi-colour display, the current within each pixel must be varied if each pixel is under CW operation, which in turn induces a strong brightness variation for the display. Knowing that the apparent average brightness of each pixel under pulsed operation can

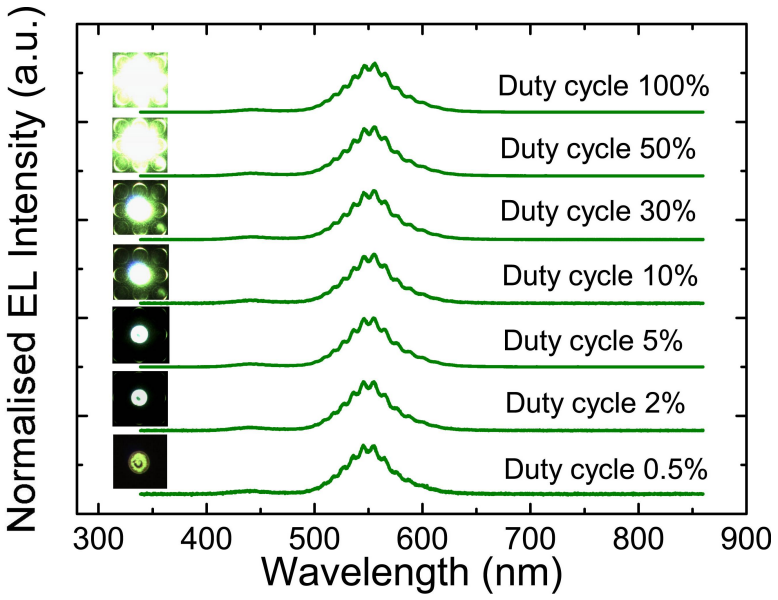

FIGURE 4.18: Duty-cycle-dependent EL spectra of the micro-LED pixel, with relevant images shown in the same figure as well.

be tuned by changing the duty cycle of injection current, specifically-designed active CMOS driver electronics have been used to drive the LED array. In other words, comparable brightness of the micro-LED pixels emitting at different colours is achieved by adjusting the duty cycle of the working micro-LED pixel by sending appropriate trigger signals to the CMOS drivers. To control the state of micro-LEDs using an external source, the trigger signal should be first adjusted to reach the logic threshold of the CMOS electronics and then sent to the CMOS chip to modulate the CMOS drivers directly. In this case, all the working micro-LED pixels, originally turned on under CW operation, will be controlled by the trigger signal. The trigger signal used here is a square wave with a peak-to-peak voltage of 2 V and a period of 20 ms (frequency of 50 Hz). Its duty cycle is adjustable, and using this pulse-width modulation to normalise the power of micro-LED pixels emitting at different colours does not influence the capability of the micro-display to deliver animated images.

Plotted in Figure 4.18 is the duty-cycle-dependent EL spectra of the micro-LED, with a peak-to-peak current of 80 mA. The apparent "glow" seen from the adjacent pixels of the inset images is due to the light scattering from the pixel sidewalls. As shown in Figure 4.18, the brightness of the micro-LED is increased, while the emission wavelength is slightly redshifted (<2 nm) with increasing the duty cycle. The redshift of the spectra is attributed to the self-heating induced bandgap shrinkage when the duty cycle is large [26]. Nevertheless, the redshift is so small that the brightness of the LED pixel can be

controlled by adjusting the duty cycle without changing the colour dramatically. In other words, the change of colour caused by the small redshift is not noticeable by the human eye and is thus not a real problem for the micro-display. The reason that changing the brightness of the micro-LED without changing its colour significantly is due to the short turn-on and turn-off time of the micro-LED device (ns regime) [144], which ensures the peak current remains basically the same when the micro-LED is turned on regardless of the duty cycle. The same results were also observed when the micro-LED is operating at lower current levels. In the duty-cycle-dependent EL measurement, the micro-LED device was driven at long enough time to reach stable EL emission at each duty cycle, and we repeated this measurement three times. Each measurement took about one hour, and we did not observe any obvious redshift at higher duty cycle in each measurement. There are two possible reasons to explain why the redshift is very small for our devices. Firstly, the screening of QCSE and the band-filling effect always dominate the emission of the main QWs of this high-indium content material [51]. Secondly, the superior thermal management of this CMOS-bonded micro-LED device will induce smaller thermal effect on its EL spectra: the micro-LED format has been proved to have better performance in thermal management than its broad-area counterpart [88], and the metal bump bonded on the p-pad of each micro-LED pixel could also help it to dissipate heat when the pixel is in operation.

Shown in Figure 4.19 (a)-(c) are representative emission patterns at red, green and yellow wavelengths generated by the CMOS-controlled micro-LED array. Approximately identical average output power for each pattern was achieved by driving the micro-LED array with different duty cycles. The red pixel is in DC operation at 0.5 mA with an output power of 0.93 μW, the green pixel is in operation under 0.5% duty cycle at 80 mA with an output power of 1.03 μW, and the yellow pixel is in operation under 2% duty cycle at 18 mA with an output power of 0.97 μW. As shown in Figure 4.19, there are some black features across the working pixels, which are caused by flip-chip bonding between micro-LED array and CMOS chip. During the flip-chip bonding process, the p-contact metal on top of the micro-LED pixel physically contacts the gold bump and the bonding force damages the Ohmic contact between the current spreading layer and p-GaN. However, this issue can be addressed by designing a dedicated bonding pad not directly on top of the micro-LED pixel, as shown in Ref [64]. The micro-LED pixels have shown good output and EL uniformity at different current densities. Due to the power

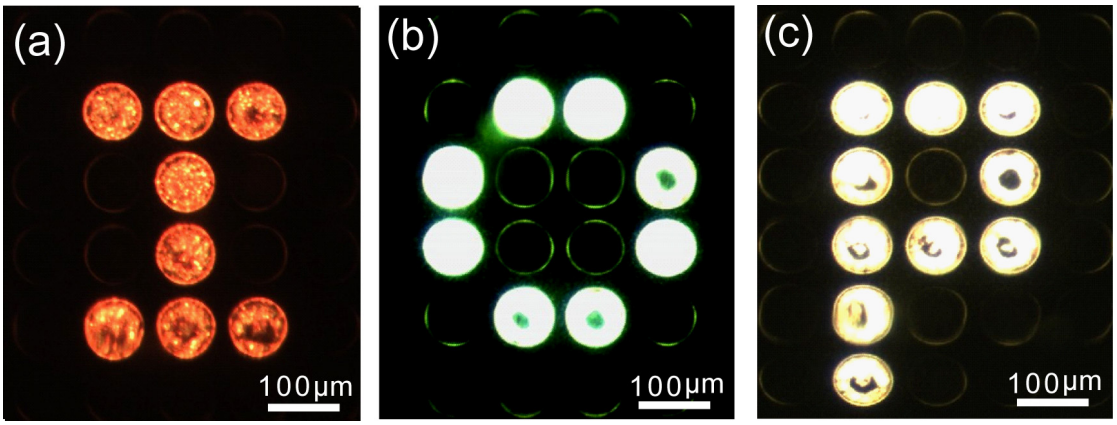

FIGURE 4.19: Controllable emission pattern 'IOP' (abbreviation for the Institute of Photonics) generated by the CMOS-controlled micro-LED array.

normalisation along with the small pixel size used, the absolute power from individual micro-LED pixels is relatively low here compared with commercial illumination LEDs. However, in this case, the power density per pixel still reaches 25.6 mW/cm^2, which is enough for practical applications such as head-mounted displays and contact lens displays [118, 121]. In addition, for some applications such as contact lens displays, the micro-LED pixels should not work at too high current with very strong output in order to meet the eye safety requirement [121]. Furthermore, according to our reliability test for a similar micro-LED device, its pixel does not show any obvious degradation of power output (less than 5%) for 2200 hours under CW operation with an injection current of 20 mA, which proves the strong reliability of such micro-display system.

Apart from being useful for multi-colour displays, further measurement shows that these CMOS-controlled micro-LED pixels have high modulation bandwidths, indicating that they can also be used for optical data transmission. The idea is to utilise this CMOS-controlled smart and colour-tunable display to deliver programmable animated images for the purpose of display and, at the same time, modulate one pixel or several of them for data communications. Such a smart display system could show dynamic images to the human eye but have additional information encoded in them, which can be received by a detector to set up an optical communication link, e.g., implemented in a cellphone format. Figure 4.20 (a) shows the frequency response of a typical micro-LED pixel with an applied bias of 6.5 V. The optical -3 dB bandwidth of the micro-LED pixel was found to be approximately 100 MHz, and the drop in the frequency response seen at 450 MHz has been attributed to the CMOS drivers not being able to modulate their output in response to signals at this high frequency. Chapter 3, section 3.4 has reported the use

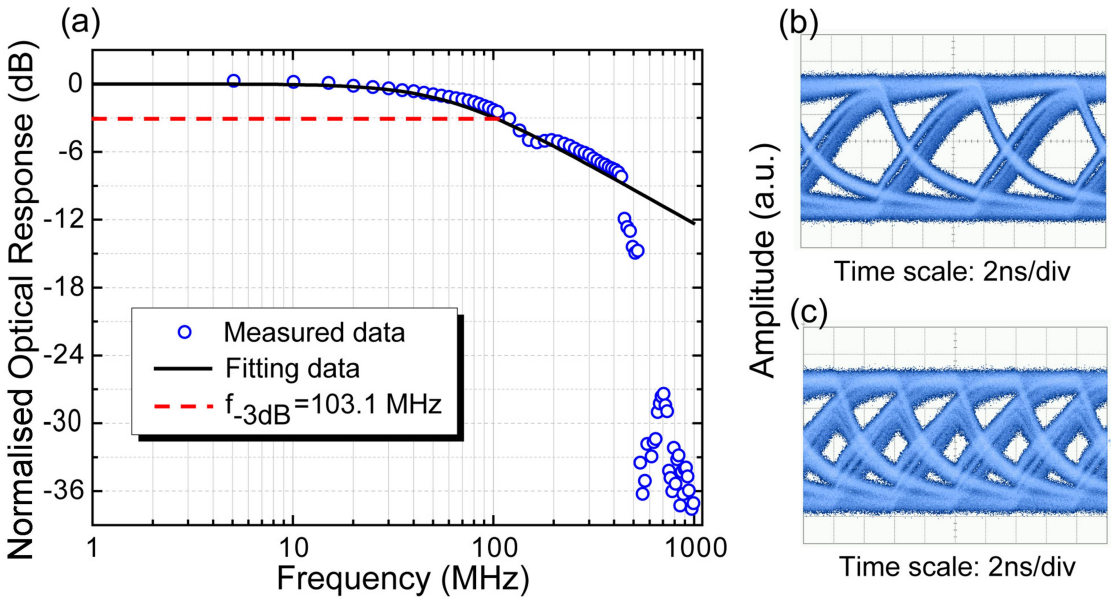

FIGURE 4.20: (a) Frequency response curve of a typical 72 μm diameter CMOS/micro-LED pixel, with a forward bias of 6.5 V, and eye diagrams taken at (b) 155 Mbit/s and (c) 250 Mbit/s.

of CMOS-controlled micro-LEDs for optical communications in detail. Compared with blue CMOS-controlled micro-LED device, the modulation bandwidth of this colour-tunable micro-LED device is lower, which is probably due to the influence of strong piezo-electric field. The strong piezo-electric field distorts the energy band of QWs so that the confining capability of QWs to carriers is weakened [26]. Therefore, the loss of carriers in the QWs causes the drop of carrier concentration, leading to longer carrier differential lifetimes and lower modulation bandwidths. A detailed investigation of the frequency responses of other CMOS-bonded micro-LED devices and the corresponding method to fit the frequency response curves have been reported in chapter 3. The CIE coordinates at 6.5 V bias are (0.37, 0.54) when the device is driven under DC conditions. At increasing modulation frequency, the colour changes slightly, which is attributed to a reduction in the effective voltage applied to the micro-LEDs due to the frequency response characteristics of the CMOS/micro-LED pixels; however, at bit rates above 50 Mbit/s, the colour coordinates remain fairly stable at (0.39, 0.53). This change in colour during modulation could be mitigated in a future CMOS design by implementing a small-signal modulation scheme, rather than an OOK scheme as shown in this work. Data transmission measurement was carried out using an individual pixel from the micro-LED array based on a bit-error ratio test system (BERT) reported in chapter 3. The data pattern output from the BERT was OOK-NRZ pseudorandom binary sequence with a

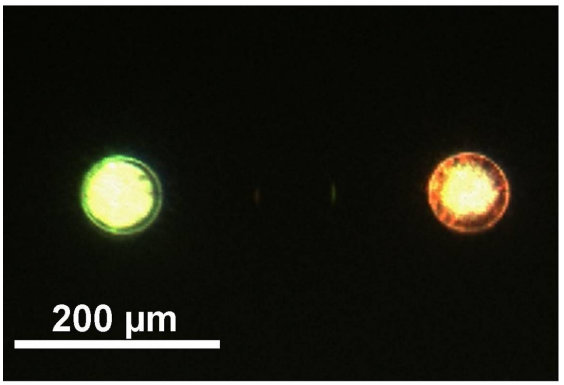

FIGURE 4.21: Microscope image of green and red emission from two micro-LED pixels from the same micro-LED array device, fabricated from the same wafer material. The red pixel is in DC operation at 2 mA and the green pixel is in operation under 0.5% duty cycle at 80 mA.

standard pattern length of 2^7-1 bits and a peak-to-peak voltage of 2 V. The data signal from the BERT reaches the logic threshold of the CMOS electronics so that it can be used to trigger the CMOS driver directly and, in this way, modulate the micro-LED pixel. The optical signal from the modulated pixel was incident on a high-speed silicon photodetector, and the electrical output from this detector was sent to a 25 dB amplifier before returning to the BERT. In this case, error-free data transmission, defined as a bit-error ratio of less than 1×10^{-10}, could be achieved for bit rates of up to 250 Mbit/s. Corresponding eye diagrams taken at 155 Mbit/s and 250 Mbit/s are also shown in Figure 4.20 (b) and (c), respectively.

Due to the limitation of the current CMOS design, the current density of each working micro-LED pixel in the array is the same. Hence, different micro-LED pixels cannot emit different colours simultaneously. However, Figure 4.21 shows a microscope image of green and red EL emission from two micro-LED pixels from a 'bare' (without being integrated with CMOS electronics) micro-LED array fabricated from the 'colour-tunable' LED material. The two pixels are driven under different conditions, whereby the red pixel is in DC operation at 2 mA and the green pixel is in operation under 0.5% duty cycle at 80 mA. Therefore, with a specifically-designed CMOS array which allows different injection currents to flow through different micro-LED pixels simultaneously, multi-colour emission should be achieved from different pixels across the micro-LED array at the same time. Another important issue is how to achieve a full-colour display system. The limiting factor for achieving a full-colour display at this stage is the very low levels

of blue light generated by the device and further investigations are needed to enhance the blue emission, e.g. by modifying the current epitaxial layer structure.

4.4 Summary

In this chapter, the realisation and performance of various micro-display systems, based on III-nitride micro-LED arrays, have been presented. In section 4.1, micro-display systems developed from conventional technologies, such as LCOS and OLED, are introduced. The experimental part starts from section 4.2. In this section, the advantages of using III-nitride materials for micro-displays are presented and matrix-addressable micro-display systems based on III-nitride micro-LED arrays are reviewed. In the matrix-addressable device, any individual pixel in the micro-LED array can be driven by electrically addressing the corresponding column and row. After being integrated with suitable driver circuitry and computer interface, a matrix-addressable micro-display system could deliver programmable high-resolution micro-scale images via convenient computer control. Apart from matrix-addressable micro-display system, individually-addressable micro-display system based on a CMOS-controlled micro-LED array has also been developed. In section 4.3, to make a further step, we have made a demonstration of a programmable colour-tunable inorganic micro-display, based on new epitaxial structures, micro-LED fabrication, and relevant CMOS technology. The micro-display system reported here is capable of delivering computer-controlled programmable dynamic images with its emitting colour changing from red to green at comparable brightness. Also, individual micro-LED pixels from this CMOS-controlled system have high-bandwidth modulation capability, so that they can be used for high-speed VLC as well. The work demonstrates a direct colour-tunable InGaN micro-display for dual applications under CMOS control and, more importantly, provides an innovative method to overcome the limitations of using thin-film InGaN-based LED for multi-colour applications in the future.

Chapter 5

VLC in plastic optical fibre and study on colour-converting materials for VLC

Using micro-LED devices for free-space visible light communications (VLC) has been systematically introduced in previous chapters. In this chapter, to make a further step, we investigate the performance of using individual pixels from a micro-LED array for high-speed plastic optical fibre (POF) communications and the results are shown in section 5.1. Furthermore, the potential of integrating efficient inorganic/organic materials with micro-LED device to realise high-speed colour-converting optical data link has been investigated in section 5.2. These colour-converting materials have fluorescence lifetimes of the order of a few tens of nanoseconds for quantum dots (QDs), and a few nanoseconds, or less, for the light-emitting polymer, whilst having high photoluminescence quantum efficiencies. When integrated with micro-LEDs, these materials offer a novel way of generating modulated light for VLC. Finally, a summary of the work presented in this chapter is given in section 5.3.

5.1 Micro-LEDs for VLC in POF

5.1.1 LED-based fibre communication system

InGaN alloy based micro-LEDs have attracted much interest recently due to their wide applications. For optical communications, micro-LEDs have been demonstrated to have wide modulation bandwidths and thus exhibited superior performance. Recent approaches of utilising micro-LEDs for optical data transmission focus on free space as many think it is possible to provide energy-efficient LED illumination with data encoded in the light for dual applications [59, 63, 145].

In addition to free space, LEDs can also be used in guided-wave communication systems, whereby individual optical fibre or fiber bundles are used as the transmission medium. Plastic optical fibre (POF) is becoming increasingly popular for short-distance communications in recent years [69, 70, 146, 147]. POF has excellent optical properties including long-term stability and can be fabricated using cost-effective methods. However, compared with conventional silica-glass fibre, POF has losses that are about 1000 times greater. Therefore, the data transmission distance in POF is limited to just a few metres to a few hundred metres, e.g. for communications within an office, home, automobile or airplane. Laser diodes and resonant-cavity LEDs are normally used for POF communications due to their narrow electroluminescence spectra and highly directional output. However, high-quality micro-cavities in such devices usually require extra complexity in growth and fabrication [111, 148]. In addition, issues such as eye safety cannot be fully addressed for such devices. Recently, 1.07 Gbit/s data transmission over a 50-m POF has been demonstrated using a 500 nm cyan micro-LED device [70]. However, the internal quantum efficiency (IQE) of the 500 nm cyan LED is much lower compared with a 450 nm blue LED, which may influence the overall performance of the cyan LED device for POF-based optical communications.

In this work, we demonstrate the modulation of a single 74 μm blue-emitting micro-LED pixel from a micro-LED array device to generate non-return-to-zero (NRZ) binary data streams in a 10-m POF. The micro-LED array was fabricated from a commercial 450 nm blue-emitting wafer and the emission of the device lies in the low absorption regime of the POF. For this system, error-free operation, defined as a bit-error ratio (BER) of less than 1×10^{-10}, is achieved at a bit rate of up to 650 Mbit/s. Furthermore, under

PAM-16 modulation scheme, a data rate of up to 4 Gbit/s is achieved in a 10-m POF using a 30 μm diameter blue-emitting micro-LED pixel as transmitter and an avalanche photodiode (APD) as receiver. Such demonstrations not only prove the feasibility of using micro-LEDs for data transmission in POF, but also pave the way towards high-speed parallel data transmission and space-division multiplexing (SDM) in POF using such micro-emitter arrays, which can be fabricated from cost-effective materials following easy processing procedures.

5.1.2 Data transmission in POF under binary data amplitude modulation

The 450 nm blue-emitting micro-LED device reported here was fabricated from a standard commercially available multi-quantum-well LED wafer grown on a *c*-plane sapphire substrate. The device is an 8×8 LED array of individually-addressable micro-disk pixels on a 200 μm centre-to-centre pitch, with each row consisting of pixels of identical size, but columns containing pixels with different diameters ranging from 14 to 84 μm in 10 μm intervals. The disk-shaped pixel mesa was defined using photolithography and inductively plasma etching, and other details of the device fabrication can be found in chapter 2, section 2.1. Due to the flip-chip format, this micro-LED device is designed to be operated inverted, with the light emission extracted from the polished sapphire substrate. Therefore, all the measurements were performed using the through-sapphire emission. To enhance the light emission from the sapphire substrate, thick metal contacting layer was used to form not only p-contact but also reflective mirror for each micro-LED pixel. Figure 5.1 shows the current-voltage (I-V) curve of a typical micro-LED pixel with 74 μm diameter, driven under DC conditions at room temperature. A top-view microscope image of part the micro-LED array is shown in the same figure as well.

To investigate the data transmission in POF using the micro-LEDs, 1-m, 5-m and 10-m standard polymethylmethacrylate (PMMA)-based step-index multi-mode POF (Mitsubishi Rayon Co. LTD. SH4001) were used. Figure 5.2 shows the attenuation of standard PMMA step-index POF with wavelength (after data sheet of Toray Industries, Ltd., 2002). The traditional preferred transmission window of POF is at around 650 nm, where the loss is of the order of 0.17-0.2 dB per metre [26, 70]. However, at even

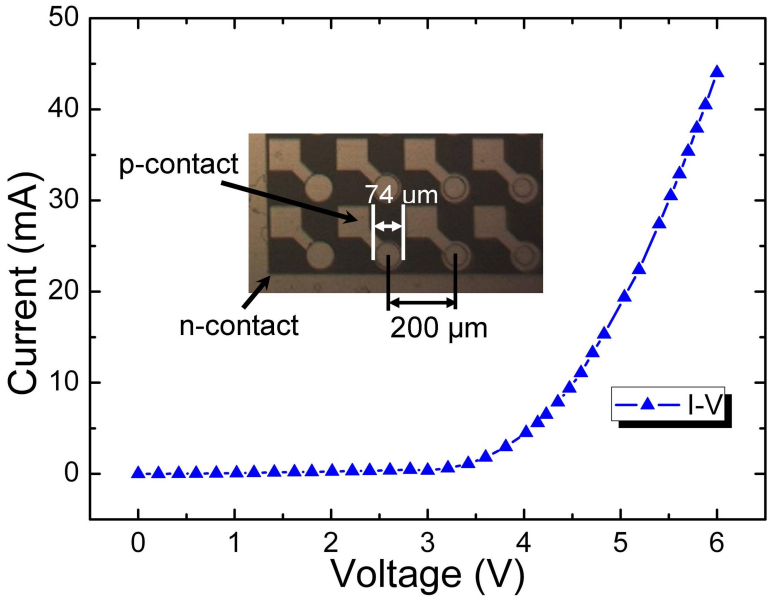

FIGURE 5.1: Characteristic I-V curve of a 74 μm diameter blue-emitting micro-LED pixel. Inset: microscope image of a segment of the micro-LED array.

shorter wavelengths, although the material dispersion increases, the attenuation in POF decreases, making it another attractive regime for data transmission [70]. The additional transmission window of POF is at around 510 nm (green regime) and it can be accessible using GaN-based semiconductor devices, which are usually less temperature sensitive than AlGaInP semiconductor devices and thus more suitable for automotive and avionic environments. However, the IQE of GaN-based LEDs drops significantly with the emission spectrum changing from blue to green regime and this phenomenon is known as the "green (spectral) gap" [24]. Nowadays, it is still quite challenging to grow green-emitting GaN-based LED materials which can be as efficient as the blue-emitting ones. Therefore, in this work, instead of using less efficient green-emitting GaN-based LED material for device fabrication, high-quality blue-emitting GaN-based LED material is used to fabricate micro-LED devices for POF communications. The inset of Figure 5.2 shows the normalised electroluminescence (EL) spectrum of a 74 μm diameter blue-emitting micro-LED pixel with an injection current of 30 mA. As shown in Figure 5.2, the attenuation of POF to the emission of the blue-emitting micro-LED device is of the order of 0.1-0.17 dB per metre, slightly higher than at 510 nm, but still low enough for short-distance POF-based data transmission.

In this work, the micro-LED/POF coupling efficiency was first investigated. Figure 5.3 shows a schematic together with an image of the experimental setup used for POF-based

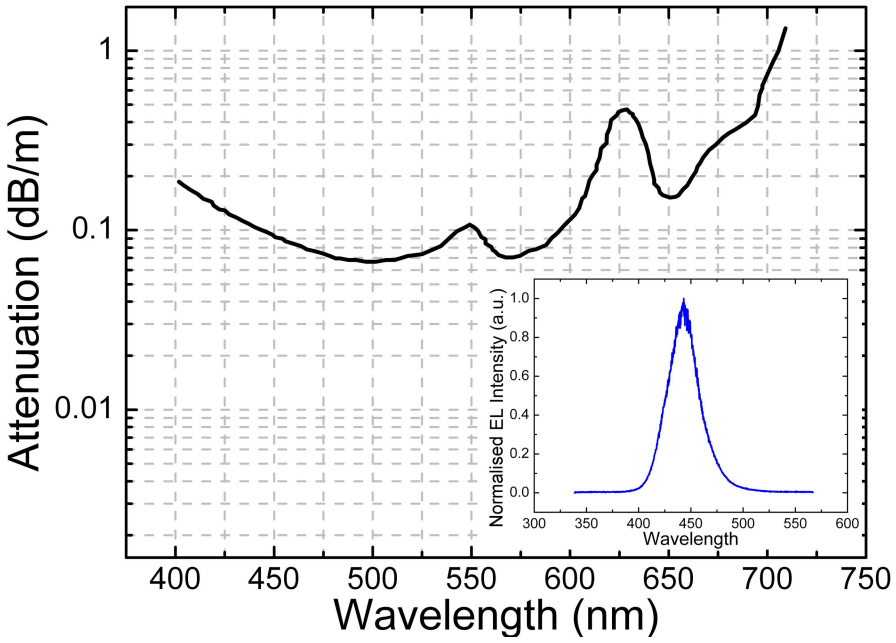

FIGURE 5.2: Attenuation of a standard PMMA step-index POF (after data sheet of Toray Industries Ltd., 2002). Inset: normalised EL spectrum of a typical 74 μm diameter micro-LED pixel, in operation at 30 mA at room temperature.

data transmission. As shown, the micro-LED device was driven by a high-speed probe and its light emission was collected by a set of lenses, which then projected the emission into the 1 mm diameter core of the POF at one end. The other end of the POF was butt-coupled with a photodetector (Femto HSA-X-S-1G4-SI, 0.8 mm effective active diameter). Both ends of the POF were mounted onto X-Y-Z stages. The CW power and/or RF signal amplitude was measured at point A (from the LED into free space), B (after the lenses) and C (after the POF) so that the coupling efficiencies from micro-LED to lenses, lenses to POF and POF to photodetector could be estimated. η_{lens} is defined as the ratio of power at point A (light emitted by the micro-LED into free space) to that at point B (after the light is collected by the lenses). A previously fabricated 99×99 μm^2 blue tessellated (square area) LED was used to evaluate the coupling efficiencies. At 20 mA injection current, the optical power of this LED device emitted into free space was approximately 1.8 mW while 0.585 mW was measured at point B, so $\eta_{lens} = 32.5\%$. η_{POF} is defined as the ratio of power at point B to that at point C (after the POF). In this measurement, 1-m POF was used as the transmission medium and it is assumed that the attenuation in the 1-m POF is negligible. Therefore, η_{POF} represents how much light collected by the lenses actually couples into POF. At 20 mA injection current, the power at point B was 0.585 mW while the power at point C was 0.422 mW, so $\eta_{POF} = 72.1\%$. Since the photodetector is AC-coupled, it is not possible to directly measure the CW

optical power incident on the photodetector. Instead, an RF signal was applied to the micro-LED and the peak-to-peak voltage of the received signal was measured with the photodetector placed at point B and C. The RF signal at point B=270 mV, at point C =106 mV and 106/270 = 0.393. This ratio includes both the coupling efficiency from the lenses to the POF, and from the POF to the photodetector. We know that the coupling efficiency from the lenses to the POF is 72.1% (η_{POF}), so we can calculate the coupling efficiency from the POF to the photodetector: $\eta_{receiver} = \frac{0.393}{\eta_{POF}} = \frac{0.393}{0.721} = 52.4\%$. In this case, the overall coupling efficiency η_{total}, e.g. from the LED to the photodetector, can be calculated as follows: $\eta_{total} = \eta_{lens} \times \eta_{POF} \times \eta_{receiver} = 32.5\% \times 72.1\% \times 54.5\% = 12.8\%$. In terms of the coupling efficiency, the experimental setup shown in Figure 5.3 is the best for data transmission in POF at the current stage. It is noted that the coupling efficiency will vary depending on how the light is collected and coupled into POF. By using specifically-designed optics, such as the integrated micro-lenses [30], it should be possible to modify the beam profile and increase the coupling efficiency of the micro-LED device into POF significantly. Since the experimental setup used here was mainly to demonstrate the feasibility of utilising micro-LEDs for POF-based data transmission, a 12.8% coupling efficiency is enough for this purpose. Figure 5.4 shows the output power of a 74 μm diameter micro-LED pixel with the change of injection current. The output power of the pixel being coupled in to 1-m, 5-m and 10-m POF are shown in the same figure as well, which was measured by using a power-meter at the other end of the POF (point C in Figure 5.3). As shown in Figure 5.4, under the same injection current, the power of the coupled light into POF drops as the length of POF increases, which is due to the attenuation of the POF. The attenuation of POF with wavelength is shown in Figure 5.2. With the increase of POF length, the attenutaion of POF to LED light increases, mainly due to the absorption of POF to LED light [26]. If the LED spectrum is assumed to have a very narrow linewidth at 450 nm, then the attenuation of 1-m, 5-m and 10-m POF to LED light are 0.09 dB, 0.45 dB and 0.9 dB, respectively (according to the data in Figure 5.2). Therefore, due to stronger attenuation, the power of the coupled LED light into POF is expected to drop as the length of POF increases, as shown in Figure 5.4.

The modulation characteristics of the micro-LED pixels in free space and POF were

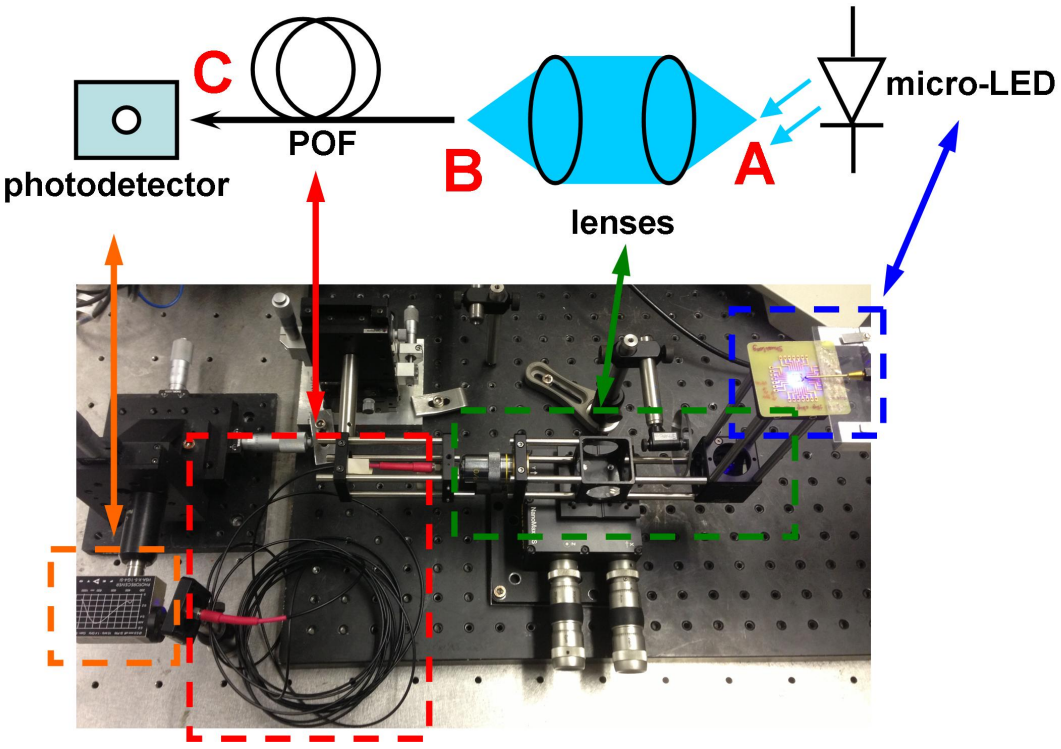

FIGURE 5.3: Schematic and actual experimental setup for micro-LED based optical communications in POF link.

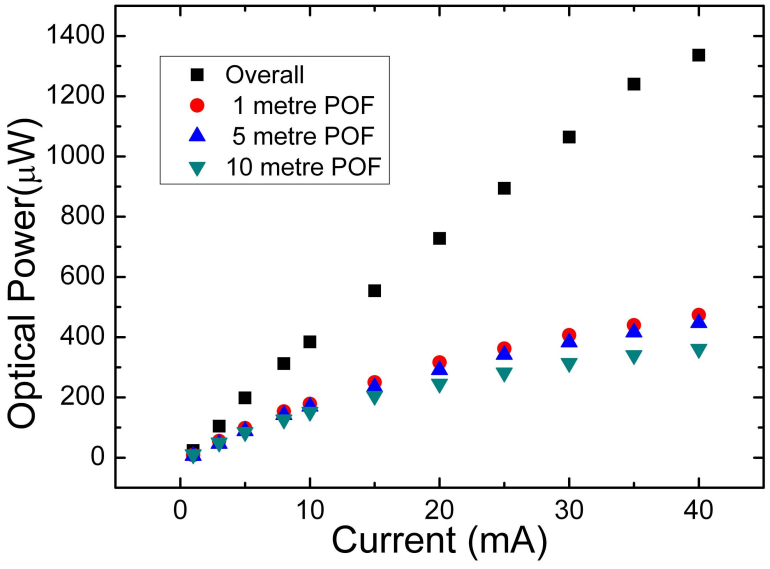

FIGURE 5.4: Overall measured optical power of a 74 μm diameter micro-LED pixel versus the bias current and the coupled power of the micro-LED pixel in 1-m, 5-m, and 10-m POF versus the bias current.

investigated using the methods presented in chapter 2, section 2.3. The frequency response of the modulated micro-LED pixel was measured under a range of biases using a high-speed AC-coupled photodetector (HAS-X-S-1G4-Si-FS) and a network analyser (Hewelett Packard 8753ES). The network analyser recorded the frequency response curves and the optical -3 dB bandwidths could be calculated from these measured frequency response curves accordingly. Figure 5.5 shows the optical -3 dB bandwidths of the 74 μm diameter micro-LED pixel with the increase of bias current in free space, 1-m, 5-m and 10-m POF, respectively. As shown in Figure 5.5, the bandwidth of the micro-LED pixel increases with the increase of injection current. This is caused by the decrease of differential carrier lifetime as the carrier density increases in the quantum wells of the micro-LED [64]. The modulation bandwidth of the micro-LED pixel in free space exceeds 400 MHz at a bias current of 40 mA, much higher than their broad-area counterparts. At the same injection current, the modulation bandwidths of the micro-LED pixel in POF are lower than those in free space and the modulation bandwidths of the micro-LED pixels decrease with the increase of POF length. We believe this is mainly caused by modal dispersion and material dispersion in the POF [26]. Modal dispersion occurs in multi-mode fibres that have a large core diameter or a large index difference between the core and the cladding than the single-mode fibres. Different optical modes correspond to light rays propagating at different paths in the core of the fibres and owing to the difference in the optical path lengths, different modes will arrive at the end of the multi-mode fibre differently. In this case, the modal dispersion is the time delay between the fastest and the slowest optical mode normalised to the length L of the fibre. A schematic model to explain the generation of modal dispersion in POF is shown in Figure 5.6. Material dispersion is another mechanism limiting the data transmission capability of optical fibres. Material dispersion is due to the dependence of the refractive index on the wavelength, which results in a difference in transmission velocity between different colours. In this case, the time delay between the leading edge and the trailing edge of an optical signal caused by velocity difference between different colours is defined as the material dispersion. Therefore, longer POF is expected to have lower bandwidth due to the influence of modal dispersion and material dispersion. For standard POF used in this work, the bandwidths of 1-m, 5-m, 10-m POF are around 800 MHz, 500 MHz and 300 MHz, respectively [149]. More details about the influence of modal dispersion and material dispersion to the micro-LED modulation bandwidth can be found elsewhere [26].

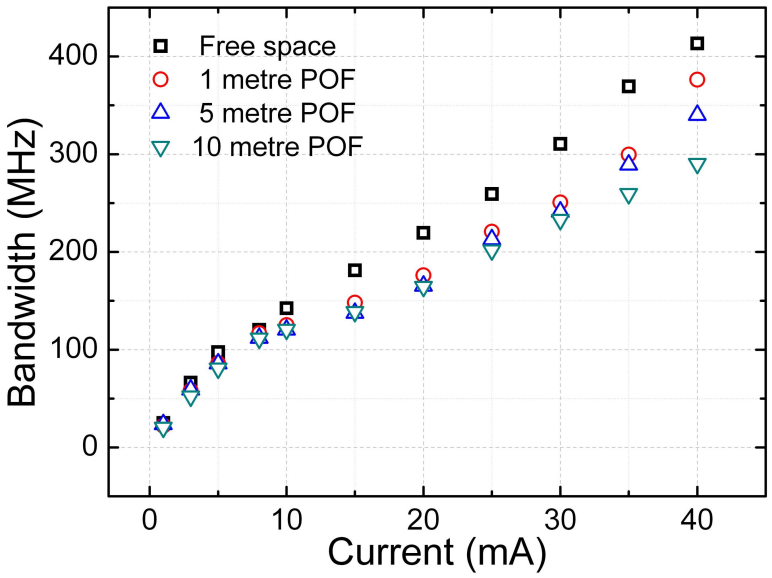

FIGURE 5.5: -3 dB optical bandwidths of a 74 μm diameter micro-LED pixel in free space, 1-m, 5-m and 10-m POF, under different bias current.

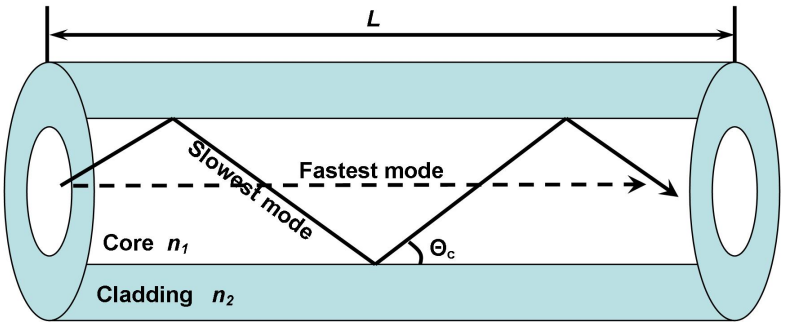

FIGURE 5.6: Schematic to explain the generation of modal dispersion in POF; light rays propagate along different paths in the core of POF, causing modal dispersion.

Data transmission tests were carried out using a 10-m POF and a single 74 μm diameter micro-LED pixel from the 8×8 blue-emitting micro-LED array. A pseudorandom binary sequence (PRBS) (2^7-1) non-return-to-zero (NRZ) data stream from a data pattern generator (Anritsu Pulse Pattern Generator MP1763C) was used to modulate the micro-LED pixel directly with a high-speed probe. The modulated emission from the micro-LED pixel was coupled into a 10-m POF on one end and received by the photodetector at the other end. The resulting electrical signal from the photodetector was then sent to a 50 dB amplifier (Hewlett-Packed 8447D OPT 011 Dual Stage Amplifier) before being sent to a real-time oscilloscope (ROHDE&SCHWARZ-RTO-1022) to adjust the alignment and record eye diagrams. In this POF-based data link, various high-rejection low pass filters (Min-Circuit VLFX) were used to improve the signal quality of the received data signal. Typical eye diagrams from the 74 μm diameter micro-LED pixel

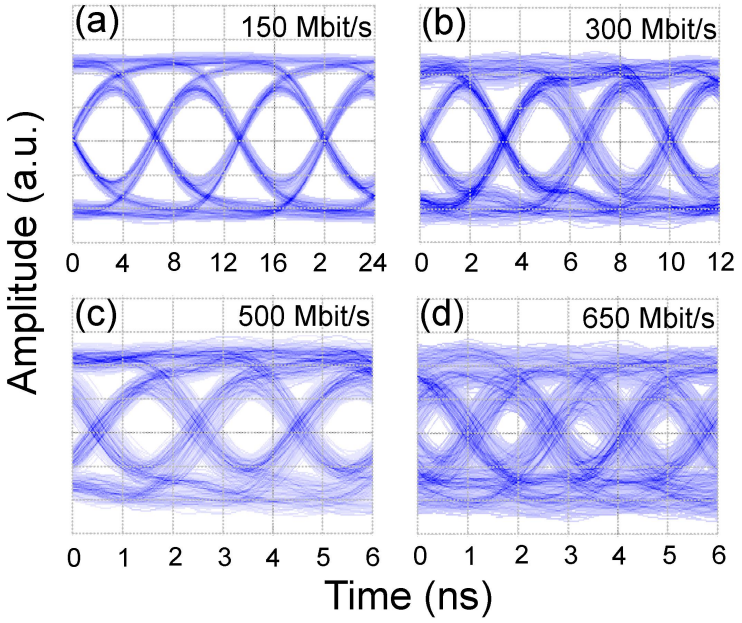

FIGURE 5.7: Eye diagrams of a 74 μm micro-LED pixel at (a) 150 Mbit/s, (b) 300 Mbit/s, (c) 500 Mbit/s and (d) 650 Mbit/s, under 35 mA bias current in a 10-m POF.

at different data rates and with a bias current of 35 mA are shown in Figure 5.7. It can be seen that open eyes are achieved at data rates of up to 650 Mbit/s, indicating the feasibility of 'error-free' data transmission in this regime. The BERs were measured as a function of the received optical power at the photodetector. A neutral density filter wheel was used to control the optical power received by the photodetector. Figure 5.8 shows the measured BERs versus received optical power at different data rates. Error-free data transmission, defined as a BER of less than 1×10^{-10}, is achieved at a data rate of up to 650 Mbit/s and this is the maximum error-free data transmission rate can be achieved for the current system. According to our reliability test for a 40 μm micro-LED pixel fabricated from similar 450 nm blue-emitting GaN-based material, it does not show any obvious degradation of power output (less than 5%) for 2200 hours under DC operation with a bias current of 20 mA, showing that the micro-LED device can be used to achieve reliable data link through POF for optical communications. It is worth noting that the data rate achieved here is based on a basic binary data amplitude modulation scheme and this data rate can be significantly increased under advanced modulation schemes, such as the PAM modulation scheme shown in the following section.

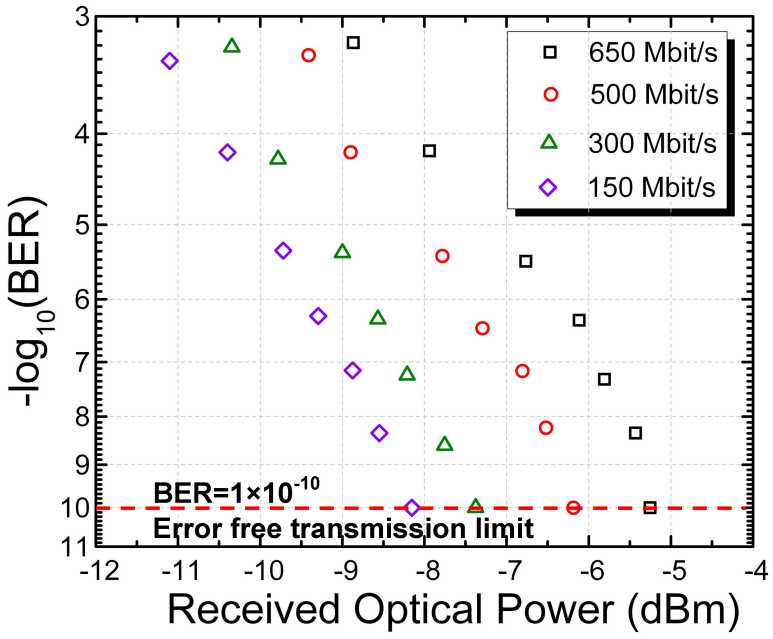

FIGURE 5.8: BERs measured from a 74 μm diameter micro-LED pixel at 150 Mbit/s, 300 Mbit/s, 450 Mbit/s and 650 Mbit/s as a function of received power at the photodetector. The bias current of the micro-LED pixel is 35 mA.

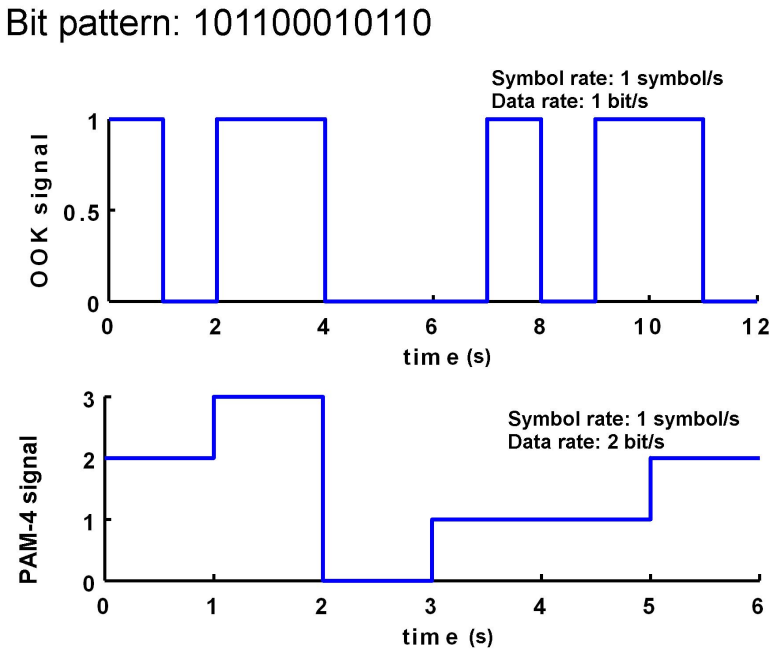

FIGURE 5.9: Waveforms of OOK signal and PAM signal with the same bit pattern.

5.1.3 Data transmission in POF under PAM-16 modulation

Schematics of the OOK and PAM-4 modulation schemes are shown in Figure 5.9. The OOK modulation scheme only uses two signal levels to represent binary data, e.g. the high level represents data '1' and the low level represents data '0'. Hence, data can only be transmitted at a rate of 1 bit per symbol. For the PAM modulation scheme, multiple signal levels are used to represent data, allowing data to be transmitted at a rate of more than one bit per symbol. The PAM modulation scheme follows the basic principle of multi-level encoding, as a symbol with X levels/amplitudes can be used to represent a binary data sequence with a length of log_2^X bits. For example, a PAM-4 modulation scheme allows data to be transmitted at a rate of 2 bits per symbol and a PAM-16 modulation scheme allows data to be transmitted at a rate of 4 bits per symbol. Therefore, under the same symbol rate, the data transmission rate based on a PAM modulation scheme is higher than that based on an OOK modulation scheme, as shown in Figure 5.9. In addition, the higher the number of signal levels for a PAM signal, the higher the number of data bits that one PAM symbol can represent. However, in order to increase the error-free data transmission rate, it is not always preferable to increase the number of PAM signal levels. For an LED device with a fixed modulation voltage swing, a PAM symbol with more levels will result in a smaller variation between the signal levels, making it difficult to differentiate individual signal level and interpret the corresponding binary data bits. If the variation between signal levels is too small to be differentiated, more bit errors will appear in the system, causing an increase of BER. In this case, we used a PAM-16 modulation scheme (one symbol represents 4 data bits) for our data transmission experiment.

The experiment was done at the Centre for Photonic Systems in Cambridge University by my colleague Dr Jonathan McKendry with the help from Dr Nikos Bamiedakis of Cambridge University and my work is to analyse and summarise the measured data. Figure 5.10 shows the schematic of the system setup. Information about the micro-LED device (transmitter), POF (transmission medium) and APD (detector) is also provided in the same figure. As shown, a field-programmable gate array (FPGA) board is used as the PRBS data generator, which generates and subsequently sends the PRBS digital data to a digital-to-analog converter (DAC). The maximum symbol rate of the DAC is 1 Gs/s, and with a PAM-16 signal the maximum data generation/transmission rate

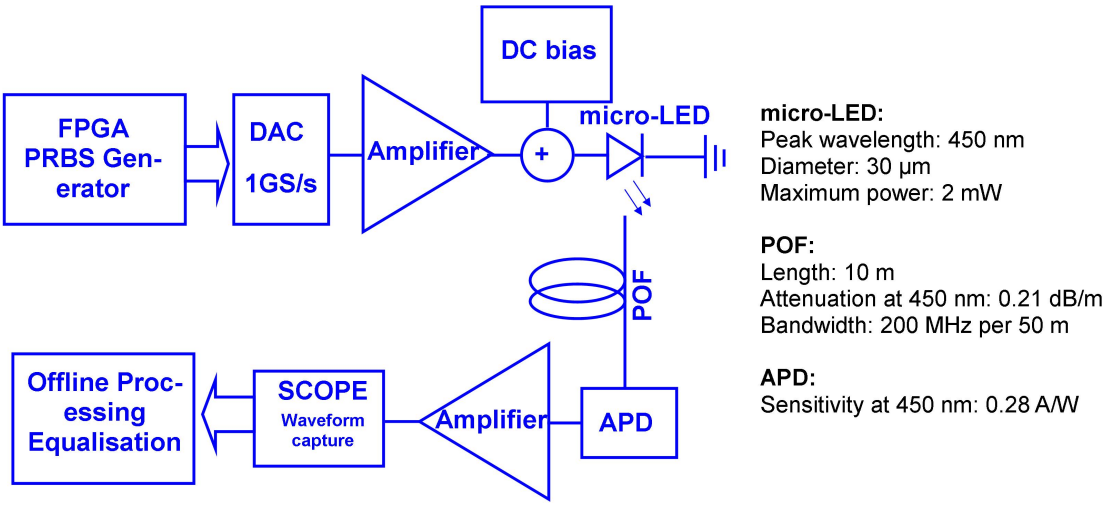

FIGURE 5.10: Schematic experimental setup of data transmission in POF under a PAM-16 modulation scheme. Information about the micro-LED, POF and APD is shown in the same figure as well.

of the DAC is 4 Gbit/s. In order to modulate the micro-LED device, the analog data signal from the DAC is first amplified and then added with a DC component to reach above the operating threshold of the micro-LED device. The modulated emission from the micro-LED device is coupled into one end of the POF, and at the other end of the POF, an APD is used as a photodetector to receive the transmitted data signal. The APD is connected to a fast oscilloscope, which captures the waveform of the received data signal. Through offline processing and equalisation, the BERs can be extracted from the captured waveforms.

Figure 5.11 shows the waveforms of the received PAM-16 signal and an ideal PAM-16 signal with a symbol rate of 1 Gs/s. The modulation signal applied to the micro-LED is made of two parts, i.e. a 5.5 V DC component and an AC component (PAM-16 signal) with a peak-to-peak voltage of 5 V. As is shown in Figure 5.11, even though severely distorted, the received PAM-16 signal still follows the shape of ideal PAM-signal at a symbol rate of 1 Gs/s (4 Gbit/s data rate), proving the superior modulation performance of the micro-LED device and the feasibility of error-free data transmission at this data rate. Since the avalanche gain of an APD is different under different applied biases, the APD bias should first be optimised to determine the best BER performance of the micro-LED-POF link. Figure 5.12 shows the 4 Gbit/s BERs of PAM-16 data transmission in 10-m POF under different APD biases. As shown, an APD bias of 80 V gives the best BER performance and a BER of 3.6×10^{-12} is achieved for PAM-16 data transmission in a 10-m POF using the micro-LED device.

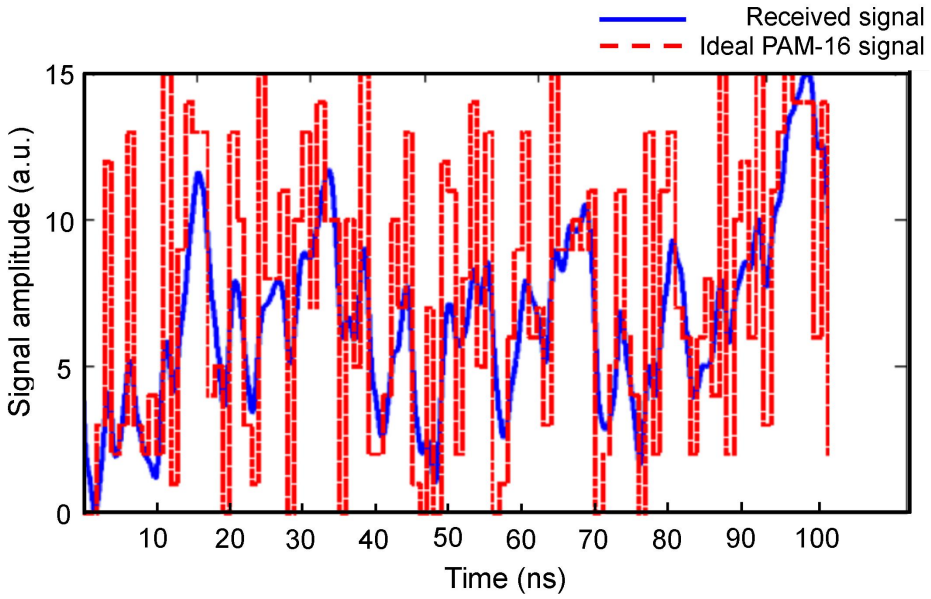

FIGURE 5.11: Waveforms of the received PAM-16 signal and ideal PAM-16 signal. The symbol rate is 1 Gs/s.

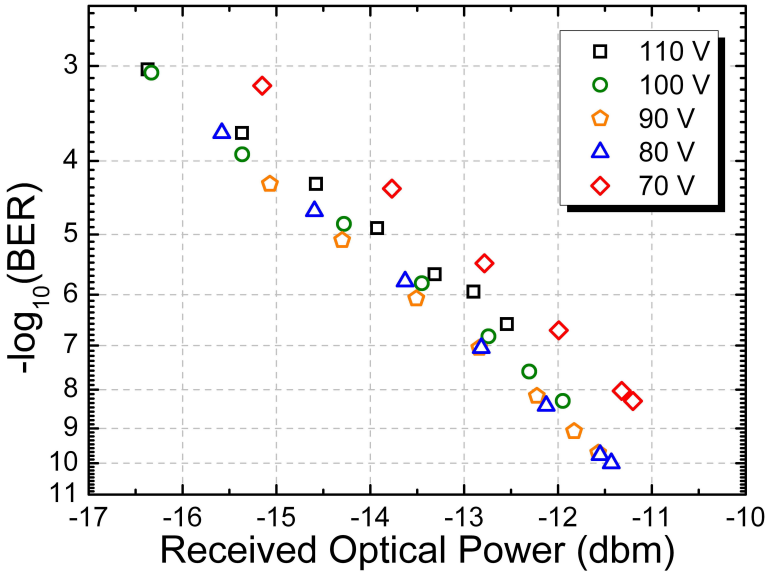

FIGURE 5.12: 4 Gbit/s PAM-16 BERs measured as a function of received optical power at the photodetector under different APD biases. A 10-m POF is used as the transmission medium.

These experimental results demonstrate that micro-LEDs can be used as powerful and efficient transmitters for high-speed optical data transmission in POF. However, it is worth mentioning that our work in this area has just started and there are still several issues needed to be addressed to improve the system performance. For example, at the current stage, data transmission in POF based on micro-LED devices is only feasible over a short distance. This is due to the large coupling loss of the output power from the micro-LED into POF. To solve this problem, our future work in this area will focus on enhancing the coupling efficiency of the output power from micro-LED into POF, providing more optical power for data transmission in the POF link. This can be achieved through integrating photonic crystal structures and specifically-designed micro-lenses on top of the micro-emitters, modifying the emission profile of micro-LED device to make it easier for the light emission from micro-LED to be coupled into POF [29, 30]. In addition, the data-transmission results reported here are only based on a single micro-LED pixel. A micro-LED array device normally contains a number of individually-addressable micro-LED pixels with each of them capable of data transmission at high rates. Therefore, if a suitable electronic driver array, such as the previously discussed CMOS driver, is integrated with a micro-LED array device and a bundle of POF is used to match the layout of the micro-LED array, it should be possible to achieve high-speed parallel data transmission at hundreds of Gbit/s in POF.

5.2 Colour-converting materials for VLC

Previous research on VLC is based on the 'bare' LED device itself. However, for the general purpose of white-light illumination, a blue-emission LED is normally combined with a yellow-emission phosphor to generate white light. In this combination, the blue LED photo-pumps the phosphor, which gives a yellow emission. By mixing the blue emission from the LED device with the down-converted yellow emission from the phosphor, white light can be generated. However, in terms of white-light communications, this approach has a shortcoming that should not be neglected. Phosphors have long phosphorescence lifetimes (μs regime) which limits the modulation bandwidth of the white light to an order of several MHz, not ideal for high-speed data transmission [150]. In order to solve this problem, several groups have reported the approach of using optical filters at the front of their receivers to remove the yellow emission from the phosphor

such that only the blue LED emission is used for data transmission [150, 151]. This method can use the fast modulation capability of LEDs, but at the cost of reducing the intensity of the received signal. Therefore, it is desirable to replace the phosphor materials with other colour-converting materials having shorter carrier lifetimes. Previous research shows that micro-LEDs can be used to photo-pump organic polymer blends and semiconductor nanocrystals for colour-conversion [134–136]. These materials have fluorescence lifetimes of the order of a few tens of nanoseconds for quantum dots (QDs), and a few nanoseconds, or less, for the polymer, whilst having high photoluminescence quantum efficiencies. Integrated with micro-LEDs, these materials offer a novel way of generating modulated white light for VLC, circumventing the restrictions imposed on the bandwidth of conventional white LEDs that use phosphors with long (μs regime) luminescent lifetimes as colour converters. Details about the modulation characteristics of QDs and polymer will be reported in the following sub-sections.

5.2.1 Frequency response model of colour-converting materials

Before measuring the frequency response of QDs and polymer, we shall first consider the frequency response model of a colour-converting material when excited by a modulated light source. To begin with, we use a sinusoidally-modulated excitation source with constant intensity to excite a fluorescent sample. In this case, the sample will emit sinusoidally-modulated light having the same frequency as the excitation source. The intensity and the phase shift of the sample emission will vary depending on the frequency of the excitation source and the fluorescent lifetime of the sample. The fluorescent lifetime of the sample can be inferred from analysing the waveform of the modulated sample emission. A mathematical model to setup a relation between the fluorescent lifetime and modulation characteristic of the sample will now be discussed [152].

The excitation source is assumed to be a sinusoidal optical signal with frequency ω, described by the equation:

$$L(t) = a + b \cdot sin\omega t \tag{5.1}$$

where a is the amplitude of the DC component, and b is the peak-to-peak amplitude of the AC signal. $m_L = b/a$ is defined as the modulation of the incident light. After being

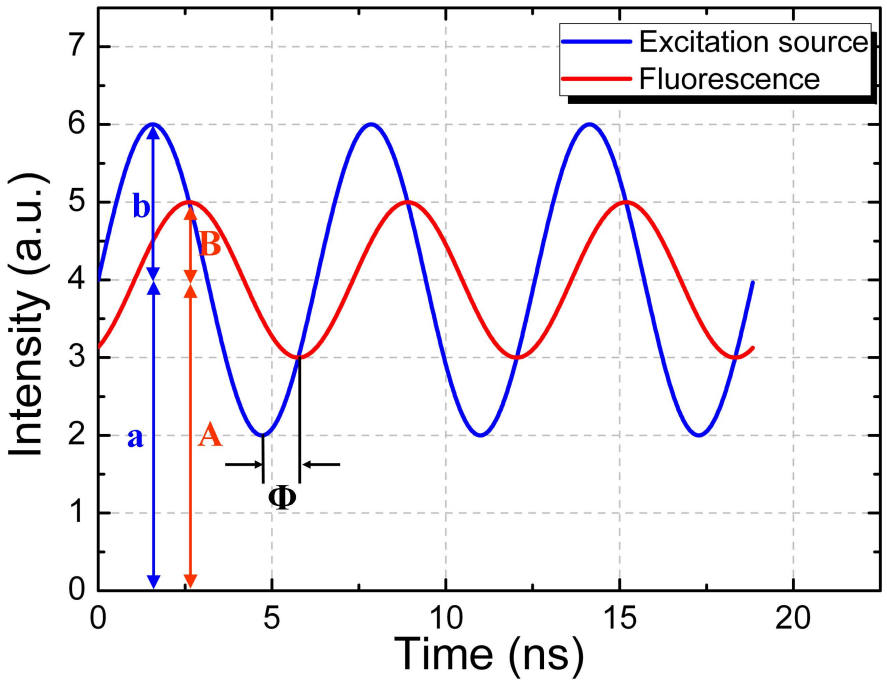

FIGURE 5.13: Illustration of the modulation and phase shift of fluorescence emission in response to the modulated optical excitation source.

excited, the fluorescence emission is forced to respond with the same frequency as the incident light, but the phase shift and modulation will be different. One can assume the fluorescence intensity of the sample at any time t to be as follows:

$$I(t) = A + B \cdot sin(\omega t - \phi) \tag{5.2}$$

where A is the amplitude of the DC component, B is the peak-to-peak amplitude of the AC component, and ϕ is the phase shift. Figure 5.13 illustrates the modulation and phase shift of a fluorescence emission $I(t)$, relative to the excitation source, $L(t)$. Equation 5.2 means the emission intensity of the fluorescent sample $I(t)$ at any time is proportional to the number of molecules in the excited state and the fluorescence intensity of the sample $I(t)$ follows the intensity of the excitation source $L(t)$. Suppose the intensity decay of the fluorescent sample following δ-function excitation is a single-exponential decay, $I(t)$ is described by:

$$I(t) = I_0 \cdot exp(-t/\tau) \tag{5.3}$$

In practise, Equation 5.3 means the fluorescence decay of the sample following short pulse excitation is a single-exponential decay. Using Equation 5.3, a differential equation can be established which describes the time-dependent excited-state population:

$$\frac{dI(t)}{dt} = -\frac{1}{\tau} \cdot I(t) + L(t) \tag{5.4}$$

The term $L(t)$ is a 'forcing function' due to the ongoing excitation from the light source, whilst the remaining term describes the transient response of the fluorescent sample. If $L(t)$ and $I(t)$ in Equation 5.4 are substituted by Equation 5.1 and Equation 5.2, then the resulting equation will change into a form describing the fluorescence intensity at any time t. Therefore, Equation 5.4 is valid when the fluorescence decay of the sample following short pulse excitation is a single-exponential decay. In addition, there should be a light source providing stable ongoing photo-excitation to the sample. By expanding the resulting equation, and equating the terms in $sin\omega t$, $cos\omega t$ and the constant terms, we can obtain the relationship between the modulation frequency ω, fluorescent lifetime τ, phase shift ϕ and the amplitude demodulation M in response to the excitation source:

$$tan(\phi) = \omega \cdot \tau \tag{5.5}$$

$$M(\omega) = \frac{B/A}{b/a} = \frac{1}{\sqrt{1 + \omega^2\tau^2}} \tag{5.6}$$

Equation 5.6 shows the frequency response of the fluorescent sample with a fluorescent lifetime τ. In a frequency domain lifetime measurement, the frequency response $M(\omega)$ would be measured and a fit would be performed to determine the value of fluorescent lifetime τ according to Equation 5.6. This model is widely used to fit the frequency responses of QDs and polymer reported in this thesis and their fluorescent lifetimes are inferred from the fitting curves accordingly. However, many light-emitting materials do not have a single-exponential decay following δ-function excitation. Therefore, the model proposed here cannot be used to fit the frequency responses of these materials. Normally, multi-exponential functions can be used to describe the radiative decays of these light-emitting materials under δ-function excitation. In this case, a new model regarding the multi-exponential decays has been developed to describe the frequency responses of

these light-emitting materials. Details of the model describing the frequency responses of light-emitting materials with multi-exponential decays are reported in [152].

It is worth noting that the model mentioned above describes the frequency response of a fluorescent sample when it is photo-pumped by an optical excitation source with a fixed intensity. For a micro-LED device under high-speed modulation, its intensity varies depending on the modulation frequency and a reduced intensity is expected under high modulation frequency. For example, if the excitation source intensity is reduced by a factor of 0.7 at a given frequency, and this intensity is reduced by a factor of 0.5 by the intrinsic frequency response of the fluorescent sample, then the frequency response of the overall intensity is reduced by a factor of $0.7\times0.5=0.35$. In this case, the frequency response of the overall intensity, $H_{overall}(\omega)$, should be the product of the frequency response of excitation source, $H_{excitation}(\omega)$, and the intrinsic frequency response of the fluorescent sample, $H_{fluorophore}(\omega)$:

$$H_{overall}(\omega) = H_{excitation}(\omega) \cdot H_{fluorophore}(\omega) \tag{5.7}$$

The calculation in Equation 5.7 is more conveniently performed when the frequency responses are expressed in decibels (dB), whereby the frequency response of the overall intensity, $M_{overall}(\omega)$, should be the sum of the frequency response of excitation source, $M_{excitation}(\omega)$, and the intrinsic frequency response of the fluorescent sample, $M_{fluorophore}(\omega)$:

$$M_{overall}(\omega) = M_{excitation}(\omega) + M_{fluorophore}(\omega) \tag{5.8}$$

Based on the model mentioned above, the intrinsic frequency response of a colour-converting material excited by a micro-LED can be analysed. The frequency response of the overall intensity, $M_{overall}(\omega)$, and the frequency response of excitation source, $M_{excitation}(\omega)$, can be measured directly from a network analyser while the intrinsic frequency response of the colour-converting material, $M_{fluorophore}(\omega)$, can be calculated accordingly from subtracting $M_{excitation}(\omega)$ from $M_{overall}(\omega)$. In particular, by fitting the intrinsic frequency response of the colour-converting material according to Equation 5.6, the lifetime of the fluorescent sample can be estimated. In the following section, we

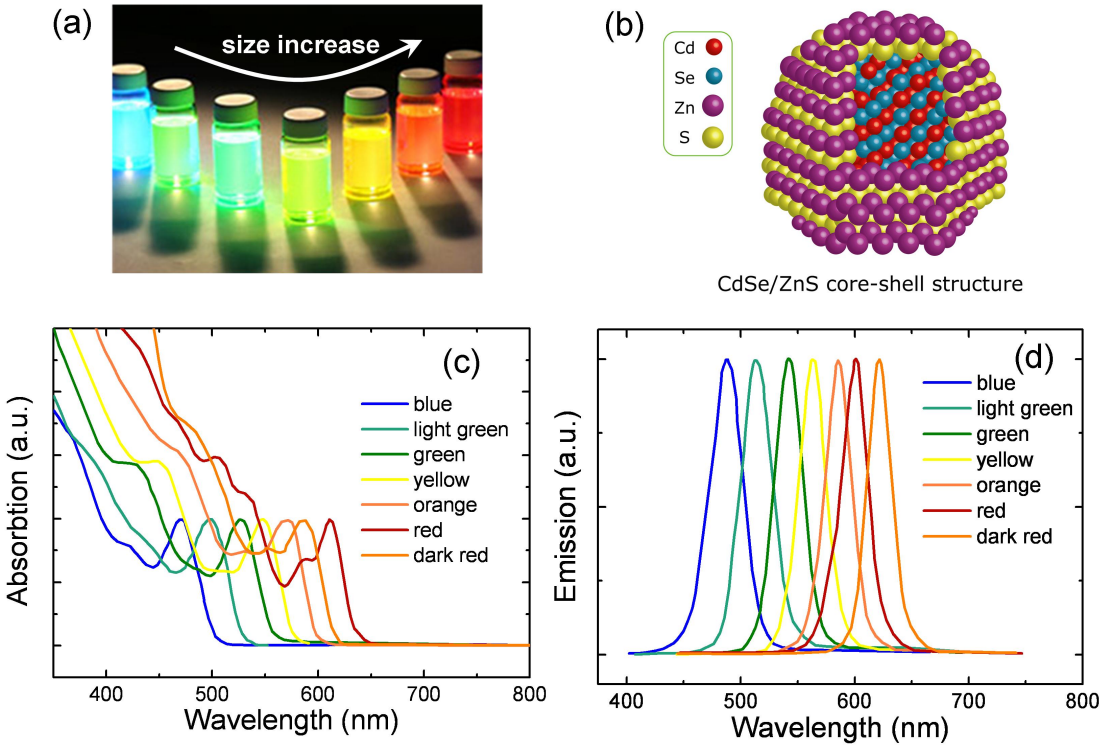

FIGURE 5.14: (a) Fluorescence images (in toluene solution), (b) schematic structure, (c) absorption spectra, and (d) emission spectra of CdSe/ZnS Core-Shell QDs with different sizes [153].

will use this method to analyse the data obtained from the experiments and characterise the modulation performance of different colour-converting materials.

5.2.2 Modulation characteristics of colloidal semiconductor quantum dots and light-emitting polymer

Background

In this sub-section, the background of material systems used in our work is first presented. So far, our work mainly focuses on inorganic semiconductor QDs, such as core-shell CdSe/ZnS colloidal quantum dots (CQDs) (Figure 5.14), and π-conjugated organic materials, such as green poly[2,5-bis(2',5'-bis(2"-ethylhexyloxy)phenyl)-p-phenylenevinylene] (BBEHP-PPV) (Figure 5.15). These kinds of materials demonstrate unique optoelectronic properties, such as high photoluminescence quantum efficiencies and short fluorescent lifetimes, suggesting that they are promising materials for colour-converting VLC. The core-shell CdSe/ZnS CQDs were purchased from Evident Technologies, Inc. The

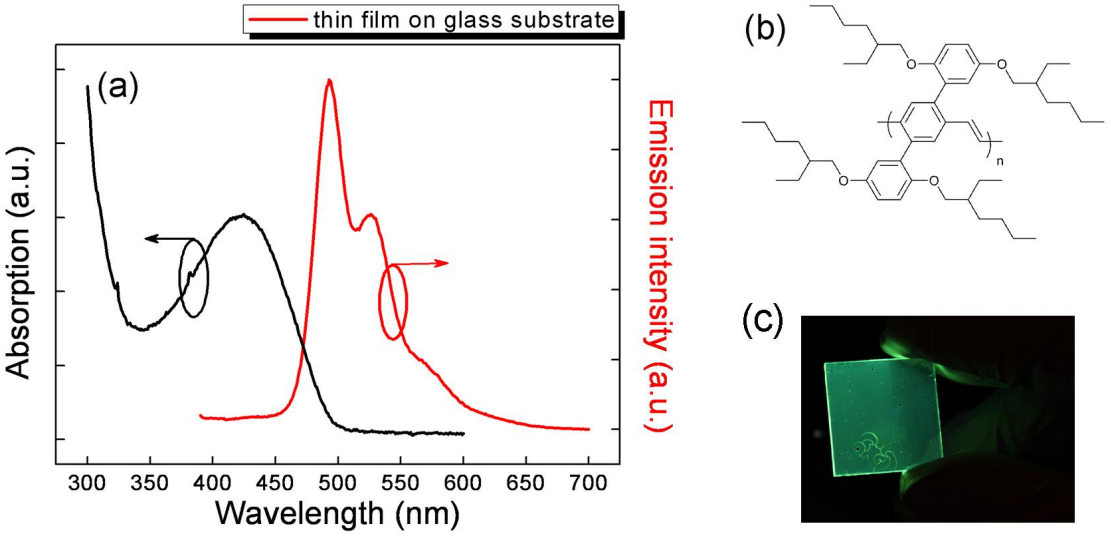

FIGURE 5.15: (a) Absorption and photoluminescence spectra of BBEHP-PPV on glass substrate, spin-coated from toluene solution (20 mg/mL); (b) chemical structure of BBEHP-PPV; (c) image of a BBEHP-PPV sample on glass substrate illuminated by UV light.

BBEHP-PPV was synthesised by Prof. Peter Skabara's research group in the Department of Pure and Applied Chemistry, University of Strathclyde.

For organic light emitters with basic vibronic structures, there are two electron states, known as the ground state S_0 and the excitation state S_1, where "S" describes the spin configuration and "0/1" describes the orbital configuration. In ground state S_0 and the excitation state S_1, there are discrete vibronic energy levels m_{S0} and n_{S1}, where m,n=0,1,2 ... Electrons in m_{S0} vibronic energy level can be excited to n_{S1} vibronic energy level via the absorption of photons. In addition, electrons in the n_{S1} vibronic energy level can relax to m_{S0} vibronic energy level via the emission of photons. However, the conformational potential minimum is different for the S_0 and S_1 state. Therefore, the relaxation a electron state will always be accompanied by a structural relaxation of the molecule. This results in the redshift of the emission spectrum compared to the absorption spectrum, known as the "Stokes-shift" [154]. Figure 5.15 (a) shows the absorption and emission spectra of BBEHP-PPV. There is a large Stokes-shift of 100 nm between the emission and absorption which is typical for organic light emitters [155]. Therefore, in Figure 5.15 (a), the emission peaks in the PL spectrum can be regarded as the counterparts of absorption peaks due to the Stokes-shift. In addition, different absorption and emission peaks correspond to different transitions between vibronic energy levels and their intensities are determined by the Franck-Condon principle, i.e. a

CQD nanocomposite sample	wavelength	volume ratio	Power conversion efficiency
CdSe/ZnS CQD (size: 7.5 nm)	535 nm	1.3%	8.5%
CdSe/ZnS CQD (size: 8.0 nm)	573 nm	1.3%	14%
CdSe/ZnS CQD (size: 8.2 nm)	600 nm	1.1%	33%
CdSe/ZnS CQD (size: 8.7 nm)	624 nm	0.8%	18%
CdSe/ZnS CQD (mixture)	mixture	1.3%	8%

TABLE 5.1: CQD-to-polyimide volume ratio and power conversion efficiency for all samples.

change from one vibrational energy level to another will be more likely to happen if the two vibrational wave functions overlap more significantly [154, 155].

CQD nanocomposite samples

The CQDs samples, prepared by Dr. Yujie Chen, Dr. Benoit Guilhabert and Dr. Nicolas Laurand, were initially dispersed in toluene solution, as provided by the manufacturer. CQDs with mean diameters of 7.5 nm, 8 nm, 8.2 nm and 8.7 nm were used for the preparation of composite samples with peak emission wavelength at 535 nm, 573 nm, 600 nm and 624 nm, respectively. The polymer matrix used to host the CQD nanocomposite samples was Corin-XLS from Mantech Co. This material is a fluorinated polyimide that offers high atomic oxygen durability, and importantly, is transparent in the visible spectrum. In addition, this polyimide is compatible with organic solvents such as toluene and Tetrahydrofuran (THF), allowing it to be processed by techniques such as spray-coating and ink-jet printing. The polyimide matrix material Corin-XLS was dissolved in THF solution at a ratio of 30 mg/mL, as provided by the manufacturer. The CQDs were first extracted from the toluene solution in a powder format by evaporating the toluene solvent. Then, the CQD powder samples were incorporated into Corin-XLS/THF solution at a ratio of 50 mg of CQDs per mL of Corin-XLS/THF. After preparing the solution samples of CQD nanocomposite, they were drop-cast onto 150 μm thick glass substrates and heated to 60 °C for 1 minute to accelerate the evaporation of THF. Once the THF is evaporated and the residue of each sample is cured on the glass substrate, the preparation of colour-converting CQD nanocomposite samples is complete. Given in Table 5.1 are the calculated CQD-to-polyimide volume ratio and the power conversion efficiency of each nanocomposite sample. Details of the method to calculate CQD-to-polyimide volume ratio and measure the power conversion efficiency of a nanocomposite sample are reported in [156].

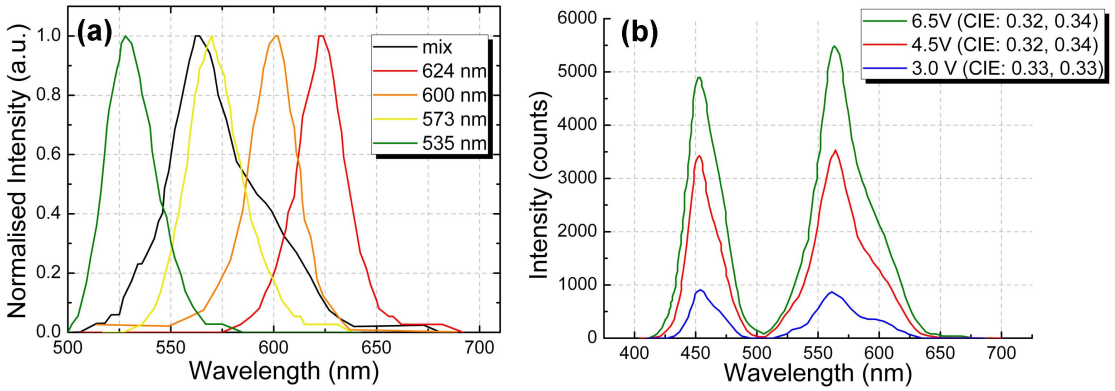

FIGURE 5.16: (a) Normalised PL spectra of different CQD nanocomposites; (b) PL spectra of white-light CQD nanocomposite photo-pumped by a micro-LED under different applied biases. The CIE coordinates, around (0.32, 0.34), are stable across different LED driving conditions.

Figure 5.16 (a) shows the normalised photoluminescence (PL) emission spectra of different nanocomposite samples. For white-light communications, it is desirable to have a nanocomposite sample capable of emitting white light once it is photo-pumped by an excitation source. In this case, a mixed nanocompsite with broad PL spectra was also fabricated by mixing 535, 573, 600 and 624 nm CQDs at respective volume percentages of 83.3%, 14%, 1.7% and 1%. Figure 5.16 (b) shows the emission spectra of the white-light composite photo-pumped by a 450 nm micro-disk LED pixel with a pixel diameter of 84 μm. For these measurements, a 300 μm thick layer of mixed nanocomposites on a glass substrate was placed directly on top of the LED pixel and the spectra were recorded at different LED driving voltages. As shown in Figure 5.16 (b), the spectral contribution around 450 nm is from non-absorbed LED light while the longer-wavelength emission is from the down-converted nanocomposite. The corresponding chromatic coordinates are around (0.32, 0.34) and do not vary significantly under different LED driving conditions, proving that the mixed nanocomposites can be used as a stable colour-converter to generate white light.

In order to study the modulation characteristics of CQD nanocomposites, an 84 μm diameter LED pixel from an 8×8 micro-LED array with a peak emission wavelength of 450 nm was used as the optical excitation source. Details about this micro-LED device have been presented in chapter 2, section 2.2. A DC voltage of 6.3 V was first combined with a small-signal chirped sine wave (peak-to-peal voltage is 1.2 V) from a network analyser (Hewlett Packard 8753ES), and then applied to the micro-LED pixel. The emission from the micro-LED pixel was imaged onto the CQD nanocomposite sample and the

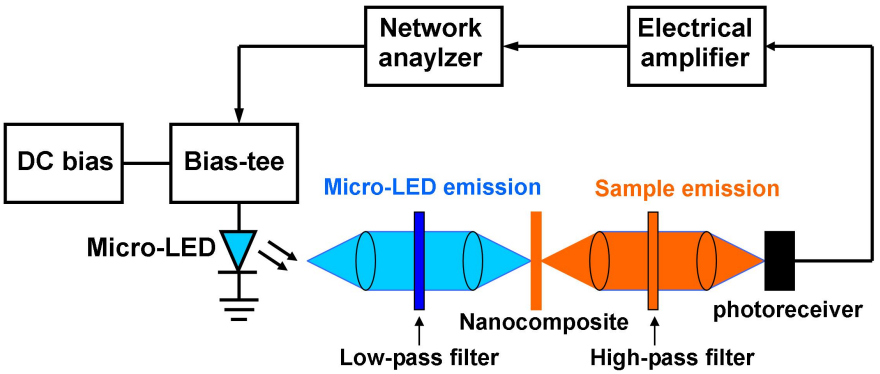

FIGURE 5.17: Schematic setup used to measure the frequency responses of CQD nanocomposite samples.

down-converted light from the sample was projected onto a photodetector (Newport 818-BB-21A, 75 kHz-1.2 GHz bandwidth). The received optical signal was first amplified by an external amplifier (HP8477D, dual stage 50 dB electrical amplifier) and subsequently returned to the input port of the network analyser for measuring the frequency response of the sample under test. Figure 5.17 shows the schematic setup used to measure the frequency responses of the nanocomposites. As shown, a 500 nm wavelength low-pass filter (Thor Labs FES0500) is placed in between the micro-LED pixel and the CQD nanocomposite and a 515 nm wavelength high-pass filter (Thor Labs FGL515) is placed in between the CQD nanocomposite and the photodetector. The low-pass filter is used to remove the longer emission from the micro-LED pixel and the high-pass filter is used to remove the unabsorbed shorter emission from the micro-LED pixel. The extinction of LED excitation light is above 20 dB using this setup and the optical power of unfiltered LED light is much lower compared with that of the sample at the photodetector. Therefore, the photodetector mostly receives the modulated emission from the CQD nanocomposites. A right angled geometry of experimental setup was not used as the current setup can collect higher optical power from the sample for frequency response measurement. After measuring the frequency responses of the nanocomposite samples, the experimental setup was modified to measure the frequency response of the micro-LED pixel and this frequency response was subsequently subtracted from the measured frequency responses of CQD nanocomposites to extract the intrinsic characteristics of the tested nanocomposite samples.

Figure 5.18 shows the measured frequency responses of different nanocomposite samples and the results are summarised in Table 5.2. The measured data was fitted according to Equation 5.6 to determine the effective carrier lifetime τ. The fitted -3 dB frequency

CQD nanocomposite sample	wavelength	-3 dB frequency (MHz)	Lifetime (ns)
CdSe/ZnS CQD (size: 7.5 nm)	535 nm	23.5	11.7
CdSe/ZnS CQD (size: 8 nm)	573 nm	25.8	10.7
CdSe/ZnS CQD (size: 8.2 nm)	600 nm	10.8	25.5
CdSe/ZnS CQD (size: 8.7 nm)	624 nm	12.4	22.2
CdSe/ZnS CQD (mixture)	mixture	19.6	14.1

TABLE 5.2: Summary of fitted -3 dB frequencies and lifetimes of the CQD nanocomposite samples.

of each sample can be obtained from the corresponding fitting curve as well. It is worth noting that the ω is Equation 5.6 can be substituted by term $2\pi f$. In this case, Equation 5.6 will be the same as Equation 2.1 in chapter 2 and the fitted -3 dB frequency can be linked with the fitted carrier lifetime τ in a more straightforward manner using Equation 2.2, i.e. $f_{-3dB} = \frac{\sqrt{3}}{2\pi\tau}$. Details of the relation between -3 dB frequency and carrier lifetime τ can be found in chapter 2, section 2.3. For a CQD nanocomposite sample, its PL decay may not be truly single-exponential and the precise measurement of its frequency response becomes very difficult when it is modulated in high-frequency regime with low output power intensity. Therefore, the experimental data of the frequency responses of CQD nanocomposite samples are more structured than the fitting curves [152]. However, the fitting curve can reasonably match up with the measured data and the effective, or mean PL lifetime that results from the recombination (radiative and non-radiative) processes is still meaningful for investigating the modulation response of the converted light from CQD samples. As shown in Figure 5.18, the frequency responses varies with CQD wavelength. This is due to the dependence of the spontaneous emission radiative rate on the CQD emission wavelength. The radiative decay lifetime of an ideal two-level exciton depends linearly on the wavelength, i.e. it is inversely proportional to the CQD size. In practise, the population distribution of excitons between bright and dark states of CdSe CQDs can modify this dependence from linear to supralinear [157]. In any case, bigger CQD, which emits at lower frequency (longer wavelength), are expected to have a longer radiative lifetime [156]. Therefore, CQDs with different wavelengths have different frequency responses. It is also worth noting that the modulation bandwidth of the white-light sample reaches approximately 20 MHz, which represents an order of magnitude increase when compared with the phosphor colour converters typically used in white LEDs. Such modulation characteristic indicates that these CQD samples are promising colour converters to substitute for phosphors, allowing white-light emission with higher bandwidth for VLC.

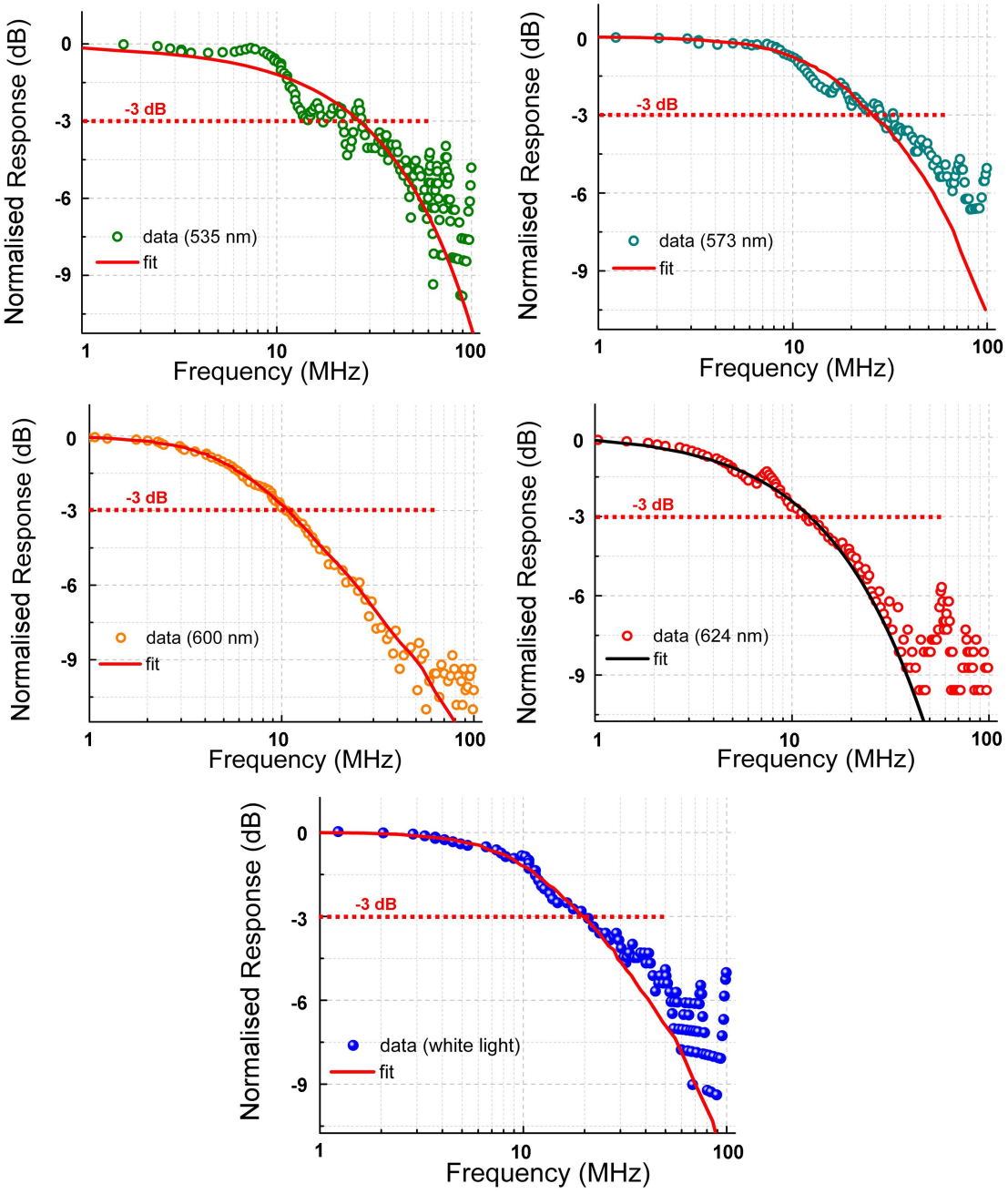

FIGURE 5.18: Measured and fitted frequency responses of different CQD nanocomposite samples at different wavelengths.

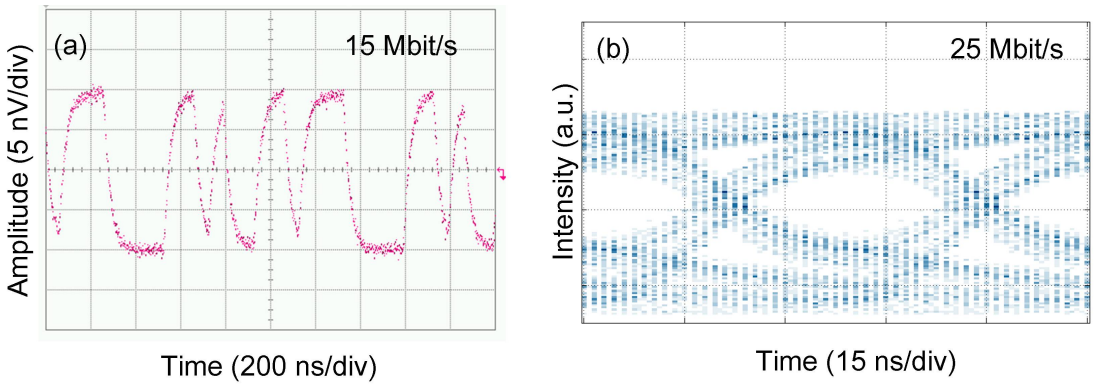

FIGURE 5.19: (a) Signal waveform of the 600 nm CQD nanocomposite sample when it is optically modulated at 15 Mbit/s; (b) eye diagram of the white-light nanocomposite sample when it is optically modulated at 25 Mbit/s. In both measurements, the LED light is filtered out so the results are based on the emission from the colour-converters only.

In this work, the quenching effect of the intensity of CQDs is mainly caused by the limitation of their carrier lifetimes as the CQDs can not respond fast enough to follow the modulation signal and the electron states are trapped [156]. For QD doped fibres, which are relevant for the research performed here, the reasons that cause the quenching effects of QDs are difficult to be clarified. Possible reasons would be the structures of QDs in the fibre are not suitable for electrons to recombine radiatively due to the deformation of QD structure, non-radiative energy transfer to defects, clustering effect, etc. Further research is needed to clarify this issue.

Proof-of-concept data transmissions were also tested with a 450 nm 84 μm diameter micro-LED pixel and different nanocomposite samples. The setup is identical to the setup shown in Figure 5.17, but the network analyser is substituted by a data pattern generator (Anritsu Pulse Pattern Generator, MP1763C). As shown in Figure 5.19 (a), a clear signal waveform of the transmitted data was achieved at a bit rate of 15 Mbit/s for the 600 nm CQD nanocomposite sample. For the white-light nanocomposite sample, which is of particular interest for the purpose of generating white light, a clear open eye diagram was observed at a bit rate of 25 Mbit/s, as shown in Figure 5.19 (b).

Light-emitting polymer

It has been demonstrated that CQDs have bandwidths from 10 MHz to 30 MHz, which is an order of magnitude higher than that of conventional phosphor materials. However, due to the limitation of fluorescent lifetimes, the modulation bandwidths of CQDs still remain an order of magnitude lower than that of micro-LED devices, and are therefore

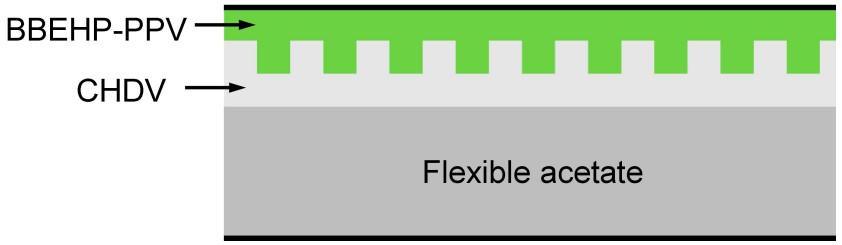

FIGURE 5.20: Cross-sectional schematic of a BBEHP-PPV sample with a PhC structure.

not ideal to realise high-speed data transmission. Therefore, it is desirable to find a colour-converter with a modulation bandwidth similar to or higher than the bandwidths of the micro-LED devices. Light-emitting polymers (LEPs) have fluorescent lifetimes typically of the order of a few nanoseconds or less, indicating that they have modulation bandwidths of up to several hundreds of MHz. Like CQDs, LEPs have the advantage of being easily processable, highly luminescent and suitable for being integrated with LEDs for colour-conversion [158]. In the following section, we will show the superior modulation characteristics of BBEHP-PPV, a type of LEP, and demonstrate its potential for being used as a colour-converter for the application of high-speed data transmission.

The optical properties of BBEHP-PPV have been systematically investigated elsewhere and the applications of BBEHP-PPV for organic lasing and explosives sensing have also been reported [87, 159–161]. As shown in Figure 5.15 (a), BBEHP-PPV absorbs light efficiently below 470 nm and is therefore suitable for integration onto highly efficient blue InGaN-based micro-LEDs for the purpose of colour-conversion. More importantly, previous fluorescence decay measurement suggests that BBEHP-PPV has a fluorescence lifetime of 0.62 ns [159], which is a particular advantage for high-frequency modulation. The BBEHP-PPV sample used here is spin-coated from a 20 mg/ml solution in toluene onto a structured film of 1,4-cyclohexyldimethanol divinyl ether (CHDV) on a flexible acetate substrate, with an estimated sample thickness of 150 nm. CHDV offers high transmittance in the visible spectrum and does not absorb much of the LED pump light. The photonic crystal (PhC) structure in the CHDV film was created by a simple soft-lithography method that has been described in detail previously [162]. Figure 5.20 shows a schematic of a BBEHP-PPV sample with a PhC structure. The PhC structure modifies the light emission profile of the polymer-integrated micro-LED device and subsequently increases the external conversion efficiency of the colour-converter. For the BBEHP-PPV sample reported here, an enhancement of the conversion efficiency from 15% to

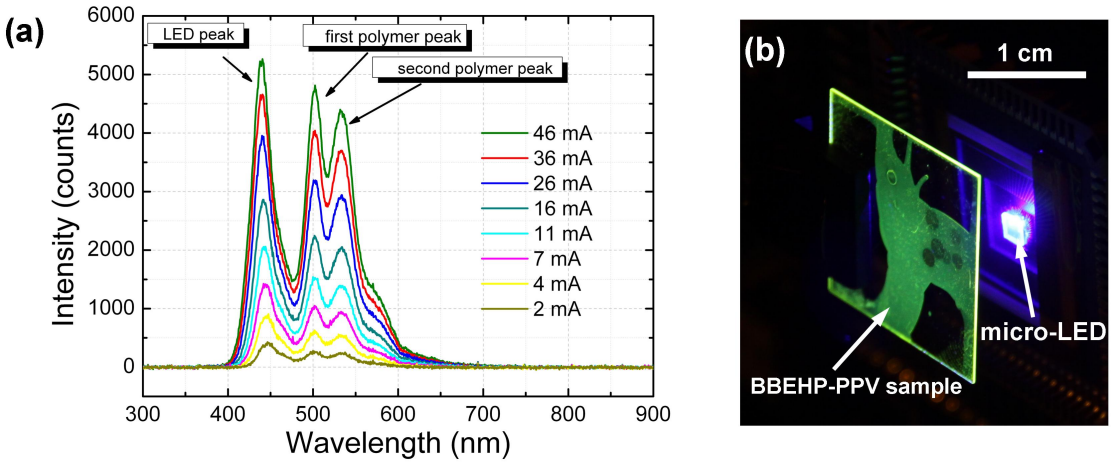

FIGURE 5.21: (a) Emission Spectra of a BBEHP-PPV sample photo-pumped by an 84 μm CMOS/micro-LED pixel at different DC currents; (b) photograph of the green emission from BBEHP-PPV sample photo-pumped by an 84 μm CMOS-controlled micro-LED pixel.

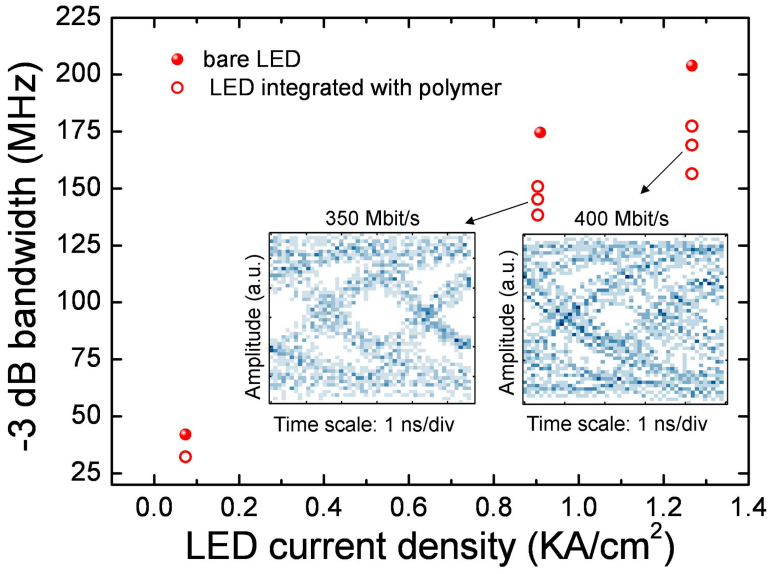

FIGURE 5.22: Optical -3 dB bandwidths of a BBEHP-PPV sample measured at different LED current densities. The insets show corresponding eye diagrams at 350 Mbit/s (0.9 kA/cm^2) and 450 Mbit/s (1.26 kA/cm^2), respectively [163].

20% due to the PhC pattern compared to an unpatterned sample is observed [163]. The spectrum and image of an unpatterned BBEHP-PPV sample photo-pumped by a 450 nm micro-LED device are shown in Figure 5.21 (a) and (b), respectively. As shown, BBEHP-PPV has broad photoluminescence spectra ranging from 460 nm to 600 nm with dominant emission peaks at around 500 nm and 530 nm. The dark spots observed on the BBEHP-PPV sample in Figure 5.21 (b) are due to the photo-degradation of the material.

The frequency response of BBEHP-PPV was measured by a network analyser whose output was used to modulate the micro-LED intensity and input was connected to a photodetector. An 84 μm diameter micro-LED pixel with a peak emission wavelength of 450 nm was used to optically modulate the BBEHP-PPV sample with a PhC pattern. The system setup is the same as the setup for measuring the frequency responses of CQDs with only the sample changed from CQD nanocomposites to BBEHP-PPV (Figure 5.17). Just as for measuring the frequency responses of the CQD samples, the LED emission was filtered out to ensure that only the response of the colour-converted light from the BBEHP-PPV sample was measured. Modulation bandwidths of BBEHP-PPV sample under different LED current densities are plotted in Figure 5.22. As shown, at an LED current density of 1.26 kA/cm^2, an optical -3 dB bandwidth of 168 MHz was achieved for the BBEHP-PPV sample. Considering the short lifetime of BBEHP-PPV (0.62 ns), this value is mainly limited by the inorganic blue LED bandwidth which under these conditions is around 200 MHz. Eye diagrams at 350 Mbit/s and 400 Mbit/s are also plotted in Figure 5.22, and the open eye diagrams suggest that data transmission at several hundred Mbit/s is feasible using these hybrid devices. These results demonstrate that LEPs with very short fluorescent lifetimes can be used to colour-convert the emission from micro-LEDs without reducing the bandwidth very much. For the purpose of generating white light, LEP blends with fluorescent lifetimes of the order of 1 ns to 2 ns have been achieved [158] and the data transmission results based on such a high-bandwidth white-emitting LEP-integrated micro-LED device have just been reported [164].

5.3 Summary

In this chapter, experimental results of using micro-LEDs for VLC in POF were first presented. POF is an interesting data transmission medium attracting a lot of interest recently due to its wide applications in short-distance communications, such as in automotive and avionic environments. The attenuation of standard PMMA-based POF is relatively small in the blue-green regime, making InGaN semiconductor devices ideal transmitters for POF-based communication systems. In section 5.1, high-bandwidth efficient GaN micro-LEDs are used as transmitters for data transmission in POF. Under binary data amplitude modulation, error-free data transmission, defined as a BER of less

than 1×10^{-10}, is achieved at a data rate of up to 650 Mbit/s in a 10-m POF based on a single 74 μm diameter micro-LED pixel. Under a PAM-16 modulation scheme, error-free data transmission rate of up to 4 Gbit/s is achieved in a 10-m POF using a 30 μm diameter pixel as transmitter and an APD as receiver. These results establish a baseline demonstration of data transmission of micro-LED devices in POF. Our future work in this area will focus on improving the coupling efficiency of the optical setup and fully utilising the 'array' nature of micro-LED device for parallel data transmission in POF. In section 5.2, colour-converters with short fluorescent lifetimes are used to integrate onto micro-LEDs to realise hybrid colour-converting optical data links. This approach aims to find alternatives to substitute conventional phosphors which are mainly used as colour-converters for white LEDs. Conventional phosphors have long (μs regime) luminescent lifetimes, which restrict the modulation bandwidth of white LEDs. In this work, CQD nanocomposites and BBEHP-PPV LEP are used as the colour-converters to be integrated with micro-LEDs for the colour-conversion and modulation test. Depending on the fluorescent lifetimes, the modulation bandwidths of CQD samples range from 10 MHz to 30 MHz while the modulation bandwidth of BBEHP-PPV reaches above 100 MHz. These modulation results demonstrate that both CQDs and BBEHP-PPV can be used as efficient colour-converters to generate modulated light for VLC, circumventing the restrictions imposed on the bandwidth of white LEDs that use conventional phosphors with long luminescent lifetimes.

Chapter 6

Capacitance study on InGaN-based micro-pixellated light-emitting diodes

Capacitance analysis is a very important method to study semiconductor devices as the capacitance of those devices not only influences their performance for practical applications like optical communications, but also provides useful insights into the device physics. In this chapter, following from previous work on micro-pixellated light-emitting diodes (micro-LEDs), we report a detailed study on size-dependent capacitance, and especially the negative capacitance (NC), in InGaN-based micro-LEDs. Firstly, the motivation to study the size-dependent capacitance of micro-LED devices is presented in section 6.1. In section 6.2, the physics of depletion capacitance, diffusion capacitance and NC of LED devices are discussed in detail. After clarifying the physics of capacitance in LED devices, especially the NC effect, a size-dependent capacitance study on micro-LED clusters under reverse and large forward bias is presented in section 6.3. Similar to conventional broad-area LEDs, micro-LEDs show NC under large forward bias. Additionally, in the conventional depletion and diffusion capacitance regimes, a good linear relationship of capacitance with device size is observed. However, the NC under high forward bias shows slight deviation from above-mentioned linear relationship with device size. This behaviour can be understood if the effects of current density and junction temperature on NC are considered. In order to further investigate the effect of

sidewall defects caused by dry etching during device fabrication, in section 6.4, the NCs of two reference broad-area LEDs were measured and compared with those of micro-LED clusters with the same total size. Finally, a summary of the capacitance study on micro-LED device is given in section 6.5.

6.1 Motivation for capacitance study in micro-LEDs

According to Shockley's model and conventional p-n junction theory [165], the capacitance of a semiconductor device containing p-n junctions is dominated by depletion capacitance under reverse bias and diffusion capacitance under forward bias. However, abnormal negative capacitance (NC) has been observed repeatedly in alternating current (AC) impedance measurements of many semiconductor devices such as light-emitting diodes (LEDs), laser diodes and quantum well infrared photodetectors [166–174]. The capacitance of a semiconductor device is usually extracted from the imaginary part of the complex impedance under direct current (DC) biased AC impedance measurements. When the transient current caused by the small modulation signal lags behind the modulation voltage, capacitance with negative values is obtained from the device under test [166]. NC has the same phase relationship between small-modulation-signal voltage and transient current as a positive inductance, however the interpretation of NC as conventional inductance or conventional capacitance with negative values is not physically meaningful [166]. Until now, the general physical explanation of the NC effect in semiconductor devices is still under debate [166, 168, 169, 173–175].

Thus far, all LEDs used for NC studies have focused on conventional broad-area LED devices, which are mainly developed for solid-state lighting (SSL) [22], and have typical emission areas ranging from 300×300 μm^2 to 1 mm^2. However, capacitances of micro-pixellated LEDs (micro-LEDs), which have typical sizes of several tens of microns or less, have not been investigated before. Due to a reduction in device self-heating and current crowding, micro-LEDs are able to be driven at much higher current densities (in excess of 10 kA/cm^2), which allows not only the study of LED characteristics in regimes not accessible to conventional broad-area LEDs [88], but also novel LED properties and applications [35, 86, 176, 177]. As the NC effect becomes more significant under high injection current density, it is important to investigate the capacitance characteristics of micro-LED devices under large forward bias with high injection current density. In

addition, conventional depletion capacitance and diffusion capacitance of LEDs scale linearly with the device size but the relation between NC and LED size has not been reported before. Since the change of LED size can significantly affect its performance in many aspects, such as the modulation bandwidth [64], the size effect on LED NC needs to be investigated in detail.

For the above reasons, in this chapter we present a systematic study of the size-dependent capacitance in InGaN-based micro-LEDs under reverse and large forward biases, based on AC impedance measurements. Details of the experimental results will be presented in section 6.3 and section 6.4 and these results shed light on the mechanisms underlying the NC effect.

6.2 Background of capacitance in LED device

Before investigating the capacitance of micro-LED device and its relationship with device size, it is important to clarify the physics of capacitance in LED devices. In general, the capacitance of an LED can be separated into three parts, i.e. depletion capacitance, diffusion capacitance and NC. The depletion capacitance and diffusion capacitance of LED device can be explained via conventional p-n junction theory and linked with charge accumulation and energy storage, similar to conventional electrostatic capacitance [165]. However, the NC of LED device is essentially different from electrostatic capacitance and cannot be explained via conventional p-n junction theory. More details about the capacitance of LEDs will be shown in the following sub-sections.

6.2.1 Depletion capacitance of LED

Under reverse bias, the capacitance of an LED device is dominated by the depletion capacitance of the p-n junction. According to the depletion approximation [165], in a p-n junction, un-neutralised impurity ions only exist in the region where p-type material interfaces n-type material. This region is known as the depletion region or barrier region of the p-n junction, as in this region, the carriers, i.e. electrons and holes, are depleted due to the diffusion-induced recombination and only the un-neutralised ions are left in this region. The un-neutralised ions form a built-in electric field which provides a barrier to the carriers from p-type region and n-type region entering into the depletion region,

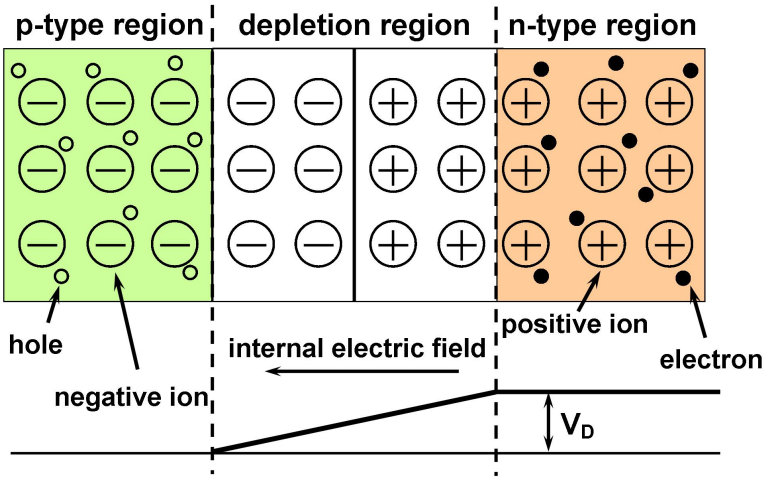

FIGURE 6.1: Schematic model of a p-n junction in dynamic equilibrium. V_D is the voltage of built-in electric field.

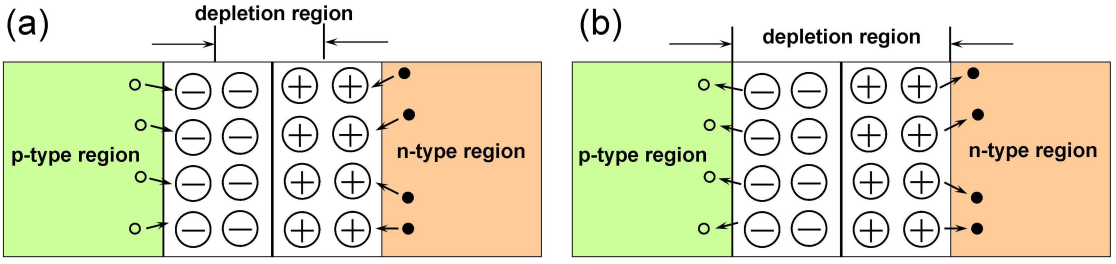

FIGURE 6.2: Schematic diagram of the depletion capacitance in (a) charging process and (b) discharging process. The carriers move either into or out from the depletion region according to the external applied bias, resulting in the change of the width of depletion region in the p-n junction.

thus the whole p-n junction reaches dynamic equilibrium. Figure 6.1 shows a schematic drawing of a typical p-n junction in dynamic equilibrium.

Under external forward bias, the built-in electric field of depletion region is weakened and the carriers from the edge between n-type/p-type region and depletion region will drift into the depletion region. These carriers will be captured by the positive and negative ions, which results in a narrower depletion region and can be regarded as a charging process for the depletion region. Whilst under external reverse bias, the carriers from the edge between the n-type/p-type region and depletion region will drift away due to the combined effect of built-in electric field and applied reverse bias, which results in a wider depletion region and can be regarded as a discharging process for the depletion region. Therefore, the width as well as the charge accumulation of the depletion region change depending on the applied bias, very similar to a traditional electrostatic capacitor. This capacitance effect is defined as the depletion capacitance of a p-n junction, which is also regarded as the dominant capacitance when the p-n junction is under reverse bias.

Figure 6.2 (a) and (b) illustrate the schematic diagrams of a p-n junction in the charging and discharging process, respectively, providing more information about the physical mechanism of the depletion capacitance. As the positive and negative ions cannot move freely under external applied bias, the depletion capacitance effect is mainly determined by the behaviours of carriers from n-type/p-type region under external bias. From the above discussion, we know that the depletion capacitance can also be regarded as a kind of variable capacitance and interpreted as the ratio between the changes of charge and the applied bias, i.e. $C = dQ/dV$. In addition, analysis shows that the value of depletion capacitance is proportional to the size of the p-n junction but has a non-linear relationship with the applied bias. Its analytic expression is denoted as [165]:

$$C_D = \frac{C_{D0}}{(1 - U/V_D)^{\frac{1}{2}}} \tag{6.1}$$

where U is the applied bias, C_{D0} is the geometric capacitance ($U = 0$), and V_D is the voltage of built-in electric field. However, under large forward bias, a lot of carriers will pass through the barrier region so that the depletion approximation in the p-n junction is no longer applicable.

6.2.2 Diffusion capacitance of LED

Under larger forward bias, the holes will pass through the barrier region and begin to accumulate in the n-type region. In order to keep electrical neutrality, electrons of the n-type region will increase and diffuse accordingly to compensate the increase of holes. This phenomenon is the same for the electrons that pass through the barrier region and accumulate in the p-type region. In this case, the charges that are stored in either the n-type region or the p-type region of the p-n junction change depending on the applied bias and this capacitance effect is known as the diffusion capacitance of the p-n junction. Diffusion capacitance can be interpreted as a change of majority carriers in the n-type and p-type region to maintain the electrical neutrality after minority carriers pass through the depletion region. The diffusion capacitance of p-n junction can be denoted as [165]:

$$C_{Diffusion} = \frac{\tau}{V_T} \cdot I \tag{6.2}$$

where τ is the lifetime of non-equilibrium minority carriers, V_T is the junction temperature and I is the forward current. Therefore, the diffusion capacitance $C_{Diffusion}$ is proportional to forward current.

The capacitance of a p-n junction contains depletion capacitance and diffusion capacitance, i.e. $C_j = C_{Diffusion} + C_{Depletion}$. Under reverse bias, junction capacitance is mainly depletion capacitance, i.e. $C_j \approx C_{Depletion}$. Under large forward bias, the capacitance of a p-n junction is mainly diffusion capacitance, i.e. $C_j \approx C_{Diffusion}$ and in this case, the diffusion capacitance increases linearly with the increase of forward current under large applied bias, as shown in Equation 6.2. However, from the experimental results, the capacitance of LEDs normally drops down to negative values under large forward bias, in contradiction to conventional p-n junction theory [166–174]. This phenomenon is known as the NC effect, which will be discussed in the following sub-section.

6.2.3 Negative capacitance of LED

NC has been widely observed in various semiconductor devices as mentioned above. A general explanation is that the NC effect is caused by the nonlinearity and dispersion of materials [175]. However, in terms of the LED devices, it is crucial for us to understand the essence of NC arising from the carrier dynamics in the LED structures. Firstly, NC cannot be denoted as a traditional capacitance, which is usually associated with charge storage and energy accumulation. Thus, NC cannot be interpreted as: $C = dQ/dV$, i.e. when dQ turns to negative while dV is positive, thus resulting in a negative junction capacitance [166]. As NC has no relation with charging effects, it cannot be explained via a conventional electrostatic definition. Secondly, NC cannot be simply interpreted as conventional positive inductance and numerically linked with $L = -\frac{1}{\omega^2 \cdot C}$ without considering the physical mechanism. For conventional inductance, its impedance $|z| = \omega \cdot L$ should increase with frequency and dominate at high frequencies. However, this is not the case for NC as has been proved by previous work [166–171], as NC becomes smaller and smaller with the increase of modulation frequency. According to the theory proposed in [166], NC can be interpreted as a positive "inductive"-like behaviour/phenomenon and it originates when the transient current caused by the small modulation signal lags behind the modulation voltage. In other words, NC has the same phase relationship between the modulation signal voltage and the transient current as a positive

inductance. To understand this explanation, we should first look at how the capacitance of a semiconductor device is measured and how it becomes into a negative value. The capacitance of a semiconductor is usually measured under small signal modulation. In this case, a small modulation signal (oscillation level around 50 mV) is combined with a DC bias and applied to the semiconductor device [166–174]. If the semiconductor device can be approximately regarded as a conductor connected with a capacitor in parallel, which is also a typical model used in most semiconductor-based capacitance research [169–174], then the admittance of the device can be measured as: $Y(\omega) = dI(\omega)/dV(\omega)$, where $I(\omega)$ is the small-signal harmonic current, $V(\omega)$ is the small-signal voltage, and $Y(\omega)$ is the device admittance. In this case, the device conductance $G(\omega)$ and the device capacitance $C(\omega)$ can be achieved through calculating the real part and the imaginary part of $Y(\omega)$, i.e $G(\omega) = Re[Y(\omega)]$ and $C(\omega) = -\frac{1}{\omega}Im[Y(\omega)]$. Under this premise, in order to evaluate the capacitance response of the device, a step voltage ΔV is applied to the device and the capacitance response can be denoted using the following equation [166, 173]:

$$C(\omega) = \underbrace{C_0}_{1} + \underbrace{\frac{1}{\omega \cdot \Delta V}\int_0^{\infty}[-\frac{dI(t)}{dt}]sin\omega t dt}_{2} \tag{6.3}$$

where C_0 is the geometric capacitance, and $I(t)$ is the transient current caused by the step voltage ΔV. When an LED device is driven and modulated at specific conditions, usually under large forward bias and low modulation frequency, the derivative of transient current $I(t)$, i.e. $dI(t)/d(t)$ is positive, which results in the integral (term 2) of Equation 6.3 into a negative value. Therefore, $C(\omega)$ is smaller than C_0 and can become negative. In other words, NC is caused by the positive-valued behaviour of the time-derivative of the transient current in response to a small voltage step. This interpretation is very persuasive in numerically characterising the appearance of NC, but less insightful in clarifying the underlying physical mechanism that is particularly interesting for NC research.

In terms of conventional reactance, NC can be numerically regarded as negative capacitive reactance, which can also be denoted as positive inductive reactance via $L = -\frac{1}{\omega^2 \cdot C}$. This inductive-like behaviour originates when a device resists the current change, which results in a retarded current lagging behind the applied voltage. According to the work

by Bansal and Datta [173, 178], this inductive-like behaviour in LEDs is caused by the carrier dynamics, which contain two main processes, i.e. the carrier radiative recombination process and a sub-bandgap defect assisted carrier trapping-de-trapping process. Under small signal modulation (a small AC signal is combined with a large DC bias and applied to LED device), radiative recombination usually consumes the minority carriers at a speed much faster than the supplement of such carriers from the sub-bandgap defects via the carrier de-trapping process. If the minority carriers from sub-bandgap defects are considered as an important contribution to replenish the minority carriers, then the quasi Fermi levels will split due to the competition between fast radiative recombination and slowly responding sub-bandgap defects. Furthermore, a transient variation of the steady state current will happen and go through over a full circle of sinusoidal period. In order to resist the split of quasi Fermi levels and deviations of steady current level, the LED devices acquire an inductive reactive response and corresponding off-phase transient current, similar to an inductor that resists any transient change of steady current level. To conclude, due to the small signal modulation, the fast and slow dynamic responses of the carriers generate off-phase transient current, which results in the NC effect. In terms of physical meaning, the essence of NC should be understood as a compensatory inductive behaviour triggered by the dynamic competition mentioned above and caused by the carrier dynamics in the LED device under specific modulation conditions.

6.3 Size-dependent capacitance study in micro-LEDs

Previous capacitance studies on LEDs focus on conventional broad-area LED devices, which have typical device sizes ranging from 300×300 μm^2 to 1 mm^2. In this section, we will investigate the size-dependent capacitance of InGaN-based micro-LEDs. Micro-LED clusters consisting of uniform-sized micro-LED pixels were chosen for the study instead of individual micro-LED pixels with different sizes, because among the latter the current spreading is quite different as the pixel size changes [88, 102]. In our micro-LED clusters, each LED pixel is 40×40 μm^2, which is also the smallest tested LED. By inter-connecting the basic micro-LED pixels (sharing p and n contacts) into square $n \times n$ clusters (n=1,...,10), micro-LED clusters with device areas ranging from 40×40 to 400×400 μm^2 are formed. For comparison purposes, two square-shaped broad-area

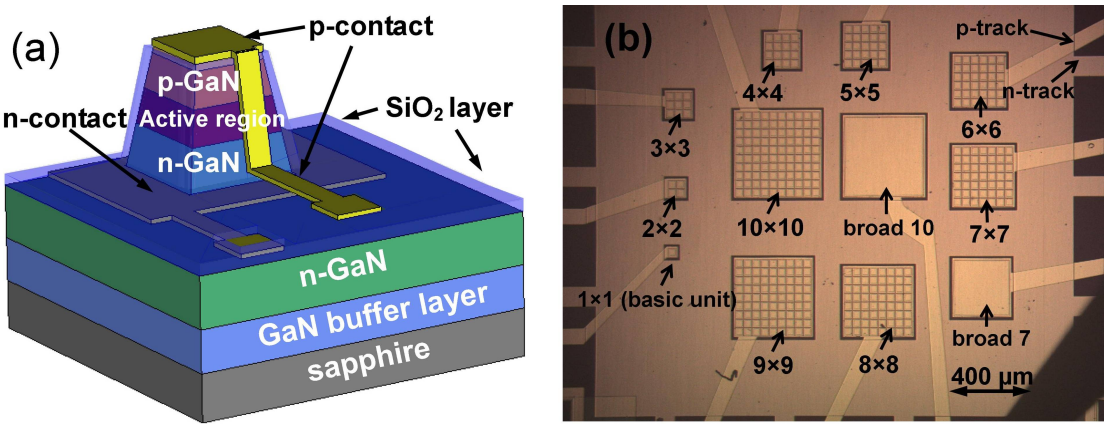

FIGURE 6.3: (a) 3D schematic (not to scale) of a typical micro-LED pixel (basic unit to form micro-LED cluster devices); (b) optical microscope image of the micro-LED cluster devices and broad-area LED devices.

LEDs were also fabricated. Each has the same total area as the 7×7 and 10×10 micro-LED clusters, and is marked as "broad 7-square" and "broad 10-square", respectively. Figure 6.3 (a) shows a 3D schematic of a typical pixel that forms the micro-LED clusters. Figure 6.3 (b) shows a top-view optical microscope image of the chip with different micro-LED clusters and broad-area LEDs, providing more specific information about the structure and layout of the fabricated devices. All the micro-LED clusters and the two broad-area LEDs were fabricated together on the same chip into flip-chip formats, so they have undergone the same processing steps. Details of the device fabrication can be found in chapter 2, section 2.1. In addition, all the fabricated devices reported here were made from a 450 nm blue-emitting wafer grown on a *c*-plane sapphire substrate by metal organic chemical vapour deposition. Its epitaxial structure begins with a 1.5-μm-thick GaN buffer layer followed by a 4-μm-thick Si-doped n-type GaN layer. Then the active region was grown, which is made up by an eleven-pair $In_{0.16}Ga_{0.84}N$ (2.8 nm)/GaN (13.5 nm) multi-quantum-well (MQW) layer. After that, a 30-nm-thick p-AlGaN electron-blocking layer (EBL) was grown on top of the active region. Finally, a 160-nm-thick Mg-doped p-type GaN layer was grown on top of the EBL.

The current-voltage (I-V) and capacitance-voltage (C-V) characteristics of the LEDs were measured by a probe station connected to an Agilent 4155C semiconductor parameter analyser and an Agilent 4294A precision impedance analyser, respectively. The C-V characteristics were measured under a small modulation signal with an oscillation level of 50 mV and a frequency of 100 Hz. The equivalent circuit model of LED for measuring C-V can be found in previous work [169–172]. The light output power was

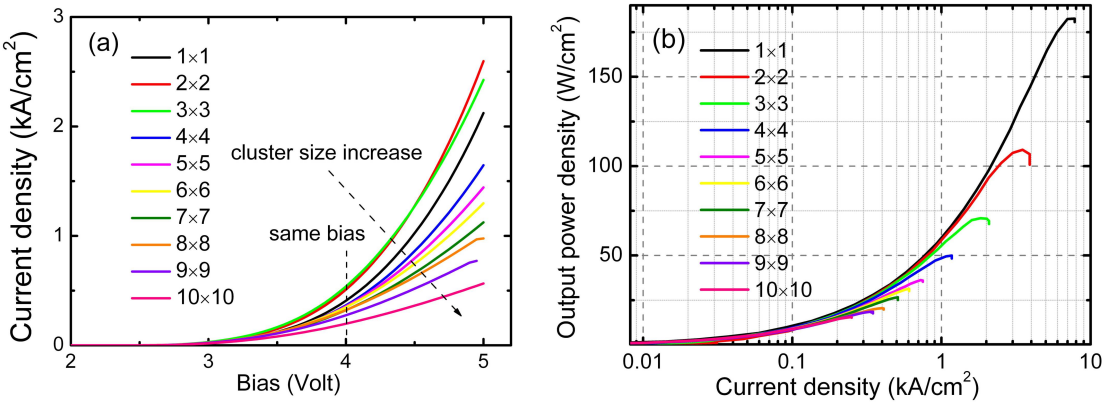

FIGURE 6.4: (a) Characteristics of current density versus applied bias of micro-LED cluster devices with different sizes; (b) semi-logarithmic plot of power density versus current density for micro-LED cluster devices.

measured by putting the silicon photodetector of a calibrated power-meter on top of the emitting surface of each LED device.

Based on the I-V measurement, the current densities of the micro-LED cluster devices are plotted as a function of applied bias in Figure 6.4 (a). As shown, a strongly size-dependent behaviour is observed across the different clusters (except for the 1×1 device). The smaller the cluster, the higher the current density obtained under the same applied bias. A similar phenomenon has also been observed in micro-LED pixels with different sizes [88]. This effect is still under investigation and may be caused by current crowding effect in the n-GaN [88, 102]. Figure 6.4 (b) shows the characteristics of current density versus output power density of micro-LED cluster devices, also showing strongly size-dependent behaviour. In general, the thermal roll-over occurs at much lower current densities (a few hundred A/cm^2) for larger-size cluster devices compared with smaller clusters (several kA/cm^2). The maximum output power density of the single pixel device (more than 170 W/cm^2) is much higher than that of the 10×10 micro-LED cluster device (less than 25 W/cm^2). Such optical performance under continuous wave (CW) operation provides an indication of the thermal management of the LED devices, as the roll-over of output power of an LED is mainly caused by the self-heating effect [88, 179]. Therefore, it is obvious that larger micro-LED clusters are less competitive in thermal management and subsequently affected more by the self-heating effect compared with their smaller counterparts [88, 179].

Figure 6.5 shows the capacitance spectroscopy of the micro-LED cluster devices with applied voltage changing from -5 V to +5 V. The capacitances of all the micro-LED

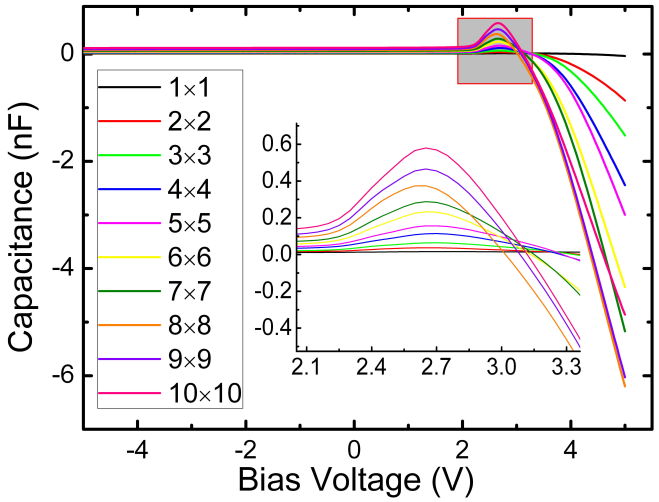

FIGURE 6.5: C-V characteristics of micro-LED clusters with different sizes, the inset shows an enlarged picture of the capacitance peaks in the shaded area.

clusters, no matter what their size, show similar trends: the value of capacitance is positive under reverse bias; then increases with forward bias to a peak (the peak area is enlarged and shown in the inset of Figure 6.5); after that, it decreases with further increasing forward bias and drops down to a negative value. Similar trends have been widely observed in conventional broad-area LED devices [170–172], proving that both micro-LEDs and broad-area LEDs are dominated by the same physical mechanism, whatever the size and format of the device. This trend of capacitance with the increase of bias can be explained by the content of section 6.2. Figure 6.6 shows the size-dependent capacitances at different bias voltages for the micro-LED cluster devices. Depletion capacitance, geometrical capacitance (capacitance at 0 V) and the peak capacitance are all plotted against device size in Figure 6.6 (a), (b) and (c). Corresponding plots in the NC regime at +4 to +5 V are shown in Figure 6.6 (d), (e) and (f). The size effect on NC under forward bias is of practical interest because all the devices are turned on at +4 V and the devices have high injection current densities at +5 V. Linear fitting of the capacitance with the device size is indicated by red-solid lines for all the data. Very good linear relationships are observed for depletion capacitance, geometrical capacitance and the peak capacitance (R-squared$\sim$0.99). As mentioned above, under reverse bias and low forward bias, the capacitance of an LED device is dominated by depletion capacitance and diffusion capacitance, respectively, which should be proportional to the area of the cross-section of the p-n junction. Therefore, the depletion capacitance and diffusion

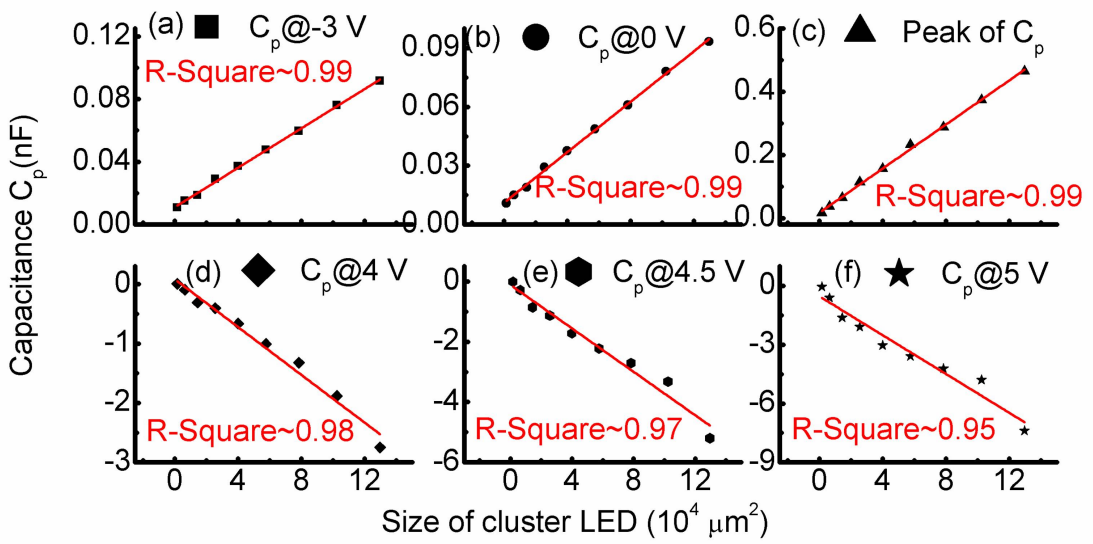

FIGURE 6.6: Size-dependent (a) depletion capacitance (capacitance at -3 V), (b) geometrical capacitance (capacitance at 0 V), (c) the peak of diffusion capacitance, and NC at (d) +4 V, (e) +4.5 V and (f) +5 V of cluster devices. Linear fitting of capacitance with LED size is shown in red-solid line for all the data, together with the R-square for each fitting.

capacitance of cluster device should scale linearly with the device size or number of micro-LED pixels.

However, in contrast to the conventional depletion and diffusion capacitance, the data points of the size-dependent NC show a systematic deviation from linearity with the increase of applied bias, as illustrated in Figure 6.6 (d), (e) and (f). Since the cluster devices are made from parallel-interconnected uniform micro-LED pixels, the capacitance of a cluster device is the sum of the capacitance of each single pixel. If each micro-LED pixel has the same NC under same driving conditions, then the NC of the micro-LED cluster should scale linearly with the number of micro-LED pixels and its own size. However, the linear relationship between NC and the device size is degraded under large forward bias. To clarify this abnormal relationship between NC and the device size, we investigated the normalised capacitance, i.e. the capacitance per device area, as a function of the applied bias for different micro-LED cluster devices.

Figure 6.7 (a) shows the characteristics of normalised capacitance versus bias voltage of different micro-LED cluster devices. The curves of normalised capacitance of different clusters overlap well under low forward bias but show a systematic trend of deviation to each other with the increase of forward bias. As shown in Figure 6.7 (a), the normalised

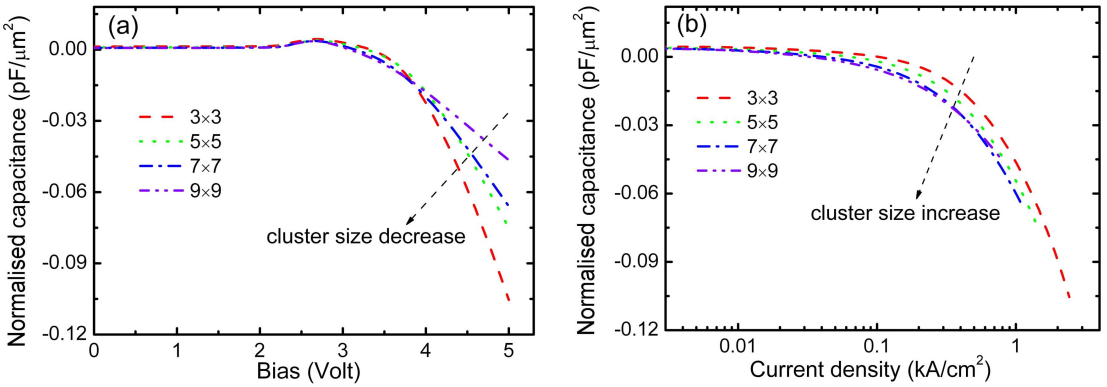

FIGURE 6.7: (a) Characteristics of normalised capacitance versus forward bias of micro-LED cluster devices; (b) characteristics of normalised capacitance versus current density of micro-LED cluster devices.

NC of the smaller cluster device is larger (absolute value) than that of the larger cluster device under the same large forward bias, causing the linearity deviation observed in Figure 6.6 (d), (e) and (f). To further explain the observed experimental results, normalised capacitances of micro-LED cluster devices are plotted as a function of injection current density and shown in Figure 6.7 (b). According to previous investigations and theoretical interpretation, the NC effect is closely related to injected carriers and carrier dynamics [172–174]. If we assume the NC effect of micro-LED cluster devices is dominated by the same carrier mechanisms, then the normalised NCs of micro-LED cluster devices should behave similarly under the same injection current density. As shown in Figure 6.7 (b), the normalised NCs of different micro-LED clusters show similar trends with the increase of current density and the variation of normalised NCs is smaller than the variation of normalised NCs shown in Figure 6.7 (a). Further analysis suggests that the observed small differences of the normalised NCs of micro-LED cluster devices under the same current densities are probably due to their different junction temperatures [88]. As mentioned above, larger micro-LED clusters are less competitive in thermal management and subsequently affected more by the self-heating effect. A further measurement of junction temperature by the spectral shift method shows that the junction temperature of a larger-size micro-LED cluster is higher than that of a smaller-size micro-LED cluster under the same current densities [88]. Figure 6.8 shows the C-V characteristics of a 5×5 cluster device with an ambient temperature increasing from 26 °C (near room temperature) to 196 °C. The inset of Figure 6.8 shows the NC as a function of temperature under a forward bias of +4 V and +5 V. This measurement was done by putting the device in a temperature-controllable oven. As shown in Figure

6.8, a clear increase of the NC with temperature can be seen and a similar trend was observed in other cluster devices as well. Therefore, different junction temperatures in different micro-LED clusters can cause the variation of normalised NC values when they are driven under the same injection current densities. Temperature-dependent NC characteristics of broad-area LEDs have been investigated before [178]. According to the theory proposed by Bansal and Datta [173, 178], the NC effect is caused by the carrier dynamics and has a close relationship with the sub-bandgap defects. The density of trapped minority carriers (here electron) by the sub-bandgap defects can be defined as [173, 178]:

$$n^{trapped}(E) = \int_{E_c - E_{Th}}^{E_{Fn}} g(E)dE \tag{6.4}$$

where $g(E)$ is the sub-bandgap defect density at energy E below the conduction band, E_{Fn} is the electron quasi Fermi level, E_c is the energy at the conduction band edge and E_{Th} is the characteristic thermal activation energy of the sub-band gap defects. E_{Th} can also be expressed as [173, 178]:

$$E_{Th} = k_b \cdot T \cdot ln(\upsilon/f) \tag{6.5}$$

where k_b is the Boltzmann constant, T is the junction temperature, υ is the thermal prefactor and f is the modulation frequency. Therefore, at any given frequency, if the junction temperature T increases, the thermal activation energy of sub-bandgap defects E_{Th} will also increase, which results in an increase of the trapped carriers by sub-bandgap defects and induces a stronger NC effect. Although the normalised NC of smaller micro-LED cluster device is smaller than that of the larger micro-LED cluster device under the same injection current density, the smaller micro-LED cluster device is able to be driven at higher current densities compared with the larger micro-LED cluster device, which allows the maximum NC value of smaller micro-LED cluster device to be higher than that of larger micro-LED cluster device, as shown in Figure 6.7 (b). Therefore, NC should be regarded as a current/carrier-dependent phenomenon and its value increases with the increase of injection current density.

These measurements suggest that the linearity deviation between NC and device size observed is mainly caused by different injection current densities in the micro-LED

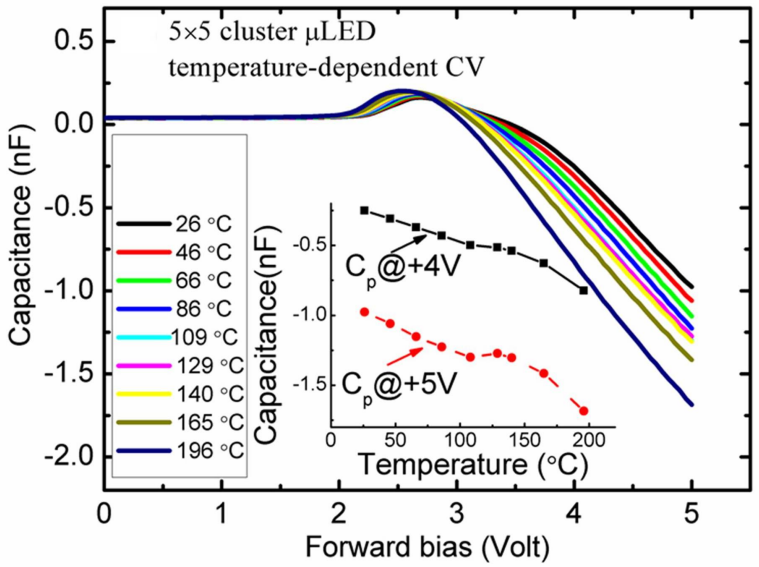

FIGURE 6.8: Temperature-dependent C-V of the 5×5 cluster device. The inset shows NC as a function of temperature under a forward bias of +4 V and +5 V, respectively.

clusters (see Figure 6.4 (a)). Therefore, a higher normalised NC value is expected in the smaller micro-LED cluster device compared with a larger micro-LED cluster device under the same bias, causing the linearity deviation between NC and the device size. These results indicate that the NC of LEDs measured at a fixed applied bias should not be used directly to characterise the size effect as the NC of LEDs is a current/carrier-dependent phenomenon, which is different from the depletion and diffusion capacitance of LEDs. Therefore, current-dependent NC characteristics are more insightful than the widely-reported voltage-dependent NC characteristics for NC research [167–174]. In addition, contrary to conventional depletion and diffusion capacitances, the normalised NCs of these micro-LED cluster devices are also influenced by other factors, such as the self-heating effect. It will also be interesting to relate these findings to other characteristics of micro-LEDs, such as the modulation bandwidth. The high modulation bandwidth of micro-LEDs in excess of 400 MHz has been demonstrated [64] and was discussed in earlier chapters. This fast modulation response occurs in a regime of high NC, i.e. the micro-LEDs are operated at high injection current densities. The investigation on the relationship between the modulation bandwidth and NC is currently underway and the findings on this relationship will be reported in due course.

6.4 Influence of side-wall etching damage to negative capacitance of micro-LEDs

To further study the influence of device format and the relevant fabrication processes to NC and shed light on the underlying physics, Figure 6.9 compares the capacitances of the 7×7 and 10×10 micro-LED cluster devices and two broad-area devices with the same total area. Due to the small pixel separation (2 μm) between micro-LED pixels that form the cluster devices, the cluster device and the broad-area device with the same total area are influenced by similar self-heating effect under the same applied bias, indicated by their similar optical performance under CW operation. In addition, the I-V characteristics of the cluster device and the broad-area device with the same total area are quite similar, indicating the injection current densities in both the cluster device and broad-area device are similar under the same applied bias. The capacitance curves of these LED devices from -1 V to +1 V are enlarged and shown in the inset of Figure 6.9. From the enlarged picture, the cluster devices and broad-area devices with the same total size have very close values of capacitance. This phenomenon is well understood because both depletion capacitance and diffusion capacitance dominating in the low bias region should be proportional to device size, as discussed in section 6.2 and confirmed by Figure 6.6. However, when forward bias further increases, the absolute values of NC for the cluster devices are larger than those of broad-area devices, no matter how large the size of the device is. This interesting phenomenon is well-aligned with the theory by Bansal and Datta [173, 178], that relates the NC effect to the number of sub-bandgap defects. Even if the total areas of active region are same, the cluster devices have more ICP-etching induced sidewall damage compared with the broad-area LEDs due to different sidewall area to volume ratios. The sidewall damage can bring more sub-band gap defects to the device, resulting in an increase of population and depopulation of trap states by carriers on the sidewall surface of LED. Therefore, the ICP-etching induced sidewall defects can increase the sub-band gap defect density and the amount of trapped states significantly, which according to the Bansal-Datta-theory corresponds to a stronger NC effect in the cluster micro-LEDs.

To provide further evidence for the above interpretation, we measured the C-V characteristics of the 7×7 micro-LED cluster device and its broad-area counterpart under

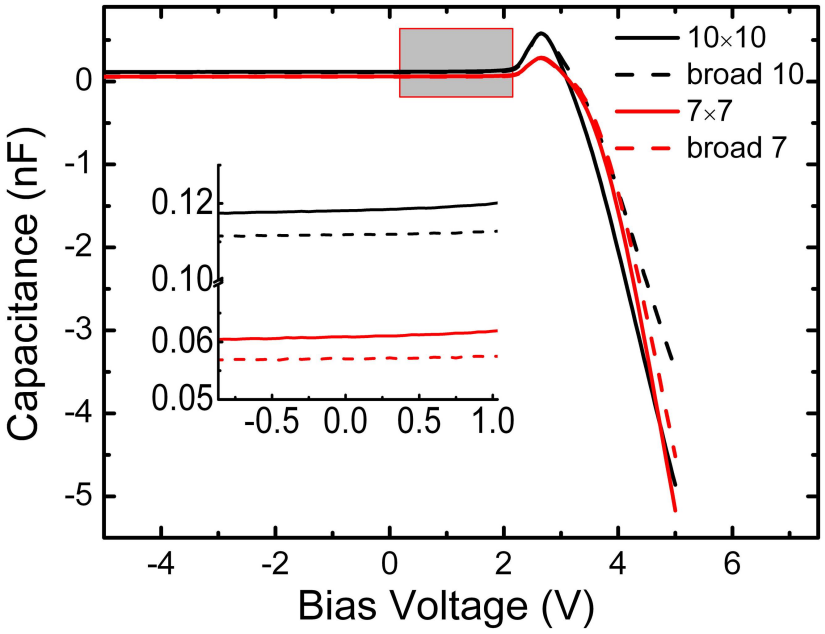

FIGURE 6.9: C-V characteristics of micro-LED clusters and broad-area LEDs with the same total area. The inset shows an enlarged picture of the capacitance from -1 to +1 V.

different modulation frequencies. In Figure 6.10 (a), the capacitances of the 7×7 cluster device with modulation frequency varied from 1 kHz to 5 MHz are shown. Under the same forward bias (>2.5 V), micro-LED cluster device shows a decreasing value of NC (absolute value) with increasing modulation frequency. In the Bansal-Datta-model [173, 178], the carriers from sub-band gap defects cannot follow the change of a high-frequency modulation signal and will be trapped at the sub-band gap defects due to finite energy. According to Equation 6.5, an increase of LED modulation frequency can result in the drop of thermal activation energy of the sub-band gap defects, decreasing the trapped carriers and weakening the NC effect. This explanation can be verified after comparing the NC value of micro-LED cluster device with that of broad LED device. As shown in Figure 6.10 (b), with the increase of modulation frequency, the difference of NC value between the micro-LED cluster device and the broad-area LED device becomes smaller and smaller at the same forward bias of +5 V. The reason is that more carriers in the sub-bandgap defects are trapped and no longer able to participate in any recombination process. Therefore, under high modulation frequency, the sub-band gap defects caused by ICP etching are no longer functional and the NC of micro-LED cluster device approaches the value of the broad-area counterpart.

From the analysis and experimental results, the NC of LED device cannot be explained

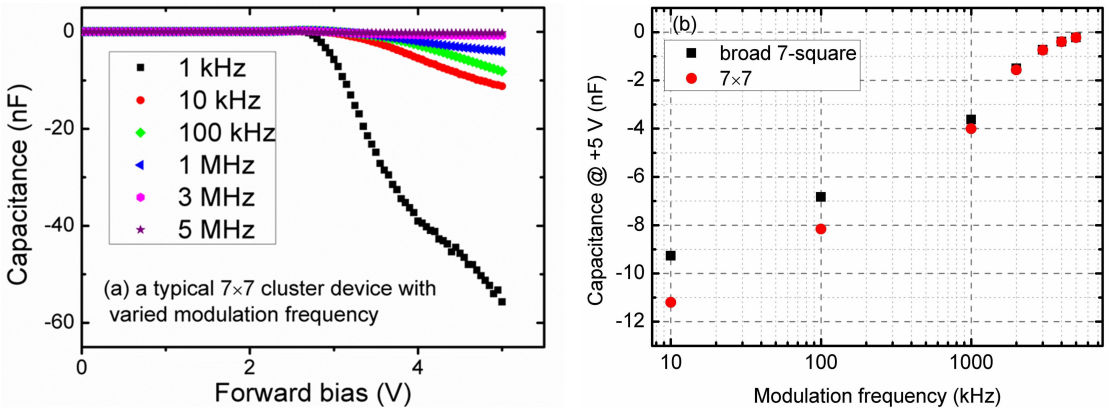

FIGURE 6.10: (a) C-V characteristics of the 7×7 cluster device with modulation frequency varied from 1 kHz to 5 MHz; (b) comparison between the NC of the 7×7 micro-LED cluster and the broad-area LED device at different modulation frequencies under +5 V applied bias.

by the concept of conventional electrostatic capacitance and is essentially different from the LED's depletion and diffusion capacitance. The NC of LED device should be regarded as a current-dependent phenomenon, which is possibly related to sub-bandgap defects and carrier dynamics. In this case, NC effect can be used to monitor and evaluate the performance of LED device. For applications requiring fast modulation, like optical communications [64, 178], LED designs should minimise the contribution of carriers de-trapped from sub-bandgap defects toward overall carriers available for radiative recombination. As for very high-speed modulation, such carriers are trapped in the sub-bandgap defects and not able to participate in the radiative recombination, hence decreasing the light output power from the modulated device [178]. In addition, the frequency-dependent characteristic of LED NC is very similar to its frequency-dependent modulation characteristic. For LED under high-frequency modulation, the carriers can not recombine fast enough to follow the modulation signal due to the limitation of carrier lifetime, resulting in the drop of modulation bandwidth. While the NC effect is also weakened in high-frequency regime, meaning the underlying physics of NC is probably quite similar to the physics of LED modulation. Besides, an increase of LED injection current increases its modulation bandwidth. While stronger NC effect is normally observed in high-current density regime. Therefore, it is fairly straightforward to relate the NC effect with the LED modulation characteristic. However, further work is still needed to prove the relevance of NC to LED modulation characteristic. The sidewall etching damage is believed to bring more sub-bandgap defects to the LED device. Therefore, it is of significance to minimise such sidewall etching damage. As for CW operation,

sidewall etching damage can also influence the device performance. Firstly, a proportion of the total current flows through the parallel leakage path of the sidewall and this current will not contribute to radiative recombination in the active region [180]. In addition, injected carriers may participate in surface recombination (which is non-radiative recombination) and Shockley-Read-Hall non-radiative recombination through sidewall defects, thus decreasing the overall light generation. Since the sidewall damage during fabrication process brings detrimental effects to the performance of LED devices, it is important to investigate the recovery of sidewall damage or minimise its influence through optimised thermal annealing and proper chemical repair [102].

6.5 Summary

In this chapter, the experimental part focuses on size-dependent capacitance study of InGaN-based micro-LED clusters under both reverse and forward biases. For these devices, both depletion capacitance under reverse bias and diffusion capacitance under low forward bias were observed to scale linearly with LED size. Under high forward bias, the NC effect was measured and size-dependent NC results show a deviation from linearity between NC and LED size, attributed to different injection current density and capability of thermal management in different micro-LED clusters. In particular, our results can consistently be interpreted by assuming that the NC effect is governed by the carrier density and the junction temperature, but not directly by the applied bias voltage. This view is well-aligned with theories that NC is an effect of carrier dynamics and/or occupation of certain states (e.g. sub-bandgap states). Compared to broad-area devices with same total area, micro-LED clusters have a similar depletion capacitance and diffusion capacitance but larger value of NC than their broad-area counterparts at large forward bias. A possible reason may be from the extra sub-band gap states contributed from the sidewall defects in micro-LED clusters induced by ICP etching damage. By investigating the size-dependent capacitance of InGaN-based micro-LEDs, this research provides insights into the mechanism underlying the NC effect observed in LED devices.

Chapter 7

Summary and future work

This thesis has presented a detailed study on fabrication, characterisation and novel applications of III-nitride micro-pixellated light-emitting diodes (micro-LEDs). Micro-LEDs are LEDs with sizes less than 100 μm in diameter or equivalent. In contrast to conventional broad-area LED devices with typical sizes of 300×300 μm^2 or more, micro-LEDs have interesting properties, in particular related to their capability of being driven at very high current densities with very high output power densities. In addition, various array formats of micro-LEDs have been developed, making them capable of generating micro-scale spatio-temporal light patterns. For the above-mentioned reasons, micro-LEDs have been successfully implemented for a wide range of applications, including parallel-channel visible light communications (VLC), micro-displays, optoelectronic tweezers, etc.. More importantly, micro-LEDs show many enhancements in device performance compared with conventional broad-area LED devices, allowing interesting physical phenomena and mechanisms to be investigated and understood.

The research on micro-LEDs reported here covers a broad range of topics, including fundamental physics, device characterisation, system integration and various applications. In this chapter, we will firstly summarise the work presented in this thesis, and then discuss some future work on micro-LEDs.

7.1 Summary

Chapter 1 provided a general introduction to LEDs, and more specifically to III-nitride LEDs and their applications in VLC. Over the last 100 years, great success has been achieved in the development of LEDs, making them reliable, versatile and efficient light sources for various applications. Particularly, efficient white LEDs are being used to replace incandescent and fluorescent bulbs for the purpose of general illumination. This LED-based application is known as the 'solid-state lighting' technology, which could potentially bring huge reduction in energy consumption and carbon emission. After introducing the development and general applications of LEDs, the operating principles of LEDs were given, including special structure designs to achieve high-performance LEDs and the carrier recombination processes in the LED active region. Then, III-nitride materials and III-nitride LEDs were introduced. Due to the wide bandgap energy, III-nitride materials can in principle emit light covering the whole visible spectrum, making them ideal materials for fabricating visible-light LEDs. The structure of a typical III-nitride LED wafer and common configurations of III-nitride LEDs were also presented. Since the III-nitride micro-LEDs are the main devices discussed in this thesis, a brief overview of III-nitride micro-LEDs was given including their formats, properties and novel applications. Finally, LED-based VLC technology was introduced. VLC is an optical communication technology which utilises visible-light signals for data communications. III-nitride LEDs have high modulation bandwidths, which allow them to be modulated in high speed for data transmission. In addition, as there is a trend of using white LEDs to replace traditional lamps, it would be interesting to use such LED-based light sources for not only general illumination but also data communications. In addition to free space, LEDs can also be used for data transmission in optical fibres.

The fabrication processes of micro-LEDs and the properties of fabricated micro-LED devices were presented in chapter 2. The fabrication of micro-LEDs starts from choosing the wafer materials. Different wafer materials have different properties and the related fabrication steps maybe different. For typical micro-LED devices based on commercial III-nitride materials grown on *c*-plane sapphire substrates, the fabrication mainly includes three steps, which are pattern definition via photolithography, pattern transfer via plasma dry etching or wet etching, and formation of individual p-type and n-type metal contacts via metal deposition. The working principles of each operation were

summarised and presented in detail. Most of the micro-LED devices reported in this thesis are micro-LED arrays, which are a novel format of LED consisting of arrays of individually-controllable sub-100 μm diameter micro-LED pixels. The electrical and optical performance of these micro-LED arrays, particularly their current-voltage (I-V) and current-power (L-I) characteristics, was investigated. It was found that the smaller-size micro-LED pixels are capable of being driven at very high current densities and with high output power densities. This is due to the superior performance of smaller-size micro-LED pixels in thermal management. The modulation characteristics of micro-LED devices were also investigated and presented. The modulation bandwidths of some the micro-LED pixels exceed 500 MHz, which is believed to be the highest modulation bandwidth for GaN-based LED devices. It was also found that the smaller-size micro-LED pixels have larger modulation bandwidths due to their capabilities to be operated in the high-current-density regime. These results prove that micro-LEDs are suitable optical data transmitters for VLC application.

Chapter 3 mainly discussed the integration of micro-LED arrays with complementary metal-oxide semiconductor (CMOS) driver arrays and the application of such CMOS-controlled micro-LED arrays for VLC. The background of CMOS technology was first presented, including CMOS field effect transistors and basic CMOS logic circuitry. Then, a specifically-designed CMOS driver array, suitable for integration with micro-LED array, was developed. The layout of the CMOS driver array and the circuitry of individual CMOS driver were presented in detail. After being integrated with micro-LED array via a flip-chip bonding process, the CMOS driver array allows each micro-LED pixel to be individually addressed and conveniently controlled via a CMOS driver board and a simple computer interface. In this case, such a CMOS-controlled micro-LED array is capable of generating programmable micro-scale light patterns easily, making many novel applications achievable. In terms of VLC application, a proof-of-concept VLC link with a data transmission rate of up to 1 Gbit/s was firstly realised using a 44 μm 'bare' micro-LED pixel (without being integrated with CMOS electronics). Then, CMOS-controlled micro-LED devices were used for VLC demonstration. The modulation bandwidths of the CMOS-controlled micro-LEDs were found to be up to 185 MHz and error-free data transmission using on-off keying was demonstrated at bit rates of up to 512 Mbit/s under single-channel operation. In addition, we also reported the characterisation of multiple-channel data transmission based on four pixels in a CMOS-controlled micro-LED array.

When four pixels were modulated simultaneously, error-free data transmission of up to 375 Mbit/s per pixel was achieved, giving an aggregate parallel data transmission rate of 1.5 Gbit/s. Analysis suggested that on-chip crosstalk, brought by modulating multiple pixels simultaneously, limited the data transmission rate. The electrical crosstalk was mainly caused by high power routing resistance in the CMOS driver array and methods to reduce these issues in future CMOS driver designs were proposed accordingly. These results demonstrate the great potential of using CMOS-controlled micro-LED array for high-speed parallel VLC.

Apart from the application on VLC, micro-LED devices can also be used for other applications, such as high-performance micro-displays. In chapter 4, the realisation and performance of various micro-display systems, based on micro-LED arrays, were presented. Compared with conventional technologies, such as LCOS and OLED, micro-display systems based on III-nitride micro-LEDs have clear advantages, such as high brightness, high reliability, long life and the capability to be operated under harsh conditions. Matrix-addressable micro-display systems based on III-nitride micro-LED arrays were first described. Operated with suitable driver circuitry and computer interface, the matrix-addressable micro-display system was capable of delivering programmable high-resolution micro-scale images via convenient computer control. An individually-addressable micro-display system based on a CMOS-controlled micro-LED array was also developed. The performance and applications of the individually-addressable micro-display system were presented. To make a further step, a colour-tunable III-nitride micro-display was also developed, which is based on new epitaxial LED wafer structures, micro-LED array fabrication, and relevant CMOS technology. This colour-tunable micro-display system was capable of delivering computer-controlled programmable dynamic images with its emitting colour changeable from red to green. Comparable brightness of the micro-LED pixels emitting at different colours was achieved by adjusting the duty cycle. Additionally, individual micro-LED pixels from this CMOS-controlled system have high modulation bandwidths, indicating that they can be used for high-speed VLC as well. Therefore, this work demonstrated a direct colour-tunable III-nitride micro-display for dual applications under CMOS control and, more importantly, provides an innovative method to overcome the limitations of using thin-film III-nitride based LED for multi-colour applications.

In chapter 5, experimental results of using micro-LEDs for VLC in plastic optical fibre (POF) were first presented. POF has become an interesting data transmission medium attracting a lot of interest recently. The attenuation of standard polymethylmethacrylate (PMMA)-based POF is relatively small in the blue-green regime, making III-nitride based LED devices suitable for POF-based communications. For III-nitride micro-LED devices, error-free data transmission was demonstrated at a data rate of up to 650 Mbit/s in a 10-m POF based on a single 74 μm diameter micro-LED pixel using on-off keying modulation scheme. Under a pulse-amplitude modulation (PAM)-16 scheme, an error-free data transmission rate of up to 4 Gbit/s was achieved in a 10-m POF using a 30 μm diameter micro-LED pixel. These results established a baseline demonstration of data transmission in POF using micro-LEDs. In chapter 5, we also investigated the modulation characteristics of novel colour-converters such as colloidal quantum dots (CQDs) and green polymer [2,5-bis(2',5'-bis(2"-ethylhexyloxy)phenyl)-p-phenylenevinylene] (BBEHP-PPV). This work aims to find alternatives to substitute phosphors which are used conventionally as colour-converters for white LEDs. Phosphors have long (μs regime) luminescent lifetimes, which restricts the bandwidth of the white LEDs to only a few MHz. In contrast, experimental results found the modulation bandwidths of CQD samples range from 10 MHz to 30 MHz while the modulation bandwidths of BBEHP-PPV samples reach above 100 MHz. These modulation results indicated that both CQD and BBEHP-PPV can be used as high-bandwidth colour-converters to generate modulated light for VLC, circumventing the restrictions imposed on the bandwidth of white LEDs that use conventional phosphors.

In chapter 6, we reported a detailed study on size-dependent capacitance, especially the negative capacitance (NC), in III-nitride micro-LEDs. Due to a reduction in device self-heating and current crowding, micro-LEDs are able to be driven at much higher current densities compared with conventional broad-area LEDs. As the NC effect becomes more significant under high injection current density, it is important to investigate the capacitance characteristics of micro-LED devices under large forward bias with high injection current density. Similar to conventional broad-area LEDs, all the tested micro-LEDs were found to show NC under large forward bias. For the size-dependent micro-LED devices, both depletion capacitance under reverse bias and diffusion capacitance under low forward bias were observed to scale linearly with LED size. However, the NC under high forward bias showed a deviation from above-mentioned linear relationship

with device size. This observation can be well interpreted by assuming the NC effect is governed by the carrier density, but not directly by the applied bias voltage. In this case, the NC effect may be related to the modulation characteristics of LEDs. To further investigate the influence of device fabrication to NC effect, the NCs of two reference broad-area LEDs were measured and compared with the NCs of micro-LED clusters with the same total size. A stronger NC effect was observed in the micro-LED clusters, which was attributed to the influence of sidewall defects to carrier dynamics. These experimental results shed light on the physical mechanism underlying the NC effect, which is beneficial to reveal the possible relations between NC effect and other characteristics of LEDs, such as their modulation bandwidths.

7.2 Future work

7.2.1 Flexible LEDs

Since their recent introduction, mechanically flexible inorganic LED devices have attracted a lot of research interest worldwide [39–42, 181–184]. Figure 7.1 (a) shows an image of red AlInGaP micro-LEDs in mechanically flexible format. An exciting and important application area of such flexible LEDs is bio-photonics, in which flexible devices can be easily integrated with soft bio-interfaces for many applications [39, 40, 42, 181]. As an example, a flexible LED device implanted underneath skin for bio-sensing is shown in Figure 7.1 (b). In addition, mechanically flexible LED devices can be made water-resistant [181] and wirelessly powered by integrated radio-frequency antennas [39, 40, 182], allowing wireless operation in a humid environment.

The key step to fabricate flexible LED devices is known as 'transfer-printing', which utilises a specifically-designed soft stamp to pick samples up from the donor substrate and place them onto the flexible receiver substrate. Our group has demonstrated that the placement accuracy of the 'transfer-printing' technology can reach 150 nm [185]. Conventional III-nitride LED materials are grown on thick and rigid sapphire substrates, which limit the flexibility of LED devices. Therefore, the sapphire substrates should be removed by laser-lift-off before the fabrication of flexible LED devices [186]. Another approach toward flexible III-nitride LEDs, which is becoming increasingly popular recently, is to use III-nitride materials grown on silicon substrates. Silicon substrates

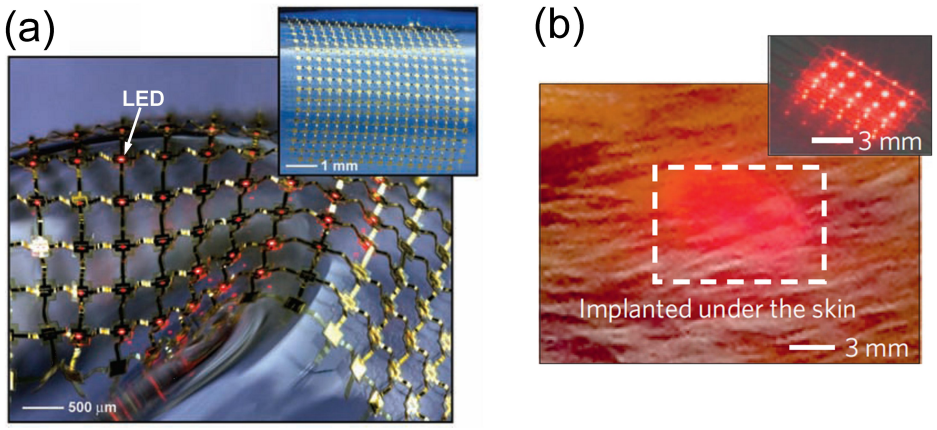

FIGURE 7.1: (a) Mechanically flexible AlInGaP micro-LEDs in bendable shape, from [41]. (b) Mechanically flexible micro-LEDs implanted into tissue underneath pig skin, from [181].

can be removed by wet etching, which is relatively easy compared with the remove of the sapphire substrate by laser-lift-off [185]. Recently, our group has reported the characterisation and applications of III-nitride micro-LEDs on silicon substrates (without removing the silicon substrate) [38]. Therefore, it is expected that the flexible micro-LEDs based on III-nitride-on-silicon materials will be fabricated in the near future. In addition, it would be interesting to investigate the applications of flexible micro-LEDs, such as bendable micro-displays and bio-sensing. More importantly, flexible micro-LEDs allow some interesting physical phenomena and mechanisms to be studied, such as their modulation bandwidths before and after bending. Our research in this area is currently underway.

7.2.2 CMOS-controlled micro-LEDs

In chapter 3, we reported the characterisation of CMOS-controlled micro-LEDs and their applications in parallel data transmission. Our future work in this area will focus on improving the performance of CMOS-controlled micro-LEDs, particularly by addressing the electrical crosstalk issue and 'Ground Bounce' effect. Figure 7.2 (a) shows the design of a new CMOS chip ('fifth-generation') and a controllable emission pattern generated by micro-LEDs controlled by the new CMOS chip. The new CMOS chip contains an array of 10×40 CMOS drivers and the power routing resistance in the CMOS driver is

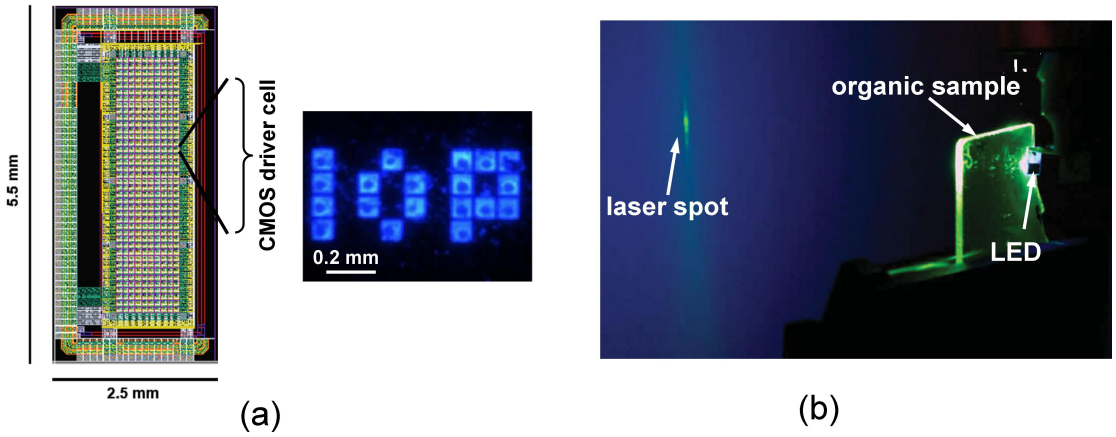

FIGURE 7.2: (a) Layout of the new CMOS chip and a controllable emission pattern 'IOP' generated by a micro-LED array controlled by the new CMOS chip; (b) III-nitride LEDs used for pumping organic lasers, from [187].

reduced by making the metal track wider. Therefore, it is expected that the new CMOS-controlled micro-LED arrays will exhibit better performance in parallel data transmission compared with previous designs. In addition, to make the overall system a proper multiple-input multiple-output (MIMO) communication system, a photo-receiver array should be developed to receive the data streams in a parallel way. It is worth mentioning that the data transmission result reported in chapter 3 was achieved under basic on-off keying modulation scheme. For the new CMOS-controlled micro-LED devices, advanced modulation and encoding schemes should be implemented to improve the data transmission rates. This work is currently ongoing under the collaboration between the groups in Institute of Photonics and University of Edinburgh. Another interesting approach to improve the data transmission rate is to utilise the array nature of the device. For example, different combinations of micro-LED pixels can be used to represent different signal levels (more than 2), thus achieving a PAM VLC system.

In addition to free space, CMOS-controlled micro-LED devices can also be used for parallel data transmission in multi-core POF. Some baseline demonstrations were reported in chapter 5. Another ambition on the new CMOS-controlled micro-LED device focuses on its application on photo-pumping organic lasers (Figure 7.2 (b)) [187–191]. This work is carrying out under the collaboration between groups in Institute of Photonics and University of St Andrews. It is anticipated that the new CMOS-controlled micro-LED device, with its output power performance improved by reducing the routing resistance and current crowding, could lead to compact hybrid inorganic/organic lasers.

7.2.3 III-nitride colour-tunable materials

In chapter 4, a colour-tunable III-nitride micro-display based on CMOS-controlled micro-LEDs was successfully demonstrated. However, the carrier dynamics in the active region of LED wafer have not yet been fully understood yet. There are two groups of multi-quantum-well (MQW) layers in the active region of the LED wafer, i.e. a five-period $In_{0.18}Ga_{0.82}N$ (3 nm)/GaN (10 nm) MQW layer emitting at 460 nm (low-indium-content QWs) and a seven-period $In_{0.4}Ga_{0.6}N$ (4 nm)/GaN (13 nm) MQW layer emitting at 600 nm (main QWs). The low-indium-content QWs are believed to function as an electron reservoir layer (ERL) to increase the carrier capture rate of the upper main QWs and improve their radiative efficiency. When the colour-tunable micro-LEDs are driven above the turn-on threshold, both ERL and main QWs will emit light. By using corresponding long-pass and short-pass filters, the emissions from ERL and main QWs can be well separated and analysed accordingly. The modulation characteristics of main QWs are very similar to the modulation characteristics of previously-reported micro-LED devices. However, the modulation characteristics of ERL show unexpected behaviours.

Figure 7.3 (a) shows the -3 dB optical bandwidths of the light emission from an 84 μm diameter micro-LED pixel below 500 nm (made from the above material). At low injection current, the light emission below 500 nm is mainly from the ERL. However, as the injection current increases to 50 mA and above, the light emission below 500 nm is no longer mainly from ERL because the spectrum of main QWs becomes wide enough to cover part of the spectrum below 500 nm. Therefore, only the optical bandwidths below 40 mA are used to analyse the carrier dynamics inside the ERL. As shown in Figure 7.3 (a), the bandwidth of the ERL increases from 800 MHz to around 1 GHz with the injection current increasing from 5 mA to 20 mA and saturates at around 1 GHz at the current regime from 20 mA to 40 mA. The change of the bandwidth of ERL with the increase of injection current is different from other previously-reported micro-LED devices, as in other micro-LED devices, the optical bandwidths usually increase with the increase of injection current [64, 111, 176]. In addition, in the current regime of 20 mA to 40 mA, the bandwidth of ERL is over 1 GHz, much higher than the bandwidths of any other micro-LEDs reported (and indeed any other LEDs). Eye diagrams of the light emission below 500 nm from an 84 μm diameter micro-LED pixel modulated at different data rates at 20 mA are shown in Figure 7.3 (b), (c) and (d). The open

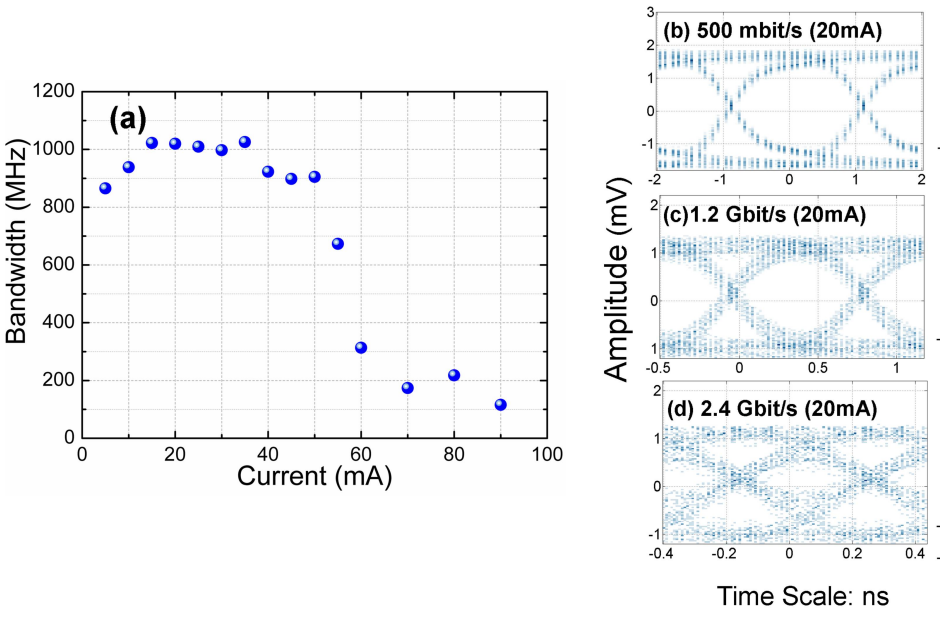

FIGURE 7.3: (a) -3 dB modulation bandwidths of the light emission below 500 nm from a typical 84 μm diameter colour-tunable micro-LED pixel, under different injection currents. Eye diagrams of the light emission below 500 nm from a typical 84 μm diameter colour-tunable micro-LED pixel, when it is modulated at (b) 500 Mbit/s, (c) 1.2 Gbit/s and (d) 2.4 Gbit/s with an injection current of 20 mA.

eye diagrams at high modulation data rates match up well with the -3 dB modulation bandwidth data shown in Figure 7.3 (a). These results indicate that there are some fast carrier recombination processes existing in the ERL, which is very different from the carrier recombination processes observed in typical LED structures. However, there are no persuasive physical explanations for this unusual phenomenon at the current stage. The research on the modulation characteristics of colour-tunable materials and related LED devices is still ongoing. For practical applications, the research on modulation characteristics of colour-tunable materials and LED devices is very meaningful, as a fully understanding of the fast carrier recombination processes is beneficial for optimising the typical LED wafer structures toward high-bandwidth optical sources, which will be particularly useful for VLC applications.

7.2.4 Colour-converting materials

In chapter 5, we investigated the modulation characteristics of CQDs and a green polymer (BBEHP-PPV), which are promising high-bandwidth colour-converters to substitute for conventional phosphors. However, a fully-integrated hybrid white micro-LED device has not yet been demonstrated. To achieve this, a few challenges need to be

carefully considered, such as the degradation of colour-converters, miscoloured emission from colour-converters, the integration of colour-converters with micro-LEDs, etc. Work is still ongoing to meet these challenges, and in the longer term a demonstration of a fully-integrated high-bandwidth white-emitting hybrid device should be feasible. (In breaking news, 1.68 Gb/s data transmission has been achieved using an integrated micro-LED/yellow organic polymer combination [164].)

7.2.5 Negative capacitance of LEDs

In chapter 6, NC effect was indentified as a current-dependent phenomenon. However, most of the NC models are based on applied voltage [170, 171]. Therefore, a new model which links NC with injection current should be developed to characterise the NC effect of the LEDs. In addition, the NC of an LED device is measured under small-signal modulation. Such measuring conditions are very similar to those used for measuring LED modulation bandwidth. More importantly, the fast modulation response occurs in a regime of high NC, i.e. the micro-LEDs are operated at high injection current densities. Therefore, it is natural to attempt to relate the NC to the modulation characteristics of micro-LEDs. Our future work in this area will focus on revealing the relation between NC effect and LED modulation bandwidth, which will be beneficial to understand the device physics under modulation conditions.

7.3 Final remark

Due to superior electrical and optical performance as well as versatile formats, III-nitride micro-LED devices have been widely used for many applications as presented in this thesis. Fundamental research on the device physics will carry on but broader research interest will focus on the applications of micro-LEDs. With the continued advances in LED materials, micro-LED fabrication and control electronics, this technology will no longer be limited to research labs but rather will find wide-spread practical uses.

This thesis focuses on the characterisation and applications of III-nitride micro-LEDs, particularly their applications on VLC. However, throughout this PhD study and thesis writing, the importance of the system integration, including LED wafer materials, micro-LED device fabrication, CMOS electronics, POF, colour-converters, modulation

schemes, etc., has been emphasised. The research on III-nitride micro-LEDs should not only focus on the device, but also the system integration.

References

[1] H. J. Round. A note on carborundum. *Electrical World*, 49(6):309, 1907.

[2] O. V. Lossev. CII. Luminous carborundum detector and detection effect and oscillations with crystals. *The London, Edinburgh, and Dublin Philosophical Magazine and Journal of Science*, 6 (39):1024–1044, 1928.

[3] G. Destriau. Scintillations of zinc sulfides with alpha-rays. *J. Chimie Physique*, 33:587, 1936.

[4] H. Welker. On new semiconducting compounds. *Zeitschrift fur Naturforschung*, 7a(39):744–749, 1952.

[5] H. Welker. On new semiconducting compounds II. *Zeitschrift fur Naturforschung*, 8a(39):248–251, 1953.

[6] R. N. Hall, G. E. Fenner, J. D. Kingsley, T. J. Soltys, and R. O. Carlson. Coherent light emission from Ga-As junctions. *Phys. Rev. Lett.*, 9(9):366–368, 1962.

[7] M. I. Nathan, W. P. Dumke, G. Burns, F. H. Dill Jr., and G. Lasher. Stimulated emission of radiation from GaAs p-n junctions. *Appl. Phys. Lett.*, 1(3):62–64, 1962.

[8] N. H. Jr and S. F. Bevacqua. Coherent (visible) light emission from $Ga(As_{1-x}P_x)$ junctions. *Appl. Phys. Lett.*, 1(4):82–83, 1962.

[9] A. H. Herzog, W. O. Groves, and M. G. Craford. Electroluminescence of diffused $GaAs_{1-x}P_x$ diodes with low donor concentrations. *J. Appl. Phys.*, 40(4):1830–1838, 1969.

[10] M. G. Craford, R. W. Shaw, A. H. Herzog, and W. O. Groves. Radiative recombination mechanisms in GaAsP diodes with and without nitrogen doping. *J. Appl. Phys.*, 43(10):4075–4083, 1972.

[11] C. B. Duke and N. Holonyak. Advances in light-emitting diodes. *Phys. Today*, 26(12):23–31, 2008.

[12] S. Nakamura, M. Senoh, and T. Mukai. P-GaN/N-InGaN/N-GaN double-heterostructure blue-light-emitting diodes. *Jpn. J. Appl. Phys.*, 32(1A):L8–L11, 1993.

[13] S. Nakamura, M. Senoh, and T. Mukai. High-power InGaN/GaN double-heterostructure violet light emitting diodes. *Appl. Phys. Lett.*, 62(19):2390–2392, 1993.

[14] S. Nakamura, T. Mukai, and M. Senoh. Candela-class high-brightness InGaN/AlGaN double-heterostructure blue-light-emitting diodes. *Appl. Phys. Lett.*, 64(13):1687–1689, 1994.

[15] S. Nakamura, M. Senoh, N. Iwasa, and S. Nagahama. High-brightness InGaN blue, green and yellow light-emitting diodes with quantum well structures. *Jpn. J. Appl. Phys.*, 34(7A):L797–L799, 1995.

[16] H. P. Maruska and J. J. Tietjen. The preparation and properties of vapor-deposited single crystalline GaN. *Appl. Phys. Lett.*, 15(10):327–329, 1969.

[17] H. Amano, N. Sawaki, I. Akasaki, and Y. Toyoda. Metalorganic vapor phase epitaxial growth of a high quality GaN film using an AlN buffer layer. *Appl. Phys. Lett.*, 48(5):353–355, 1986.

[18] H. Amano, M. Kito, K. Hiramatsu, and I. Akasaki. P-type conduction in Mg-doped GaN treated with low-energy electron beam irradiation (LEEBI). *Jpn. J. Appl. Phys.*, 28(12):L2112–L2114, 1989.

[19] S. Nakamura, N. Iwasa, and M. Senoh. Method of manufacturing p-type compound semiconductor. *US patent 5, 306, 662*, 1994.

[20] K. H. Huang and T. P. Chen. Light-emitting diode structure. *US patent 5, 661, 742*, 1997.

[21] M. R. Krames, M. Ochiai-Holcomb, G. E. Höfler, C. Carter-Coman, E. I. Chen, I. H. Tan, P. Grillot, N. F. Gardner, H. C. Chui, J. W. Huang, S. A. Stockman, F. A. Kish, M. G. Craford, T. S. Tan, C. P. Kocot, M. Hueschen, J. Posselt, B. Loh, G. Sasser, and D. Collins. High-power truncated-inverted-pyramid $(Al_xGa_{1-x})_{0.5}In_{0.5}P$/GaP light-emitting diodes exhibiting $> 50\%$ external quantum efficiency. *Appl. Phys. Lett.*, 75(16):2365–2367, 1999.

[22] S. Pimputkar, J. S. Speck, S. P. DenBaars, and S. Nakamura. Prospects for LED lighting. *Nature Photon.*, 3(4):180–182, 2009.

[23] J. K. Kim and E. F. Schubert. Transcending the replacement paradigm of solid-state lighting. *Opt. Express*, 16(26):21835–21842, 2008.

[24] M. R. Krames, O. B. Shchekin, R. Mueller-Mach, G. O. Mueller, L. Zhou, G. Harbers, and M. Craford. Status and future of high-power light-emitting diodes for solid-state lighting. *J. Display Technol.*, 3(2):160–175, 2007.

[25] M. Fukuda. Optical semiconductor devices. *John Wiley & Sons*, 1999.

[26] E. F. Schubert. Light-emitting diodes. *Cambridge University Press, second edition*, 2008.

[27] J. M. Shah, Y. L. Li, Th. Gessmann, and E. F. Schubert. Experimental analysis and theoretical model for anomalously high ideality factors (n$\gg$2.0) in AlGaN/GaN pn junction diodes. *J. Appl. Phys.*, 94(4):2627–2630, 2003.

[28] R. P. Green, J. J. D. McKendry, D. Massoubre, E. Gu, M. D. Dawson, and A. E. Kelly. Modulation bandwidth studies of recombination processes in blue and green InGaN quantum well micro-light-emitting diodes. *Appl. Phys. Lett.*, 102(9):091103, 2013.

[29] K. H. Li, C. Feng, and H. W. Choi. Analysis of micro-lens integrated flip-chip InGaN light-emitting diodes by confocal microscopy. *Appl. Phys. Lett.*, 104(5):051107, 2014.

[30] H. W. Choi, C. Liu, E. Gu, G. McConnell, J. M. Girkin, I. M. Watson, and M. D. Dawson. GaN micro-light-emitting diode arrays with monolithically integrated sapphire microlenses. *Appl. Phys. Lett.*, 84(13):2253–2255, 2004.

[31] E. Matioli and C. Weisbuch. Impact of photonic crystals on LED light extraction efficiency: approaches and limits to vertical structure designs. *J. Phys. D: Appl. Phys.*, 43(35):354005, 2010.

[32] I. Vurgaftman and J. R. Meyer. Band parameters for nitrogen-containing semiconductors. *J. Appl. Phys.*, 94(6):3675–3696, 2003.

[33] S. J. Chang, Y. C. Lin, Y. K. Su, C. S. Chang, T. C. Wen, S. C. Shei, J. C. Ke, C. W. Kuo, S. C. Chen, and C. H. Liu. Nitride-based LEDs fabricated on patterned sapphire substrates. *Solid-State Electron.*, 47(9):1539–1542, 2003.

[34] D. Zhu, D. J. Wallis, and C. J. Humphreys. Prospects of III-nitride optoelectronics grown on Si. *Rep. Prog. Phys.*, 76(10):106501, 2013.

[35] S. Zhang, Z. Gong, J. J. D. McKendry, S. Watson, A. Cogman, E. Xie, P. Tian, E. Gu, Z. Chen, G. Zhang, R. K. Henderson, A. E. Kelly, and M. D. Dawson. CMOS-controlled color-tunable smart display. *IEEE Photon. J.*, 4(5):1639–1646, 2012.

[36] Y. J. Hong, C. H. Lee, A. Yoon, M. Kim, H. K. Seong, H. J. Chung, C. Sone, Y. J. Park, and G. C. Yi. Visible-Color-Tunable Light-Emitting Diodes. *Adv. Mater.*, 23(29):3284–3288, 2011.

[37] B. Damilano, P. Demolon, J. Brault, T. Huault, F. Natali, and J. Massies. Blue-green and white color tuning of monolithic light emitting diodes. *J. Appl. Phys.*, 108(7):073115, 2010.

[38] P. Tian, J. J. D. McKendry, Z. Gong, S. Zhang, S. Watson, D. Zhu, I. M. Watson, E. Gu, A. E. Kelly, C. J. Humphreys, and M. D. Dawson. Characteristics and applications of micro-pixelated GaN-based light emitting diodes on Si substrates. *J. Appl. Phys.*, 115(3):033112, 2014.

[39] D. H. Kim, N. Lu, R. Ma, Y. S. Kim, R. H. Kim, S. Wang, J. Wu, S. M. Won, H. Tao, A. Islam, K. J. Yu, T. Kim, R. Chowdhury, M. Ying, L. Xu, M. Li, H. J. Chung, H. Keum, M. McCormick, P. Liu, Y. W. Zhang, F. G. Omenetto, Y. Huang, T. Coleman, and J. A. Rogers. Epidermal electronics. *Science*, 333(6044):838–843, 2011.

[40] T. Kim, J. G. McCall, Y. H. Jung, X. Huang, E. R. Siuda, Y. Li, J. Song, Y. M. Song, H. A. Pao, R. H. Kim, C. Lu, S. D. Lee, I. S Song, G. Shin, R. Al-Hasani, S. Kim, M. P. Tan, Y. Huang, F. G. Omenetto, J. A. Rogers, and M. R. Bruchas. Injectable, cellular-scale optoelectronics with applications for wireless optogenetics. *Science*, 340(6129):211–216, 2013.

[41] S. I. Park, Y. Xiong, R. H. Kim, P. Elvikis, M. Meitl, D. H. Kim, J. Wu, J. Yoon, C. J. Yu, Z. Liu, Y. Huang, K. Hwang, P. Ferreira, X. Li, K. Choquette, and J. A. Rogers. Printed assemblies of inorganic light-emitting diodes for deformable and semitransparent displays. *Science*, 325(5943): 977–981, 2009.

[42] T. Kim, R. Kim, and J. A. Rogers. Microscale inorganic light-emitting diodes on flexible and stretchable substrates. *IEEE Photon. J*, 4(2):607–612, 2012.

[43] S. C. Jain, M. Willander, J. Narayan, and R. V. Overstraeten. III-nitrides: Growth, characterization, and properties. *J. Appl. Phys.*, 87(3):965–1006, 2000.

[44] J. Singh. Electronic and optoelectronic properties of semiconductor structures. *Cambridge University Press*, 2005.

[45] M. H. Kim, M. F. Schubert, Q. Dai, J. K. Kim, E. F. Schubert, J. Piprek, and Y. Park. Origin of efficiency droop in GaN-based light-emitting diodes. *Appl. Phys. Lett.*, 91(18):183507, 2007.

[46] N. F. Gardner, J. C. Kim, J. J. Wierer, Y. C. Shen, and M. R. Krames. Polarization anisotropy in the electroluminescence of m-plane InGaN-GaN multiple-quantum-well light-emitting diodes. *Appl. Phys. Lett.*, 86(11):111101, 2005.

[47] F. Bernardini, V. Fiorentini, and D. Vanderbilt. Spontaneous polarization and piezoelectric constants of III-V nitrides. *Phys. Rev. B*, 56(16):R10024, 1997.

[48] D. A. B. Miller, D. S. Chemla, T. C. Damen, A. C. Gossard, W. Wiegmann, T. H. Wood, and C. A. Burrus. Band-edge electroabsorption in quantum well structures: the quantum-confined Stark effect. *Phys. Rev. Lett.*, 53(22):2173, 1984.

[49] J. H. Ryou, P. D. Yoder, J. Liu, Z. Lochner, H. Kim, S. Choi, H. J. Kim, and R. D. Dupuis. Control of quantum-confined stark effect in InGaN-based quantum wells. *IEEE J. Sel. Top. Quant. Electron.*, 15(4):1080–1091, 2009.

[50] A. Khan, K. Balakrishnan, and T. Katona. Ultraviolet light-emitting diodes based on group three nitrides. *Nature photon.*, 2(2):77–84, 2008.

[51] Z. Gong, N. Y. Liu, Y. B. Tao, D. Massoubre, E. Y. Xie, X. D. Hu, Z. Z. Chen, G. Y. Zhang, Y. B. Pan, M. S. Hao, I. M. Wastson, E Gu, and M. D. Dawson. Electrical, spectral and optical performance of yellow–green and amber micro-pixelated InGaN light-emitting diodes. *Semicond. Sci. Technol.*, 27(1):015003, 2012.

[52] A. Koukitu and H. Seki. Thermodynamic analysis on molecular beam epitaxy of GaN, InN and AlN. *Jpn. J. Appl. Phys.*, 36(6B):L750, 1997.

[53] C.-H. Chen, S.-J. Chang, and Y.-K. Su. High-indium-content InGaN/GaN multiple-quantum-well light-emitting diodes. *Jpn. J. Appl. Phys.*, 42(4S):2281, 2003.

[54] H. S. Chen, D. M. Yeh, Y. C. Lu, C. Y. Chen, C. F. Huang, T. Y. Tang, C. C. Yang, C. S. Wu, and C. D. Chen. Strain relaxation and quantum confinement in InGaN/GaN nanoposts. *Nanotechnology*, 17(5):1454, 2006.

[55] E. Y. Xie, Z. Z. Chen, P. R. Edwards, Z. Gong, N. Y. Liu, Y. B. Tao, Y. F. Zhang, Y. J. Chen, I. M. Watson, E. Gu, R. W. Martin, G. Y. Zhang, and M. D. Dawson. Strain relaxation in InGaN/GaN micro-pillars evidenced by high resolution cathodoluminescence hyperspectral imaging. *J. Appl. Phys.*, 112(1):013107, 2012.

[56] P. Waltereit, O. Brandt, A. Trampert, H. T. Grahn, J. Menniger, M. Ramsteiner, M. Reiche, and K. H. Ploog. Nitride semiconductors free of electrostatic fields for efficient white light-emitting diodes. *Nature*, 406(6798):865–868, 2000.

[57] S. M. Hwang, Y. G. Seo, K. H. Baik, I. S. Cho, J. H. Baek, S. Jung, T. G. Kim, and M. Cho. Demonstration of nonpolar a-plane InGaN/GaN light emitting diode on r-plane sapphire substrate. *Appl. Phys. Lett.*, 95(7):071101, 2009.

[58] A. G. Bell. Selenium and the photophone. *Nature*, 22(569):500–503, 1880.

[59] D. O'Brien, G. Parry, and P. Stavrinou. Optical hotspots speed up wireless communication. *Nature Photon.*, 1(5):245–247, 2007.

[60] H. Elgala, R. Mesleh, and H. Haas. Indoor optical wireless communication: potential and state-of-the-art. *IEEE Commun. Mag.*, 49(9):56–62, 2011.

[61] L. Grobe, A. Paraskevopoulos, J. Hilt, D. Schulz, F. Lassak, F. Hartlieb, C. Kottke, V. Jungnickel, and K. D. Langer. High-speed visible light communication systems. *IEEE Commun. Mag.*, 51 (12):60–66, 2013.

[62] Cisco visual networking index: Global mobile data traffic forecast update, 2013-2018.

[63] G. Cossu, A. M. Khalid, P. Choudhury, R. Corsini, and E. Ciaramella. 3.4 Gbit/s visible optical wireless transmission based on RGB LED. *Opt. Express*, 20(26):B501–B506, 2012.

[64] J. J. D. McKendry, D. Massoubre, S. Zhang, B. R. Rae, R. P. Green, E. Gu, R. K. Henderson, A. E. Kelly, and M. D. Dawson. Visible-light communications using a CMOS-controlled micro-light-emitting-diode array. *J. Lightwave Technol.*, 30(1):61–67, 2012.

[65] D. Tsonev, H. Chun, S. Rajbhandari, J. J. D. McKendry, S. Videv, E. Gu, M. Haji, S. Watson, A. K. Kelly, G. Faulkner, M. D. Dawson, H. Haas, and D. O'Brien. A 3-Gb/s single-LED OFDM-based wireless VLC link using a gallium nitride μLED. *IEEE Photon. Technol. Lett.*, 26(7): 637–640, 2014.

[66] Y. Kawamura and T. Tanaka. Transmission of the LED light from the space to the ground. *AIP Adv.*, 3:102110, 2013.

[67] C. A. Burrus and B. I. Miller. Small-area, double-heterostructure aluminum-gallium arsenide electroluminescent diode sources for optical-fiber transmission lines. *Opt Commun*, 4(4):307–309, 1971.

[68] T. Kibler, S. Poferl, G. Bock, H. P. Huber, and E. Zeeb. Optical data buses for automotive applications. *J. Lightwave Technol.*, 22(9):2184–2199, 2004.

[69] F. Aznar, C. Sánchez-Azqueta, S. Celma, and B. Calvo. Gigabit receiver over 1 mm SI-POF for home area networks. *J. Lightwave Technol.*, 30(16):2668–2674, 2012.

[70] J-M Wun, C-W Lin, W. Chen, J-K Sheu, C-L Lin, Y-L Li, J. E. Bowers, J-W Shi, J. Vinogradov, R. Kruglov, and O. Ziemann. Gan-based miniaturized cyan light-emitting diodes on a patterned sapphire substrate with improved fiber coupling for very high-speed plastic optical fiber communication. *IEEE Photon. J.*, 4(5):1520–1529, 2012.

[71] C. H. Yeh, Y. F. Liu, C. W. Chow, Y. Liu, P. Y. Huang, and H. K. Tsang. Investigation of 4-ASK modulation with digital filtering to increase 20 times of direct modulation speed of white-light LED visible light communication system. *Opt. Express*, 20(15):16218–16223, 2012.

[72] J. Vučić, C. Kottke, S. Nerreter, K. Langer, and J. W. Walewski. 513 Mbit/s visible light communications link based on DMT-modulation of a white LED. *J. Lightwave Technol.*, 28(24):3512–3518, 2010.

[73] J. L. Wei, L. Geng, D. G. Cunningham, R. V. Penty, and I. H. White. Gigabit NRZ, CAP and optical OFDM systems over POF links using LEDs. *Opt. Express*, 20(20):22284–22289, 2012.

[74] F. M. Wu, C. T. Lin, C. C. Wei, C. W. Chen, Z. Y. Chen, H. T. Huang, and S. Chi. Performance comparison of OFDM signal and CAP signal over high capacity RGB-LED-based WDM visible light communication. *IEEE Photon. J.*, 5(4):7901507–7901507, 2013.

[75] UP-VLC project: Ultra-parallel visible light communications. URL `http://up-vlc.photonics.ac.uk/`.

[76] H. X. Zhang, D. Massoubre, J. McKendry, Z. Gong, B. Guilhabert, C. Griffin, E. Gu, P. E. Jessop, J. M. Girkin, and M. D. Dawson. Individually-addressable flip-chip AlInGaN micropixelated light emitting diode arrays with high continuous and nanosecond output power. *Opt. Express*, 16(13): 9918–9926, 2008.

[77] Z. Gong, E. Gu, S. R. Jin, D. Massoubre, B. Guilhabert, H. X. Zhang, M. D. Dawson, V. Poher, G. T. Kennedy, P. W. H. French, and M. A. A. Neil. Efficient flip-chip InGaN micro-pixellated light-emitting diode arrays: promising candidates for micro-displays and colour conversion. *J. Phys. D: Appl. Phys.*, 41(9):094002, 2008.

[78] A. J. C. Kuehne, D. Elfström, A. R. Mackintosh, A. L. Kanibolotsky, B. Guilhabert, E. Gu, I. F. Perepichka, P. J. Skabara, M. D. Dawson, and R. A. Pethrick. Direct laser writing of nanosized oligofluorene truxenes in UV-transparent photoresist microstructures. *Adv. Mater.*, 21(7):781–785, 2009.

[79] D. Elfström, B. Guilhabert, J. McKendry, S. Poland, Z. Gong, D. Massoubre, E. Richardson, B. R. Rae, G. Valentine, G. Blanco-Gomez, E. Gu, J. M. Cooper, R. K. Henderson, and M. D. Dawson. Mask-less ultraviolet photolithography based on CMOS-driven micro-pixel light emitting diodes. *Opt. Express*, 17(26):23522–23529, 2009.

[80] A. C. Small, J. H. Johnston, and N. Clark. Inkjet printing of water soluble doped ZnS quantum dots. *Eur. J. Inorg. Chem.*, 2010(2):242–247, 2010.

[81] Y. Zhang. Diamond and GaN waveguides and microstructures for integrated quantum photonics. *PhD thesis, University of Strathclyde*, 2012.

[82] E. Xie. High performance microstructured light emitting diodes - mechanisms and processes. *PhD thesis, University of Strathclyde*, 2013.

[83] J. Day, J. Li, D. Y. C. Lie, C. Bradford, J. Y. Lin, and H. X. Jiang. III-nitride full-scale high-resolution microdisplays. *Appl. Phys. Lett.*, 99(3):031116, 2011.

[84] H. X. Jiang, S. X. Jin, J. Li, J. Shakya, and J. Y. Lin. III-nitride blue microdisplays. *Appl. Phys. Lett.*, 78(9):1303–1305, 2001.

[85] J. J. D. McKendry, B. R. Rae, Z. Gong, K. R. Muir, B. Guilhabert, D. Massoubre, E. Gu, D. Renshaw, M. D. Dawson, and R. K. Henderson. Individually addressable AlInGaN micro-LED arrays with CMOS control and subnanosecond output pulses. *IEEE Photon. Technol. Lett.*, 21 (12):811–813, 2009.

[86] A. H. Jeorrett, S. L. Neale, D. Massoubre, E. Gu, R. K. Henderson, O. Millington, K. Mathieson, and M. D. Dawson. Optoelectronic tweezers system for single cell manipulation and fluorescence imaging of live immune cells. *Opt. Express*, 22(2):1372–1380, 2014.

[87] Y. Wang, B. R. Rae, R. K. Henderson, Z. Gong, J. Mckendry, E. Gu, M. D. Dawson, G. A. Turnbull, and I. D. W. Samuel. Ultra-portable explosives sensor based on a CMOS fluorescence lifetime analysis micro-system. *AIP Adv.*, 1:032115, 2011.

[88] Z. Gong, S. Jin, Y. Chen, J. McKendry, D. Massoubre, I. M. Watson, E. Gu, and M. D. Dawson. Size-dependent light output, spectral shift, and self-heating of 400 nm InGaN light-emitting diodes. *J. Appl. Phys.*, 107(1):013103, 2010.

[89] J. Herrnsdorf, Y. Wang, J. J. D. McKendry, Z. Gong, D. Massoubre, B. Guilhabert, G. Tsiminis, G. A. Turnbull, I. D. W. Samuel, N. Laurand, E. Gu, and M. D. Dawson. Micro-LED pumped polymer laser: A discussion of future pump sources for organic lasers. *Laser Photon. Rev.*, 7(6): 1065–1078, 2013.

[90] T. Mukai, D. Morita, and S. Nakamura. High-power UV InGaN/AlGaN double-heterostructure LEDs. *J. Cryst. Growth*, 189(190):778–781, 1998.

[91] F. Bernardini, V. Fiorentini, and D. Vanderbilt. Spontaneous polarization and piezoelectric constants of III-V nitrides. *Phys. Rev. B*, 56(16):R10024, 1997.

[92] A. Chakraborty, B. A. Haskell, S. Keller, J. S. Speck, S. P. Denbaars, S. Nakamura, and U. K. Mishra. Demonstration of nonpolar m-plane InGaN/GaN light-emitting diodes on free-standing m-plane GaN substrates. *Jpn. J. Appl. Phys.*, 44(5):L173–L175, 2005.

[93] D. F. Feezell, J. S. Speck, S. P. DenBaars, and S. Nakamura. Semipolar $(20\bar{2}\bar{1})$ InGaN/GaN light-emitting diodes for high-efficiency solid-state lighting. *J. Display Technol.*, 9(4):190–198, 2013.

[94] Y. Zhao, S. H. Oh, F. Wu, Y. Kawaguchi, S. Tanaka, K.i Fujito, J. S. Speck, S. P. DenBaars, and S. Nakamura. Green semipolar ($20\bar{2}\bar{1}$) InGaN light-emitting diodes with small wavelength shift and narrow spectral linewidth. *Appl. Phys. Express*, 6(6):062102, 2013.

[95] J. J. D. McKendry. Micro-pixellated AlInGaN light-emitting diode arrays for optical communications and time-resolved fluorescence lifetime measurements. *PhD thesis, University of Strathclyde*, 2011.

[96] G. H. B. Thompson. Analysis of radiative and nonradiative recombination law in lightly doped InGaAsP lasers. *Electron. Lett.*, 19(5):154–155, 1983.

[97] M. Meneghini, N. Trivellin, G. Meneghesso, E. Zanoni, U. Zehnder, and B. Hahn. A combined electro-optical method for the determination of the recombination parameters in InGaN-based light-emitting diodes. *J. Appl. Phys.*, 106(11):114508, 2009.

[98] A. David and M. J. Grundmann. Droop in InGaN light-emitting diodes: A differential carrier lifetime analysis. *Appl. Phys. Lett.*, 96(10):103504, 2010.

[99] W. G. Scheibenzuber, U. T. Schwarz, L. Sulmoni, J. Dorsaz, J. F. Carlin, and N. Grandjean. Recombination coefficients of GaN-based laser diodes. *J. Appl. Phys.*, 109(9):093106, 2011.

[100] Y. C. Shen, G. O. Mueller, S. Watanabe, N. F. Gardner, A. Munkholm, and M. R. Krames. Auger recombination in InGaN measured by photoluminescence. *Appl. Phys. Lett.*, 91(14):141101, 2007.

[101] K. T. Delaney, P. Rinke, and C. G. Van de Walle. Auger recombination rates in nitrides from first principles. *Appl. Phys. Lett.*, 94(19):191109, 2009.

[102] P. Tian, J. J. D. McKendry, Z. Gong, B. Guilhabert, I. M. Watson, E. Gu, Z. Chen, G. Zhang, and M. D. Dawson. Size-dependent efficiency and efficiency droop of blue InGaN micro-light emitting diodes. *Appl. Phys. Lett.*, 101(23):231110, 2012.

[103] R. J. Baker. CMOS: circuit design, layout, and simulation. *John Wiley and Sons, third edition*, 2011.

[104] A. R. Hambley. Electrical engineering principles and applications. *Prentice Hall, second edition*, 2002.

[105] B. R. Rae. Micro-systems for time-resolved fluorescence analysis using CMOS single-photon avalanche diodes and micro-LEDs. *PhD thesis, University of Edinburgh*, 2009.

[106] A. Zarowna-Dabrowska, S. L. Neale, D. Massoubre, J. J. D. McKendry, B. R. Rae, R. K. Henderson, M. J. Rose, H. Yin, J. M. Cooper, E. Gu, and M. D. Dawson. Miniaturized optoelectronic tweezers controlled by GaN micro-pixel light emitting diode arrays. *Opt. Express*, 19(3):2720–2728, 2011.

[107] B. R. Rae, K. R. Muir, Z. Gong, J. J. D. McKendry, J. M. Girkin, E. Gu, D. Renshaw, M. D. Dawson, and R. K. Henderson. A CMOS time-resolved fluorescence lifetime analysis micro-system. *Sensors*, 9(11):9255–9274, 2009.

[108] B. R. Rae, C. Griffin, J. J. D. McKendry, J. M. Girkin, H. X. Zhang, E. Gu, D. Renshaw, E. Charbon, M. D. Dawson, and R. K. Henderson. CMOS driven micro-pixel LEDs integrated with single photon avalanche diodes for time resolved fluorescence measurements. *J. Phys. D: Appl. Phys.*, 41(9):094011, 2008.

[109] B. Guilhabert, D. Massoubre, E. Richardson, J. J. D. McKendry, G. Valentine, R. K. Henderson, I. M. Watson, E. Gu, and M. D. Dawson. Sub-micron lithography using InGaN micro-LEDs: mask-free fabrication of LED arrays. *IEEE Photon. Technol. Lett.*, 24(24):2221–2224, 2012.

[110] J. J. D. McKendry, B. R. Rae, Z. Gong, K. R. Muir, B. Guilhabert, D. Massoubre, E. Gu, D. Renshaw, M. D. Dawson, and R. K. Henderson. Individually addressable AlInGaN micro-LED arrays with CMOS control and subnanosecond output pulses. *IEEE Photon.Technol. Lett.*, 21(12): 811–813, 2009.

[111] J. J. D. McKendry, R. P. Green, A. E. Kelly, Z. Gong, B. Guilhabert, D. Massoubre, E. Gu, and M. D. Dawson. High-speed visible light communications using individual pixels in a micro light-emitting diode array. *IEEE Photon.Technol. Lett.*, 22(18):1346–1348, 2010.

[112] A. M. Khalid, G. Cossu, R. Corsini, P. Choudhury, and E. Ciaramella. 1-Gb/s transmission over a phosphorescent white LED by using rate-adaptive discrete multitone modulation. *IEEE Photon. J.*, 4(5):1465–1473, 2012.

[113] L. Zeng, D. O'Brien, H. Minh, G. Faulkner, K. Lee, D. Jung, Y. J. Oh, and E. T. Won. High data rate multiple input multiple output (MIMO) optical wireless communications using white LED lighting. *IEEE J. Select. Areas Commun.*, 27(9):1654–1662, 2009.

[114] Y. A. Alqudah and M. Kavehrad. MIMO characterization of indoor wireless optical link using a diffuse-transmission configuration. *IEEE Trans. Commun.*, 51(9):1554–1560, 2003.

[115] S. Jivkova, B. A. Hristov, and M. Kavehrad. Power-efficient multispot-diffuse multiple-input-multiple-output approach to broad-band optical wireless communications. *IEEE Trans. Veh. Technol.*, 53(3):882–889, 2004.

[116] K. D. Dambul, D. O'Brien, and G. Faulkner. Indoor optical wireless MIMO system with an imaging receiver. *IEEE Photon. Technol. Lett.*, 23(2):97–99, 2011.

[117] A. H. Azhar, T. Tran, and D. O'Brien. A Gigabit/s indoor wireless transmission using MIMO-OFDM visible-light communications. *IEEE Photon. Technol. Lett.*, 25(2):171–174, 2013.

[118] Z. Y. Fan, J. Y. Lin, and H. X. Jiang. III-nitride micro-emitter arrays: development and applications. *J. Phys. D: Appl. Phys.*, 41(9):094001, 2008.

[119] Image source: `http://www.google.co.uk/glass/start/what-it-does/`.

[120] H. X. Jiang and J. Y. Lin. Nitride micro-LEDs and beyond-a decade progress review. *Opt. Express*, 21(103):A475–A484, 2013.

[121] A. R. Lingley, M. Ali, Y. Liao, R. Mirjalili, M. Klonner, M. Sopanen, S. Suihkonen, T. Shen, B. P. Otis, H. Lipsanen, and B. A. Parviz. A single-pixel wireless contact lens display. *J. Micromech. Microeng.*, 21(12):125014, 2011.

[122] Z. J. Liu, W. C. Chong, K. M. Wong, K. H. Tam, and K. M. Lau. A novel BLU-free full-color LED projector using LED on silicon micro-displays. *IEEE Photon. Technol. Lett.*, 25(23):2267–2270, 2013.

[123] I. D. W. Samuel and G. A. Turnbull. Organic semiconductor lasers. *Chem. Rev.*, 107(4):1272–1295, 2007.

[124] Z. J. Liu, W. C. Chong, K. M. Wong, C. W. Keung, and K. M. Lau. Investigation of forward voltage uniformity in monolithic light-emitting diode arrays. *IEEE Photon. Technol. Lett.*, 25(13): 1290–1293, 2013.

[125] S. X. Jin, J. Li, J. Z. Li, J. Y. Lin, and H. X. Jiang. Gan microdisk light emitting diodes. *Appl. Phys. Lett.*, 76(5):631–633, 2000.

[126] C. W. Jeon, K. S. Kim, and M. D. Dawson. Fabrication of two-dimensional InGaN-based micro-LED arrays. *Phys. Stat. Sol. (a)*, 192(2):325–328, 2002.

[127] C. W. Jeon, H. W. Choi, and M. D. Dawson. Fabrication of matrix-addressable InGaN-based microdisplays of high array density. *IEEE Photon. Technol. Lett.*, 15(11):1516–1518, 2003.

[128] H. W. Choi, C. W. Jeon, and M. D. Dawson. High-resolution 128×96 nitride microdisplay. *IEEE Electron Device Lett.*, 25(5):277–279, 2004.

[129] Z. Gong, H. X. Zhang, E. Gu, C. Griffin, M. D. Dawson, V. Poher, G. Kennedy, P. M. W. French, and M. A. A. Neil. Matrix-addressable micropixellated InGaN light-emitting diodes with uniform emission and increased light output. *IEEE Trans. Electron Devices*, 54(10):2650–2658, 2007.

[130] J. Herrnsdorf, E. Xie, I. M. Watson, N. Laurand, and M. D. Dawson. Planar micro-and nano-patterning of gan light-emitting diodes: Guidelines and limitations. *J. Appl. Phys.*, 115(8):084503, 2014.

[131] V. Poher, N. Grossman, G. T. Kennedy, K. Nikolic, H. X. Zhang, Z. Gong, E. M. Drakakis, E. Gu, M. D. Dawson, P. M. W. French, P. Degenaar, and M. A. A. Neil. Micro-LED arrays: a tool for two-dimensional neuron stimulation. *J. Phys. D: Appl. Phys.*, 41(9):094014, 2008.

[132] D. Vettese. Microdisplays: Liquid crystal on silicon. *Nature Photon.*, 4(11):752–754, 2010.

[133] S. R. Forrest. The path to ubiquitous and low-cost organic electronic appliances on plastic. *Nature*, 428(6986):911–918, 2004.

[134] G. Heliotis, P. N. Stavrinou, D. D. C. Bradley, E. Gu, C. Griffin, C. W. Jeon, and M. D. Dawson. Spectral conversion of InGaN ultraviolet microarray light-emitting diodes using fluorene-based red-, green-, blue-, and white-light-emitting polymer overlayer films. *Appl. Phys. Lett.*, 87(10): 103505, 2005.

[135] M. Wu, Z. Gong, A. J. Kuehne, A. L. Kanibolotsky, Y. J. Chen, I. F. Perepichka, A. R. Mackintosh, E. Gu, P. J. Skabara, R. A. Pethrick, and M. D. Dawson. Hybrid GaN/organic microstructured light-emitting devices via ink-jet printing. *Opt. Express*, 17(19):16436–16443, 2009.

[136] B. Guilhabert, A. Kuehne, D. Massoubre, H. X. Zhang, S. R. Jin, A. R. Mackintosh, E. Gu, R. Pethrick, and M. D. Dawson. Integration by self-aligned writing of nanocrystal/epoxy composites on InGaN micro-pixelated light-emitting diodes. *Opt. Express*, 16(23):18933–18941, 2008.

[137] C. F. Lu, C. F. Huang, Y. S. Chen, W. Y. Shiao, C. Y. Chen, Y. C. Lu, and C. C. Yang. Phosphor-free monolithic white-light LED. *IEEE J. Sel. Top. Quant. Electron.*, 15(4):1210–1217, 2009.

[138] B. Damilano, H. Kim-Chauveau, E. Frayssinet, J. Brault, S. Hussain, K. Lekhal, P. Vennéguès, P. D. Mierry, and J. Massies. Metal organic vapor phase epitaxy of monolithic two-color light-emitting diodes using an InGaN-based light converter. *Appl. Phys. Express*, 6(9):092105, 2013.

[139] S. Lee, H. S. Paek, H. Kim, T. Jang, and Y. Park. Monolithic InGaN-based white light-emitting diodes with blue, green, and amber emissions. *Appl. Phys. Lett.*, 92(8):081107–081107, 2008.

[140] I. Ozden, E. Makarona, A. V. Nurmikko, T. Takeuchi, and M. Krames. A dual-wavelength indium gallium nitride quantum well light emitting diode. *Appl. Phys. Lett.*, 79(16):2532–2534, 2001.

[141] N. Otsuji, K. Fujiwara, and J. K. Sheu. Electroluminescence efficiency of blue InGaN/ GaN quantum-well diodes with and without an n-InGaN electron reservoir layer. *J. Appl. Phys.*, 100 (11):113105, 2006.

[142] C. Huang, C. Chen, C. Lu, and C. C. Yang. Reduced injection current induced blueshift in an InGaN/GaN quantum-well light-emitting diode of prestrained growth. *Appl. Phys. Lett.*, 91(5): 051121, 2007.

[143] K. S. Kim, M. G. Cheong, C. H. Hong, G. M. Yang, K. Y. Lim, E. K. Suh, and H. J. Lee. Hole transport in Mg-doped GaN epilayers grown by metalorganic chemical vapor deposition. *Appl. Phys. Lett.*, 76(9):1149–1151, 2000.

[144] S. X. Jin, J. Shakya, J. Y. Lin, and H. X. Jiang. Size dependence of III-nitride microdisk light-emitting diode characteristics. *Appl. Phys. Lett.*, 78(22):3532–3534, 2001.

[145] E. F. Schubert and J. K. Kim. Solid-state light sources getting smart. *Science*, 308(5726):1274–1278, 2005.

[146] M. Atef, R. Swoboda, and H. Zimmermann. 250 Mbit/s over 100 m SI-POF with RCLED source using integrated post-equaliser. *Electron. Lett.*, 48(12):718–720, 2012.

[147] D. Visani, C. Okonkwo, S. Loquai, H. Yang, Y. Shi, H. V. D. Boom, T. Ditewig, G. Tartarini, J. Lee, T. Koonen, and E. Tangdiongga. Beyond 1 Gbit/s transmission over 1 mm diameter plastic optical fiber employing DMT for in-home communication systems. *J. Lightw. Technol.*, 29 (4):622–628, 2011.

[148] M. M. Dumitrescu, M. J. Saarinen, M. D. Guina, and M. V. Pessa. High-speed resonant cavity light-emitting diodes at 650 nm. *IEEE J. Sel. Topics Quantum Electron.*, 8(2):219–230, 2002.

[149] I. Mollers, D. Jager, R. Gaudino, A. Nocivelli, H. Kragl, O. Ziemann, N. Weber, T. Koonen, C. Lezzi, A. Bluschke, and S. Randel. Plastic optical fiber technology for reliable home networking: overview and results of the EU project pof-all. *IEEE Commun. Mag.*, 47(8):58–68, 2009.

[150] H. Le Minh, D. O'Brien, G. Faulkner, L. Zeng, K. Lee, D. Jung, Y. Oh, and E. T. Won. 100-Mb/s NRZ visible light communications using a postequalized white LED. *IEEE Photon. Technol. Lett.*, 21(15):1063–1065, 2009.

[151] J. Vucic, C. Kottke, S. Nerreter, A. Buttner, K-D. Langer, and J. Walewski. White light wireless transmission at 200 Mb/s net data rate by use of discrete-multitone modulation. *IEEE Photon. Technol. Lett.*, 21(20):1511–1513, 2009.

[152] J. R. Lakowicz. Principles of Fluorescence Spectroscopy. *Springer, 3rd edition*, 2006.

[153] Data source: `http://www.evidenttech.com/`.

[154] J. H. L. Herrnsdorf. Organic lasers and nanostructured organic films for hybrid integration. *PhD thesis, University of Strathclyde*, 2012.

[155] H. Rabbani-Haghighi, S. Forget, S. Chénais, A. Siove, M. Castex, and E. Ishow. Laser operation in nondoped thin films made of a small-molecule organic red-emitter. *Appl. Phys. Lett.*, 95(3): 033305, 2009.

[156] N. Laurand, B. Guilhabert, J. J. D. McKendry, A. E. Kelly, B. Rae, D. Massoubre, Z. Gong, E. Gu, R. Henderson, and M. D. Dawson. Colloidal quantum dot nanocomposites for visible wavelength conversion of modulated optical signals. *Opt. Mater. Express*, 2(3):250–260, 2012.

[157] A. F. Van Driel, G. Allan, C. Delerue, P. Lodahl, W. L. Vos, and D. Vanmaekelbergh. Frequency-dependent spontaneous emission rate from CdSe and CdTe nanocrystals: influence of dark states. *Phys. Rev. Lett.*, 95(23):236804, 2005.

[158] C. R. Belton, G. Itskos, G. Heliotis, P. N. Stavrinou, P. G. Lagoudakis, J. Lupton, S. Pereira, E. Gu, C. Griffin, B. Guilhabert, I. M. Watson, A. R. Mackintosh, R. A. Pethrick, J. Feldmann, R. Murray, M. D. Dawson, and D. D. C. Bradley. New light from hybrid inorganic-organic emitters. *J. Phys. D: Appl. Phys.*, 41(9):094006, 2008.

[159] A. Rose, Z. Zhu, C. F. Madigan, T. M. Swager, and V. Bulović. Sensitivity gains in chemosensing by lasing action in organic polymers. *Nature*, 434(7035):876–879, 2005.

[160] Y. Chen, J. Herrnsdorf, B. Guilhabert, A. L. Kanibolotsky, A. R. Mackintosh, Y. Wang, R. A. Pethrick, E. Gu, G. A. Turnbull, P. J. Skabara, I. D.W. Samuel, N. Laurand, and M. D. Dawson. Laser action in a surface-structured free-standing membrane based on a π-conjugated polymer-composite. *Org. Electron.*, 12(1):62–69, 2011.

[161] Y. Chen, Y. Zhang, N. Laurand, A. L. Kanibolotsky, E. Gu, P. J. Skabara, and M. D. Dawson. Organic polymer composite random laser operating underwater. *Opt. Lett.*, 37(24):5160–5162, 2012.

[162] J. Herrnsdorf, B. Guilhabert, Y. Chen, A. Kanibolotsky, A. Mackintosh, R. Pethrick, P. Skabara, E. Gu, N. Laurand, and M. D. Dawson. Flexible blue-emitting encapsulated organic semiconductor DFB laser. *Opt. Express*, 18(25):25535–25545, 2010.

[163] J. Herrnsdorf, B. Guilhabert, J. J. D. McKendry, Z. Gong, D. Massoubre, S. Zhang, S. Watson, A. E. Kelly, E. Gu, N. Laurand, and M. D. Dawson. Hybrid organic/GaN photonic crystal light-emitting diode. *Appl. Phys. Lett.*, 101(14):141122, 2012.

[164] H. Chun, P. Manousiadis, S. Rajbhandari, D. A. Vithanage, G. Faulkner, D. Tsonev, J. J. D. McKendry, S. Videv, E. Xie, E. Gu, M. D. Dawson, H. Haas, G. A. Turnbull, I. D. W. Samuel, and D. C. O'Brien. Visible light communication using a blue GaN μLED and fluorescent polymer colour converter. *IEEE Photon. Technol. Lett.*, 26(20):2035–2038, 2014.

[165] S. M. Sze and K. K. Ng. Physics of Semiconductor Devices. *John Wiley & Sons*, 2006.

[166] M. Ershov, H. C. Liu, L. Li, M. Buchanan, Z. R. Wasilewski, and A. K. Jonscher. Negative capacitance effect in semiconductor devices. *IEEE Trans. Electron Dev.*, 45(10):2196–2206, 1998.

[167] J. Werner, A. F. J. Levi, R. T. Tung, M. Anzlowar, and M. Pinto. Origin of the excess capacitance at intimate Schottky contacts. *Phys. Rev. Lett.*, 60(1):53, 1988.

[168] A. G. U. Perera, W. Z. Shen, M. Ershov, H. C. Liu, M. Buchanan, and W. J. Schaff. Negative capacitance of GaAs homojunction far-infrared detectors. *Appl. Phys. Lett.*, 74(21):3167–3169, 1999.

[169] C. D. Wang, C. Y. Zhu, G. Y. Zhang, J. Shen, and L. Li. Accurate electrical characterization of forward AC behavior of real semiconductor diode: giant negative capacitance and nonlinear interfacial layer. *IEEE Trans. Electron Dev.*, 50(4):1145–1148, 2003.

[170] L. F. Feng, Y. Li, C. Y. Zhu, H. X. Cong, and C. D. Wang. Negative terminal capacitance of light emitting diodes at alternating current (AC) biases. *IEEE J. Quant. Electron.*, 46(7):1072–1075, 2010.

[171] Y. Li, C. D. Wang, L. F. Feng, C. Y. Zhu, H. X. Cong, D. Li, and G. Y. Zhang. Elucidating negative capacitance in light-emitting diodes using an advanced semiconductor device theory. *J. Appl. Phys.*, 109(12):124506, 2011.

[172] L. F. Feng, Y. Li, D. Li, X. D. Hu, W. Yang, C. D. Wang, and Q. Y. Xing. Precise relationship between voltage and frequency at the appearance of negative capacitance in InGaN diodes. *Appl. Phys. Lett.*, 101(23):233506, 2012.

[173] K. Bansal and S. Datta. Voltage modulated electro-luminescence spectroscopy to understand negative capacitance and the role of sub-bandgap states in light emitting devices. *J. Appl. Phys.*, 110(11):114509, 2011.

[174] C. Y. Zhu, L. F. Feng, C. D. Wang, H. X. Cong, G. Y. Zhang, Z. J. Yang, and Z. Z. Chen. Negative capacitance in light-emitting devices. *Solid-State Electron.*, 53(3):324–328, 2009.

[175] J. Shulman, Y. Y. Xue, S. Tsui, F. Chen, and C. W. Chu. General mechanism for negative capacitance phenomena. *Phys. Rev. B*, 80(13):134202, 2009.

[176] S. Zhang, S. Watson, J. J. D. McKendry, D. Massoubre, A. Cogman, E. Gu, R. K. Henderson, A. E. Kelly, and M. D. Dawson. 1.5 Gbit/s multi-channel visible light communications using CMOS-controlled GaN-based LEDs. *J. Lightwave Technol.*, 31(8):1211–1216, 2013.

[177] N. McAlinden, D. Massoubre, E. Richardson, E. Gu, S. Sakata, M. D. Dawson, and K. Mathieson. Thermal and optical characterization of micro-led probes for in vivo optogenetic neural stimulation. *Opt. Lett.*, 38(6):992–994, 2013.

[178] K. Bansal and S. Datta. Temperature dependent reversal of voltage modulated light emission and negative capacitance in AlGaInP based multi quantum well light emitting devices. *Appl. Phys. Lett.*, 102(5):053508, 2013.

[179] N. L. Ploch, H. Rodriguez, C. Stoelmacker, M. Hoppe, M. Lapeyrade, J. Stellmach, F. Mehnke, T. Wernicke, A. Knauer, V. Kueller, M. Weyers, S. Einfeldt, and M. Kneissl. Effective thermal management in ultraviolet light-emitting diodes with micro-LED arrays. *IEEE Trans. Electron Dev.*, 60(2):782–786, 2013.

[180] L. Hirsch and A. S. Barriere. Electrical characterization of InGaN/GaN light emitting diodes grown by molecular beam epitaxy. *J. Appl. Phys.*, 94(8):5014–5020, 2003.

[181] R. H. Kim, D. H. Kim, J. Xiao, B. H. Kim, S. Park, B. Panilaitis, R. Ghaffari, J. Yao, M. Li, Z. Liu, V. Malyarchuk, D. G. Kim, A. P. Le, R. G. Nuzzo, F. G. Kaplan, D. L.and Omenetto, Y. Huang, Z Kang, and J. A. Rogers. Waterproof AlInGaP optoelectronics on stretchable substrates with applications in biomedicine and robotics. *Nat. Mater.*, 9(11):929–937, 2010.

[182] R. H. Kim, H. Tao, T. Kim, Y. Zhang, S. Kim, B. Panilaitis, M. Yang, D. H. Kim, Y. H. Jung, B. H. Kim, Y. Li, Y. Huang, F. G. Omenetto, and J. A. Rogers. Materials and designs for wirelessly powered implantable light-emitting systems. *Small*, 8(18):2812–2818, 2012.

[183] T. Kim, Y. H. Jung, J. Song, D. Kim, Y. Li, H. Kim, I. Song, J. J. Wierer, H. A. Pao, Y. Huang, and J. A. Rogers. High-efficiency, microscale GaN light-emitting diodes and their thermal properties on unusual substrates. *Small*, 8(11):1643–1649, 2012.

[184] A. Russo, B. Y. Ahn, J. J. Adams, E. B. Duoss, J. T. Bernhard, and J. A. Lewis. Pen-on-paper flexible electronics. *Adv. Mater.*, 23(30):3426–3430, 2011.

[185] A. J. Trindade, B. Guilhabert, D. Massoubre, D. Zhu, N. Laurand, E. Gu, I. M. Watson, C. J. Humphreys, and M. D. Dawson. Nanoscale-accuracy transfer printing of ultra-thin AlInGaN light-emitting diodes onto mechanically flexible substrates. *Appl. Phys. Lett.*, 103(25):253302, 2013.

[186] J. Chun, Y. Hwang, Y. S. Choi, T. Jeong, J. H. Baek, H. C. Ko, and S. J. Park. Transfer of GaN LEDs from sapphire to flexible substrates by laser lift-off and contact printing. *IEEE Photon. Technol. Lett.*, 24(23):2115–2118, 2012.

[187] Y. Wang, P. O. Morawska, A. L. Kanibolotsky, P. J. Skabara, G. A. Turnbull, and I. D. W. Samuel. Led pumped polymer laser sensor for explosives. *Laser Photon. Rev.*, 7(6):L71–L76, 2013.

[188] Y. Yang, I. D. W. Samuel, and G. A. Turnbull. The development of luminescent concentrators for pumping organic semiconductor lasers. *Adv. Mater.*, 21(31):3205–3209, 2009.

[189] Y. Yang, G. A. Turnbull, and I. D. W. Samuel. Hybrid optoelectronics: A polymer laser pumped by a nitride light-emitting diode. *Appl. Phys. Lett.*, 92(16):163306, 2008.

[190] G. Tsiminis, Y. Wang, A. L. Kanibolotsky, A. R. Inigo, P. J. Skabara, I. D. W. Samuel, and G. A. Turnbull. Nanoimprinted organic semiconductor laser pumped by a light-emitting diode. *Adv. Mater.*, 25(20):2826–2830, 2013.

[191] J. Herrnsdorf, Y. Wang, J. J. D. McKendry, Z. Gong, D. Massoubre, B. Guilhabert, G. Tsiminis, G. A. Turnbull, I. D. W. Samuel, N. Laurand, E. Gu, and M. D. Dawson. Micro-LED pumped polymer laser: A discussion of future pump sources for organic lasers. *Laser Photon. Rev.*, 7(6): 1065–1078, 2013.

List of Publications

Journals

Drafted/submitted

1. S. Zhang, E. Xie, T. Yan, W. Yang, J. Herrnsdorf, Z. Gong, I. M. Watson, E. Gu, M. D. Dawson, and X. Hu, "Effective hole transportation into bottom QWs assisted by piezoelectric field in dual-wavelength high-indium-content GaN micro light-emitting diodes", **in preparation**.

2. J. Herrnsdorf, J. J. D. McKendry, S. Zhang, E. Xie, R. Ferreira, D. Massoubre, A. M. Zuhdi, R. K. Henderson, I. Underwood, S. Watson, A. E. Kelly, E. Gu, and M. D. Dawson, "Active-matrix GaN micro light-emitting diode display with unprecedented brightness", **submitted to *IEEE Transactions on Electron Devices***.

Published

3. W. Yang, S. Zhang, J. J. D. McKendry, J. Herrnsdorf, P. Tian, Z. Gong, Q. Ji, I. M. Watson, E. Gu, M. D. Dawson, L. Feng, C. Wang, and X. Hu, "Size-dependent capacitance study on InGaN-based blue micro-light-emitting diodes", *Journal of Applied Physics*, vol. 110, no. 3, pp. 033114, 2014. **S. Zhang is the shared first author of this paper.**

4. P. Tian, J. J. D. McKendry, Z. Gong, S. Zhang, S. Watson, D. Zhu, I. M. Watson, E. Gu, A. E. Kelly, C. J. Humphreys, and M. D. Dawson, "Characteristics and applications of micro-pixelated GaN-based light emitting diodes on Si substrates", *Journal of Applied Physics*, vol. 115, no. 3, pp. 033112, 2014.

5. S. Zhang, S. Watson, J. J. D. McKendry, D. Massoubre, A. Cogman, E. Gu, R. K. Henderson, A. E. Kelly, and M. D. Dawson, "1.5 Gbit/s multi-channel visible light communications using CMOS-controlled GaN-based LEDs", *Journal of Lightwave Technology*, vol.

31, no. 8, pp. 1211-1216, 2013. **Front cover of *Journal of Lightwave Technology*, 2013 issue.**

6. S. Zhang, Z. Gong, J. J. D. McKendry, S. Watson, A. Cogman, E. Xie, P. Tian, E. Gu, Z. Chen, G. Zhang, A. E. Kelly, R. K. Henderson, and M. D. Dawson, "CMOS-Controlled Color-Tunable Smart Display", *IEEE Photonics Journal*, vol. 4, no. 5, pp. 1639-1646, 2012.

7. J. Herrnsdorf, B. Guilhabert, J. J. D. McKendry, Z. Gong, D. Massoubre, S. Zhang, S. Watson, A. E. Kelly, E. Gu, N. Laurand, and M. D. Dawson, "Hybrid organic/GaN photonic crystal light-emitting diode", *Applied Physics Letters*, vol. 101, no.14, pp. 141122, 2012.

8. J. J. D. McKendry, D. Massoubre, S. Zhang, B. R. Rae, R. P. Green, E. Gu, R. K. Henderson, A. E. Kelly, and M. D. Dawson, "Visible-light communications using a CMOS-controlled micro-light-emitting-diode array", *Journal of Lightwave Technology*, vol. 30, no. 1, pp. 61-67, 2012.

Conferences

(Presenter highlighted by bold letters)

9. P. Tian, J. J. D. McKendry, Z. Gong, S. Zhang, S. Watson, D. Zhu, I. M. Watson, E. Gu, A. E. Kelly, C. J. Humphreys, and **M. D. Dawson**, "Characteristics and applications of InGaN micro-light emitting diodes on Si substrates", (Oral), *2013 IEEE Photonics Conference* (Seattle, Washington, USA, September 2013). Detailed paper (ME3.6) in conference proceedings, page: 97-98.

10. P. Tian, J. J. D. McKendry, Z. Gong, S. Zhang, S. Watson, D. Zhu, I. M. Watson, E. Gu, A. E. Kelly, **C. J. Humphreys**, and M. D. Dawson, "Micro-pixelated InGaN/GaN light emitting diodes on Si substrates", (Oral) *10th International Conference on Nitride Semiconductors* (Washington, D.C., USA, August, 2013).

11. **J. J. D. McKendry**, L. Geng, S. Zhang, S. Watson, D. Massoubre, M. Haji, E. Gu, A. E. Kelly, R. V. Penty, I. H. White, and M. D. Dawson, "Gigabit data transmission over 10m polymer optical fiber using a blue-emitting micro-light-emitting diode", (Oral), *UK Nitrides Consortium 2013 Annual Conference* (Cardiff, UK, January 2013).

12. **S. Watson**, J. J. D. McKendry, S. Zhang, D. Massoubre, B. R. Rae, R. P. Green, E. Gu, R. K. Henderson, A. E. Kelly, and M. D. Dawson, "High speed GaN micro-light-emitting

diode arrays for data communications", (Oral), *SPIE 2012 conference*, (Edinburgh, UK, October 2012). Detailed paper in conference proceedings, volumn: 8540.

13. S. Zhang, S. Watson, J. J. D. McKendry, D. Massoubre, A. Cogman, E. Gu, R. K. Henderson, A. E. Kelly, and **M. D. Dawson**, "High-bandwidth parallel data transmission using GaN/CMOS micro-LED array", (Oral), *2012 IEEE Photonics Conference* (San Francisco, California, USA, September, 2012). Detailed paper (ME5) in conference proceedings, page: 38-39.

14. S. Zhang, J. J. D. McKendry, Z. Gong, B. R. Rae, S. Watson, E. Xie, P. Tian, **E. Richardson**, E. Gu, Z. Chen, G. Zhang, A. E. Kelly, R. K. Henderson, and M. D. Dawson, "Directly color-tunable smart display based on a CMOS-controlled micro-LED array", (Oral), *2012 IEEE Photonics Conference* (San Francisco, California, USA, September 2012). Detailed paper (WC5) in conference proceedings, page: 435-436.

15. **J. J. D. McKendry**, S. Zhang, S. Watson, J. Herrnsdorf, D. Massoubre, A. Cogman, B. Guilhabert, N. Laurand, E. Gu, R. K. Henderson, A. E. Kelly and M. D. Dawson, "Micro-pixellated light-emitting diode arrays: novel sources for data transmission over POF", (Invited talk), *21st International Conference On Plastic Optical Fibres* (Georgia, Atlanta, USA, September 2012).

16. **S. Zhang**, Z. Gong, J. J.D. McKendry, B. R. Rae, S. Watson, E. Gu, Z. Chen, G. Zhang, A. E. Kelly, R. K. Henderson, and M. D. Dawson, "Colour-tuneable inorganic microdisplay based on a CMOS-controlled III-nitride micro-LED array", (Oral), *9th International Symposium on Semiconductor Light Emitting Devices* (Berlin, Germany, July 2012).

17. **A. E. Kelly**, J. J. D. McKendry, S. Zhang, D. Massoubre, B. R. Rae, R. P. Green, R. K. Henderson, and M. D. Dawson, "High-speed GaN micro-LED arrays for data communications", (Invited talk), *14th International Conference on Transparent Optical Networks* (Coventry, UK, July 2012). Detailed paper (We.B4.2) in conference proceedings, page: 1-5.

18. **J. J. D. McKendry**, S. Zhang, D. Massoubre, E. Gu, R. K. Henderson, A. E. Kelly and M.D. Dawson, "Data communications with gallium nitride LEDs", (Oral), *UK Nitrides Consortium 2012 Annual Conference* (Bath, UK, January 2012).

19. **J. Herrnsdorf**, B. Guilhabert, J. J. D. McKendry, Z. Gong, D. Massoubre, Y. Chen, S. Zhang, A. L. Kanibolotsky, A. R. Mackintosh, P. J. Skabara, A. E. Kelly, E. Gu, N. Laurand and M. D. Dawson, "Hybrid GaN/organic polymer photonic crystal LED", (Oral), *2011 IEEE Photonics Conference* (Arlington, Virginia, USA, October 2011). Detailed paper (TuX3) in conference proceedings, page: 389-390.

20. **J. J. D. McKendry**, A. E. Kelly, S. Zhang, J. Vinogradov, D. Massoubre, B. R. Rae, R. P. Green, N. Laurand, E. Gu, O. Ziemann, R. K. Henderson and M.D. Dawson, "High-Speed GaN Micro-LED Arrays for Data Communications", (Invited talk), *the 20th International Conference on Plastic Optical Fibres* (Bilbao, Spain, September 2011).

21. J. J. D. McKendry, S. Zhang, A. E. Kelly, B. R. Rae, D. Massoubre, Z. Gong, E. Gu, R. K. Henderson and M. D. Dawson, "CMOS-controlled micro-LED arrays for visible light communications", (Poster), *9th International Conference on Nitride Semiconductors* (Glasgow, UK, July 2011).